Numéro d'ordre : 102076

Doctoral School : Sciences pour l'ingenieur nº 072

PH. D. THESIS

In order to become doctor from

University of Lille

Speciality "Construction Robotics"

Presented and defended by

Othman Lakhal

on November 16, 2018

Contribution to the modeling and control of hyper-redundant robots: application to additive manufacturing in the construction

Committee members

Pr. Geneviève DAUPHIN-TANGUY	Central Lille, France	President
Pr. Kamal YOUCEF-TOUMI	Massachusetts Institute of Technology, USA	Reviewer
Pr. Abdelaziz BENALLEGUE	University of Versailles S.Q.Y., France	Reviewer
Pr. Sergey DRAKUNOV	Embry-riddle Aeronautical University, USA	Examiner
Pr. Antonella MASTRORILLI	ENSAPL School, France	Examiner
Dr. Achille MELINGUI	University of Yaoundé 1, Cameroon	Examiner
Pr. Rochdi MERZOUKI	University of Lille, France	Supervisor

Centre de Recherche en Informatique Signal et Automatique de Lille (CRIStAL)
UMR CNRS 9189, GROUPE CI2S ; ÉQUIPE MOCIS

Numéro d'ordre : 102076

Doctoral School : Sciences pour l'ingenieur nº 072

THÈSE

pour obtenir le grade de docteur delivre par

l'université de Lille

Spécialité : "Automatique, productique"

présentée et soutenue publiquement par

Othman Lakhal

le 16 novembre 2018

Contribution à la modélisation et à la commande des robots hyper-redondants : application à l'impression additive dans la construction

Jury

Pr. Geneviève DAUPHIN-TANGUY	Central Lille, France	Presidente
Pr. Kamal YOUCEF-TOUMI	Massachusetts Institute of Technology, USA	Rapporteur
Pr. Abdelaziz BENALLEGUE	University of Versailles S.Q.Y., France	Rapporteur
Pr. Sergey DRAKUNOV	Embry-riddle Aeronautical University, USA	Examinateur
Pr. Antonella MASTRORILLI	ENSAPL School, France	Examinateur
Dr. Achille MELINGUI	University of Yaoundé 1, Cameroon	Examinateur
Pr. Rochdi MERZOUKI	University of Lille, France	Superviseur

Centre de Recherche en Informatique Signal et Automatique de Lille (CRIStAL)
UMR CNRS 9189, GROUPE CI2S ; ÉQUIPE MOCIS

Université de Lille Sciences et Technologies
École Polytech Lille
École Doctorale Sciences pour l'Ingénieur
Centre de Recherche en Informatique Signal et Automatique de Lille
Équipe Méthodes et Outils pour la Conception Intégrée de Systèmes
Cité Scientifique
Boulevard Paul Langevin
59655 Villeneuve d'Ascq
France.

Abstract

Additive manufacturing technology has been identified as one of the major digital innovations that has revolutionized not only industry, but also building. From a research point of view, additive manufacturing remains a very relevant topic. It is an automated process for depositing materials layer by layer to print houses or small structures for on-site assembly. In additive manufacturing processes, the deposition of materials is generally followed by a printing quality control step. However, the geometry of structures printed with funicular surfaces is sometimes complex, as robots with rigid structures cannot reach certain areas of the structure to be inspected. In this thesis, a flexible and highly redundant manipulator equipped with a camera is attached to the end-effector of a mobile manipulator robot for the quality inspection process of the printed structures. Indeed, soft manipulators can bend along their surrounded 3D objects; and this inherent flexibility makes them suitable for navigation in crowded environments. As the number of controlled actuators is greater than the dimension of the workspace, this thesis can be summarized as a trajectory tracking of hyper-redundant robots. In this thesis, a hybrid approach that combines the advantages of model-based approaches and learning-based approaches is developed to model and solve the kinematics of soft and hyper-redundant manipulators. The principle is to develop mathematical models with reasonable assumptions, and to improve their accuracy through learning processes. The performance of the proposed approach is validated by performing a series of simulations and experiments applied to the Compact Bionic Handling Arm (CBHA) robot.

Résumé

La technologie de fabrication additive a été identifiée comme l'une des innovations numériques majeures qui a révolutionné non seulement le domaine de l'industrie, mais aussi celui de la construction. D'un point de vue de recherche, la fabrication additive reste un sujet d'actualité. C'est un procédé automatisé de dépôt de matériaux couche par couche afin d'imprimer des maisons ou des structures de petites dimensions pour un montage sur site. Dans la fabrication additive, l'étape de dépôt des matériaux est généralement suivie d'une étape de contrôle de la qualité d'impression. Cependant, le contrôle de qualité des objets imprimés ayant des surfaces funiculaires est parfois complexe à réaliser avec des robots rigides, ne pouvant atteindre des zones mortes. Dans cette thèse, un manipulateur souple et hyper-redondant a été modélisé et commandé cinématiquement, placé comme un effecteur d'un manipulateur rigide et mobile, afin d'effectuer une inspection des structures imprimées par des techniques de la fabrication additive. En effet, les manipulateurs souples peuvent fléchir et du coup suivre la forme géométrique de surfaces funiculaires. Ainsi, une approche hybride a été proposée pour modéliser la cinématique du robot souple et hyper-redondant, combinant une approche analytique pour la génération des équations cinématiques et une méthode qualitative à base des réseaux de neurones pour la résolution de ces dernières. Les performances de l'approche proposée sont validées à travers des expériences réalisées sur le robot CBHA.

To my wife Ghada, who supported and encouraged me throughout the writing of this thesis.

Acknowledgement

I have been able to complete this research program with the support and active cooperation of concerned bodies and authorities and several persons. I owe my debt and would like to express my deep feelings of gratitude to my teacher and thesis supervisor, Pr.Rochdi Merzouki for giving me the opportunity to bring out my knowledge. His support, his encouragements and wise guidance allowed me to complete this work.

I would like to acknowledge Pr.Belkacem Ould Bouamama, director of the Methods and Tools for Integrated Systems Design group (MOCIS) for welcoming me, and for giving me the opportunity to integrate an interesting research group. My thanks also go to the members of the MOCIS team at the CRIStAL laboratory for the valuable exchanges that we had during the research.

I would also like to thank Pr.Kamal Youcef-Toumi, Massachusetts Institute of Technology, USA and Pr.Abdelaziz Benallegue, University of Versailles S.Q.Y., France who have honored me with the privilege of being the reviewers for this work. I would like to thank them for their critical and relevant opinions, their advices and their good disposition towards my manuscript.

I would like to thank Pr.Geneviève Dauphin-Tanguy, Central Lille, for the honour he has granted me by chairing the jury members.

I express my sincere thanks to Pr. Sergey Drakunov, Embry-riddle Aeronautical University, USA, Pr.Antonella Mastrorilli, ENSAPL School, France and Associate Professor Achille Melingui, University of Yaoundé 1, Cameroon, for participating as members of my thesis committee.

I also thank all the members of the jury for their constructive comments and for all the fruitful discussions we had as well as the fresh view they add at my work.

I would also like to express my deep gratitude to Professor Taha Chettibi and Achille Melingui for their invaluable help. I appreciated all their contributions, their detailed corrections and their long support and help.

It is with great pleasure that I thank the laboratory technicians Mr. Michel Pollart and Mr. Olivier Scrive, as well as the lab Engineers Mr. Abdelkader Belarouci and Doc. Vincent Coelen, with whom I had the pleasure of sharing a part of my work. They have invested a lot of time and energy working with me on this topic. Their cooperation has been very fruitful.

I also thanks Mr. Gerald Dherbomez CNRS research engineer that was great support

for the last technical experiences.

I would also like to thank the AIP cluster for providing me with several equipment that allowed me to achieve my research.

My thanks also go to my colleagues and friends of the MOCIS team for the enriching exchanges that it has had in the context of the research.

I would also like to thank all members of the MATRICE project for their very constructive support and cooperation. Mainly Renaud, Mohammad, Francesco, Sebastien, Noura, Vincent, Thierry, Antonella et Eric

I would also like to thank Mr. Zoubeir Lafhaj, teacher at Central school for his precious help and for the provision of the pump which allowed us to advance on the project.

I also thank my colleagues for their friendship and help, especially Blaise, Aziz, Nizar, Mohit, Pushpendra, Thor, Xian, Mayank, Nicolas, Coralie, Achille, Ziad, Mahdi, Adel, Ismail, Inderjeet, ... I appreciated that they awarded me: technical and scientific help, writing tips and moral support.

I would like to thank the members of the Xperium project who have set up a specially arranged and scripted to welcome the public and present my scientific experiences.

I express also my thanks to the INRIA research institute for providing the measuring instruments. The support of engineer Mario Sanz was very important.

A deeper way, I want to thank my parents who have consistently supported me in my choices and have done everything that I succeed in my studies. I would also like to thank my parents-in-law for their constant support while throughout my PhD.

Finally, I reserve a singular place for my wife Ghada for her trust, support and love.

Contents

List of Figures

List of Tables

Chapter 1

General Introduction

Contents

1.1 Contractual setting context: The MATRICE project

This research work has been conducted within the MATRICE[1] project (2015-2017) which was co-funded by the FEDER[2] and the region Haut-de-France (HDR) [3] in France. The project has involved eight multidisciplinary higher education institutes and aimed at experimenting on additive manufacturing in the construction sector. This was achieved through a scientific co-operation between researchers and engineers specialized in: architectural design, computing, robotics, and materials. The main purpose was to develop a new concept of additive manufacturing in case of complex geometrical shapes of objects in the construction domain. There are five work packages (WPs) in MATRICE project (Figure 1.1), described as follows:

WP1 : 3D shape : Piloted by the National School of Architecture and Landscape of Lille (ENSPL[4]), which was interested in the theory of minimal and funicular shape as

[1] http://www.matrice-impression3d.fr
[2] European Regional Development Funds, Fund created in 1975.
[3] www.hautsdefrance.fr
[4] http://www.lille.archi.fr/

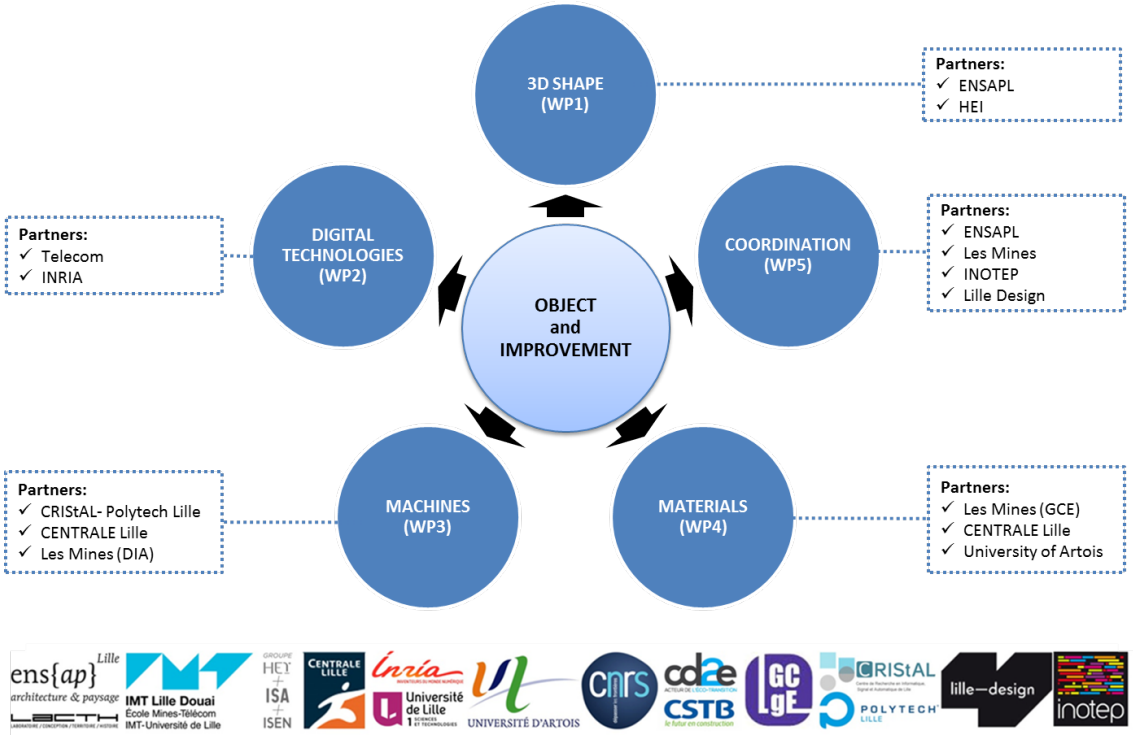

Figure 1.1 – Description of the actors of the MATRICE project

characterized by architectonic elements, that are hard to realize through conventional methods of Construction. Additive Manufacturing makes it possible to deal with pertaining to mechanical behavior and form topological optimization.

WP2 : Digital technologies : Piloted by the National Institute of Research in Computer Science and Automation (INRIA[5]) with the contribution of Computer and Network Department (DIR) of the IMT institute of Lille-Douai [6] which have carried out the research work about the human machine interface. This consists in adapting or developing from exiting digital tools as a human-machine interface in the context of additive manufacturing.

WP3 : Machines : Piloted by the Research Centre in Computer Science, Signal and Automation of Lille (CRIStAL[7]) at Polytech[8] institute of the University of Lille[9] and with the collaboration of CENTRALE Lille[10] and the Computer and Automatic Department (DIA) at the IMT Lille-Douai. The aim of this WP is to design two types of machines for the additive manufacturing based on cement and clay materials. One machine would be mobile so that it can be used for both indoor or outdoor construction sites, whereas the second machine would be intended for the prefabrication.

WP4 : Materials : Piloted by the Department of Civil and Environmental Engineering (GCE) at the IMT Lille-Douai, with the participation of University of Artois [11], the

[5]https://www.inria.fr/centre/lille
[6]http://imt-lille-douai.fr/
[7]https://www.cristal.univ-lille.fr/
[8]http://www.polytech-lille.fr/ecole-d-ingenieurs.html
[9]https://www.univ-lille.fr/
[10]http://centralelille.fr/
[11]http://www.univ-artois.fr/

Laboratory of Civil Engineering and Geo-Environment (LGCgE) and the Labo-ratory of Mechanics of Lille (LML), which have been working on the elaboration and sustainable cement and clay formulations for the context of additive manufacturing.

WP5 : Coordination : It involves the spreading among a large public of the research results conducted within the MATRICE project. This goal is to be achieved through several testing campaign and regional events.

1.2 Research and development context

Additive manufacturing technology [12] has been identified as one of the major digital innovations that revolutionized not only the field of industry but also that of construction. Indeed, additive manufacturing in the field of construction is one of the emerging techniques, drawing on similar 3D printing methods for the production of sequentially stratified objects (Gardiner and Janssen, 2014).

Furthermore, additive manufacturing in the building sector is regarded as a breakthrough method that combines cost effectiveness and affordability besides being environmentally friendly. It can also enhance both efficiency and safety in the workplace and helps to save time in a considerable manner (Mathur, 2016). Roughly speaking, we can distinguish two eras in building development. The first one is a prehistorical period during which building took considerable time but was unique and customized. The second one is a post-historical era where building has become faster thanks to intensive production, but has lost its uniqueness. Thus, additive manufacturing has bridged the gap between customization and productivity.

From a research point of view, additive manufacturing in construction is a multidisciplinary process, combining the '**shape**' with its geometric properties, the '**Material**' with its sustainability and the '**Machine**' which improves productivity. For this reason, the design of performing additive manufacturing concept in the field of the construction is based on a compromise between the shape, the material, and the machine.

Several laboratories have been working on the design of machines for additive manufacturing, based on the principle of rapid prototyping, which makes it possible to improve performances related to fast printing, accuracy of the deposit and repeatability of the printing task. This leads us to ask the following questions: Is additive manufacturing technology in the field of the construction efficient and cost-effective? To what extent can additive manufacturing replace or improve traditional construction methods? What are the optimal applications of this technology in the field of the construction?

In this thesis, we have defined specifications on the shape and the material, so as to set the framework of the research from the **machine** side, in such a large field as the additive manufacturing, as follows:

Shape: Considered geometric shapes are characterized by those with funicular behavior, describing optimized shapes and have rational logic between geometry and physics.

Two basic parameters have been chosen, namely "intrados" and "extrados" (Figure 1.2b). A zigzag (Figure 1.2c) shaped inner surface is generated to fill the gap between

[12] Known under the name of 3D printing

the two sides. We should note that the zigzag is initially generated on the first layer, then it adjusts locally to the surface for the following layers. The main issue in this studied shapes was to find a rationale (logic) of zigzag adaptation on the surface of each layer (Figure 1.2d) and, at the same time to ensure the continuity of the interpolation without any obstacle or interruption.

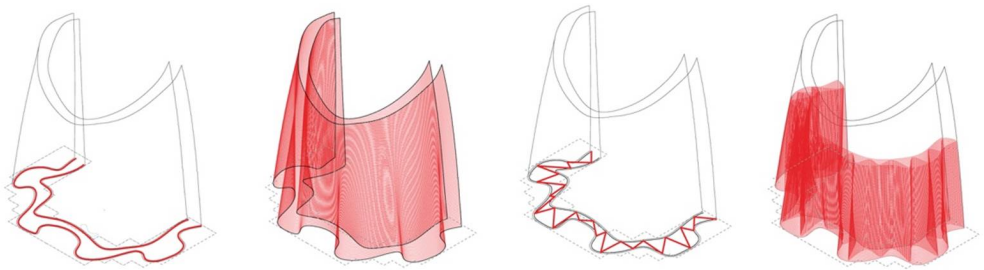

(a) (b) (c) (d)

Figure 1.2 – Slicing with adapted zigzag filling

Material: Material exclusively used for the additive deposit and without any other reinforcing elements. We have centered the work on the manufacturing of modular parts based on cement (Figure 1.3a) and clay (Figure 1.3b), and that can be assembled and used in urban furniture.

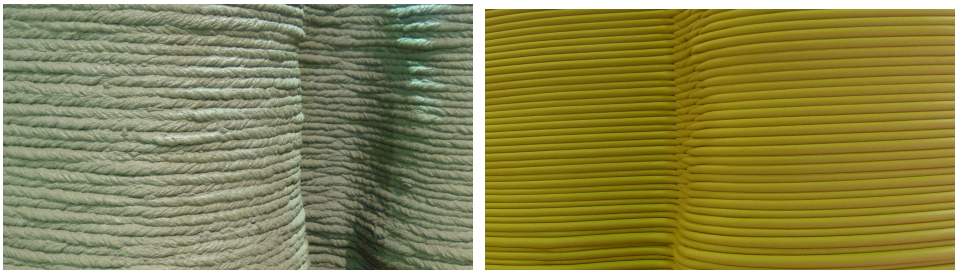

(a) Cement based materials (b) Clay based materials

Figure 1.3 – Materials

1.3 Objectives of the thesis

Additive manufacturing has continued evolving in the last few years, thanks to the development of various materials that have the property of maintaining the shape under pressure. The challenge behind this technological innovation lies in the identification of complex shapes that can be printed with such materials and by using the techniques proper to additive manufacturing.

The main objective of the contractual research within the MATRICE framework is the development of an additive manufacturing concept, allowing a continuous deposit of the material, for producing novel funicular shapes in the construction industry. The machine to be designed should meet the following requirements:

- Automatic guidance of the printing nozzle using a continuous additive deposit by using a kinematic redundant omnidrive mobile-rigid manipulator of Figure 1.4.

- Quality inspection of the material and the printed object in different configurations, by using a soft manipulator robot of Figure 1.5.

As far as guidance, we were concerned with the design of a robotized device describing a mobile and rigid manipulator, carrying a nozzle, and which can synchronize the printing speed and the pumping flow of the material. For quality inspection of the printed shapes according to their topology, a soft and hyper-redundant manipulator (Elephant's trunk) has been used as a gripper element of the mobile-manipulator, guiding a camera and allowing to scan dead-zone areas of the printed objects.

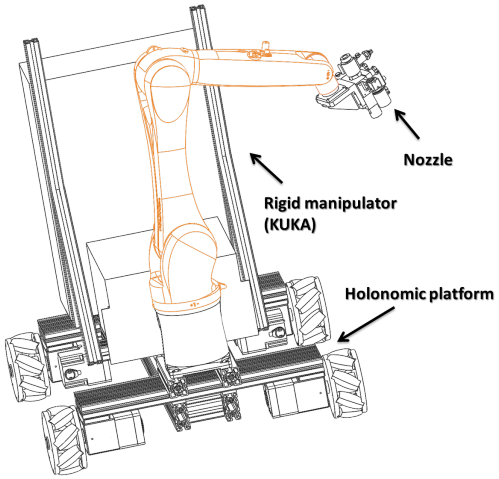

Figure 1.4 – Additive manufacturing prototype

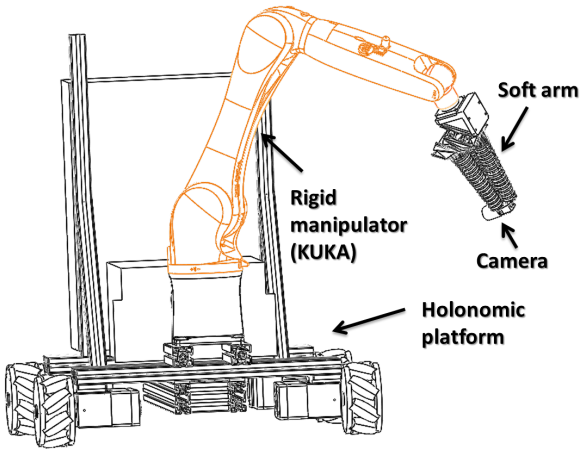

Figure 1.5 – The quality inspection robot

1.4 Scientific issue

The scientific issue tackled in the fundamental research consists on **modeling and real-time kinematic control of a class of hyper-redundant manipulators**, used for quality inspection of printed surfaces during and after the additive manufacturing process, in the context of MATRICE project. This class of manipulators describes soft-continuum manipulators, characterized by their continuum property [13]. These manipulators are also

[13] Set of interconnected elements in a continuous or homogeneous configuration

designed with techniques of 3D printing, using plastic-based materials. In the literature, several kinematic approaches for modeling and control of soft and hyper-redundant manipulators have been studied and tested for various applications.

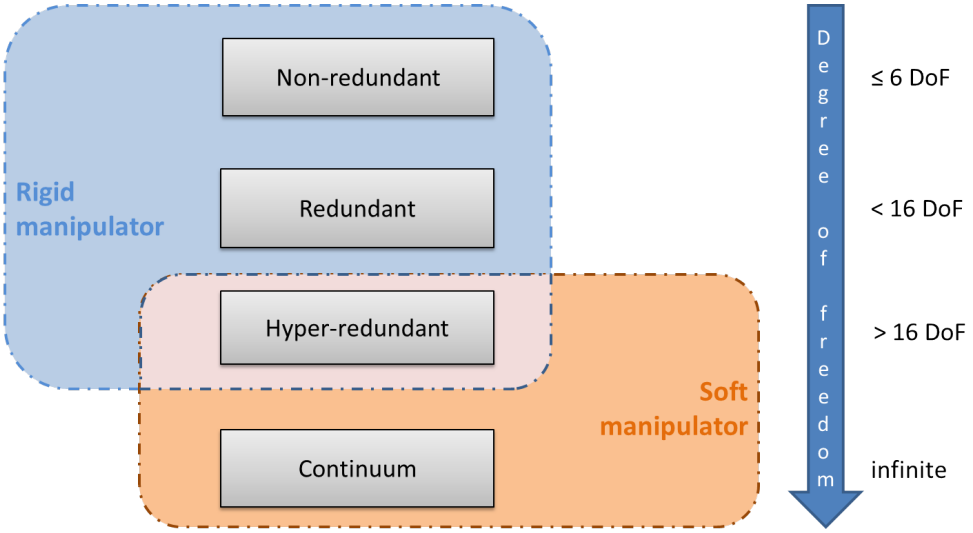

Figure 1.6 – Characteristics of rigid and soft hyper-redundant manipulators

Two types of hyper-redundant manipulators are mentioned in the literature (Figure 1.6), which differ from their kinematic design and operative functions. The first type describes the hyper-redundant manipulator with an infinity of Degree of Freedom (DoF), where their overall behavioral model approaches those of soft-based continuum manipulator (Figure 1.7a). This because the robot structure is based on soft materials. The second type describes the hyper-redundant manipulator with multiple and identified DoFs, designed with the principle of a concatenation between non-redundant rigid robots, attached each others in serial-parallel configuration (Figure 1.7b). Their overall behavioral model approaches those of rigid-based continuum manipulator. This because the robot structure is based on rigid material.

This thesis deals with the modeling and kinematics solving of a class of hyper redundant manipulators with soft-continuum behavior. This is done after discretizing the soft continuum manipulator by a chain of parallel modules, reconstructing the overall kinematic properties of bending and shape of the soft-continuum manipulator. Kinematic modeling of continuum robots remains a real challenge, especially because of the absence of well-structured modeling and diversity of continuum platforms. Quantitative[14] and qualitative[15] approaches are commonly used for modeling kinematics of soft-continuum manipulators.

Quantitative modeling approaches are also known as model-based methods, consist to formulate mathematically a relationship between the causes and effects by using kinematic and dynamic fundamental equations.They usually suffer from several assumptions which yield inaccurate models, and one generally faces time consuming or mathematical intractable issues to deduce the Inverse Kinematic Model (IKM) directly from the Forward Kinematic Model (FKM) (Figure 1.8).

[14] mathematical equation-based models
[15] Learning-based models

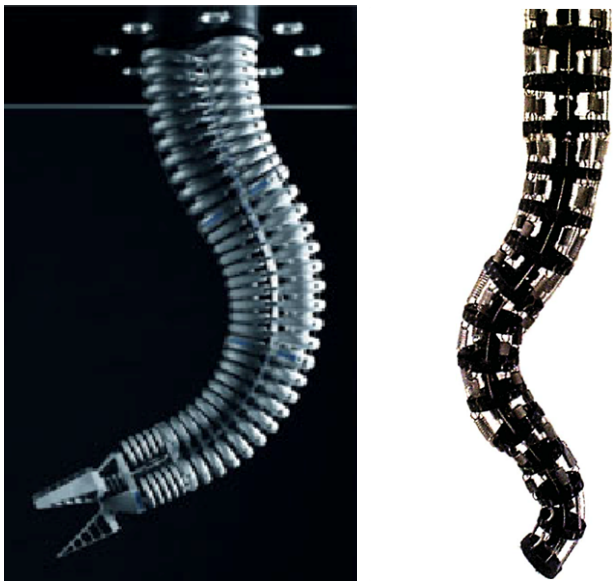

(a) soft-based continuum (Falkenhahn et al., 2017) (b) rigid-based continuum (Hannan and Walker, 2001)

Figure 1.7 – Continuum Manipulator

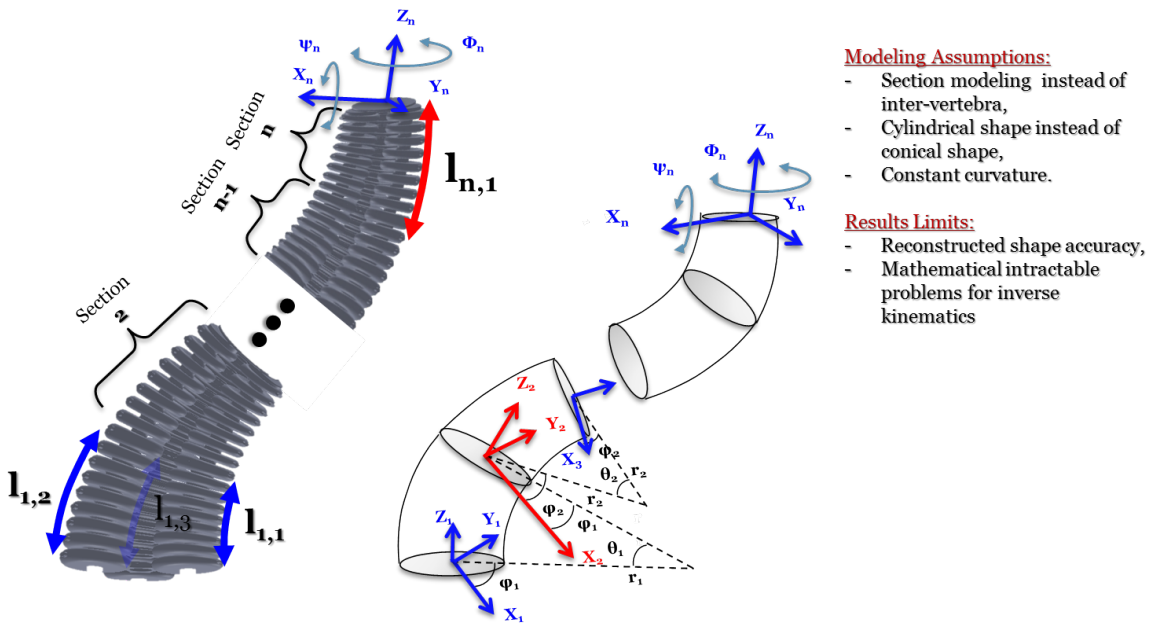

Figure 1.8 – Quantitative modeling

Qualitative modeling approaches or learning-based approaches consist in dividing the parameter space into several classes according to the well-known modes of operation, and then determining by learning the mathematical relations between the effects (sensor measurements of Cartesian or joint positions), and causes (inputs of voltage, pressure,...). They generally suffer from the explosion of the learning database which increases with the number of DoFs; and it is often difficult to establish well-structured control laws (Figure 1.9).

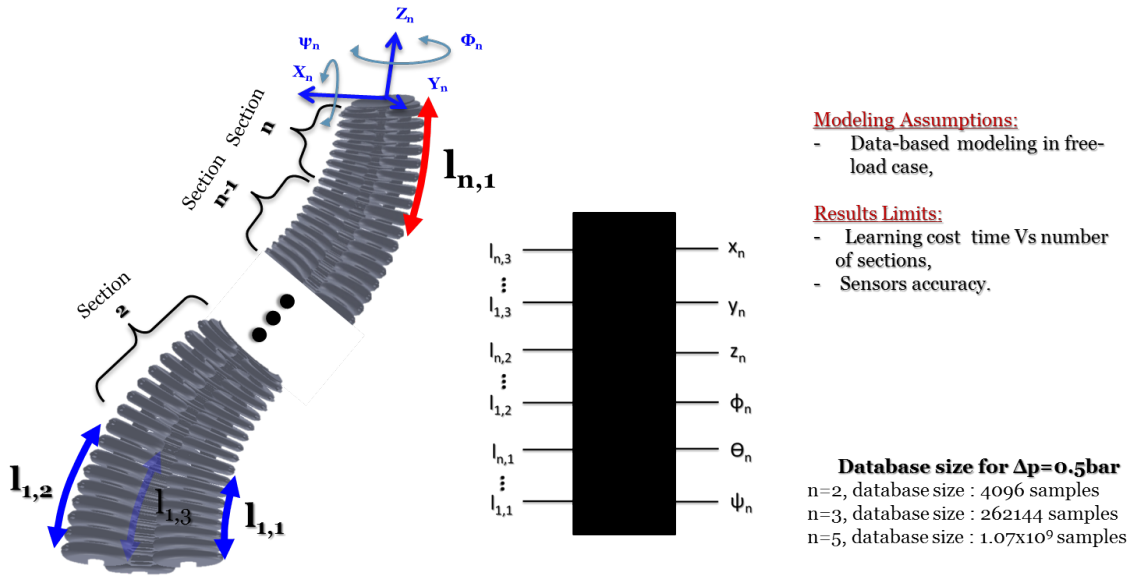

Figure 1.9 – Qualitative modeling

A hybrid approach that was developed in this thesis work, combines the advantages of quantitative and qualitative approaches, for modeling and solving the kinematics of hyper-redundant manipulators (Figure 1.10). The idea here is to build a mathematical model of the robot, but with reasonable assumptions, and to improve its precision by identifying or approximating certain nonlinearities of the model using a qualitative approach. The main advantage of the hybrid approach is the ability to derive the learning database directly from the mathematical model. Besides, another significant advantage is the possibility to reconstruct the robot shape in real time. This is very useful for quality inspection of printed objects using robotized additive manufacturing technique.

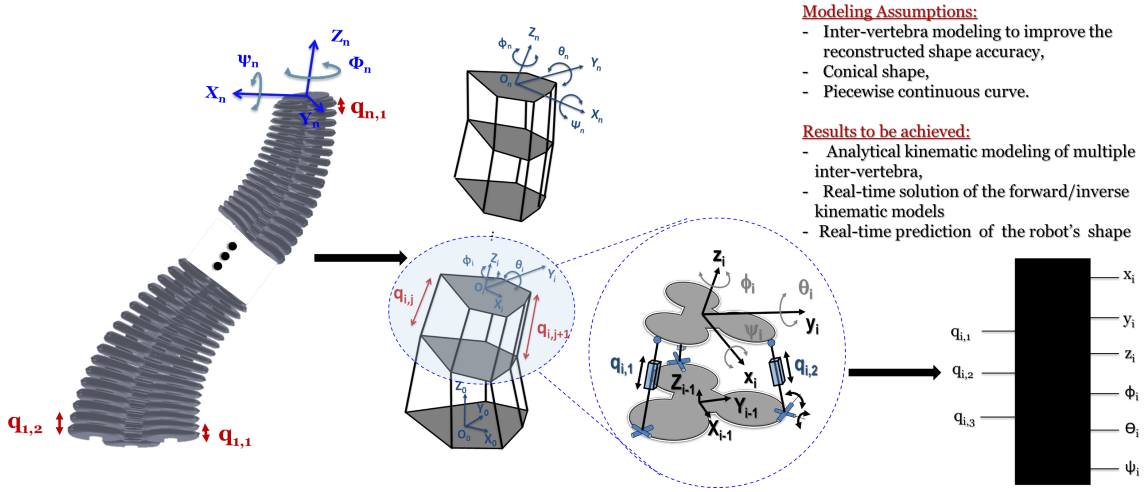

Figure 1.10 – Hybrid modeling

In this work, the modeling approach was inspired from the modeling concept of parallel rigid manipulators. The mathematical model is obtained by considering the continuum manipulator as a concatenation of multiple parallel robots (modules).

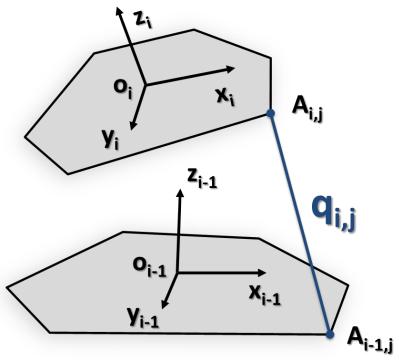

Figure 1.11 – Geometric relationship of i^{th} module

The inverse kinematics is obtained from the mathematical model of one parallel robot platform (Figure 1.11), including its pose (position and orientation), under the assumptions of perfect universal joint (U) and spheric joint (S), and assembled prismatic joint (P), as follows:

$$q_{i,j}{}^2 = ({}^{i-1}\mathbf{P}_{\mathrm{A}_{i,j}} - {}^{i-1}\mathbf{P}_{\mathrm{A}_{i-1,j}})^{\mathrm{T}}({}^{i-1}\mathbf{P}_{\mathrm{A}_{i,j}} - {}^{i-1}\mathbf{P}_{\mathrm{A}_{i-1,j}}) \tag{1.1}$$

Where $\mathrm{A}_{i-1,j}$ and $\mathrm{A}_{i,j}$ denote the centers of the universal and spherical joints, respectively. ${}^{i-1}\mathbf{P}_{\mathrm{A}_{i,j}}$ and ${}^{i-1}\mathbf{P}_{\mathrm{A}_{i-1,j}}$ denote the coordinates of the connection points $\mathrm{A}_{i,j}$ and $\mathrm{A}_{i-1,j}$ in frames $\Re_{i-1}$ and $\Re_i$, respectively. i and j denote the module frame and the active joint indexes.

Regarding the kinematics solving, the FKM of the robot structure can be obtained by solving the Inverse Kinematic Equations (IKEs) of each constitutive module of the manipulator. However, these equations are strongly nonlinear that the usual numerical solving techniques (ie. Newton's method, Broyden's method, Finite Difference method, ...) require a huge computation time or do not satisfy the constraints of implementation in real-time, according to the number of the modules. In this thesis, we make use of the qualitative approach to provide a solution that can be implemented in real-time.

For the IKM, the principle consists in predicting the coordinate frame of each module from a given Tool Center Position (TCP), and deducing the IKM by summing the elongations of the different modules. The modeling problem can be summarized to an optimization problem with implicitly time constraint, because the objective is to solve the modelling problem with sufficient accuracy and reasonable time consuming. The objective function of the inverse kinematic issue can be expressed as:

$$\begin{cases} \min f(q) \\ q_{i,\min} \leq q_{i,j} \leq q_{i,\max} \end{cases} \tag{1.2}$$

where $f(q) = \sqrt{\lambda_{\max}(\mathrm{Q}^{\mathrm{T}}\mathrm{Q})}$ with $\lambda_{\max}(\mathrm{Q}^{\mathrm{T}}\mathrm{Q})$ the maximum eigenvalue of $\mathrm{Q}^{\mathrm{T}}\mathrm{Q}$, and Q is the normalization matrix consisting of prismatic variables $q_{i,j}$. Once more, for real-time implementation constraints, a qualitative approach was adopted for inverse kinematic problem solving.

The proposed kinematic modeling approach is implemented to a class of soft continuum manipulators, called CBHA[16]. This type of robot is designed from additive manufacturing polyamide [17]. This robot is developed by the company Festo AG[18] and is ex-

[16] Compact Bionic Handling Arm
[17] Body resulting from the reaction of a poly-acid with a poly-amine, constituting several plastic materials.
[18] https://www.festo.com/group/fr/cms/10241.htm

clusively used by the CRIStAL laboratory through a research partnership. With only a unique polyamide material, a concatenation of more rigid vertebrae through less rigid inter-vertebrae is formed. This justifies the use of a emulated parallel-serial rigid robot on this type of robot. In the Framework of MATRICE project, the CBHA is used for the quality inspection of printed objects through the technique of robotized additive manufacturing with the cement (Figure 1.3a) and the clay (Figure 1.3b) materials, which will be developed in the following chapters.

1.5 Scientific positioning within the CRIStAL Lab.

The research work done in this thesis has been conducted at the Research Center in Computer Science, Signal and Automation of Lille (CRIStAL UMR CNRS 9189) within the Methods and Tools for Integrated Systems Design group (MOCIS[19]), partner of the MATRICE project and whose goal is to design an integrated prototype of an autonomous robot. This is used first for additive deposits of cement and clay materials and then for quality inspection of the deposit and the printed objects. MOCIS is a research group specialized on the integrated design of multi-physical systems. Figure 1.12 shows the organization of the research topics within the MOCIS group. The work done within this thesis falls into the modeling and control of multi-physical and hyper-redundant robots.

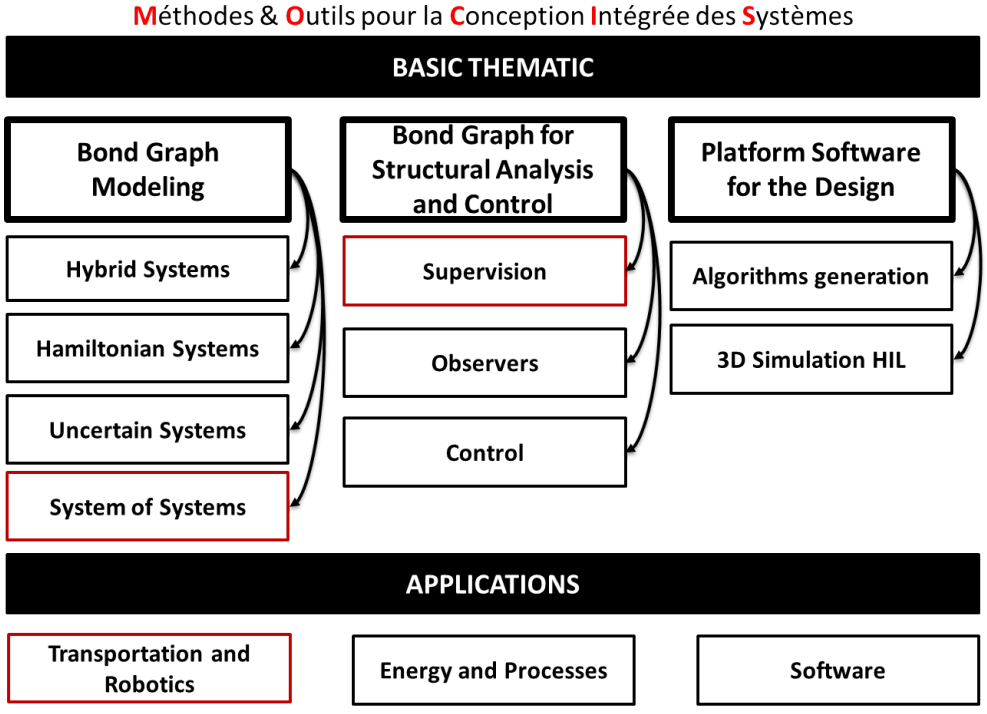

Figure 1.12 – Organization of MOCIS research team

The MOCIS group has been working since 2012 on the kinematic modeling of a class of soft-continuum manipulators. The aim of this research is to improve the performances of the modeling and control kinematics of soft-continuum manipulators, in terms of real-time optimization and tracking accuracy. This type of robot is lightness, flexible and compliant. But because it is hyper redundant, it is hard to achieve the same control performances as in the case of non-redundant manipulators. Thus, the work of the MOCIS

[19] https://www.cristal.univ-lille.fr/?rubrique27eid=24

group during the last years has been focused on the development of kinematic models of the CBHA, which can run in real-time using several approaches:

- A quantitative approach through the method of arc geometry (Escande et al., 2015), the computational mechanics method using finite element method (Bieze et al., 2018) and the Pythagorean Hodograph method for the shape reconstruction of the robot using synthetic-parametric curves (Singh et al., 2018).
- A qualitative approach by using neural approximations for modeling and control (Melingui et al., 2015).

Thus, this research work is a continuity of the work already carried out within the MOCIS team on soft-continuum manipulators. It proposes a **the hybrid approach combining a quantitative method for CBHA modeling and a qualitative method for solving the kinematic model.**

1.6 Scientific Results

The main contributions in this thesis work can be summarized as follows:

- Kinematic modeling of a class of soft-continuum manipulators, with a hyper redundant behavior. This latter is reproduced through the emulation of a concatenation of multiple parallel-serial rigid robots.
- The FKM of soft-continuum manipulator CBHA is approximated using a neural network method. It is an alternative for solving non-linear equations of high dimension system.
- The IKM of soft-continuum manipulator CBHA is obtained based on two approaches. Quantitative to model the kinematic behavior of the robot and qualitative for real-time solving.
- Autonomous navigation of the redundant omnidrive mobile-rigid manipulator in printing 3D objects in the construction.
- Validation of model-based kinematic control of the CBHA for quality inspection in additive manufacturing for the construction.

1.7 Research Contributions

The main contributions of this thesis work have been published in:

1.7.1 Journal Papers:

- **O. Lakhal**, A. Melingui, and R. Merzouki, 'Hybrid Approach for Modeling and Solving of Kinematics of Compact Bionic Handling Assistant Manipulator', IEEE/ASME Transactions on Mechatronics, Vol. 21, 3 : pp. 1326 - 1335, 2016.
- Melingui, J. J-B. Mvogo Ahanda, **O. Lakhal**, J-B. Mbede, R. Merzouki, 'Adaptive Algorithms for Performance Improvement of a Class of Continuum Manipulators', IEEE Transactions on Systems, Man, and Cybernetics: Systems, vol. 48, 9 : pp. 1531 - 1541, 2017.

- Melingui,**O. Lakhal**, B. Daachi, J. B. Mbede, and R. Merzouki, 'Adaptive Neural Network Control of a Compact Bionic Handling Arm', IEEE/ASME Transactions on Mechatronics, Vol. 20, 6 : pp. 2862 - 2875, 2015.

1.7.2 Conference Papers:

- **O. Lakhal**, A. Melingui, A. Chibani, C. Escande and R. Merzouki, 'Inverse Kinematic Modeling of a class of Continuum Bionic Handling Arm', 2014 IEEE/ASME International Conference on Advanced Intelligent Mechatronics (AIM) July 8-11, 2014, Besançon, France, pp. 1337 – 1342, 2014.

- **O. Lakhal**, A. Melingui, T.M. Bieze , C. Escande, B. Conrard, and R. Merzouki. On the kinematic modeling of a class of continuum manipulators. In Robotics and Biomimetics (ROBIO), 2014 IEEE International Conference on (pp. 368-373), 2014.

- I. Singh, **O. Lakhal**, Y. Amara, V. Coelen, P. Pathak, R. Merzouki, Performances Evaluation of Inverse Kinematic Models of a Compact Bionic Handling Assistant. IEEE Conference on Robotics and Biomimetics (ROBIO), Macau, China, 2017.

1.7.3 Submitted Papers:

- **O. Lakhal**, A. Melingui, T. Chettibi, P. Kumar , A. Belarouci, G. Dherbomez, M. Pollart, V. Coelen and R. Merzouki, 'Development of an omnidirectionnel mobile manipulator for additive manufacturing in construction industry'. Submitted at International Journal Construction Robotics, Springer, 2018.

- **O. Lakhal**, A. Melingui, P. Kumar, G. Dherbomez, and R. Merzouki, 'Control of a Hyper-Redundant Robot for Quality Inspection in Additive Manufacturing for Construction'. Submitted at RoboSoft 2019, IEEE International Conference on Soft Robotics, 2018.

1.8 Thesis organization

This thesis manuscript is organized as follows:

CHAPITRE 2. Robotized Additive Manufacturing in the Construction

In the second chapter, a state of the art of robot-machines and techniques used in the additive manufacturing in the construction domain are presented. It also includes the literature review on modeling and control kinematics of soft-continuum manipulators. This state of art allows making the scientific and innovative positioning of the thesis contributions.

CHAPITRE 3. Technical specifications for designing MATRICE Robot

In the first chapter, it is discussed the technical specifications allowing the integrated design of the robotized concept for additive manufacturing and quality inspection in construction, within the MATRICE project. The technical and environmental assumptions for the concept design are discussed.

CHAPITRE 4. Additive Manufacturing Robot-Machine in Construction

In this chapter, it is discussed the development of kinematic modeling and autonomous navigation of the redundant omnidrive mobile-rigid manipulator, developed in the fra-mework of the additive manufacturing in construction for the MATRICE project. Experimental results are presented and commented.

CHAPITRE 5. Modeling and control of the hyper-redundant robot for the quality inspection

This fifth chapter describes the main scientific contributions in modeling and kinematic control of soft-continuum and hyper-redundant manipulator, namely CBHA, used for quality inspection of printed 3D objects by additive manufacturing technique. The model validation and obtained results are discussed in this chapter.

CHAPITRE 6. General conclusions and prospectives

In this sixth chapter, it is concluded the main deliverables of the MATRICE project. In addition, analysis of the research results carried out about the modeling and the control kinematics of soft-continuum manipulators, based on the proposed hybrid approach. Some future research prospectives are listed at the end of this chapter.

Annexe 1. Overview of 3D Objects in MATRICE project

This annexe, it is shown an overview on printed 3D objects using the robot-machine developed in the framework of MATRICE project.

Chapter 2

Robotized Additive Manufacturing in the Construction

Contents

2.1 Introduction

Nowadays, additive manufacturing or 3D printing in construction has been getting more and more accessible in terms of: costs, variety of printable materials, and technology printing techniques. The principle of additive manufacturing can be explained on two main steps; the first concerns the continuous deposit of the material, while the second consists on the quality inspection of the printed objects. Nowadays, there are more and more printable cement-based materials that can be used not only in making prototypes but also in the manufacturing of technologically transferable products.

Several projects on additive manufacturing have been successfully conducted since 2010, thanks to the mastery of printable materials. The actual techniques consist on extrusion of materials such as cement, clay, wax polymer, followed by an accurate deposit along a predefined trajectory. Then come the superposition of layers (slices), in order to construct a 3D complex shapes.

Nowadays, several robots have been developed and in use for additive manufacturing in the construction field. These systems have been tested either on site or in the laboratory. Static structure platforms such that Contour-Crafting and Cable-Suspended platforms are primarily used for building one-piece constructions, whereas Freeform Construction and D-Shape were designed for making single building elements for subsequent assembly. However, the robot-machine is of fixed size, with a limited printing envelope, (Lim et al., 2011; Lim et al., 2012). The size of printed objects is therefore limited by the size of the machine itself and, in most cases, scaling the machine for printing large scale structures is generally impractical and costly. For example, how high should a size of a gantry be to enable the additive construction of a skyscraper? Thus, the increase of gantry size introduces potential issues related to the transportability and mobility of the solutions in question. Mobile platforms are subsequently integrated into printing processes in order to overcome restrictions in the size of printed structures or objects and introduce a significant amount of flexibility into the printing operations (Werfel et al., 2014; Hunt et al., 2014; Labonnote et al., 2016).

The pre-stage and post-stage of additive manufacturing require the quality inspection of the printed shapes for norms validation or default diagnosis. This quality inspection can be controlled, thus, permitting the detection of cracks if any and as well as checking the adhesion between printed slicers. However, the geometry of printed shapes with funicular surfaces is sometimes complex, where rigid structure of robots cannot reach certain zones to scan their surfaces. The use of soft robotics platforms also known as soft-continuum manipulators become necessary to deal with complex geometry .

The remainder of this chapter are follows: Section 3.2 gives some relevant technological solutions for additive construction based on cement materials. The robotic platforms developed in additive manufacturing construction is presented, thereafter. The existing techniques in quality inspection of printed structures is presented in Section 3.4, where the necessity of integrating soft robot structures is highlighted. Some concluding remark ends the section.

2.2 Additive Manufacturing Techniques of cement-based materials

3D manufacturing is a combination of processes capable of producing solid or flexible objects that are complex and free-form. This is done directly from digital 3D models. Three techniques can be distinguished (Beaman et al., 1997) :

- **Subtractive manufacturing** which consists in taking away material from a block of material. This method is difficult to apply in the field of construction.
- **Conventional manufacturing** based on the re-molding of raw materials. It is an expensive method, limited in form and requiring a lot of time. In addition, the conventional in-house molding method in the construction requires labor and time with considerable expense for scaffolding and form work. In many cases, the formwork and scaffolding systems have been adapted to the specific characteristics of the site. The limits of this conventional manufacturing have encouraged the development of a continuous construction method, without formwork and even without scaffolding.
- **Additive manufacturing** based on the additive deposit of materials to create geometrically complex objects. It is seen as an innovative, economical, affordable and

environmentally friendly technique. It can also increase the efficiency, the safety in the work and significantly reduce the construction time (Mathur, 2016). This technology can be used to print architectural models and large-scale buildings. This thesis focuses mainly on this technique.

So far, three additive manufacturing techniques were developed. A comparison study was proposed by Khoshnevis et al. (Perkins and Skitmore, 2015). They were the first to propose a new method of extrusion and shaping of ceramics, called Contour Crafting, developed from 1995. It is a layered manufacturing technology whose objective is the use of Contour Crafting technology in the construction of habitats on other planets (Khoshnevis et al., 2017). However, due to technological limitations, it was in the 2000s that USC Vertibi's Khoshnevis team started focusing on 3D printing of cement and ceramic pastes. On another 3D printing technique, called D-shape, was patented in 2005 by Enrico Dini (Colla and Dini, 2013). This is one of the larger-scale 3D printing technologies that exploit sand by employing a powder bonding technique. Finally, Loughborough's research team has developed a 3D concrete printing technology called Concrete Printing. The latter is similar to Contour Crafting technique and it is able to build a predefined element by superimposing layers on each other. The material is poured from a nozzle without the need for vibration. Unlike the Contour Crafting technique, the Concrete Printing technique does not smooth the layers during material deposition and thus a ribbed surface appears strongly dependent on the thickness of the layer (Lim et al., 2011). The following subsections presents respectively the three techniques, namely the Contour Crafting, D-shape, and Concrete Printing technique.

2.2.1 Contour Crafting

This extrusion technique called Contour Crafting (Khoshnevis and Dutton, 1998), was proposed by the University of Southern California (USC) in 1995. It deals with additive manufacturing based on ceramic materials. It is a layered manufacturing technology intended to be applied in housing construction on other planets (Khoshnevis et al., 2017), as shown in Figure 2.1a. However, the Khoshnevis [1] team being limited by the technology of this time period. Thus, they delayed their ceramic printing structures after the 2000s.

Contour Crafting is based on two upper and lateral trowels (Zareiyan and Khoshnevis, 2017), controlled and fixed at the nozzle (Figure 2.1b). This technique makes it possible to print structures with smooth, accurate, flat and free-form surfaces. When the material is extruded, the trowels create smooth outer and upper surfaces. The side trowel can be deflected to create non-orthogonal surfaces. After complete the layering, a concrete is used to fill the area defined by the extruded edges.

2.2.2 DShape

Later, Enrico Dini from Monolite Ltd, developed a 3D printer machine based on the large-scale stereo-lithography technique called D-Shape [2] (Colla and Dini, 2013). This machine was designed in 2010 in Pontedera (Italy) and used to build the pavilion 'Radiolaria', designed by the Italian architect Andrea Morgante, which is about a monumental work of 10 meters in height (Figure 2.2).

[1] http://www.bkhoshnevis.com/
[2] https://www.d-shape .com /

(a) Future Construction robots for lunar and mars planet environments imagined by the NASA

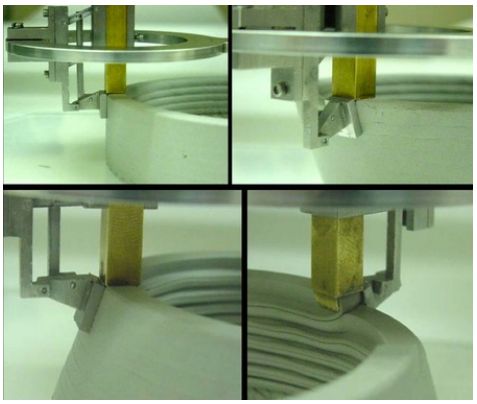

(b) Contour Crafting manufacturing technology

Figure 2.1 – Contour Crafting method from university of Southern California

Figure 2.2 – D-Shape : Solidification from sand

D-Shape machine is capable of printing by using natural materials, such as sand and clay. It consists of 300 different nozzles, supported by four aluminum pylons between which the object will take shape from the base to the top. The manufacturing is done by the deposition of layers of a thickness of five to ten millimeters. These layers are made from sand and an inorganic bond. Uncured sand temporarily supports the upper layers, creating shapes that can not be created by single-material extrusion. This technology has been used in the field of construction (Wu et al., 2016). However, this technique requires the sand to be spread and compacted for each layer. Once the element is finished, all unused sand must be removed.

2.2.3 Concrete Printing

The research group at Loughborough University in UK has developed a 3D concrete printing technology called Concrete Printing [3] for the manufacturing of architectural components and large-scale construction. This is a 3D printing method, similar to Contour Crafting method and able to make a predefined element by superposing layers (slicers). The material is poured from a nozzle without the need for formwork. Unlike Contour Crafting, the Concrete Printing technique does not smooth the layers during the deposit of the material. Thus, a ribbed surface appears on the printed layers. However, this technique has a lower resolution and allows better control of internal and external geometries (Lim et al., 2011).

Figure 2.3 – Concrete Printing from Loughborough university

The technique is used for prototyping and producing industrial sized components. Several construction companies have adopted this method to improve the shape of certain surfaces.

Indeed, this technique minimizes the duration of the construction process in comparison with conventional methods (Rouhana et al., 2014). The Chinese company WinSun [4] has recently demonstrated the benefits of additive manufacturing for the construction by printing 10 houses (Figure 2.4) in less than 24 hours (Charron, 2015). WinSun estimates that additive manufacturing technology can save between 30 and 60% of construction materials and reduce production time by 50 to 70%, while reducing labor costs by 50% to 80%.

In addition, additive manufacturing offers a flexibility in the construction of structural shapes, difficult to build using a conventional approach, and provides an improvement in the overall impact related to the safety and the sustainability of the structure.

[3] http://www.lboro.ac.uk/enterprise/3dcp/
[4] http://www.winsun3d.com

Figure 2.4 – Housing Construction with prefabricated elements using additive manufacturing

In the following, a literature review on the automation of the process of additive manufacturing in the construction is presented.

2.3 Robots for additive manufacturing in construction

Additive manufacturing robots open new perspectives for manufacturing and construction. Nowadays, many approaches have been applied such as manufacturing on site or in the laboratory, using different technologies. Some use Cartesian robots to print prefabricated parts in laboratory and transport them to the site afterwards. For example, WinSun Decoration Design Engineering has succeeded in building houses from construction components printed in prefabricated elements and assembled on site (Hager et al., 2016). Others use a gantry system like WinSun (Winsun, 2014), WASP (BigDelta, 2016) TotalKustom (Camacho et al., 2017), BetAbram (BetAbram, 2014) or robotics system like XtreeE (Xtreee, 2015), Sika (Sika, 2015), Apis cor (Apis-Cor, 2017). Nevertheless, these systems have limited workspace and are often complicated or slow to implement. Other researchers have designed a machine to automate and facilitate the setup and printing process. The IAAC University of Barcelona has designed a family of mobile robots for small-scale construction and easy to install. After the print phases, each robot must perform a diverse task. Except that it slows down the printing process and limits the architectural form to print. Recently, the emergence of mobile robots (rolling or flying) is increasingly present in the field of additive manufacturing in the building like (Zhang et al., 2018). The use of mobile robots for 3D printing combines the advantages of gantry and robot handling systems by printing on the outside and inside. But also, to employ multiple mobile robots printing concurrently a large, single-piece, structure (Zhang et al., 2018). Additive manufacturing structures can be grouped into two main classes, namely, static and mobile structures, described below.

2.3.1 Static Structures

Initially, Cartesian robots fixed on the ground were used to print prefabricated components in the laboratory. Indeed, WinSun has succeeded in building houses using additive manufacturing technology (Figure 2.5b). In this case, prefabricated elements are assembled on site (Hager et al., 2016) using conventional construction materials. In addition, this company built a 5-levels building (Figure 2.5c) and a villa (Figure 2.5a).

The printer machine used by WinSun measures 6.6 meters high, 10 meters wide, and 150 meters long (Figure 2.5b). It is the first large-size machine for continuous deposit of cement-based material (Wu et al., 2016). The size of the printer makes it possible to increase by 10 the capacity of the production. However, printed architectural shapes are the standard architecture, because it is difficult to print complex geometric shapes using a Cartesian machine.

The innovative startup XtreeE [5] produce ultra-high-performance concrete complex architectonic elements (Gaudillière et al., 2018) . It has been able to print architectural components based on biomimetic shapes with additive manufacturing technique (Figure 2.6b). The structures are inspired from natural shapes and created with digital technologies and additive manufacturing methods. The structures are printed in a modular process, allowing the assembly of several pavilions and thus creating structures with different configurations. XtreeE used an experimental cement developed by Lafarge-Holcim [6] and an ABB industrial robot [7], suitable for 3D printing (Figure 2.6a). XtreeE's architects

[5] https://www.xtreee.eu/
[6] https://www.lafargeholcim.com/
[7] https://new.abb.com/products/robotics/en/

(a) Villa with indoor and oudoor decorations

(b) WinSun's concept

(c) Five levels building

Figure 2.5 – Designed products using WinSun techniques

and engineers used the Dassault System [8] 3D Experience platform for the design development, simulation, 3D digital validation of shape, topology, and manufacturing of the structure. Figure 2.6b reveals the 3D pavilion inspired from the shape of a coffee bean, with walls alluding to the shapes found in the forests.

(a)

(b)

Figure 2.6 – Spherical Industrial Robot of XtreeE concept

These types of machines/robots involve an extra cost for their transportation and installation, where their workspace depends on their sizes.

Printing on sites has progressed steadily. The Russian company Apis Cor [9] has designed a printer that is capable of printing inside buildings while they are built (Figure 2.7a). It is a transportable cylindrical manipulator with a hydraulic elevation system. The

[8] https://www.3ds.com/en
[9] http://apis-cor.com

printer which has compact size measures 4 meters in height, 1.5 meters in width and 1.5 meters in length and weighs 2 tons. The printer can be installed without being fixed to the ground thanks to its stabilization system in the form of two counterweights and so the installation on the site does not require a long preparation before the work starting. Besides, the robot consumes only 8 kilowatts. The printer machine can cover only a printing area of nearly $132m^2$.

(a) (b)

Figure 2.7 – Apis Cor 3D Printer

Others use a gantry system which also implies a limit in the dimensions of the products to be printed. For example, the BigDelta printer which is 12 meters tall and 6 meters in circumference and which was made in Italy by a company called WASP[10] (figure 2.8a). The printer machine allows the manufacturing of forms that have a large volume. Moreover, it has a rotative nozzle equipped with a mixer. Only ten watts are required for its functioning.

(a) (b)

Figure 2.8 – BigDelta WASP printer

The Large scale 3d printing system developed at the university of Southern California [11], uses a gantry crane moving on two rails for building customized homes of $230m^2$ in a few hours. Beams are positioned to assemble the framing tips (Figure 2.9). This system allows the construction of architectural objects on a very large scale, using a fibrous concrete which according to its inventor has a resistance to compression of nearly 70 megaPascals[12].

[10] www.wasproject.it
[11] https://www.usc.edu/
[12] we talk about very high performance concretes beyond 50 megaPascals

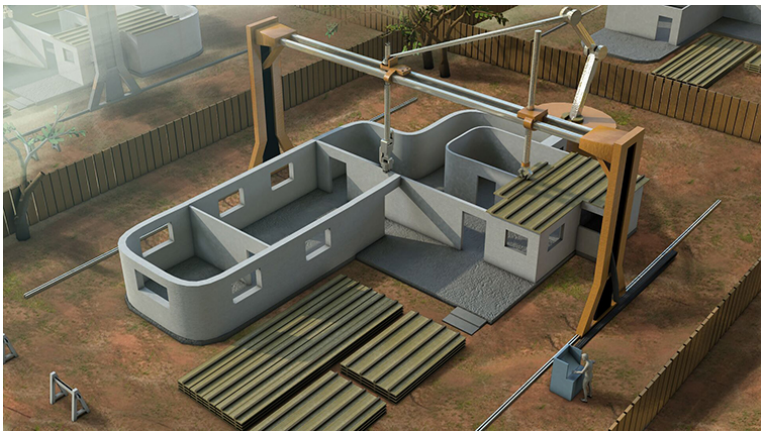

Figure 2.9 – Southern California University 3D printing machine

In Copenhagen, a 50m^2 3D printed office has been realized by the Danish company Printhuset [13] using a 3D printer for concrete. This work should normally meet the European official requirements. 3D Printhuset uses a machine called BOD (Figure 2.10) which looks like a crane and measures 6 meters in height, 8 meters in width and 8 meters in length and which has a printing speed of 2.5 m/min. It can create layers of 20 mm in height and a width varying between 50 and 70 mm.

(a) (b)

Figure 2.10 – 3D Printhuset BOD

In another context, the US army has participated in a three year programmes called automated construction of expeditionary structures (ACES). It has led to the construction of a 3D barrack known as B-Hut (Figure 2.11b). This project has been conducted in collaboration with the Construction Engineering Research Laboratory (CERL [14]) in Champaign, Illinois (USA). This barracks building of 150m^2 has been built using resistant concrete and a gantry system (Figure 2.11a).

In 2015, It was in the Philippines that Andrey Rudenko has presented another illustration [15]. He contributed to the realization of the extension of Lewis Grand Hotel in the city of Àngeles. This private house of 135m^2 which has 3 rooms, various bathrooms and also a lounge with a jacuzzi, has been realized with a robotic arm based on a concept that Andrey Rudenko developed in his garage. He used the same arm to construct the first medieval miniature castle in concrete in his garden (Figure 2.12) in two years.

[13] https://3dprinthuset.dk/
[14] https://www.erdc.usace.army.mil/Locations/CERL/
[15] https://3dprint.com/tag/andrey-rudenko/

(a) (b)

Figure 2.11 – Barracks building printed from local concrete by the US Army

(a) (b)

Figure 2.12 – Concrete miniature castle by 3D printing

The extension of the Lewis Grand Hotel (Figure 2.13) was the first dwelling aiming at the reception of the public. It took 100h hours to build this structure with a special sand, hard to extrude and composed of volcanic ashes. This sand offers satisfactory performance in terms of resistance and setting up. Additional time is naturally required for laying the networks, the insulation and the cladding.

(a) (b)

Figure 2.13 – Lewis Grand Hotel extension

In 2016, the Swiss industrialist Sika [16], specialized in chemistry has set up in the Widen technological parc in Switzerland, a 3D center dedicated to automation in construction. The machine, a 3D printing gantry, can print modules that are 4 meters wide and 3 meters long and height up to 6 meters (Figure 2.14a). This allows continuous printing for hours. This device is made up of a cement based material controlled at the printing nozzle. This process allows the realization of custom made concrete elements layer by layer, with varied and stylized shapes, as shown in the Figure 2.14b. Furthermore, the machine

[16] https://www.sika.com/

can reach a fast printing speed, thanks to its automated control process with the Sika Pulsment system and the Sika MiniShot extruder. In fact, the layers are deposited with a flow rate of 1 m/sec, and can print up to 4 tons of material per hour.

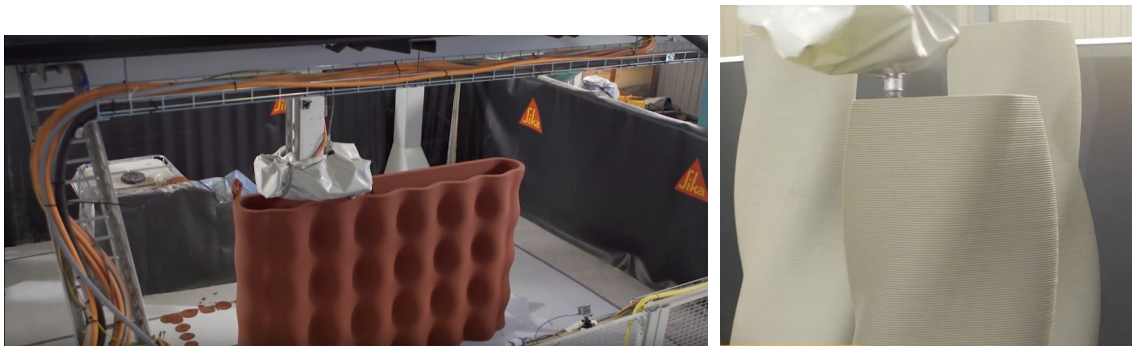

(a) (b)

Figure 2.14 – Concrete printing Sika 3D

Otherwise, in 2015 the Dutch company MX3D [17] revealed a revolutionary urban building project. Imagined by the Dutch designer Joris Laarman, this project called MX3D Bridge, aimed at building a steel bridge printed in 3D and joining the two sides of Oudezijds Achterburgwal canal of Amsterdam (Figure 2.15). So far, no concrete is printed but only metal and resin. This printing process does not use 3D printing filament, but prints by matter point.

Figure 2.15 – Project of a steel bridge printed in 3D

2.3.2 Mobile structures

Additive manufacturing machines described above have a limited workspace, due to their kinematics depending on the size of the object to be printed. Actually, to print a house from outside, the ideal solution consists of using a 3D of the gantry type. This requires time both for the setup and the uninstall. Consequently, before the building is started, the companies have to study the transport and installation of the machine on the site. Besides, printing inside requires less installation time, and makes the start easier. But this requires an inside access point adapted to the size of the robot. Thus, mobile robots (rolling or flying) are more and more present in the field of additive manufacturing in the

[17] mx3d.com/projects/bridge/

construction industry. In fact, this technology makes the setting up easier on the site and the printing procedure more automatized. Thus, the IAAC research team from the university of Barcelone has designed the Mini Builder[18] (Figure 2.16). It belongs to the kind of mobile robots designed for the construction of objects of small, medium and even very large dimensions. After the printing step, the robot must perform a reconfiguration task which slows down the printing process and limits the architectural form to be printed.

Figure 2.16 – IAAC Mini Builder from the University of Barcelona

The use of mobile robots for 3D printing combines the advantages of gantry systems with those of manipulator robots by printing both indoors and outdoors. For example the Dutch building company CyBe [19], specialized in 3D concrete printing, has developed a 3D mobile concrete printing machine called RC 3Dp (Figure 2.17). It was the first tracked machine of cement which allowed an easy movement in the site. It prints concrete at an average speed of 200 mm / sec and can go up to 600 mm / sec. This printer machine is able to print objects measuring 4.5 m in height, thanks to the two cylinders fixed on the mobile basis. Besides, the CyBe researchers have tested a new technology for the manufacturing of building elements. Recently, the company has designed, through additive manufacturing, 27 elements that make up the laboratory R&Drone of 168m^2 in Dubai, during 3 weeks.

Figure 2.17 – CyBe RC 3Dp mobile 3D printing robot

Among the category of mobile robots tracks and intended for additive manufacturing, we can find the digital building platform (DCP [20]) designed by researchers at the Massachussetts Institute of Technology MIT [21] (Figure 2.18). It is also equipped with solar

[18] robots.iaac.net/
[19] https://cybe.eu/
[20] http://matter.media.mit.edu/tools/details/digital-construction-platform-dcp
[21] http://www.mit.edu/

panels to manage the autonomous power of the robot. The system consists of a tracked vehicle that carries a large, industrial robot arm, which has a smaller, precision-motion second robot arm at its end. The MIT research team has demonstrated the performance of the technology after constructing a dome that is 12 meters high and 15 meters wide. The system fabricated a foam-insulation framework used to form the finished concrete structure. The whole structure has been done in 14 hours.

Figure 2.18 – 3D autonomous Robot-printer from MIT

In France, the company CONSTRUCTION-3D [22] has redesigned a machine that can print objects on site. It is a mobile hydraulic actuation machine with tracks. Its arm has 4 telescopic axes allowing the printing in a $201m^2$ space and can reach the height of 8 meters (Figure2.19).

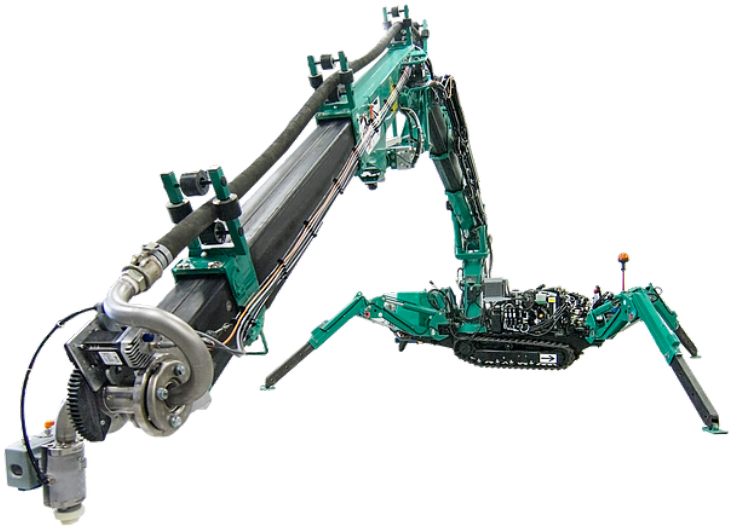

Figure 2.19 – Robot of 3D construction company

Globally, mobile robots in additive manufacturing are stable on the ground. The mobile part is only used to facilitate the transport to the construction site. It is not the case for the robot of the startup Cazza Construction[23], of the Silicon Valley (Figure 2.20). Cazza

[22] https://www.constructions-3d.com/
[23] https://cazza.co/

wants to automatize as much as possible the construction process by using the mobile basis during the printing. The Cazza X1 is mobile manipulator robot with tracks. The payload of the manipulator is 90 kg with a robot arm telescopic range extender of 4.7m and maximum height of 5.5 m thanks to a hydraulic height extender support base. However, the startup does not communicated much about the technology used, the manufacturing process or the printable materials.

Figure 2.20 – Cazza 3D Robot-based Construction Printer

On the other hand, another technology elaborated by the researchers at the Nantes Digital Sciences Laboratory LS2N [24] from University of Nantes for additive manufacturing called the BatiPrint3D [25] (Figure 2.21) has been designed. The concept consists of an industrial manipulator arm that is fixed to a lifting truck. The latter is controlled by a supervision system. But its manoeuvrability is rather hard because its mobile platform was designed to be guided on the ground. Thanks to the elevating part, it is able to reach a height of 7 m. The tip of the robot is guided by a laser sensor that follows a digital model of the habitat drawn on the ground.

Figure 2.21 – 3D printing machine from University of Nantes

In 2018, Dedibot company [26], presented a concept of a 3D flying printer called 'Fly Elephant' (Figure 2.22), designed to print high buildings at the TCT show [27] Asia 2018. This printer machine is composed of drone and an elephant trunk functioning as printing

[24] https://www.ls2n.fr/
[25] batiprint3d.fr/
[26] http://www.dedibot.com/en/
[27] http://www.tctasia.com.cn/en/

nozzle. This concept is still at prototyping level,and no results have been communicated so far.

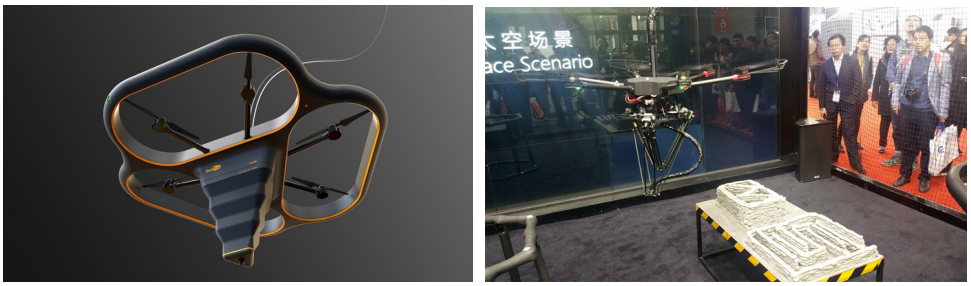

(a) Fly-Elephant (b) Presentation at TCT Asia

Figure 2.22 – Elephant 3D printer from Debibot company

The following step of the additive manufacturing of complex shapes consists on quality inspection of the printed surfaces. To deal with this issue, rigid-structure robots have a limited bending, not allowing to track all the dead-zones of the shape. Thus, the use of soft manipulators can be helpful to automatize the process of quality inspection of the printed complex objects from additive manufacturing technique.

Date	Machine	Type	Workspace	Area	Architectural shape	Material	Country
1998	Contour Crafting	Rail-gantry crane	230m2	On-site	linear	Fibrous concrete	USA
2003	D-shape	Gantry	H.10 x L.6 x W.6	Factory	Concaves/ convexes	Sand and binder	Italy
2004	Winsun	Gantry	H.7 x L.10 x W.10	Factory	linear	Fibre mortar	China
2007	Concrete printing	Gantry	H.2 x L.2.5 x W.5	Factory	Complex geometry	Cement	UK
2012	BetAbram	Rail gantry with 3-axis arm	H.2 x L.16 x W.9	Factory	House structure	Mortar	Slovenia
2012	Wasp	BigDelta	Perimeter : 6m Height : 12m	On-site/ Factory	Concaves/ convex	Clay	Italy
2013	Mini-Builder	Serial of mobile robots	Varying	On-site/ Factory	Concaves/ convexe	Artificial marble	Spain
2014	Totalkustom	Gantry	Not indicated	On-site	Concaves/ convex	Concrete	USA
2015	XtreeE	Manipulator	Not indicated	Factory	Biometrics	Concrete	France
2015	MX3D	Manipulator	Not indicated	Factory	Bridge	Metal/ resin	Netherlands
2016	Construction3D	Mobile manipulator	Height: 10m	On-site	Concaves/ convex	Concrete	France
2016	Sika 3D	Gantry	H.6 x L.3 x W.4	Factory	Complex geometry	Cement	Switzerland
2017	Apis Cor	Cylindrical manipulator	H.5 x L.1.6 x W.1.5	On-site/ Factory	Circular shape	Mortar	Russia
2017	CyBe RC 3Dp	Mobile manipulator	Height: 4.5m	On-site/ Factory	Concaves/ convex	Mortar	Netherlands
2017	MIT-3DCP	Mobile manipulator	Height: 14m	On-site	Concaves/ convexe	Insulating foam	USA
2017	Cassa X1	Mobile manipulator	Height: 5.5m	On-site	Concaves/ convex	Concrete	USA
2017	BatiPrint3D	Mobile manipulator	Height: 4m	On-site	Concaves/ convexe	Insulating foam	France
2017	B-hut	Gantry	150m2	On-site	Concaves/ convex	Cement	USA
2017	MATRICE	Mobile holonomic manipulator	Height: 1m	On-site/Factory	Funicular surface	Cement/ Clay	France
2018	Fly-Elephant	Drone	Varying	Factory	Concaves/ convex	Cement	China
2018	Nanyang University of Technology	Mobile holonomic manipulator	Not indicated	Factory	Concaves/ convex	Cement	Singapore

Table 2.1 – Existing robot-based machine for additive manufacturing in the construction

2.4 Soft-continuum manipulator in Construction

In 3D printing process, it is essential to inspect the quality of the printed or repaired object of construction during or after the printing phases. This monitoring phase can be automated to detect the appearance of crack, have a return on the quality of the surface, and check the adhesion between the printed layers or slicers. Several systems have been developed to automate the inspection process in some specific environments, such as subway tunnel (Zhang et al., 2014), flexible pavement surfaces (Oliveira and Correia, 2013), (Shi et al., 2016), bridge decks (Prasanna et al., 2016) and building (Yan et al., 2017),(Chen et al., 2016).

In (De Paz et al., 2013), a hexapod robot, named Hex-piderix, with a stereo camera has been used to inspect the cracking on surfaces as walls or roofs of a building. Access to these places is sometimes very difficult for operators. Some use Unmanned Aerial Vehicles (UAV) systems in the visual inspection of buildings. The crack detection is essential for health monitoring of built infrastructure. An integrated system that enables revisiting crack locations during building inspections by means of a quadrature UAV is presented in (Kucuksubasi and Sorguc, 2018). In (Phung et al., 2017), a UAV used for the data collection in order to create a 3D model of the targeted structure by using laser scanners. Thanks to 3D printing and 3D scanning, it is possible to check the impression quality and repair very complex details.

However, the geometry of the printed objects, with minimal surfaces can sometimes be complex as traditional rigid structure robots, which cannot reach certain critical areas of the objects. Recently, soft-continuum robots, which can bend at any point along a 3D targeted objects have emerged. This inherent flexibility makes them suitable for various applications, including navigation and operation in complex and congested environments (Casper and Murphy, 2003; Simaan et al., 2004). In this work, the flexibility of the robot has been exploited to navigate through complex objects during the print quality inspection step.

This section is organized as follows: The following subsection gives some soft continuum platforms with their actuation modes. The existing contributions on the kinematic modeling of soft-continuum manipulators is presented, thereafter.

2.4.1 Soft-continuum platforms

This subsection presents, depending on the actuation mode, some developed soft-continuum manipulator platforms. It includes pneumatically actuated soft manipulators, cable-tendon actuated soft manipulators, and soft manipulators with both actuating modes.

Pneumatically actuated soft manipulators

Festo Company has conducted several projects inspired by nature (Festo, 2013b) with the purpose of developing new bio-inspired robots actuated pneumatically. Among these projects, the project of the manipulator arm inspired from the elephant trunk, BHA (Figure 2.23a), and its compact version named CBHA. The latter is fixed on an omnidirectional mobile platform (Festo, 2013a) called Robotino (Figure 2.23b). A new type of manipulator called the octopus (Figure 2.23c) has just been developed. It is made almost entirely of soft muscles and is flexible and manoeuvrable.

A pneumatically robot called Octarm (Walker et al., 2005) robot was also designed by

(a) Bionic Handling Assistant soft manipulator

(b) RobotinoXT

(c) Octopus Gripper robot

Figure 2.23 – bionic Robots manufactured by FESTO

Pennsylvania State University and Clemson University, Figure 2.24a. The movements are generated by pneumatic muscles, also known as McKibben actuators. These actuators provide a high force/weight ratio and the constraint required to grasp an object (McMahan et al., 2006). Figure 2.24b shows a soft robot made of silicone rubber (Lee et al., 2017). It comprises three inflatable cylindrical chambers that can be operated separately in order to generate a bending moment when subjected to an input pressure. We also find the soft-arm presented in the Figure 2.24c which is a robot with five soft segments (Della Santina* et al., 2018).

Soft manipulators actuated by cable-tendon

Most soft-continuum manipulators was actuated by forces and moments applied from inside of robot's tubes. In the last decade, researchers used cable-tendon as actuators in the development of soft-continuum manipulators (Anderson, 1967). They have been implemented on a soft manipulator inspired by the octopus, described in (Cianchetti et al., 2011; Calisti et al., 2010). It is composed of a one conical silicone piece actuated by several cables immersed in the body (Figure 2.25b). Thus, the manipulator can be twisted and folder by pulling the cables. This manipulator has been designed to be used in water to exploit the material's mechanical properties and interaction with the environment. We also find, the Elephant Trunk robot manipulator (Figure 2.25c) actuated by two pairs of tendon cables arranged in an antagonistic manner. The kinematics of the latter is presented in (Hannan and Walker, 2001).

These robots have been designed for medical applications, research, rescue, industrial inspection, nuclear decontamination, undersea and space applications. For example, OC Robotics[28] and Airbus develop flexible snake-shaped robots (Figure 2.25a) to perform as-

[28] http://www.ocrobotics.com/

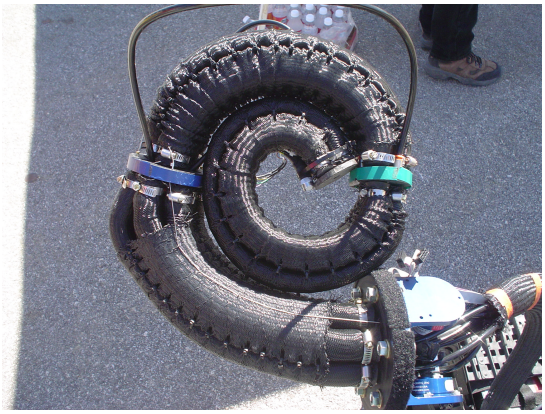

(a) Octarm (Walker et al., 2005)

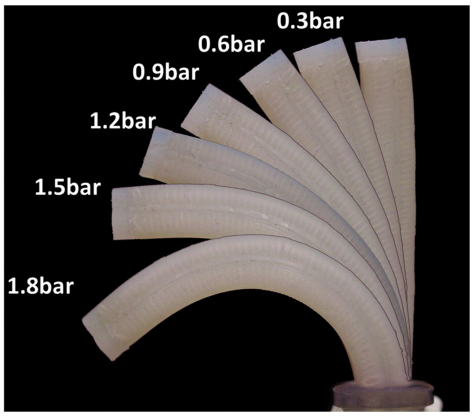

(b) Silicone soft-manipulator (Lee et al., 2017)

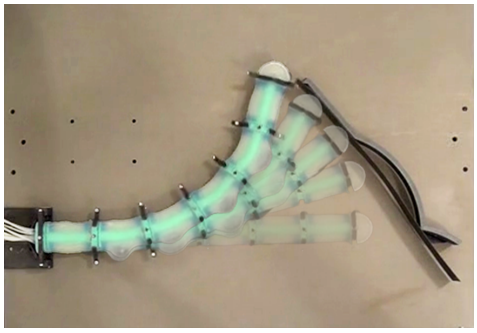

(c) Softarms (Della Santina* et al., 2018)

Figure 2.24 – Pneumatically actuated bionic robots

sembly tasks in wing box, an area currently inaccessible for automation (Buckingham et al., 2007). It has a series of rigid links attached mechanically by cables allowing to obtain a flexible structure to reach the dead zones (Figure 2.25a). The MiniOct is a continuous three-section device(Frazelle et al., 2018). The mechanical design of the latter has been inspired from the spring and cable system that exist in the elephant trunk manipulator (Figure 2.25c).

Soft manipulators actuated by a combination of different actuators

Air-Octor, designed by (Jones and Walker, 2006a) shown in Figure 2.26a, has two sections, with six degrees of freedom. It uses a combination of DC motors and pneumatic pressure for operation. On the other hand, a MIT team has reproduced a multi-segment manipulator that looks like in elephant-trunk, called TrunkBot, presented in (Cheng et al., 2012). It is actuated with four cables placed around segments. By changing the volume of liquid in each segment, a bending movement is generated (Figure 2.26b).

2.4.2 Modeling of soft-continuum manipulators

The contributions on the modeling of soft robots can be grouped according to three approaches: quantitative, qualitative, and hybrid. All these approaches are based on the information available to describe the robot's behaviors. Quantitative modeling approach are also known as model-based methods, consist to formulate mathematically a relationship between the causes and effects by using kinematic and dynamic fundamental equations. Qualitative modeling approach or learning-based approach consists in dividing the

(a) Snake Manipulator (Buckingham et al., 2007)

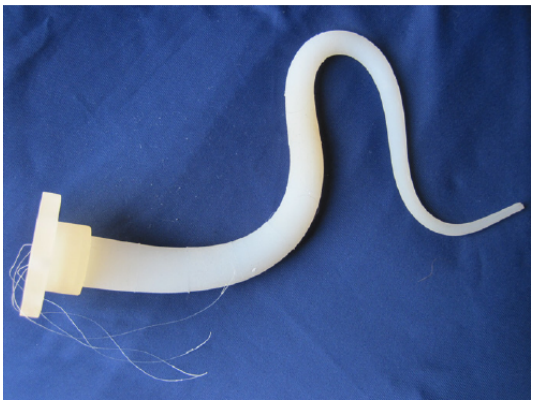

(b) Octopus Manipulator (Cianchetti et al., 2011)

(c) Elephant Trunck (Hannan and Walker, 2001)

(d) MiniOct (Frazelle et al., 2018)

Figure 2.25 – Bionic robots actuated by cable-tendon

(a) Air-Octor (Jones and Walker, 2006a)

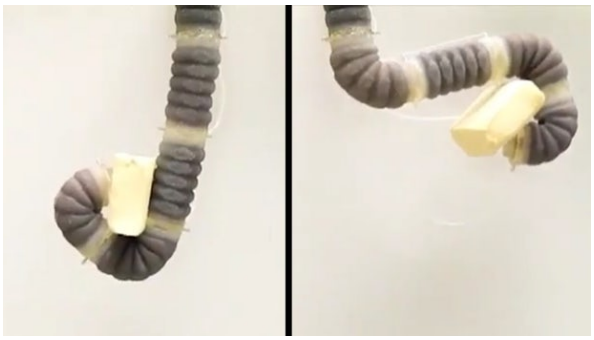

(b) Trunkbot (Cheng et al., 2012)

Figure 2.26 – Bionic robots with two actuator types

parameter space into several classes according to the well-known modes of operation, and then determining by learning the mathematical relations between the effects (sensor measurements of Cartesian or joint positions), and causes (inputs of voltage, pressure,...). Hybrid approaches combine the quantitative and qualitative approaches to better exploit their advantages, specially for model solving in real-time.

Quantitative approaches

Regarding model-based methods, various approaches have been proposed for solving the kinematic problem of continuum robots. Hannan et al. (Hannan and Walker, 2000) used differential geometry and the Denavit-Hartenberg procedure to develop an intuitive kinematic model of a continuum manipulator for planar and spatial scenarios. Generally, this geometrical approach considers the structural assumption of constant curvature of the backbone (Webster and Jones, 2010). Jones and Walker (Jones and Walker, 2006a) extended this result by considering multiple sections of the manipulator. The same approach was used in (Bardou et al., 2010) to control a flexible endoscopic system, and in (Zhao and Gao, 2010) to describe the kinematics of a tendon-based manipulator. Godage et al. (Godage et al., 2011b) presented a new three dimensional kinematic model for multi-section continuum arms using a novel shape function-based approach (Godage et al., 2011a), which incorporates geometrically constrained structure of the arm. Another interesting approach is the one presented in (Rolf and Steil, 2012a); where the authors used torus segments to represent the sections of the BHA manipulator. Escande et al. (Escande et al., 2012) developed the FKM of the CBHA based on the constant curvature assumption. A geometrical approach to solve the inverse kinematics of continuum robots was proposed and applied to OctArm in (Neppalli et al., 2008), where the endpoint for all sections of a multi-section arm are assumed to be known. Recently, Pythagorean Hodograph curves were used to deal with the inverse kinematic problem of continuum manipulators (Inderjeet Singh, 2018). A 3D shape of the continuum manipulator is first reconstructed and the inverse kinematics are derived thereafter. A comparative study of the different approaches developed in the case of CBHA robot is presented in (Singh et al., 2017b; Singh et al., 2017a). A metaheuristic approach based on an optimization algorithm has also been proposed in (Amouri et al., 2017).

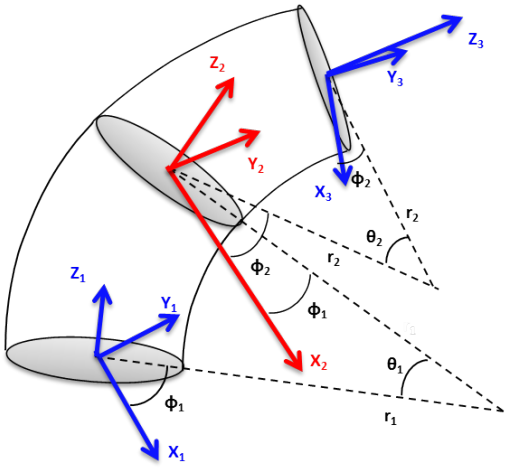

Figure 2.27 – Constant curvature (Escande et al., 2012)

Concerning the modeling of kinematic behaviors of continuum manipulators as a se-

ries of parallel robots, Mahl et al. (Mahl et al., 2012) proposed a forward kinematic model of a continuum robot considering each section as a series of 3-DoF parallel mechanisms. Rongjie et al. (Kang et al., 2013) solved the problem of multiple solutions of the inverse kinematics of continuum manipulators using a spline interpolation method. The latter is used to generate the backbone curve of the manipulator assuming that the proximal and distal parts of the continuum manipulator remain straight, and the bends only occur on the middle part of the manipulator. Chirikjian and Burdick (Chirikjian and Burdick, 1994) developed a modal-approach for hyper-redundant manipulator kinematics. The hyper-redundant manipulators are abstractly represented by backbone curves that either exactly or closely capture the important macroscopic geometric features of the robot. An optimal curve is used to generate the continuous backbone curve. The optimality criteria are used to choose the curve that satisfies task constraints, while optimizing additional criterion. A serial-parallel platform have been modeled as a basic element of a hyper-redundant robot in Chibani et al (Chibani et al., 2015). An emulation to the CBHA robot has been produced. Espinoza et al (Espinoza et al., 2012) proposed an IKM for a 10-DoF hyper-redundant robot based on error optimization algorithms.

However, most of the aforementioned modeling techniques lead to less accurate models especially when precision is needed in the robot task, such as handling. In addition, it is often difficult to deduce the inverse kinematics directly from the forward kinematics. Usually, we make use of numerical methods (least squares (Hollerbach and Wampler, 1996), Newton-Raphson methods (Goldenberg et al., 1985), etc.) which are computationally intensive.

Qualitative approaches

Concerning qualitative approaches, Giorelli et al. (Giorelli et al., 2013) approximated the IKM of a soft manipulator using a feed-forward Neural Networks (NN). To control a soft extensible manipulator, Braganza et al. (Braganza et al., 2007) used NN to compensate for the dynamic uncertainties. Rolf et al. (Rolf and Steil, 2012b) introduced goal babbling approach to solve the inverse kinematic model of the BHA robot. Melingui et al. (Melingui et al., 2014c) used NN in distal supervised learning scheme to approximate the IKM of the CBHA robot. Then, an adaptive neural network control of the CBHA robot is proposed in (Melingui et al., 2015; Melingui et al., 2017). In (Thuruthel et al., 2016b; Thuruthel et al., 2016a), a learning-based approach to obtain the inverse kinematic model solution for soft-continuum robots is presented. The method differs from others on the unique formulation of inverse kinematics. However, this approach has only been validated by simulations. Another advantage of such an approach is that it provides multiple solutions to the problem and can work even if some actuators are not functional after the learning process. A similar modeling method reinforced with a controller has been experimentally validated in (George Thuruthel et al., 2017). It has also been observed that even with a simple controller, intelligent behaviors have been achieved in an unstructured environment.

Generally, qualitative approaches lead to more approximate accurately complex models. However, the more significant the number of degrees of freedom of the robots becomes (beyond 10-DoF), the more difficult or time-consuming it becomes to calculate their kinematic models.

Hybrid Approach (quantitative and qualitative)

An alternative to model the kinematic behavior of robots is to combine the two previous approaches in order to take the best of them. In literature, the use of qualitative approaches to improve the performance of quantitative models can be found in (Karlik and Aydin, 2000; Bingul et al., 2005; Daachi et al., 2012; Guez, 1988), where neural networks were used to approximate a large number of robot manipulator models in presence of nonlinearities. A hybrid controller combining both the model-based and neural network approaches has been proposed in (Jiang et al., 2017) and (Reinhart et al., 2017). In (Jiang et al., 2017), the authors present a control algorithm for a manipulator that can be extended to several segments in a 2D plane. Its kinematics is solved on two levels. In the first level, an analytical model based on the gradient descent method is used to determine the optimized positions of all segment peaks based on predefined measurements. The second level uses neural networks to determine the pressures of each segment, taking into account the viscoelasticity property. Reinhardt et al. (Reinhart et al., 2017) proposed a hybrid, data-driven analytical approach for the early control of a bionic manipulator BHA. The effectiveness of this approach was demonstrated by a reduction in tracking error, which represents less than half of the error observed when using the analytical model. In our previous work, A multilayer neural network has been used in (Lakhal et al., 2014b) to approximate the solutions of the inverse kinematic equations of the CBHA robot, where the time-allocation for the learning process was considerable, due to the complex kinematic of the robot. A qualitative approach has also been used to approximate the CBHA kinematics (Melingui et al., 2014a; Melingui et al., 2014c) and to develop a kinematic controller (Melingui et al., 2015).

Hybrid approach introduced in this thesis is an extension of initiated works on CBHA modeling (Lakhal et al., 2014b), to a real-time solving of the CBHA modeling. It is extended in this PhD work by adding a real-time resolution and implementation in case of trajectory tracking. A methodology of kinematic modeling and synthesis of its approximate solutions is proposed for the case of continuum manipulator of type CBHA. The modeling approach is issued from a quantitative modeling of parallel rigid manipulators. Structurally, the CBHA is assimilated to a series of parallel manipulator under the following assumptions: the CBHA's backbone represents a series of vertebrae, an inter-vertebra is modeled as three Universal-Prismatic-Spheric (UPS) and one Universal-Prismatic (UP) joints, the robot torsion is not considered because the robot is driven at low velocities and also due to the memory effect of its constuitive material. The CBHA's kinematic models are deduced merely from the inverse kinematic equations of each inter-vertebra and generalized for whole the hyper-redundant robot. The obtained inverse kinematic equations are highly nonlinear and mathematically intractable for the CBHA manipulators. For this issue, a multilayer neural network is used to provide approximated solutions of the IKE which can be used for real-time implementation. The advantages of the proposed hybrid modeling-solving approach compared to quantitative methods is that the obtained models are more accurate and computationally inexpensive. Compared to qualitative approaches, the proposed approach can be implemented for platforms including a significant number of DoFs; because the training database is deducted directly using the inverse kinematic equations. This avoids to operate the robot for a long-period for learning database.

2.5 Conclusion

In this chapter, as a first step, some robot-machines dedicated to 3D printing in the construction were presented as well as the manufacturing methods. These robotic systems have been designed with the aim of providing new technical solutions that would meet expectations: saving time and improving quality in additive manufacturing in the construction. Thus, 3D printing bridges the gap between mass production and personalization. In a second step, a state of the art on soft-continuum manipulators was presented for the case of inspection quality in the construction. Soft materials and new actuating mechanisms ensure smooth movements and high adaptability of soft robots to their environment, but also increase the difficulty and complexity of construction control systems. Solving this problem is the topic of chapter 5 of this thesis. Subsequently, a focus on the design and selection of the elements of the additive manufacturing machine in the construction will be done, in accordance with requirements and specifications in the framework of MATRICE project, detailed in the following chapter.

Chapter 3

Technical specifications for designing MATRICE Robot

Contents

3.1 Introduction

This chapter describes the technical requirements specifications to design the robot-machine of MATRICE project. These requirements justify the considered assumptions for the kinematic modeling and control introduced in the other chapters. The main idea behind additive manufacturing is the management of the flow of architectural design within the automatized performance process. This involves converting all that is designed in a virtual environment using CAD tools, into real physical object. Within the MATRICE project, a robot (machine) dedicated to additive manufacturing has been designed in such a way that it meets the requested requirements and specifications of printing in the construction field. In fact, the objective was the automation of additive manufacturing in printing funicular geometrical objects, characterized by the "intrados" shape which is always different from the "extrados" shape. In this context, the robot is supposed to follow the dimensions as well as the geometrical shape, designed by the experts (architects).

The additive manufacturing in construction needs to be controlled in terms of deposit quality during the printing process and the quality inspection of the printed object after the termination of the printing process. The quality of the deposit depends on the accurate superposition of the constitutive layers with the suitable material. Thus, two types of materials have been used, based on clay and cement materials. The purpose is to adapt the use of these materials according to the kinematic of the robot and the shapes to be printed. The main challenge lies in obtaining printable forms whose rheology and geometry can be mastered and reproduced. This chapter attempts to clarify the proposed solution in the context of robotized additive manufacturing for MATRICE's project.

3.2 Collaborative research

MATRICE project aims to design a prototype of robotized additive manufacturing in the construction field. This designed concept should has a Technology Readiness Level (TRL) of 6 in a scale of 8. This level of pre-maturation, where the technology should be demonstrated in relevant environment industrially relevant environment in the case of key enabling technologies. It is called concept because it regroups multiple disciplines of the shape, the robot and the material of Figure 3.1. The main objective of this collaborative research is to build a communicated bridge between these three dependent topics. Thus, the challenge is to establish a compromise between which large-scale shapes can be printed using specific materials for construction.

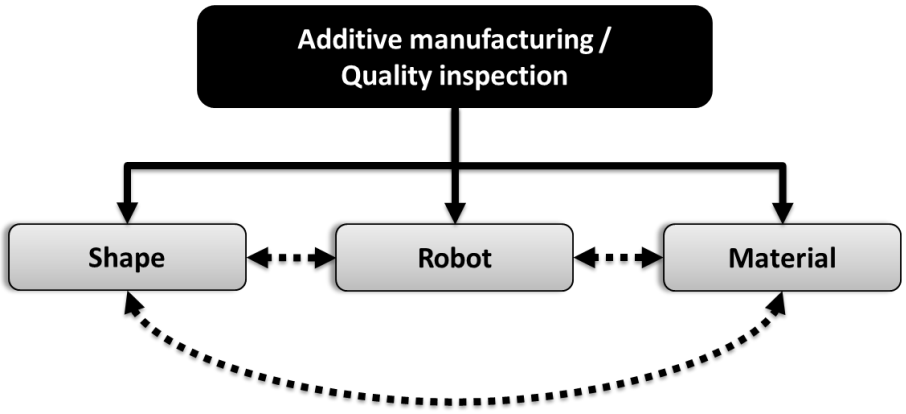

Figure 3.1 – Additive Manufacturing

3.3 Materials

Two printable materials have been considered and used during the printing process. The cement-based mortar material developed by the Civil and Environmental Engineering Department of IMT Lille Douai (Figure3.2a) and the clay printable material developed by the University of Artois (Figure3.2b). The formulation of the printable materials is essential as they must be enough fluid to be extruded. It must also lend itself so that it can resist its own weight.

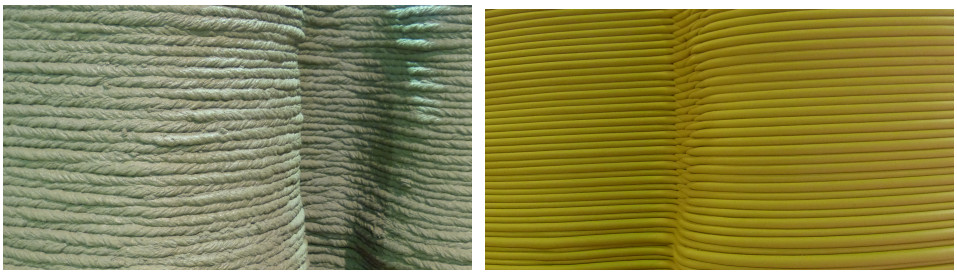

(a) Cement based materials (b) Clay based materials

Figure 3.2 – Materials

However, the printable material must meet the requirements of very demanding specifications. Thus, four main criteria have to be respected:

Extrudability : First the material must be mixed to obtain a homogeneous product then it must be pumped and extruded through the designed nozzle guided by the robot-machine. This process must be carried out without any interruption of the material pumping and without separation phase. All those characteristics are called extrudability.

Buildability : After the extrusion, the deposit of the material is done through the nozzle and guided by the robot-machine. Besides, it must also sustain the additional material layers (slicers). The buildability is defined as the maintaining of the shape while the extrusion is under way and the gradual hardening of the material. This is to sustain the material while increasing the weight after adding a new layer.

Resistance : After getting hardened, the material must behave like any other conventional construction material and fulfill the set of functions of the printing process. Those functions can be numerous (thermal and acoustic properties, mechanical resistance). However, in the MATRICE project, only the mechanical resistance has been taken into consideration.

Sustainability : The material must also be sustainable enough to fulfill the functions which it has been designed for during and after the printing process.

Thus, material that has both Sustainability and extrudability characteristics is described as a printable material.

3.3.1 Cement-based materials

Meeting the requirements of both extrudability and buildability is a difficult thing. Indeed, in order to be extrudable, the mortar must have the fluidity necessary to flow easily in the pumping pipes and through the extrusion nozzle. On the other hand, in order to be buildable, the mortar must be firm to keep its shape and support the weight of the upper layers. These two criteria contradict each other but, fortunately, they do not occur simultaneously during the printing process. The mortar is first pumped and then extruded only after being deposited in layers. Therefore, the formulation of cement-based inks requires the development of materials whose rheological behavior changes over time. These research works, realized in (Khalil et al., 2017; El Cheikh et al., 2017), made it possible to define two types of formulation. First, a Portland-based cement designed for the realization of extended items whose superposition speed is slow and therefore does not need

to be hardened quickly. Second, a mixture of Portland cement and sulfo-aluminous cement which allows stiffening and hardening of the material. This method is used for the production of small size pieces.

Two types of cement have been used: OPC(CEM I 52.5) EXTREMAT CEM I 52.5N-SR3 CE PM-CP2 NF I (99% Clinker) and Calcium Sulfo Aluminate Alpenat cement, both from Vicat Company. A new generation polyvalent non chlorated acrylic copolymer superplasicizer(SP), witrh high water reducer (SIKA VISCOCRETE TEMPO 11) was used. A calcareous crushed sandwith containing of 19% particles smaller than 63mm was used provided by Carrieres du Boulonnais.

3.3.2 Clay-based materials

The earthen materials Raw earthen and vegetates co-products play an essential role in the development of the additive manufacturing in the construction sector, as they allow the use of locally available and inexpensive materials. Russel (Russell, 2015) has shown the enormous potential of the earthen materials as an innovative solution to the housing problem faced by developing countries.

In this context, the team in charge of materials of the LGCgE – University of Artois has developed printable material formulations based on earthen. Some of these formulations were supposed to be structural or self-supporting (Partitioning, interior facing) and the others are intended for insulating. The aim was to propose a complete building wall for individual residentials, which could also serve as a partition or an interior siding associated with the insulating material (Dubois et al., 2018).

The earthen materials studied in this research work comes from the Company Carrières du Boulonnais. It results from the process of extracting limestone rocks used in a crushed form in concrete manufacturing. This rock contains a clayey gangue which must be removed in order for the limestone granules to conform to the characteristics necessary for concrete manufacturing. The rocks are thus washed and the washing muds are deposited in a settling basin. A few weeks, or even months later, the sediment mud can be extracted to be dried and ground into powder by attrition. The product obtained is referred to as quarry fines in this study. The trade name is AC 0100.The earthen materials are quarry fines (QF) coming from aggregates washing. The quarry fines include limestone ($\approx$ 62%), kaolinite ($\approx$ 12%), illite ($\approx$ 7%), quartz ($\approx$ 11%), goethite ($\approx$ 3%) and dolomite ($\approx$ 5%). The particle size ranges from 0.1 and 100 mm. Quarry fines are defined as Ap (low plastic clay) according to the USCS classification. A blast furnace cement (C) is chosen for its high rate of blast furnace to promote the reuse of waste and is referenced CEM III/A 52.5 L CE PM-ES-CP1 NF.

Clay with short flax fibers and shives is a very viscous material that requires more time to solidify. Thus, the superposition speed must be slow.

To control the setting time, a retarder is included in the mix design of the structural mix. This additive also plays the role of plasticizer. After some laboratory tests, the composition chosen for 3D printing tests includes 70% of QF and 30% of C. The proportion of retarder was 0.8% according to the cement part. The water content is chosen to have a sufficiently fluid mixture for a correct extrudability or filling while allowing a rapid hardening.

First, all the dry elements (dry powders and flax products) are placed in the bowl or tank. The Water is introduced progressively for 30 s once the mixer is turned on to avoid the loss of powders. The retarder is poured at the same time. The mixing continues for 90 s, then the mixer is stopped. Once the mixer is stopped, the workability of the mix is

tested.

3.4 Architectural shapes

Generally speaking, there are two main approaches used by researchers working in the field of large-scale additive manufacturing. In the first approach, the economic and industrial aspects of this technology play an essential role, which means that the form remains morphologically simple and standardized. In other words, the objective is to build as quickly as possible. The second approach emphasizes the capacities of robotics and digital design so as to produce non-standardized complex geometries. This approach implies that we take into consideration the tight link between geometry, structure, and architecture. The researches carried out at the ENSAPL institute have been tackled on the second approach.

Besides, the geometry of the printed structure plays a significant role in the behavior of the material during the printing process. Indeed, the different large scale printing constraints and parameters require precision at the level of the structure geometry.

3.4.1 Funicular shape

To describe the concept of funicular structural systems, it is worth quoting one paragraph from Schodek (Schodek and Bechthold, 2008). “A cable subjected to external loads will obviously deform according to the magnitude and location of the external forces. The form acquired is often called the funicular shape of the cable (the term funicular is derived from the Latin word for “rope”). Only tension forces will be developed in the cable. The Inverting of the structural shapes obtained will yield a new structure that is exactly analogous to the cable structure, except that compression rather than tension forces are developed. Theoretically, the shape found could be constructed from simply stacked elements that are non rigidly connected (compression chain) and the resultant structure would be stable.” Gaudí’s use of funicular structural systems to develop his architectural designs is well known (Collins and Nonell, 1981). But, the construction system was excessively complex and fragile.

In the context of additive manufacturing, architects were able to make use of purely compressed behavior of funicular surfaces using parametric software. These software can model architectural elements with pronounced curves and shape them according to the structural stability characteristics permitted by the materials. To realize this, the Kangaroo plugin on the Grasshopper platform [1] has been used to generate funicular surfaces. Parametric modeling of funicular surfaces ensures a larger flexibility on the same basis by adjusting the parameters such as the resistance, the rigidity or the density of the mesh. Consequently, the parametrization of the surface has made it possible to adjust the inclination of the structures with regard to the material type. A phase of evaluation, verification, and structural analysis was added to refine the generative algorithm.

The architectural form depends not only on the material but also on the constraints of the machine. In the context of the MATRICE project, the considered version of the nozzle can not control the pump flow. The efforts have been done on controling the nozzle motion. Thus, generating the printing path was harder to achieve. Because it must ensure a continuous interpolation of the robot targets without any intersection. To achieve this, two basic parameters have been chosen, namely "intrados" and "extrados" (Figure.

[1] https://www.rhino3d.com/6/new/grasshopper

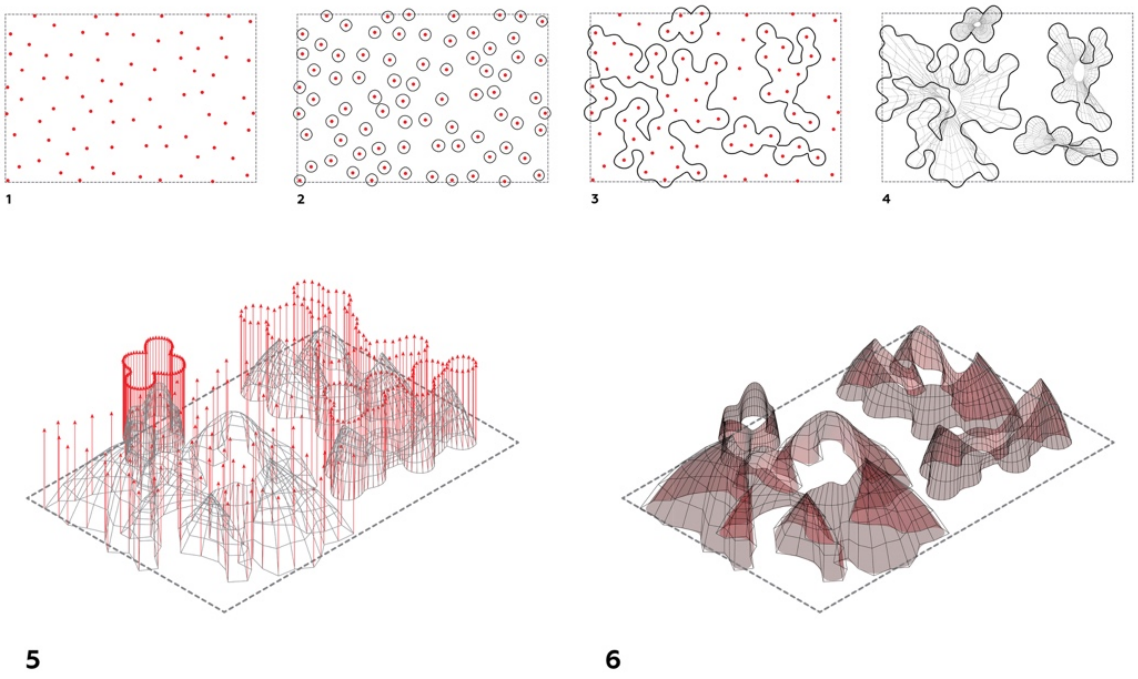

Figure 3.3 – The exploration of the morphological variation in funicular shapes generated with a random point logarithm

3.4b). A zigzag (Figure. 3.4c) shaped inner surface is generated to fill the gap between the two sides. We should note that the zigzag is initially generated on the first layer, then it adjusts locally to the surface for the the following layers. Contrary to the codes used in plastic printing machines, it is not possible in our case to use a simple infill. This because the surfaces can have a curvature variation in all directions and the deposit of the material is continuous. The main problem in this part was to find a rationale (logic) of zigzag adaptation on the surface of each layer (Figure. 3.4d) and, at the same time to ensure the continuity of the interpolation without any obstacle or interruption.

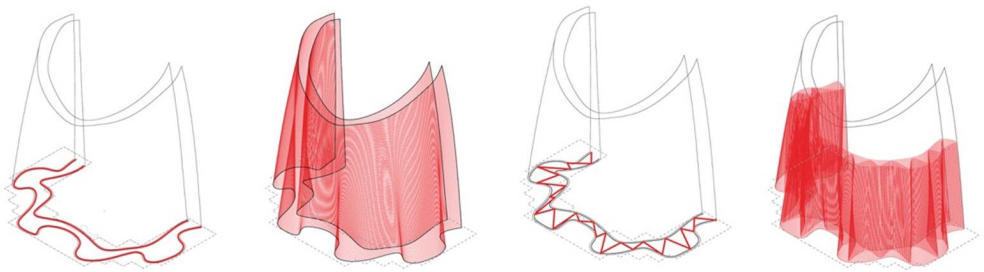

(a) (b) (c) (d)

Figure 3.4 – Slicing with adapted zigzag filling

3.4.2 Digital validation of the structure

This step raises the issue of the stability of the structure to be printed. In particular, digital tools have been set up to meet the challenge of structural problems during the different steps of the process and mainly those of manufacturing, installation and safety.

3.4.3 Structural analysis and stability

Whether it is large or small, the inclination of the printed structures constitutes one of the major constraints to be taken into consideration. In fact, conventional plastic printers generate supports when the inclination of the structure becomes significant. This tilt limit is defined according to the type of plastic used. The problem remains the same when using a large scale concrete printing machine. However, the solution becomes more complex because of the scale effect. Indeed the first step consists in finding the inclination limits. Thus, an algorithm has been generated after having carried out various tests on the maximum height and the feasible inclinations. This algorithm allows a morphological change of the parameters of the surface (Figure 3.5). The limit value of the feasible inclination of the structural form, the filling optimal density and the depth control of the extruded concrete have been taken in account on the basis of the ratio between the flow rate of the material and the printing velocity.

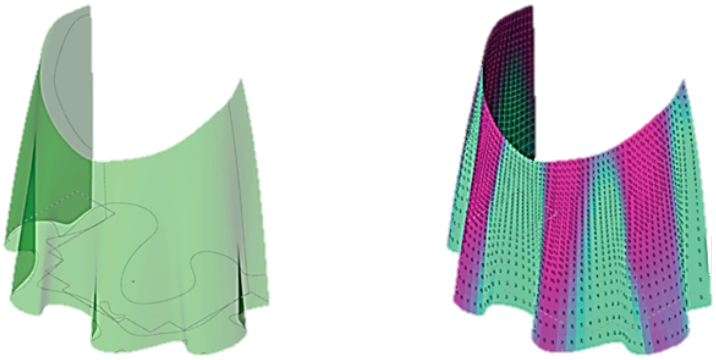

Figure 3.5 – Inclination test resulting from the mean average of the surface structure

To set the parameters and ensure interoperability, designed tools allow the updating of any change and the significant reduction of the time taken by the design and the shape checking. This code which has been developed in Cast3m [2] allows to evaluate the structural constraints and the movements undergoing an arbitrary charge, starting from points generated by Grasshoper. In order to automate the process and interoperate from the first stages of the design, a cyclical procedure takes in charge the acquisition of the points generated. First by using a parametric modeling, then optimizing the mesh according to the conditions of the limits and the type of analysis to be done. The elements used for generating the mesh structural belong to the dkt type [3]. Those elements are iso triangular parametric elements. The use of these types of elements allows an optimal ratio relation between the cost of the required calculation and the minimization of the error between the analytical solution and the result obtained through discretization. The mesh procedure is conceived to model structure wall gates of 15 cm in average thickness. Figure 3.6

[2] http://www-cast3m.cea.fr/index.php?xml=tutoriels
[3] DiGiTIAL THUNDER Drum Kit Format

illustrates an example of a meshing test result carried out on the final structure of the pavilion (3D object).

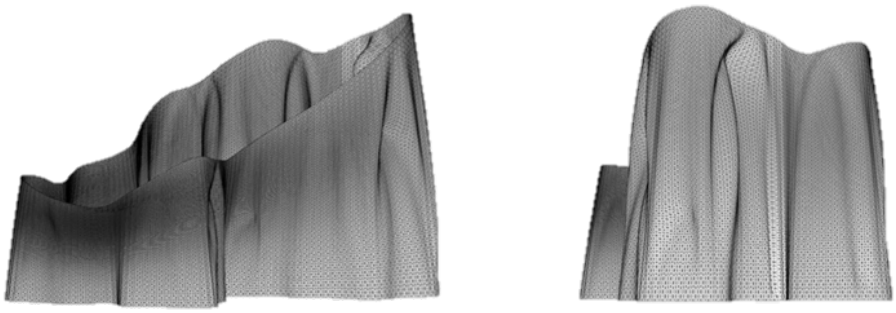

Figure 3.6 – Inclination check resulting from the average surface area of the structure.

3.4.4 Optimization of the structural topology

Additive manufacturing makes possible the exploitation of forms that have geometrical complexity, far beyond what can be achieved by conventional manufacturing technologies. The optimization of the topology is developed with the purpose of creating light mechanical components used for the car and space industry. The advantages that a similar technology applied to additive manufacturing can be summarized as follows:

- High performance design process;
- Optimization of free form research;
- Minimization of mass components which means saving time, energy and material, and improving the cost efficiency ratio.

Topological optimization consists in finding the ideal distribution of mass in a given volume undergoing constraints. Solving the problem is done through the discretization of the item by the finite elements method. Thus, we can either decide what quantity of material is to be used so as to realize the optimum forms or directly look for a form minimizing the material to be made as light as possible. This is to be done while respecting constraint limits.

3.5 Specifications of the robot-machine

The CRIStAL laboratory located at Polytech-Lille, is mainly involved in the prototype design of a 3D printing robot-machine dedicated to the construction. The prototype can print elements of complex architectural shapes of about $1m^2$ in static configuration (without displacing) using clay or cement material. The same prototype can make a quality inspection of printed surfaces. This printing robot-machine must fulfil several functions:

- Main function (MF): function that directly meets the needs
- Constraint function (CF): function which does not meet directly the needs but adapts the machine to its environment.
- Under main function (UMF): function allowing the realization of a chosen solution to fulfill a MF.

- Under constraint function (UCF): function making it possible to realize a chosen solution to meet an CF.

Figure 3.7 shows how we can relate the system to its outside environment.

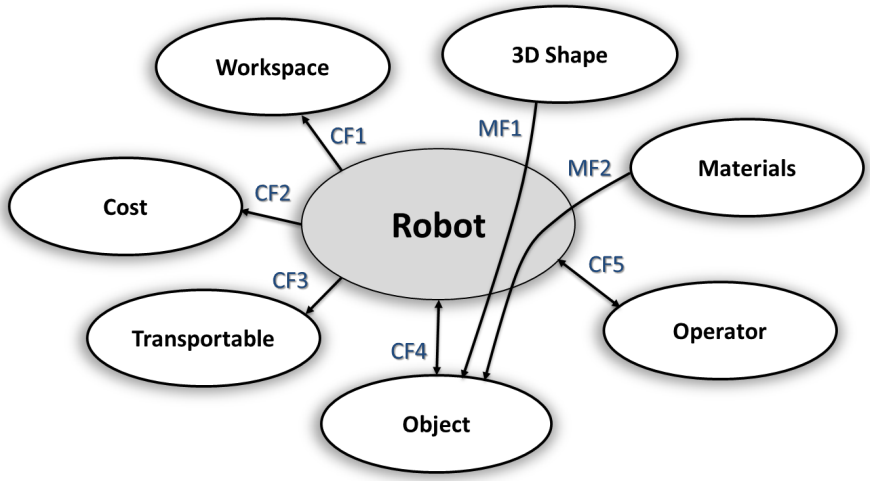

Figure 3.7 – 3D printer environment diagram

Here is a list of the MF and CF :

- MF1: Trajectory generation starting from the 3D architectural form.
- MF2: Conveying the material through a nozzle, flow control and material presence detection.
- CF1: Printing area.
- CF2: Budget constraint.
- CF3: Measurements and weight adapted for placing the robot on a $10m^3$ lorry and a door width measuring $1,2m$.
- CF4: Quality inspection of the object.
- CF5: User interface and operator security.

3.5.1 Description of the product functions

MF1: Trajectory generation starting from the 3D architectural form

Trajectory generation means the calculation functions to obtain the joint variables of the robot. The latter are intended to actuator commands that allow moving the robot and achieving the specified end-effector (Nozzle) motion. It will be essential to define the file format that can be interpreted by the robot so as to retrieve the point positions of the 3D form as defined by the architects.

MF2: Conveying the material through a nozzle, flow control and material presence detection

The mortar or its components must be conveyed towards the nozzle exit. The mortar is a mixture of aggregates and binding materials. First, it has a pasty appearance that facilitates the process of shaping the object. However, this pasty state must be sufficiently fluid for the object to take shape, and strong enough to maintain it under constraints such as gravity, ambient temperature, and humidity. During the second stage, the mortar acquires a solidity in which the shape will be preserved durably against any external constraint. Passage from the pasty state to the solid state usually occurs through a chemical reaction or a thermal reaction. The purpose of this function is to provide a mortar sufficiently flexible to be handled by the robot and sufficiently resistant to meet the needs of civil engineering.

CF1: Printing area

The main objective of the MATRICE project is to print complex shape elements in clay or cement $1m^3$ when the robot-machine is static and not moving . In this static configuration, the robot-machine must have a reachable $1m^3$ workspace.

CF2: Budget constraint

To remain within the limits of the allocated budget while dealing with unforeseen events related to an innovative collaborative project.

CF3: Dimension and weight adapted for moving the robot on a $10m^3$ lorry and a door gate measuring $1,2m$

The printing campaigns are made in various spots such as the laboratory, the workshops, the exhibitions and other events. The machine must be mobile on the printing site so that the work can be carried out on the site.

CF4: Quality inspection of the object

Automation of the print quality inspection phase (crack detection, verification of adhesion between layers of material, etc.)

CF5: User interface and operator security

Ensure that starting a 3D mortar printer machine is as easy as starting a plastic 3D printer. The knowledge of only a few technical things should be required for starting. This is to prevent any accidents in the construction site in the printing area, blockage of mortar in the pipe to avoid dangerously rising pressure.

3.5.2 Search for solutions

The design strategy adopted is to design a non-bulky, easy-to-carry, self-contained robot-machine to print large scale objects and reach difficult access areas. The design of the machine itself is of great importance for the definition of the construction project, to determine the future implementation and even the formal characteristics of the architecture.

The main objectives are :

- Design and integrate performances of the existing robots and adapt them to the additive manufacturing in the construction context;
- Identify the stakes of the robot-machine; use in factory or on site, continuous or sequential printing ...;
- Automating the printing (material deposit) process ;
- Design and sensors implementation of the printing tool (Nozzle);
- Budget management and constraints;
- Technologically transferable;
- Quality inspection of the printed shape;
- Adapting the robot-machine to the rheological parameters of the materials;
- Reflection on the dimensions, complexity, feasibility and limits of the architectural shapes.

MF1: Path generation using the architectural 3D shape

Digital chain solution Figure 3.8 summarizes the different robot machine understandable instructions for moving from a 3D format to a physical object.

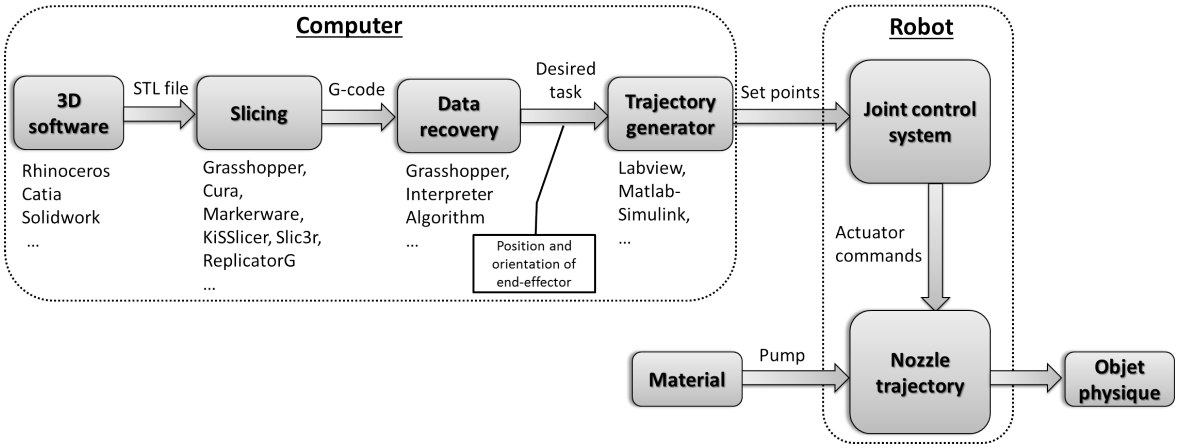

Figure 3.8 – Digital manufacturing chain

Robot solution A six-axis rigid manipulator is mounted on the mobile platform (Figure 3.9), which makes it possible to move a tool for the material deposit.

Omnidirectional platform solution The mobile platform is an holonomic mobile robot equipped with Swedish mecanum, wheel encoders, inertial measurement unit (IMU), and an indoor navigation system. The mobile platform has 3-DoF, two translations (lateral and longitudinal displacements) and one rotation (yaw). The mobile platform is capable of translating in all directions forward and backward but also to the right side and the left side and turn on the spot; this is achieved thanks to its omnidirectional wheels as shown in Figure 3.10. This is particularly useful when one has to maneuver in a narrow space or to print a large scale 3D objects.

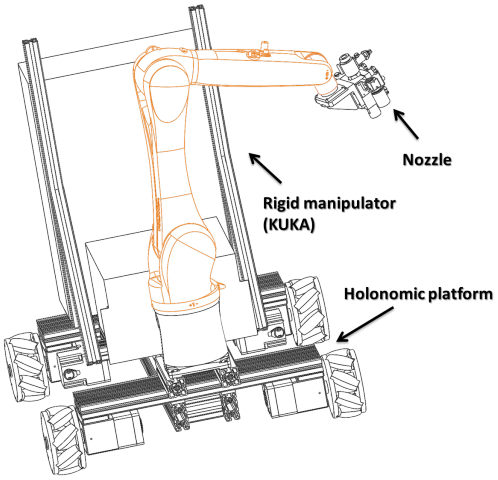

Figure 3.9 – Additive manufacturing prototype

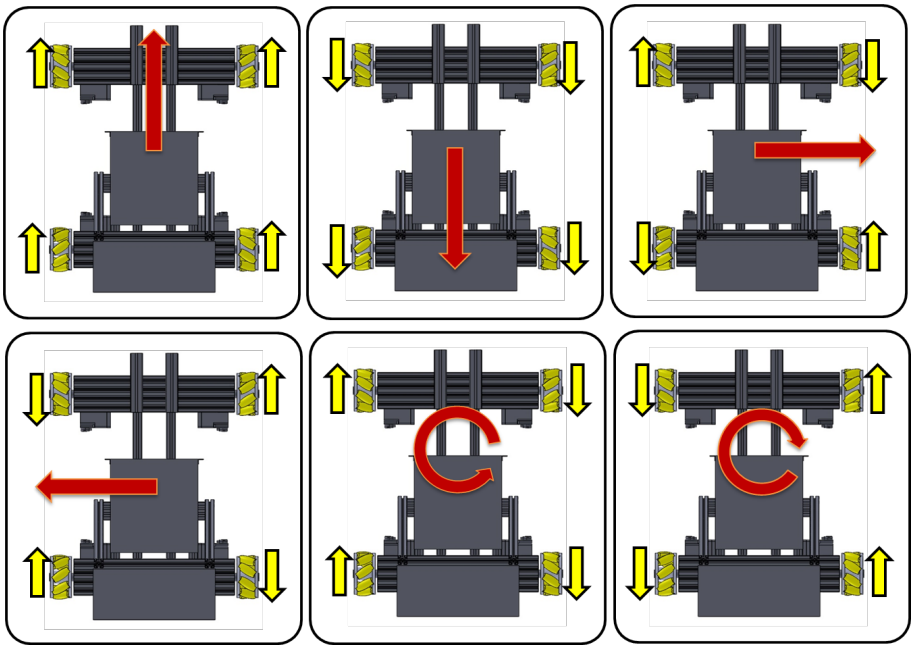

Figure 3.10 – Movement of the robot according to the wheels angular speed

Rigid manipulator solution The rigid manipulator is an industrial robot, a KUKA Agilus R1100 manipulator, with high repeatability and precision of 0.1mm. These properties ensure a very high deposit quality. The robot controller communicates with the sensor system via a network connection capable of operating in real time. The data is transmitted via the Ethernet UDP/IP protocol. With this interface, it is possible to control the robot motion or modify the execution program. The protocol is used to adjust the positioning errors of the mobile platform caused by sliding.

Figure 3.11 – KUKA Agilus R1100 manipulator

Navigation solution Marvelmind[4] Indoor Navigation System is a standard interior navigation system, designed to provide precise location information,$\pm 2cm$. This system is used to track the displacements of the mobile platform. The navigation system consists of a network of stationary ultrasonic beacons interconnected via radio interface in a license-free band, one or more mobile beacons and modem providing a gateway to PC system or other computers. Mobile beacon's location is calculated based on a propagation delay of an ultrasonic pulse between stationary and mobile beacons using trilateration algorithm.

Controller solution The CompactRio made by National Instruments [5] is used as controller. This is an onboard controller featuring two treatment targets processing: a real-time processor for communication and signal processing, and an FPGA user programmable. This latter allows the implementation of a high velocity command as well as a timing and a trigger system directly in the material. It is composed of entrance exit industrial input/output modules configured to communicate with different elements of the robot that is the mobile platform, the pump, the nozzle, the manipulator, the indoor navigation system and the inertial system.

MF2: Conveyance of the material through the nozzle, flow rate control, and material detection

Solution applied to the preparation of the material The choice made by the GCE Department is to prepare the mortar using the concrete mixer IMER 120.

[4] https://marvelmind.com/
[5] http://www.ni.com/fr-ch.html

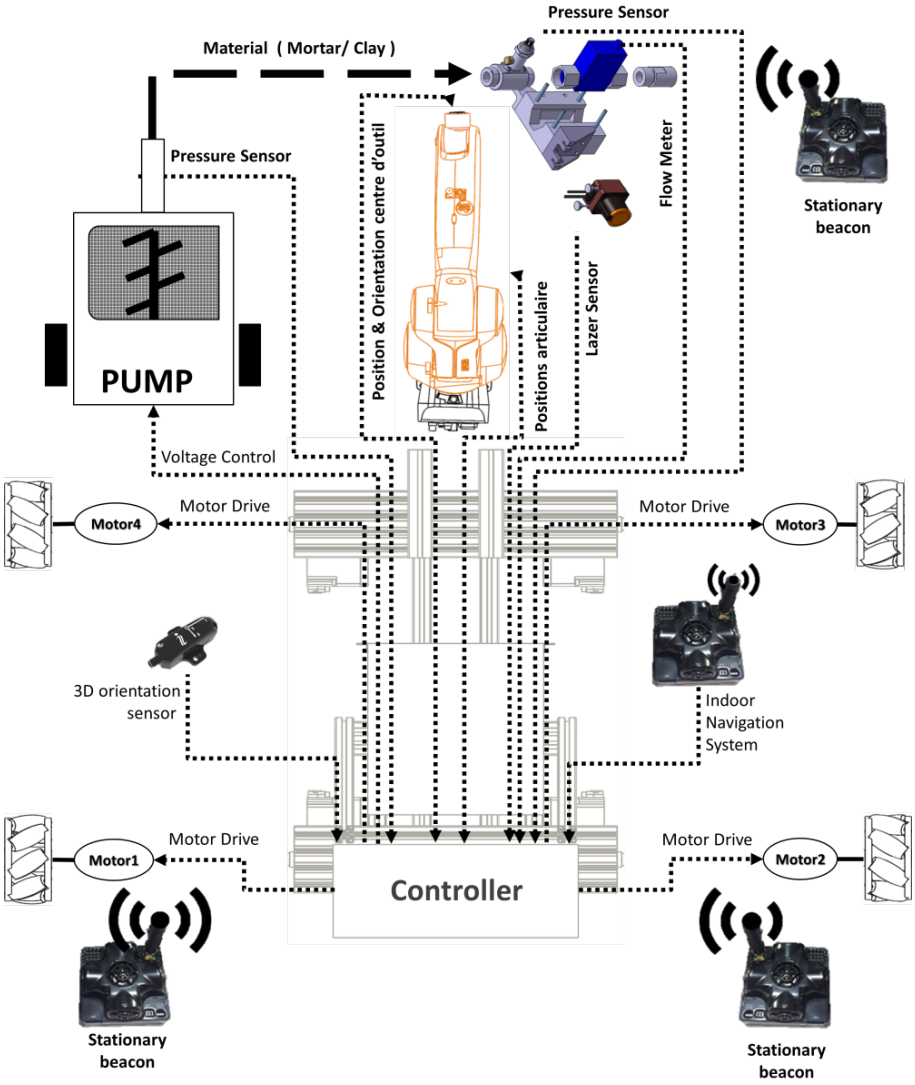

Figure 3.12 – Robot components

Figure 3.13 – IMER 120 Mixer

Pump solution The GCE department has acquired a Putzmeister [6] SP5 pump. The drawback of this solution is the high flow rate of the pump. Moreover, the pump circulates the material in 5m long pipeline which means that we cannot control the flow at the nozzle output. Then, a nozzle regulating system is to be found. Besides, a cable is made connecting the robot controller to the pump. This cable allows to control the input voltage of the pump.

Figure 3.14 – Putzmeister SP5 pump

Flow controller solution As stated above, the flow rate of the SP5 pump is not well adapted to the printing rate. So it is necessary to control the flow rate during the printing process. To do this, a SIka VMZ 204 flow-meter, is mounted on the nozzle side, so as to be as close as possible to the material outflow. In addition, it will also permit the online measuring of the rheological characteristics of the printing material.

Figure 3.15 – Nozzle instrumentation

Material detection solution The nozzle is equipped with a pressure sensor for material or plug detection (Figure 3.15). If the material dries fast, it is imperative to stop printing for safety reasons and to avoid damaging the robot-machine.

[6] http://www.putzmeister.fr

Material deposit control solution The control of material deposit is performed via a laser scan (Hokuyo UST 10 LX) (Figure 3.15). The latter permits to maintain the depth and width of the cement layers by decreasing or increasing the printing rate. Indeed, this control is very important during the printing phase. First, the geometry of the shape to be printed depends strongly on the depth and width of the material layers. If these are not respected, it will entail a deformation of the form. In a second step, the superposition of the material must be maintained according to the fluidity of the materials. In this case, the velocity of the nozzle needs to be controlled according to the fluidity of the materials.

Calibration of the printing basis solution The use of a camera (Figure 3.15) enable us to calibrate the robot before the printing phase. On the site or in the factory, the ground is rarely straight flat. Thus, the camera allows a compensation of calibration errors.

CF1: Printing area

Workspace solution Boarding a manipulator arm which can reach the height of 1m on an omnidrive platform offers a large workspace.

CF3: Dimension and weight adapted for moving the robot in a $10m^3$ lorry and a $1,2m$ door gate

The dimensions of the machine have been chosen in such a way that they allow an entrance of 1.20m. The machine measures 1000x800x1500 mm and weights of 250 kilos.

CF4: Quality inspection of the structure

Soft arm solution The quality inspection step allows the robot to find out any cracks, to review the quality of the surface and to check the adhesion between the layers of material after the printing. In order to do this, a pneumatic soft arm equipped with a 3D camera and a 3D scanner is mounted on the end of the rigid manipulator to ensure a reliable quality inspection and to reach narrow spots.

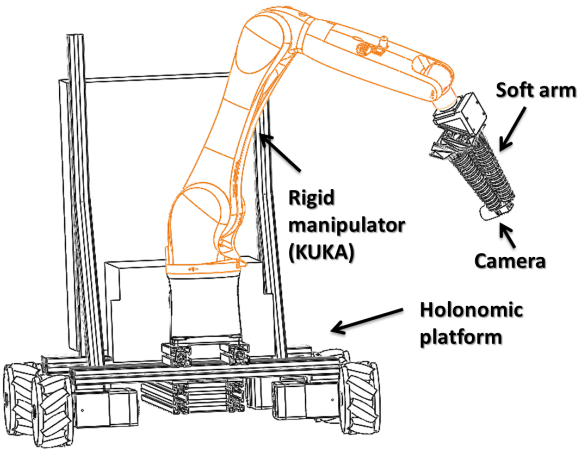

Figure 3.16 – The quality inspection robot

3.6 Conclusion

In this chapter, we have described the choices made when designing the robot machine dedicated to the additive manufacturing. In fact, it is a 400 kg weight omnidrive mobile-manipulator robot, kinematically redundant, used for the automation of the additive deposit of cement and clay for the construction of complex shapes. The automation of the process is adapted to different drying time. Moreover, the maneuverability of the robot allows printing large-scale 3D objects and access to some narrow places. Furthermore, it is capable of navigating in an autonomous configuration and of continuous printing on long distances. Consequently, the reachable height of the printed objects is limited to 1 meter according to the manipulation requirements. The mobile-manipulator is controlled kinematically according to the position of the tip of the nozzle. Finally, a soft-continuum manipulator has been placed as a gripper to the mobile-manipulator for the purpose of quality inspection after printing process completion.

Chapter 4

Additive Manufacturing Robot-Machine in Construction

Contents

4.1 Introduction

This chapter describes the modeling and kinematic control of a redundant omni-drive mobile-rigid manipulator system, used for printing 3D objects using additive manufacturing technique in the construction

Generally, coordination of manipulation and locomotion for a redundant mobile manipulator is a complex problem and has attracted the attention of many researchers. The proposed control schemes can be classified into two categories. The first one is based on a decentralized control scheme, where the manipulator and the platform are considered as two independent entities. The second category integrates the entire mobile and manipulator as a one system.

Among referred works from the literature, Yamamoto et al. (Yamamoto and Yun, 1992) considered the mobile manipulator as two independent subsystems. The manipulator is static during the mobile platform motion, and the platform is stopped during manipulator motion. They proposed a planning and control algorithms for the mobile platform so that the manipulator is always positioned at the preferred configurations. Haddad et

al. (Haddad et al., 2009) decomposed the system motion into simple and interdependent movements for each subsystem. This makes it possible to solve the redundancy by decomposing the system into many linear systems.(Dos Santos et al., 2006) used a visual presentation of the system to minimize the movement of an underwater manipulator whenever possible in order to solve the inverse kinematic of redundant systems.(Antonelli and Chiaverini, 2003) have put forward an approach based on a priority task strategy to solve the redundancy of a manipulator mobile robot. The latter is combined with a fuzzy logic technique to solve the coordination of the manipulator. (Scheurer et al., 2016) have realized a closed-loop priority task strategy of the inverse kinematics of a mobile manipulator robot using a least squares operator damped on Jacobian matrices. In this thesis, we focus on the second category for redundancy resolution and kinematic controller design.

This chapter is organized as follows: The following section presents the kinematic modeling of the experimental robot-machine for additive manufacturing. Section 4.3 presents the kinematic control architecture. Simulation and experimental results are given in section 4.4.

4.2 Kinematic modeling of the redundant omnidrive mobile manipulator

Kinematic models allow expressing the relationship between the joint variables of the robot and the pose of the end-effector (printing nozzle), defined in the task space and vice-versa. This section develops the kinematic models of the MATRICE platform. Denavit and Hartenberg method (Denavit, 1955) and the Paul's method (Paul, 1981b) are used to perform forward and inverse kinematic modeling, respectively.

4.2.1 FKM of the redundant omnidrive mobile manipulator

The FKM represents the set of relations expressing the pose of the tip of the nozzle in terms of the joint variables. This subsection deals with the methodology used for establishing the FKM in case of the MATRICE's robot. For an easy understanding, the omidrive mobile base is represented by a series of interconnected joint-links, as shown in Figure 4.1. Lateral and longitudinally motions of the mobile platform are represented by two prismatic joints, while the yaw rotation is represented by a revolute joint.

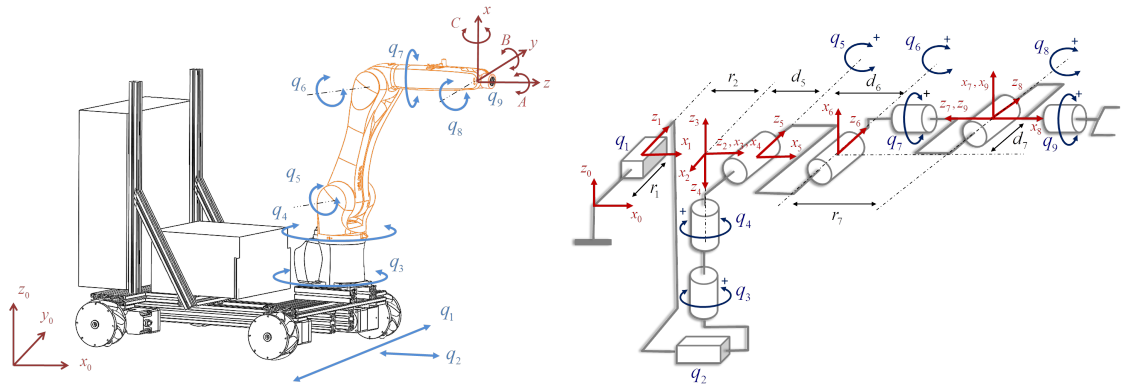

(a) Redundant omnidrive mobile - rigid manipulator

(b) Frame assignment

Figure 4.1 – Description of joint-link parameters for the mobile manipulator

Table 4.1 – D-H parameters

Link	σ_i	μ_i	α_i	r_i	θ_i	d_i	q_i
1	1	1	$-90°$	r_1	$-90°$	0	r_1
2	1	1	$-90°$	r_2	$90°$	0	r_2
3	0	0	$90°$	0	$-\theta_3+90°$	0	θ_3
4	0	0	$180°$	0	θ_4	0	θ_4
5	0	0	$90°$	0	θ_5	d_5	θ_5
6	0	0	$0°$	0	$\theta_6-90°$	d_6	θ_6
7	0	0	$-90°$	r_7	$-\theta_7$	d_7	θ_7
8	0	0	$-90°$	0	$-\theta_8$	0	θ_8
9	0	0	$-90°$	0	θ_9	0	θ_9

The forward kinematic model of an open chain is often calculated with a sequence of homogeneous transformations starting from the robot base up to its end-effector. These homogeneous transformations are determined by rotational homogeneous matrices (Rx, Ry, Rz) and translation vector (Tx, Ty, Tz). Various methods are used to define in a generic way the kinematic models of serial robots. For simple open kinematic chains, the most often used method is that of D-H (Hartenberg and Denavit, 1955). The D-H parameters permit along with the minimum number of parameters, to obtain the elementary homogeneous transformation matrices relating frames $\Re_i$, $i = 0,...,9$. To establish the FKM of the studied mobile manipulator robot, we considered a modified version of the D-H. Within the modeling process, the mobile base of the robot is represented by a virtual carrier forming the three degrees of freedom (longitudinal, lateral and yaw). This consists in using virtual links describing a simple chain linking the base of the rigid manipulator KUKA to the reference frame $\Re_0$ as shown in Figure 4.1b. Thus, the mobile base is modeled by two prismatic and one rotation joints representing the three possible motions. The frame $\Re_i$ fixed on the joint i is defined as follows:

- z_i axis is aligned with the joint axis i
- x_i axis is aligned with the common normal between z_i and z_{i+1}.

The set of parameters of the modified D-H Convention are listed below:

The matrix ${}^{i-1}T_i$, where i is the number of serial joints, represents the so-called D-H matrix. This matrix is expressed according to the parameters mentioned in the table above:

$$ {}^{i-1}T_i = \begin{bmatrix} \cos(\theta_i) & -\sin(\theta_i) & 0 & d_i \\ \cos(\alpha_i)\sin(\theta_i) & \cos(\alpha_i)\cos(\theta_i) & -\sin(\alpha_i) & -r_i\sin(\alpha_i) \\ \sin(\alpha_i)\sin(\theta_i) & \sin(\alpha_i)\cos(\theta_i) & \cos(\alpha_i) & r_i\cos(\alpha_i) \\ 0 & 0 & 0 & 1 \end{bmatrix} \tag{4.1} $$

Thus, the homogeneous matrix ${}^0T_9$ is expressed as follows:

$$ {}^0T_9 = {}^0T_1\,{}^1T_2\,{}^2T_3\,{}^3T_4\,{}^4T_5\,{}^5T_6\,{}^6T_7\,{}^7T_8\,{}^8T_9 = u \tag{4.2} $$

Where u corresponds to the desired posture :

$$u = \begin{pmatrix} n_x & o_x & a_x & \mathrm{P}_x \\ n_y & o_y & a_y & \mathrm{P}_y \\ n_z & o_z & a_z & \mathrm{P}_z \\ 0 & 0 & 0 & 1 \end{pmatrix} \tag{4.3}$$

The transformation matrices for successive frames of the robot are presented as follows :

$$^{0}\mathrm{T}_1 = \begin{bmatrix} 0 & 1 & 0 & 0 \\ 0 & 0 & 1 & q_1 \\ 1 & 0 & 0 & 0 \\ 0 & 0 & 0 & 1 \end{bmatrix} \tag{4.4}$$

$$^{1}\mathrm{T}_2 = \begin{bmatrix} 0 & -1 & 0 & 0 \\ 0 & 0 & 1 & q_2 \\ -1 & 0 & 0 & 0 \\ 0 & 0 & 0 & 1 \end{bmatrix} \tag{4.5}$$

$$^{2}\mathrm{T}_3 = \begin{bmatrix} \sin(q_3) & -\cos(q_3) & 0 & 0 \\ 0 & 0 & -1 & 0 \\ \cos(q_3) & \sin(q_3) & 0 & 0 \\ 0 & 0 & 0 & 1 \end{bmatrix} \tag{4.6}$$

$$^{3}\mathrm{T}_4 = \begin{bmatrix} \cos(q_4) & -\sin(q_4) & 0 & 0 \\ -\sin(q_4) & -\cos(q_4) & 0 & 0 \\ 0 & 0 & -1 & 0 \\ 0 & 0 & 0 & 1 \end{bmatrix} \tag{4.7}$$

$$^{4}\mathrm{T}_5 = \begin{bmatrix} \cos(q_5) & -\sin(q_5) & 0 & d_5 \\ 0 & 0 & -1 & 0 \\ \sin(q_5) & \cos(q_5) & 0 & 0 \\ 0 & 0 & 0 & 1 \end{bmatrix} \tag{4.8}$$

$$^{5}\mathrm{T}_6 = \begin{bmatrix} \sin(q_6) & \cos(q_6) & 0 & d_6 \\ -\cos(q_6) & \sin(q_6) & 0 & 0 \\ 0 & 0 & 1 & 0 \\ 0 & 0 & 0 & 1 \end{bmatrix} \tag{4.9}$$

$$^{6}\mathrm{T}_7 = \begin{bmatrix} \cos(q_7) & \sin(q_7) & 0 & d_7 \\ 0 & 0 & 1 & r_7 \\ \sin(q_7) & -\cos(q_7) & 0 & 0 \\ 0 & 0 & 0 & 1 \end{bmatrix} \tag{4.10}$$

$$^{7}\mathrm{T}_8 = \begin{bmatrix} \cos(q_8) & \sin(q_8) & 0 & 0 \\ 0 & 0 & 1 & 0 \\ \sin(q_8) & -\cos(q_8) & 0 & 0 \\ 0 & 0 & 0 & 1 \end{bmatrix} \tag{4.11}$$

$$^{8}\mathrm{T}_9 = \begin{bmatrix} \cos(q_9) & -\sin(q_9) & 0 & 0 \\ 0 & 0 & 1 & 0 \\ -\sin(q_9) & -\cos(q_9) & 0 & 0 \\ 0 & 0 & 0 & 1 \end{bmatrix} \tag{4.12}$$

Now, we tackle the method that permits the representation of the posture of the nozzle by considering the orientation angles which can be described using (Khalil and Dombre, 2004):

- Roll-Pitch-Yaw angles,
- Euler angles,
- Bryant angles,
- Quaternions.

The rotation theorem of Euler states that any displacement of a rigid body, except in the case of pure translation, can be represented by a rotation around an axis called the rotation axis. In that case, the orientation is determined by specifying the three angles corresponding to the three successive rotations (z-x-z). Bryant angles are a convention of (z-y-x) of Euler angles. In fact, the convention used in the kinematic programming language of KUKA robots is based on Bryant convention. The coordinate system z-y-x corresponding to Bryant convention are: C angle around x axis ; B angle around y axis and A angle around z axis. The composition of these three rotations allows the calculation of the orientation matrix R_{bry}.

$$\mathrm{R}_{bry} = \mathrm{R}(z,\mathrm{A}).\mathrm{R}(y,\mathrm{B}).\mathrm{R}(x,\mathrm{C}) \Leftrightarrow$$
$$\mathrm{R}_{bry} = \begin{bmatrix} \cos\mathrm{A}\cos\mathrm{B} & \cos\mathrm{A}\sin\mathrm{B}\sin\mathrm{C} - \sin\mathrm{A}\cos\mathrm{C} & \cos\mathrm{A}\sin\mathrm{B}\cos\mathrm{C} + \sin\mathrm{A}\sin\mathrm{C} \\ \sin\mathrm{A}\cos\mathrm{B} & \sin\mathrm{A}\sin\mathrm{B}\sin\mathrm{C} + \cos\mathrm{A}\cos\mathrm{C} & \sin\mathrm{A}\sin\mathrm{B}\cos\mathrm{C} - \cos\mathrm{A}\sin\mathrm{C} \\ -\sin\mathrm{B} & \cos\mathrm{B}\sin\mathrm{C} & \cos\mathrm{B}\cos\mathrm{C} \end{bmatrix} \tag{4.13}$$

Thus, the extraction of Bryant's angles is obtained by the following relationships:

$$\begin{aligned} \mathrm{A} &= \mathrm{atan2}\,(n_z, a_z) \\ \mathrm{B} &= \mathrm{atan2}\,(-s_z, a_z\cos(\mathrm{A}) + n_z\sin(\mathrm{A})) \\ \mathrm{C} &= \mathrm{atan2}\left(-n_x\cos(\mathrm{A}) + a_x\sin(\mathrm{A}), n_y\cos(\mathrm{A}) + a_y\sin(\mathrm{A})\right) \end{aligned} \tag{4.14}$$

where atan2 is a function that calculates the arc-tangent and returns a value based on the quadrant in which the point is located. The advantages of this function are that it returns an angle bounded between $-\pi$ and π.

Finally, the FKM of the robot is given by 6 equations from the matrix ${}^0\mathrm{T}_9$, allowing to express the positions (X,Y,Z) and orientations (A,B,C) of the tip of the nozzle.

Note that S_i and C_i refer to sine and cosine of q_i, respectively And S_{ij} and C_{ij} refer to sine and cosine of $q_i + q_j$.

$$\begin{cases} \mathrm{X} = & q_1 + \mathrm{C}_{34}\mathrm{S}_{56}d_7 + \mathrm{C}_{34}\mathrm{C}_{56}r_7 + \mathrm{C}_{34}(\mathrm{C}_5 d_6 + d_5) \\ \mathrm{Y} = & q_2 - \mathrm{S}_{34}\mathrm{S}_{56}d_7 - \mathrm{S}_{34}\mathrm{S}_{56}r_7 - \mathrm{S}_{34}(\mathrm{C}_5 d_6 + d_5) \\ \mathrm{Z} = & \mathrm{C}_{56}d_7 - \mathrm{S}_{56}r_7 - \mathrm{S}_5 d_6 \\ \mathrm{A} = & -\mathrm{atan2}(-\mathrm{S}_9(\mathrm{C}_{56}\mathrm{C}_7\mathrm{C}_8 - \mathrm{S}_{56}\mathrm{S}_8) - \mathrm{C}_{56}\mathrm{S}_7\mathrm{C}_9, \mathrm{C}_{56}\mathrm{C}_7\mathrm{S}_8 + \mathrm{S}_{56}\mathrm{C}_8) \\ \mathrm{B} = & \mathrm{atan2}(\mathrm{C}_9(\mathrm{C}_{56}\mathrm{C}_7\mathrm{C}_8 - \mathrm{S}_{56}\mathrm{S}_8) - \mathrm{C}_{56}\mathrm{S}_7\mathrm{S}_9, -\mathrm{C}_\mathrm{A}(\mathrm{C}_{56}\mathrm{C}_7\mathrm{S}_8 + \mathrm{S}_{56}\mathrm{C}_8) - \\ & \mathrm{S}_\mathrm{A}(\mathrm{C}_{56}\mathrm{C}_7\mathrm{C}_8 + \mathrm{S}_{56}\mathrm{S}_8\mathrm{S}_9 + \mathrm{C}_{56}\mathrm{S}_7\mathrm{C}_9)) \\ \mathrm{C} = & \mathrm{atan2}(-\mathrm{C}_\mathrm{A}(-\mathrm{S}_9(\mathrm{C}_8(\mathrm{C}_{34}\mathrm{S}_{56}\mathrm{C}_7 + \mathrm{S}_{34}\mathrm{S}_7) + \mathrm{C}_{34}\mathrm{C}_{56}\mathrm{S}_8) - \mathrm{C}_9(\mathrm{C}_{34}\mathrm{S}_{56}\mathrm{S}_7 - \mathrm{S}_{34}\mathrm{C}_7))) \\ & -\mathrm{S}_\mathrm{A}(\mathrm{S}_8(\mathrm{C}_{34}\mathrm{C}_{56}\mathrm{C}_7 + \mathrm{S}_{34}\mathrm{S}_7) - \mathrm{C}_{34}\mathrm{C}_{56}\mathrm{C}_8), \mathrm{C}_\mathrm{A}(-\mathrm{S}_9(\mathrm{C}_8(-\mathrm{S}_{34}\mathrm{S}_{56}\mathrm{C}_7 + \mathrm{C}_{34}\mathrm{S}_7) - \mathrm{S}_{34}\mathrm{C}_{56}\mathrm{S}_8) \\ & -\mathrm{C}_9(-\mathrm{S}_{34}\mathrm{S}_{56}\mathrm{S}_7 - \mathrm{C}_{34}\mathrm{C}_7)) + \mathrm{S}_\mathrm{A}(\mathrm{S}_8(-\mathrm{S}_{34}\mathrm{S}_{56}\mathrm{C}_7 + \mathrm{C}_{34}\mathrm{S}_7) + \mathrm{S}_{34}\mathrm{C}_{56}\mathrm{C}_8))) \end{cases} \tag{4.15}$$

4.2.2 IKM of the redundant omnidrive mobile manipulator

The IKM allows calculating the joint variables $[q_1 ... q_9]$ from the pose (position and orientation) of the printing nozzle.

The main issue is the fact that FKM is non-linear and the robot is redundant with respect to the printing task so, it is difficult to invert the model directly. Since the solution of the inverse kinematic model is not unique, we have to optimize the choice of the robot joints configurations for each posture defined in the operational space.

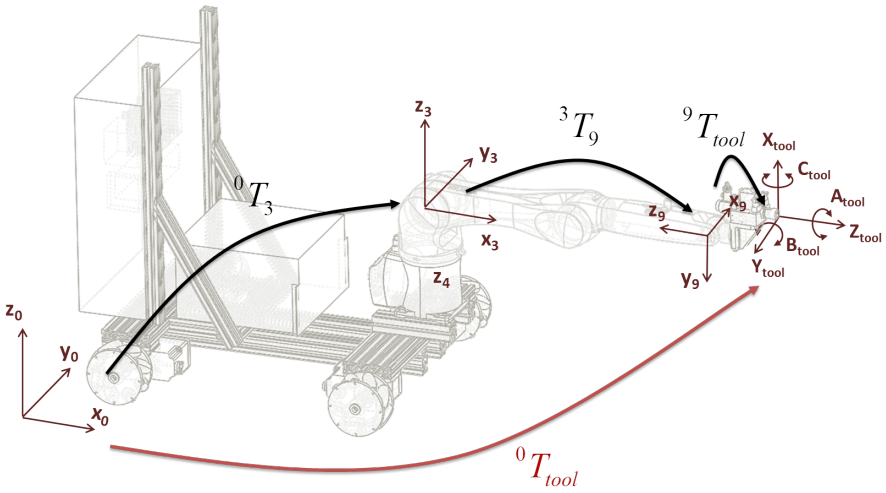

Figure 4.2 – location of end-effector frame relative to base frame

As shown in the Figure 4.2, the transformation matrix from frame $\Re_{tool}$ to frame $\Re_0$, represents the overall transformations for the mobile manipulator. It is expressed as follows:

$$^0\mathrm{T}_{tool} = {}^0\mathrm{T}_3(q_1, q_2, q_3).{}^3\mathrm{T}_9(q_4, q_5, q_6, q_7, q_8, q_9).{}^9\mathrm{T}_{tool} \tag{4.16}$$

For the case of IKM, $^0\mathrm{T}_{tool}$ and $^9\mathrm{T}_{tool}$ and their inverse are supposed known matrices, where $^0\mathrm{T}_{tool}$ describes the kinematic coordinates of 3D object to be printed in the frame $\Re_0$, and $^9\mathrm{T}_{tool}$ describes the coordinates of the TCP or the tip of the nozzle. Then, the unknown matrix $^0\mathrm{T}_9$ can be computed as follows:

$$^0\mathrm{T}_9 = {}^0\mathrm{T}_{tool}\left({}^9\mathrm{T}_{tool}\right)^{-1} = \begin{pmatrix} s_x & n_x & a_x & \mathrm{P}_x \\ s_y & n_y & a_y & \mathrm{P}_y \\ s_z & n_z & a_z & \mathrm{P}_z \\ 0 & 0 & 0 & 1 \end{pmatrix} \tag{4.17}$$

From equations (4.16) and (4.17), we can express differently the the matrix $^0\mathrm{T}_9$:

$$\underbrace{{}^0\mathrm{T}_3(q_1, q_2, q_3)}_{\text{Mobile platform}}.\underbrace{{}^3\mathrm{T}_9(q_4, q_5, q_6, q_7, q_8, q_9)}_{\text{Rigid manipulator}} = \begin{pmatrix} s_x & n_x & a_x & \mathrm{P}_x \\ s_y & n_y & a_y & \mathrm{P}_y \\ s_z & n_z & a_z & \mathrm{P}_z \\ 0 & 0 & 0 & 1 \end{pmatrix} \tag{4.18}$$

Thus, to solve equation (4.18), we proceed in two steps; first, we calculate the joint variables for the omnidrive mobile platform in presence of redundant equations, in order to obtain the optimal configuration. Then, the obtained variables are used to calculate the joint variables of the rigid manipulator by using Paul's method.

Calculation of joint variables for the omnidrive mobile platform

For the calculation of the joint variables (q_1, q_2, q_3) corresponding to the omnidrive platform, we start from equation (4.18) allowing to express the following equations:

$$\begin{cases}
((C_4S_{56}C_7 + S_4S_7)C_8 + C_4C_{56}S_8)C_9 - (C_4S_{56}S_7 - S_4C_7)S_9 = S_3n_y + C_3n_x \\
((-S_4S_{56}C_7 + C_4S_7)C_8 - S_4C_{56}S_8)C_9 - (-S_4S_{56}S_7 - C_4C_7)S_9 = -C_3n_x + C_3n_y \\
(C_{56}C_7C_8 - S_{56}S_8)C_9 - C_{56}S_7S_9 = n_z \\
-((C_4S_{56}C_7 + S_4S_7)C_8 + C_4C_{56}S_8)S_9 - (C_4S_{56}S_7 - S_4C_7)C_9 = S_3o_y + C_3o_x \\
-((-S_4S_{56}C_7 + C_4S_7)C_8 - S_4C_{56}S_8)S_9 - (-S_4S_{56}S_7 - C_4C_7)C_9 = -S_3o_x + C_3o_y \\
-(C_{56}C_7C_8 - S_{56}S_8)S_9 - C_{56}S_7C_9 = o_z \\
(C_4S_{56}C_7 + S_4S_7)S_8 - C_4C_{56}C_8 = S_3a_y + C_3a_x \\
(-S_4S_{56}C_7 + C_4S_7)S_8 + S_4C_{56}C_8 = -S_3a_x + C_3a_y \\
C_{56}C_7S_8 + S_{56}C_8 = a_z \\
C_4S_{56}d_7 + C_4C_{56}r_7 + C_4(C_5d_6 + d_5) = -S_3q_1 - C_3q_2 + C_3P_x + S_3P_y \\
-S_4S_{56}d_7 - S_4C_{56}r_7 - S_4(C_5d_6 + d_5) = -C_3q_1 + S_3q_2 - S_3P_x + C_3P_y \\
C_{56}d_7 - S_{56}r_7 - S_5d_6 = P_z
\end{cases} \tag{4.19}$$

From equation (4.19), we isolate the two non-linear and redundant equations containing q_1 and q_2:

$$\begin{cases}
C_4S_{56}d_7 + C_4C_{56}r_7 + C_4(C_5d_6 + d_5) &= -S_3q_1 - C_3q_2 + C_3P_x + S_3P_y \\
-S_4S_{56}d_7 - S_4C_{56}r_7 - S_4(C_5d_6 + d_5) &= -C_3q_1 + S_3q_2 - S_3P_x + C_3P_y
\end{cases} \tag{4.20}$$

The left side of the equations (4.20) describes the relationship between joint variable of the rigid-manipulator, while the right side describes the relationship between joint variables of the mobile platform. We notice that there are an infinite number of solutions for q_1 and q_2 (only 2 equations for 6 unknown variables). The objective is to propose an optimization process to select best solutions for q_1 and q_2.

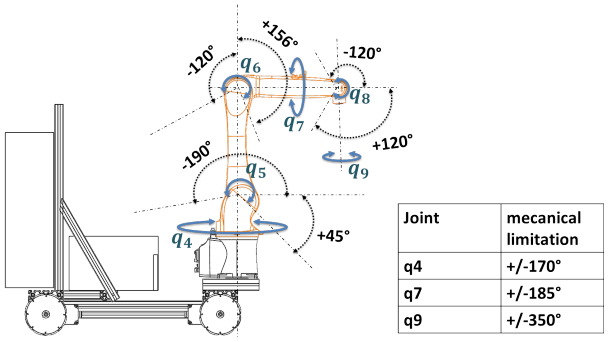

Joint	mecanical limitation
q4	+/-170°
q7	+/-185°
q9	+/-350°

Figure 4.3 – Initial configuration and joint boundaries

In fact, in our case, the manipulator can have multiple configurations to reach a point from the workspace. Some of those configurations can not be reachable due to physical constraints inherent to the mobile-manipulator or its surrounding environment. Example, printing from the back side of the robot is not possible due to the presence of the pumping system for the material, the reason why q_4, q_5 and q_6 should be limited. In addition, the additive deposit of the material does not require the rotation of the nozzle, so $q_9 = 0$, Thus, these constraints can be summarized as follows:

$$\begin{cases} -30^\circ \leq q_4 \leq 30^\circ \\ -90^\circ \leq q_5 \leq 0^\circ \\ 0^\circ < q_6 \leq 90^\circ \\ -2.5^\circ \leq q_7 \leq 2.5^\circ \\ 0^\circ < q_8 \leq 90^\circ \\ q_9 = 0^\circ \end{cases} \tag{4.21}$$

Therefore, the limitation of the joint variables implies a delimitation of the reachable points by the rigid manipulator. Thus, from the FKM, it is possible to calculate the reachable workspace (sub-workspace) for the printing task from the overall workspace of the manipulator, according to the defined joint boundaries. This sub-workspace has been chosen in such a way to reach the maximum printing height starting from the ground as shown in Figures 4.4a. This manipulator's sub-workspace can move according to the motion of the mobile platform in case of printing large size 3D objects .

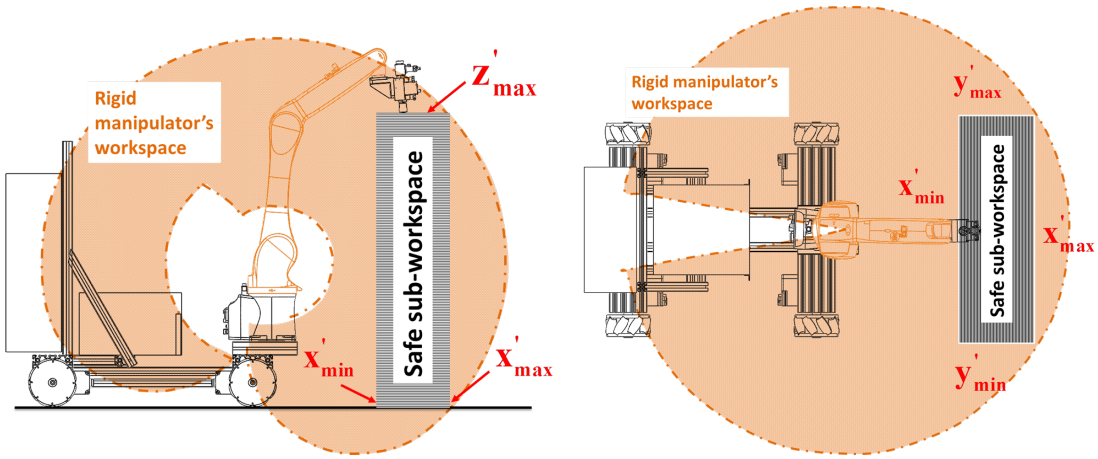

(a) Front view (b) Top view

Figure 4.4 – Safe sub-workspace of the rigid manipulator

As shown in Figure 4.4, the limits of the manipulator's sub-workspace are expressed in the frame $\Re_3$ by the bounds ($x'_{\min}$, $x'_{\max}$, $y'_{\min}$, $y'_{\max}$, $z'_{\min}$ and $z'_{\max}$). By replacing the inequalities (4.21) in the left side of equations (4.20), then the following inequations are obtained:

$$\begin{aligned} x'_{\max} &\geq \mathrm{P}_y\mathrm{S}_3 - q_1\mathrm{S}_3 + \mathrm{P}_x\mathrm{C}_3 - q_2\mathrm{C}_3 \geq x'_{\min} \\ y'_{\max} &\geq -\mathrm{P}_x\mathrm{S}_3 + \mathrm{P}_y\mathrm{C}_3 - q_1\mathrm{C}_3 + q_2\mathrm{S}_3 \geq y'_{\min} \end{aligned} \tag{4.22}$$

In order to solve the non-linear programming problem, to get the joint variable of the mobile platform, we use an optimization technique based on quadratic programming (Frank and Wolfe, 1956). Thus, the relations (4.22) can be rewritten as follows:

$$\begin{aligned} \mathrm{A}\mathbf{x} &\leq b \\ l_b \leq \mathbf{x} &\leq u_b \end{aligned} \tag{4.23}$$

where

- $\mathbf{x} = [q_1, q_2]$

- $A = \begin{bmatrix} -\begin{bmatrix} C_3 & S_3 \\ -S_3 & C_3 \end{bmatrix} & \begin{bmatrix} C_3 & S_3 \\ -S_3 & C_3 \end{bmatrix} \end{bmatrix}^T$
- $b = \begin{bmatrix} -\begin{bmatrix} y'_{min} \\ x'_{min} \end{bmatrix} - \begin{bmatrix} C_3 & S_3 \\ -S_3 & C_3 \end{bmatrix} \begin{bmatrix} P_y \\ P_x \end{bmatrix} \\ \begin{bmatrix} y'_{max} \\ x'_{max} \end{bmatrix} + \begin{bmatrix} C_3 & S_3 \\ -S_3 & C_3 \end{bmatrix} \begin{bmatrix} P_y \\ P_x \end{bmatrix} \end{bmatrix}$

$\mathbf{x}$ corresponds to the linear displacements (longitudinal and lateral) of the mobile platform. The elements of the matrix A and the column vector b are identified from inequalities (4.22). Besides, we assume that there is an achievable solution and that the linear displacements of the mobile platform is included inside $[l_b, u_b]$, where l_b and u_b describe bounds for the planar motion of the omnidrive mobile-manipulator.

Since the robot is redundant, there is an infinity of solution for IKM. Consequently, secondary performance criteria can be optimized, such as (Khalil and Dombre, 2004):

- minimizing the norm of the joint velocities
- avoiding obstacles
- avoiding singular configurations
- avoiding joint limits
- minimizing driving joint torques

In our study, we chose the following optimization criterion :

$$\min \left((P_x - q_2)^2 + (P_y - q_1)^2 \right) \tag{4.24}$$

This criterion permits to select the nearest configuration of the mobile-platform, it can be rewritten as follows:

$$\min_{\mathbf{x}} \frac{1}{2} \mathbf{x}^T H \mathbf{x} + g^T \mathbf{x} \tag{4.25}$$

Where:

$$\begin{aligned} H &= \begin{bmatrix} 2 & 0 \\ 0 & 2 \end{bmatrix} \\ g &= \begin{bmatrix} -2P_x & -2P_y \end{bmatrix} \end{aligned} \tag{4.26}$$

The problem composed of the cost function (4.25) and the constraints (4.23) is a quadratic programming problem that can be solved using the interior-point-convex algorithm available with the Matlab function "**quadprog**".

It is worth-noting that in order to find the variables q_1 and q_2, we need to calculate first the orientation q_3 of the mobile platform (Yaw angle). The latter appears in the constraints formulation. q_3 is calculated such that the printing zone is facing the mobile platform as shown in Figure 4.5. It is obtained through the calculus of the components of the normal unit vector on selected points on the printing path (Figure 4.5).

Assume that the path S to be tracked is parametrized by its curvilinear abscissa s. We note by ds the elementary displacement from the current point $(P_x(s), P_y(s))$ to the a future point $(P_x(s+ds), P_y(s+ds))$. Then, the value of ds is obtained by the following equation:

$$ds = \sqrt{(P_x(s+ds) - P_x(s))^2 + (P_y(s+ds) - P_y(s))^2} \tag{4.27}$$

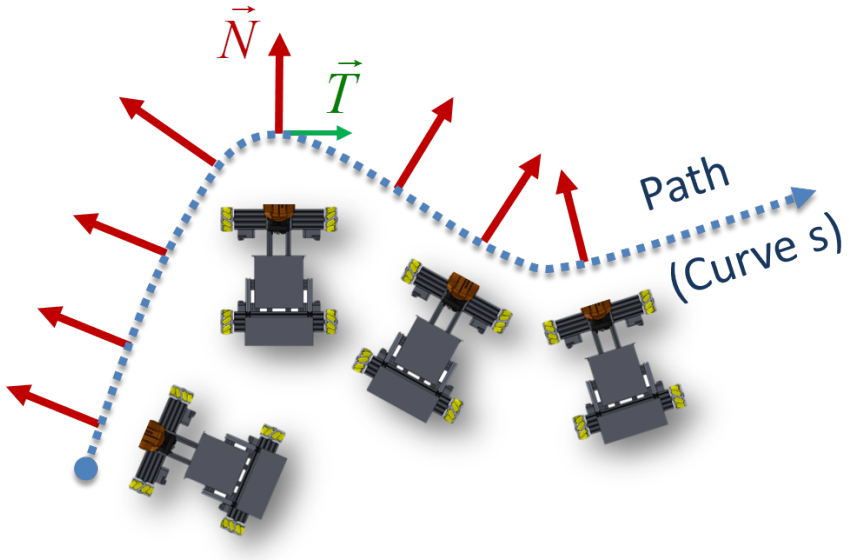

Figure 4.5 – Orientation of the mobile platform in respect of the printing path

We note $\vec{\mathrm{T}}(s)$ (3×1) the unit tangent vector at a point (of coordinate s) on the path S :

$$\vec{\mathrm{T}}(s) = \begin{bmatrix} \frac{\mathrm{P}_x(s+ds)-\mathrm{P}_x(s)}{ds} \\ \frac{\mathrm{P}_y(s+ds)-\mathrm{P}_y(s)}{ds} \\ 0 \end{bmatrix} \tag{4.28}$$

The binormal vector $\vec{\mathrm{B}}(s)$ (3×1) is given by :

$$\vec{\mathrm{B}} = [0,0,1]^{\mathrm{T}} \tag{4.29}$$

The normal vector $\vec{\mathrm{N}}(s)$ (3×1) is then obtained by :

$$\vec{\mathrm{N}}(s) = \vec{\mathrm{B}}(s) \times \vec{\mathrm{T}}(s) \tag{4.30}$$

The desired orientation q_3 of the mobile platform is obtained simply as follows :

$$q_3 = \mathrm{atan2}\left(\mathrm{N}_y, \mathrm{N}_x\right) \tag{4.31}$$

Calculation of joint variables for the rigid manipulator

Once the values of q_1 ,q_2 and q_3 have been obtained, the Paul's method (Paul, 1981a) can be used to calculate the manipulator's joint variables (q_4 ,q_5, q_6, q_7, q_8 and q_9) from the desired position and orientation of the end-effector (Nozzle). Indeed, most commercially robots can be solved using this method. But, it exists a number of methods for the calculation of the IKM. For example, the Pieper's method (Peiper, 1968) provides an analytical solution for the IKM of 6-DoF robots with three prismatic joints or three revolute joints whose axes intersect at a point. Or, the Raghavan-Roth's method (Raghavan and Roth, 1990) applied to robots having 6-DoF with a geometry using, at most, a sixteen degree polynomial, to calculate the IKM. The Paul's method allows to obtain an explicit solution for robots with relatively simple geometry that have many zero distances and parallel or perpendicular joint axes. This method consists in successively premultiplying the two members of the transformation matrix by the matrices ${}^{i}\mathrm{T}_{i-1}$ enabling to isolate

and identify one by one the unknown i^{th} joint variables. By successively premultiplying the equation (4.18) by the inverse of ${}^0\mathrm{T}_3$, we obtain the following equation:

$$\underbrace{{}^3\mathrm{T}_9(q_4,q_5,q_6,q_7,q_8,q_9)}_{\text{Rigid manipulator}} = \underbrace{\left({}^0\mathrm{T}_3(q_1,q_2,q_3)\right)^{-1}}_{\text{Mobile platform}} . \begin{pmatrix} s_x & n_x & a_x & \mathrm{P}_x \\ s_y & n_y & a_y & \mathrm{P}_y \\ s_z & n_z & a_z & \mathrm{P}_z \\ 0 & 0 & 0 & 1 \end{pmatrix} = \begin{pmatrix} s_x' & n_x' & a_x' & \mathrm{P}_x' \\ s_y' & n_y' & a_y' & \mathrm{P}_y' \\ s_z' & n_z' & a_z' & \mathrm{P}_z' \\ 0 & 0 & 0 & 1 \end{pmatrix} \tag{4.32}$$

We obtain the variable q_4 and q_5 by successively premultiplying the equation (4.32) by the matrix ${}^4\mathrm{T}_3$ to isolate and determine sequentially the joint variables:

$${}^4\mathrm{T}_3\left(q_4\right) u' = {}^4\mathrm{T}_5\left(q_5\right) {}^5\mathrm{T}_6\left(q_6\right) {}^6\mathrm{T}_7\left(q_7\right) {}^7\mathrm{T}_8\left(q_8\right) {}^8\mathrm{T}_9\left(q_9\right) \tag{4.33}$$

Then, we obtain the following system of equations:

$$\begin{cases} d_7\mathrm{S}_{56} + r_7\mathrm{C}_{56} + d_6\mathrm{C}_5 + d_5 &= -\mathrm{P}_y'\mathrm{S}_4 + \mathrm{P}_x'\mathrm{C}_4 \\ 0 &= -\mathrm{P}_x'\mathrm{S}_4 - \mathrm{P}_y'\mathrm{C}_4 \\ -d_7\mathrm{C}_{56} + r_7\mathrm{S}_{56} + d_6\mathrm{S}_5 &= -\mathrm{P}_z' \end{cases} \tag{4.34}$$

where $\mathrm{C}_{56} = \cos(q_5 + q_6)$ and $\mathrm{S}_{56} = \sin(q_5 + q_6)$.

The second equation of the system (4.34) allows to deduce the variable q_4. Then, we obtain:

$$q_4 = \mathrm{atan2}\left(\frac{\mathrm{P}_y'}{-\mathrm{P}_x'}\right) \tag{4.35}$$

The first and third equations of the system (4.34) can be written as follows:

$$\begin{aligned} \mathrm{W}.\mathrm{S}_5 - \mathrm{Z}_1 &= \mathrm{X}.\mathrm{S}_{56} - \mathrm{Y}.\mathrm{C}_{56} \\ \mathrm{W}.\mathrm{C}_5 - \mathrm{Z}_2 &= \mathrm{X}.\mathrm{C}_{56} + \mathrm{Y}.\mathrm{S}_{56} \end{aligned} \tag{4.36}$$

where :

$\mathrm{W} = d_6$, $\mathrm{X} = r_7$, $\mathrm{Y} = -d_7$, $\mathrm{Z}_1 = -\mathrm{P}_z'$ and $\mathrm{Z}_2 = -\mathrm{P}_y'\mathrm{S}_4 + \mathrm{P}_x'\mathrm{C}_4 - d_5$

By adding these last equations, beforehand put squared, we obtain the following equation:

$$\begin{aligned} (\mathrm{W}.\mathrm{S}_5 - \mathrm{Z}_1)^2 + (\mathrm{W}.\mathrm{C}_5 - \mathrm{Z}_2)^2 &= \mathrm{X}^2 + \mathrm{Y}^2 \Leftrightarrow \\ \mathrm{Z}_1.\mathrm{S}_5 + \mathrm{Z}_2.\mathrm{C}_5 &= \mathrm{Z}_3 \end{aligned} \tag{4.37}$$

where : $\mathrm{Z}_3 = \frac{\mathrm{X}^2+\mathrm{Y}^2-\mathrm{W}^2-{\mathrm{Z}_1}^2-{\mathrm{Z}_2}^2}{-2.\mathrm{W}}$

We can calculate q_5 by solving the equation (4.37) :

$$\begin{aligned} \mathrm{S}_5 &= \frac{\mathrm{Z}_3.\mathrm{Z}_1 + \varepsilon.\mathrm{Z}_2\sqrt{{\mathrm{Z}_1}^2+{\mathrm{Z}_2}^2-{\mathrm{Z}_3}^2}}{{\mathrm{Z}_1}^2+{\mathrm{Z}_2}^2} \\ \mathrm{C}_5 &= \frac{\mathrm{Z}_3.\mathrm{Z}_2 - \varepsilon.\mathrm{Z}_1\sqrt{{\mathrm{Z}_1}^2+{\mathrm{Z}_2}^2-{\mathrm{Z}_3}^2}}{{\mathrm{Z}_1}^2+{\mathrm{Z}_2}^2} \end{aligned} \tag{4.38}$$

where $\varepsilon = \pm 1$.

From these two relations, the following cases can be considered:

$$\begin{cases} q_5 = \mathrm{atan2}\left(-\frac{\mathrm{Z}_2}{\mathrm{Z}_1}\right) & ,\text{if } \mathrm{Z}_3 = 0 \\ q_5 = \mathrm{atan2}\left(\frac{\mathrm{S}_5}{\mathrm{C}_5}\right) & ,\text{if } \mathrm{Z}_3 \neq 0 \end{cases} \tag{4.39}$$

By successively premultiplying the equation (4.33) by the matrix ${}^{5}T_{4}$, we can determine the joint variable q_6 :

$$ {}^{5}T_{4}\left(q_5\right){}^{4}T_{3}\left(q_4\right)u' = {}^{5}T_{6}\left(q_6\right){}^{6}T_{7}\left(q_7\right){}^{7}T_{8}\left(q_8\right){}^{8}T_{9}\left(q_9\right) \tag{4.40} $$

then, the following equations are resulted:

$$ \begin{cases} d_7S_6 + r_7C_6 + d_6 &= P_x'C_5C_4 - P_y'S_4C_5 - P_z'S_5 - d_5C_5 \\ -d_7C_6 + r_7S_6 &= -P_x'S_5C_4 + P_y'S_5S_4 - P_z'C_5 + d_5S_5 \\ 0 &= P_x'S_4 + P_y'C_4 \end{cases} \tag{4.41} $$

The first two equations of the system (4.41) can be written as follows:

$$ \begin{aligned} X.C_6 - Y.S_6 &= B1 \\ X.S_6 + Y.C_6 &= B2 \end{aligned} \tag{4.42} $$

where:
$B_1 = -d_6 + P'_xC_4C_5 - P'_yS_4C_5 - P'_zC_5, B_2 = -P'_xC_4S_5 + P'_yS_4S_5 - P'_zC_5 + d_5S_5$, $X = r_7$ et $Y = -d_7$.
We can calculate q_6 by solving the equation (4.42):

$$ \begin{aligned} S_6 &= \frac{B_2X - B_1Y}{X^2+Y^2} \\ C_6 &= \frac{B_1X + B_2Y}{X^2+Y^2} \end{aligned} \tag{4.43} $$

So, q_6 is then expressed as follows:

$$ q_6 = \operatorname{atan2}\left(\frac{B_2X - B_1Y}{B_1X + B_2Y}\right) \tag{4.44} $$

We obtain the variable q_7 and q_9 by successively premultiplying the equation (4.40) by the matrix ${}^{6}T_{5}$ to isolate and determine sequentially the joint variables:

$$ {}^{6}T_{5}\left(q_6\right){}^{5}T_{4}\left(q_5\right){}^{4}T_{3}\left(q_4\right)u' = {}^{6}T_{7}\left(q_7\right){}^{7}T_{8}\left(q_8\right){}^{8}T_{9}\left(q_9\right) \tag{4.45} $$

The matrix ${}^{3}T_{6}$ is written

$$ {}^{6}T_{9} = \begin{bmatrix} C_4C_8C_9 - S_7S_9 & -C_7C_8S_9 - S_7C_9 & C_7S_8 & d_7 \\ S_8C_9 & -S_8S_9 & -C_8 & d_7 \\ S_7C_8C_9 + C_7S_9 & -S_7C_8S_9 + C_7C_9 & S_7S_8 & 0 \\ 0 & 0 & 0 & 1 \end{bmatrix} \tag{4.46} $$

the following system of equations are obtained:

$$ \begin{cases} S_8C_9 &= C_{56}(n_x'C_4 - n_y'S_4) - n_z'S_{56} \\ -S_8S_9 &= C_{56}(o_x'C_4 - o_y'S_4) - o_z'S_{56} \\ C_7S_8 &= a_x'C_4S_{56} - a_y'S_4S_{56} + a_z'C_{56} \\ S_7S_8 &= a_x'S_4 + a_y'C_4 \end{cases} \tag{4.47} $$

From these equations, we can obtain:

$$ q_7 = \operatorname{atan2}\left(\frac{a_x'S_4 + a_y'C_4}{a_x'C_4S_{56} - a_y'S_4S_{56} + a_z'C_{56}}\right) \tag{4.48} $$

The variable q_8 can be determined by using Arcsinus function. As this function is less precise than the Arctan, the premultiplying of the equation (4.45) by the matrix ${}^{7}T_{6}$ is

more suitable for calculating the variable q_8. On the other hand, the variable q_9 can be calculated in relation to q_7 thank to this premultiplying. Thus, we obtain:

$$ {}^{7}\mathrm{T}_{6} = \begin{bmatrix} \mathrm{C}_8\mathrm{C}_9 & -\mathrm{C}_8\mathrm{S}_9 & \mathrm{S}_8 & 0 \\ -\mathrm{S}_9 & -\mathrm{C}_9 & 0 & 0 \\ \mathrm{S}_8\mathrm{C}_9 & -\mathrm{S}_8\mathrm{S}_9 & -\mathrm{C}_8 & 0 \\ 0 & 0 & 0 & 1 \end{bmatrix} \tag{4.49} $$

then, the following equations are obtained:

$$ \begin{cases} \mathrm{S}_9 = {n_x}'(\mathrm{S}_4\mathrm{C}_7 - \mathrm{C}_4\mathrm{S}_{56}\mathrm{S}_7) + {n_y}'(\mathrm{S}_4\mathrm{S}_{56}\mathrm{S}_7 + \mathrm{C}_4\mathrm{C}_7) - {n_z}'\mathrm{C}_{56}\mathrm{S}_7 \\ \mathrm{C}_9 = {o_x}'(\mathrm{S}_4\mathrm{C}_7 - \mathrm{C}_4\mathrm{S}_{56}\mathrm{S}_7) + {o_y}'(\mathrm{S}_4\mathrm{S}_{56}\mathrm{S}_7 + \mathrm{C}_4\mathrm{C}_7) - {o_z}'\mathrm{C}_{56}\mathrm{S}_7 \\ \mathrm{S}_8 = {a_x}'(\mathrm{S}_4\mathrm{S}_7 + \mathrm{C}_4\mathrm{S}_{56}\mathrm{C}_7) + {a_y}'(\mathrm{C}_4\mathrm{S}_{56}\mathrm{C}_7 + \mathrm{S}_4\mathrm{S}_7) - {a_z}'\mathrm{C}_{56}\mathrm{C}_7 \\ \mathrm{C}_8 = -{a_x}'\mathrm{C}_4\mathrm{C}_{56} - {a_y}'\mathrm{S}_4\mathrm{C}_{56} + {a_z}'\mathrm{S}_{56} \end{cases} \tag{4.50} $$

where,

$$ q_8 = \mathrm{atan2}\left(\frac{{a_x}'(\mathrm{S}_4\mathrm{S}_7 + \mathrm{C}_4\mathrm{S}_{56}\mathrm{C}_7) + {a_y}'(\mathrm{C}_4\mathrm{S}_{56}\mathrm{C}_7 + \mathrm{S}_4\mathrm{S}_7) - {a_z}'\mathrm{C}_{56}\mathrm{C}_7}{-{a_x}'\mathrm{C}_4\mathrm{C}_{56} - {a_y}'\mathrm{S}_4\mathrm{C}_{56} + {a_z}'\mathrm{S}_{56}} \right) \tag{4.51} $$

and

$$ q_9 = \mathrm{atan2}\left(\frac{{n_x}'(\mathrm{S}_4\mathrm{C}_7 - \mathrm{C}_4\mathrm{S}_{56}\mathrm{S}_7) + {n_y}'(\mathrm{S}_4\mathrm{S}_{56}\mathrm{S}_7 + \mathrm{C}_4\mathrm{C}_7) - {n_z}'\mathrm{C}_{56}\mathrm{S}}{{o_x}'(\mathrm{S}_4\mathrm{C}_7 - \mathrm{C}_4\mathrm{S}_{56}\mathrm{S}_7) + {o_y}'(\mathrm{S}_4\mathrm{S}_{56}\mathrm{S}_7 + \mathrm{C}_4\mathrm{C}_7) - {o_z}'\mathrm{C}_{56}\mathrm{S}_7} \right) \tag{4.52} $$

A rigid manipulator robot with 6-DoF features three kinds of singularity: wrist, shoulder, and elbow singularity. Figure 4.6a presents a singular configuration of the robot, when the origin of the frame $\Re_8$ lies on the z_3 axis. This means that $\mathrm{P}'_x = 0$ and $\mathrm{P}'_y = 0$. Consequently, in the field of 3D printing, this configuration need to be avoided for safety reasons and in order to keep the material far from the robot. Figure 4.6b presents the wrist singularity of the robot when $q_8 = 0$, so infinity solutions for q_7 and q_9 can be found, where $q_9 = -q_7$. For a small amplitude of motion induce an important variation of q_7, which is impossible to do due to the velocity limits of the actuator. This singularity is not to be neglected in printing as the deposit velocity needs to be regular. Finally, Figure 4.6c shows the elbow singularity of the robot when $q_6 = 0$. This singularity does not affect the IKM computation but the kinematics of the robot because the velocities of some joints can increase rapidly.

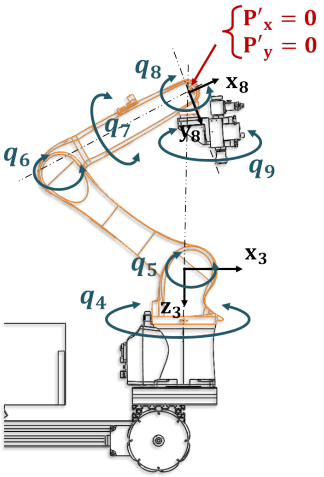

(a) Shoulder singularity ($P'_x = 0$) and ($P'_y = 0$)

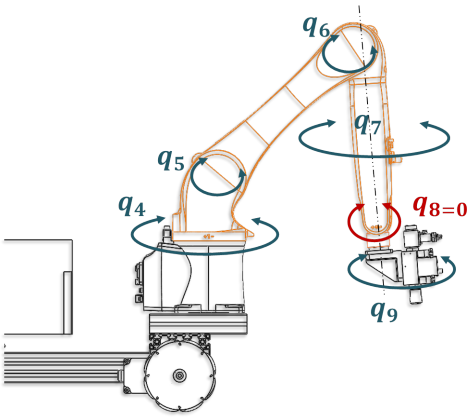

(b) Wrist singularity ($q_8 = 0$)

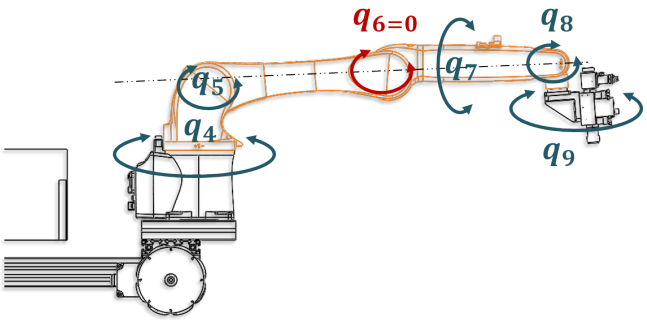

(c) Elbow singularity ($q_6 = 0$)

Figure 4.6 – Singular positions of rigid manipulator

But the constraints used in the calculation of the proposed IKM allow to avoid the singularity positions. Indeed, the safe sub-workspace of the rigid manipulator has been defined as follows:

$$\begin{cases} P'_X \neq 0 \text{ and } P'_X \neq 0; \\ q_8 \neq 0; \\ q_6 \neq 0. \end{cases} \tag{4.53}$$

The robot can print large scale 3D objects since it can cover a wide workspace with its mobile platform. However, to minimize the positioning error, the workspace may be limited. It may also be limited by the length of the material flow pipe. In the case of MATRICE project, 3D objects up to $2m^3$ have been printed using the mobile platform. But, during the printing, the velocity of the material deposit must be maintained in order to respect the architecture of the shape.

4.2.3 Differential kinematic modeling

In the previous section, the forward and inverse kinematic models of the omnidrive mobile-rigid manipulator were presented. They establish the relationships between the mobile manipulator's joint displacements and operational coordinates of its end-effector (nozzle). These allow to elaborate a position-based and orientation-based control of the

mobile-manipulator in identified printing workspace. However, it is also important to control the velocity of the nozzle allowing to reach the target point. This requires the coordination of the instantaneous velocity of the nozzle and the joints velocities. Thus, the Velocity kinematic model (VKM) allows to establish the relationship between the velocity of the mobile manipulator's joints and the instantaneous velocity of its nozzle.

Differential equations of the mobile platform

The robot mobile base is represented by a serial link-joint that makes up the 3 DoF, two prismatic and one rotary joint are represented respectively by q_1, q_2 and q_3. Thus, the platform operational speed $\dot{q}_1$, $\dot{q}_2$, and $\dot{q}_3$ is ensured by the wheel speed $\dot{\omega}_{1..4}$. This definition is similar to that of the kinematic model of the mobile platform. The latter is made up with 4 Swedish omnidirectional wheels (Figure 4.7).

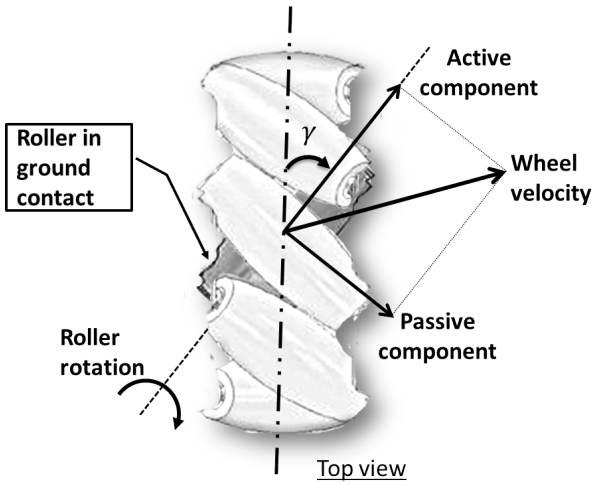

Figure 4.7 – Swedish omnidirectional wheels.

The advantage of this design is that it permits a movement with no friction and in several possible directions. It is necessary to remember here the rotation that the rolls are not actuated and that only the wheel shaft is actuated. The wheel speed can be divided into components in the active direction and in the passive one. The active component is directed along the axis of the roll that is in contact with the ground whereas the passive one is perpendicular to the roll axis. The γ is the angle between the roll axis in contact with the ground and the main wheel axis as shown in Figure 4.7.

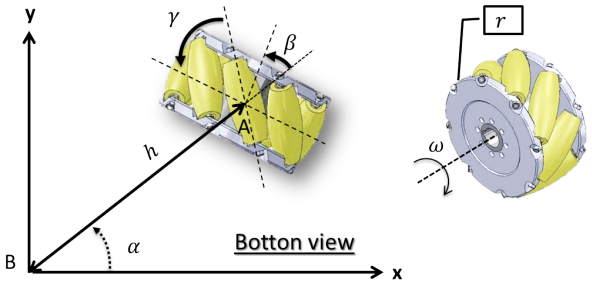

Figure 4.8 – Parameter of the holonomic wheel

Figure 4.8 represents the mobile basis parameters. Point A is a fixed point on the framework of the platform ad it refers to the wheel center.The coordinates of A in the fixed

mark of the body B can be given by the height h and the fixed angle α. The orientation of the wheel plane with respect to the body of the moving platform is indicated by the angle β which is constant in the case of a mechanical wheel.The four wheels are identical in radius r with ω as the rotation angle around the wheel shaft which varies with time. The mobile platform depicted in Figure 4.9 is omnidirectional and holonomic mobile robot because degree of mobility (DoM)=DoF=3. It can be seen as an over-actuated system, because four actuators used to obtain three DoF.

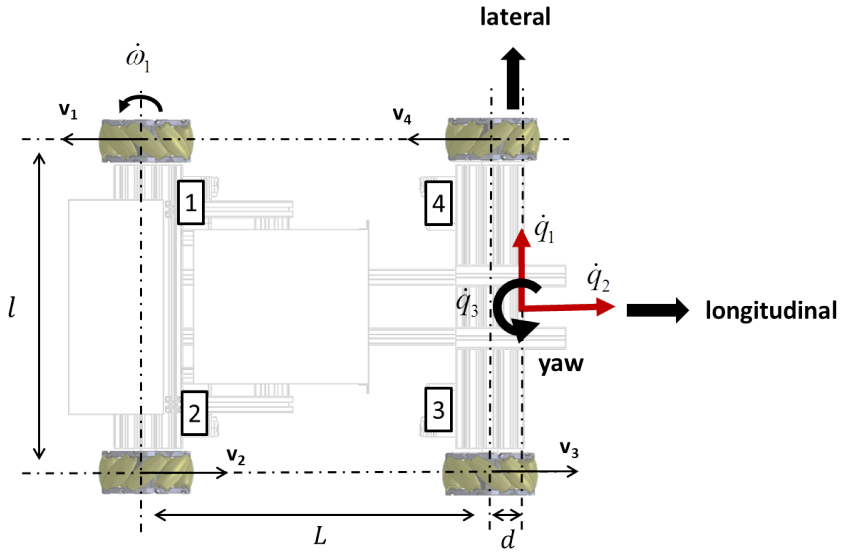

Figure 4.9 – Mobile platform parameters

Thus, the speed of the wheel centre v_i with $i = 1...,4$ being the number of wheel, can be expressed as a function of linear velocities $\dot{q}_2$ and $\dot{q}_1$ (longitudinal and lateral) and of angular velocity $\dot{q}_3$ (Yaw):

$$\begin{aligned} v_1 &= \cos(\alpha+\beta+\gamma)\dot{q}_1 + \sin(\alpha+\beta+\gamma)\dot{q}_2 + h\cos(\beta+\gamma)\dot{q}_3 \\ v_2 &= \cos(\alpha+\beta+\gamma)\dot{q}_1 - \sin(\alpha+\beta+\gamma)\dot{q}_2 + h\cos(\beta+\gamma)\dot{q}_3 \\ v_3 &= -\cos(\alpha+\beta+\gamma)\dot{q}_1 - \sin(\alpha+\beta+\gamma)\dot{q}_2 + h\cos(\beta+\gamma)\dot{q}_3 \\ v_4 &= -\cos(\alpha+\beta+\gamma)\dot{q}_1 + \sin(\alpha+\beta+\gamma)\dot{q}_2 + h\cos(\beta+\gamma)\dot{q}_3 \end{aligned} \tag{4.54}$$

Where v_i can be expressed as a function of the wheel rotation $\dot{\omega}_i$:

$$v_i = r\dot{\omega}_i \cos(\gamma) \tag{4.55}$$

The consraint α, h, and γ can be calculated according to the length L, width l, and the distance d, linking the centers of the wheels. In our case :

$$\begin{aligned} \alpha_1 &= -\alpha_2 = \arctan\left(\frac{L+d}{l/2}\right) + \frac{\pi}{2} \\ \alpha_4 &= -\alpha_3 = \arctan\left(\frac{L+d}{l/2}\right) + \frac{\pi}{2} \\ h1 &= h2 = \sqrt{(L+d)^2 + (l/2)^2} \\ h4 &= h3 = \sqrt{d^2 + (l/2)^2} \end{aligned} \tag{4.56}$$

Jacobian of the Mobile Manipulator

The operational speeds (linear and angular) of the effector are linked in a linear way to the joints speed. Indeed, as these changes take place in an infinitesimal time, we are actually looking for a correspondence between the instantaneous speeds of the effector (in the Cartesian space) to instantaneous speeds of the articulations (in joint space). This correspondence between the differential variations is linear and can be described by the Jacobian matrix (Orin and Schrader, 1984; Mittal and Nagrath, 2003):

$$\mathbf{V}(t) = \mathrm{J}(q)\dot{\mathbf{q}}(t) \tag{4.57}$$

where $\mathbf{V}(t) = 6 \times 1$: Cartesian velocity vector,
$\mathrm{J}(q) = 6 \times n$: Jacobian matrix,
$\dot{\mathbf{q}} = n \times 1$: vector of n joint velocities.

The equation 4.57 represents the kinematics model with the Jacobian, illustrated in Figure 4.10, depending on the joint variable.

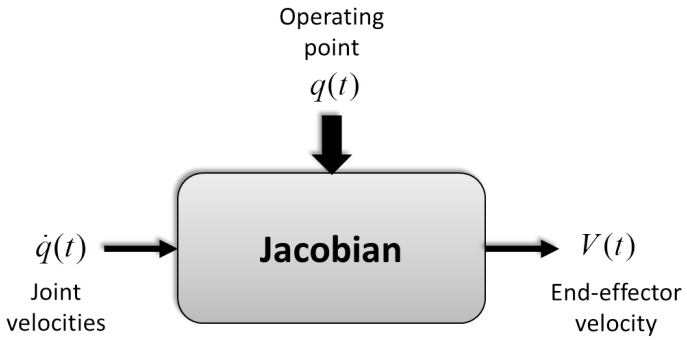

Figure 4.10 – Kinematics model

The first three columns of the Jacobian $\mathrm{J}(q)$ are associated to the linear speed of the end-effector whereas the last three columns correspond to the angular speed of the end-effector ω. Each manipulator articulation generates a linear speed or angular at the end of the effector. The column of the Jacobian matrix is thus composed of three components of linear speeds and three components of angular speeds and can be expressed as:

$$\mathrm{J}_i(q) = \begin{bmatrix} j_{\upsilon ki} \\ j_{\omega ki} \end{bmatrix} \tag{4.58}$$

Where $j_{\upsilon ki}$ and $j_{\omega ki}$ represent component k of the linear speed and angular speed respectively and resulting from the articulation i, where $k = x, y, z$ et $i = 1, 2, ...n$. The columns j_i are calculated according to the kind of articulation i prismatic or rotary. Actually, the prismatic articulation cannot add any angular speed to the end effector $\omega_i = 0$. Thus, the matrix $\mathrm{J}_i(q)$ for a prismatic articulation can be calculated as follows:

$$\mathrm{J}_i(q) = \begin{bmatrix} j_{\upsilon ki} \\ j_{\omega ki} \end{bmatrix} = \begin{bmatrix} \mathrm{U}_{i-1} \\ 0 \end{bmatrix} \tag{4.59}$$

The vector U_{i-1} in the above equation is calculated by using the coordinate transformations of the frame $\Re_0$ in relation to frame $\Re_{i-1}$. In fact, the vector is the transformation of the unit vector of the frame $\Re_{i-1}$ along z_{i-1} axis in relation to the base frame $\Re_0$. The vector U_{i-1} is obtained as follows:

$$U_{i-1} = {}^{0}R_{i-1}\begin{bmatrix}0 & 0 & 1\end{bmatrix}^{T} \tag{4.60}$$

where ${}^{0}R_{i-1}$ is the rotation matrix 3×3 of ${}^{0}T_{i-1}$.

On the other hand, for a rotary joint, the angular velocity will be given by:

$$\omega_i = U_{i-1}\dot{\theta}_i \tag{4.61}$$

Furthermore, the angular speed of connection i also produces a linear speed at the effect end of the effector because of the rotation of all the connection around the origin O_{i-1} of frame $\Re_{i-1}$.Thus, the linear velocity is generated by the scalar product of the angular speed ω_i and the position vector ${}^{i-1}P_n$. Basing ourselves on the equation 4.61 the linear speed can be expressed with the equation 4.62 .

$$\nu_i = \omega_i \times {}^{i-1}P_n = \left(U_{i-1} \times {}^{i-1}P_n\right)\dot{\theta}_i \tag{4.62}$$

Thus, $J_i(q)$ matrix for the rotary joint can be calculated as follows:

$$J_i(q) = \begin{bmatrix} j_{\upsilon ki} \\ j_{\omega ki}\end{bmatrix} = \begin{bmatrix} U_{i-1} \times {}^{i-1}P_n \\ U_{i-1}\end{bmatrix} \tag{4.63}$$

However, for any random articulation and if the movement axis is not the z axis. The above equations have to be modified appropriately. We notice that the Jacobian matrix depends on the frame in which the end-effector speed is expressed. Starting from the individual transformation matrices (4.4, 4.5, 4.6, 4.7, 4.8, 4.9, 4.10, 4.11, and 4.12), we can calculate the position vectors ${}^{i-1}P_n$ deduced by the product of the transformation matrices ${}^{i-1}T_n$, where $i = 1..n$ and n the number of joint.

$$\begin{aligned}
{}^{0}P_9 &= {}^{0}T_1\,{}^{1}T_2\,{}^{2}T_3\,{}^{3}T_4\,{}^{4}T_5\,{}^{5}T_6\,{}^{6}T_7\,{}^{7}T_8\,{}^{8}T_9 O_0 \\
{}^{1}P_9 &= {}^{1}T_2\,{}^{2}T_3\,{}^{3}T_4\,{}^{4}T_5\,{}^{5}T_6\,{}^{6}T_7\,{}^{7}T_8\,{}^{8}T_9 O_0 \\
&\vdots \\
{}^{7}P_9 &= {}^{7}T_8\,{}^{8}T_9 O_0 \\
{}^{8}P_9 &= {}^{8}T_9 O_0
\end{aligned} \tag{4.64}$$

where $O_0 = \begin{bmatrix}0 & 0 & 0 & 1\end{bmatrix}^{T}$

Depending on D-H parameters, the rotation matrices of each articulation can be expressed in the following way:

$${}^{i-1}R_i = \begin{bmatrix} \cos(\theta_i) & -\sin(\theta_i) & 0 \\ \cos(\alpha_i)\sin(\theta_i) & \cos(\alpha_i)\cos(\theta_i) & -\sin(\alpha_i) \\ \sin(\alpha_i)\sin(\theta_i) & \sin(\alpha_i)\cos(\theta_i) & \cos(\alpha_i)\end{bmatrix} \tag{4.65}$$

Thus, we obtain the vectors U_{i-1}, where $i = 1..9$, as following:

$$\begin{aligned}
U_0 &= {}^{0}R_0\begin{bmatrix}0 & 0 & 1\end{bmatrix}^{T} \\
U_1 &= {}^{0}R_1\begin{bmatrix}0 & 0 & 1\end{bmatrix}^{T} \\
U_2 &= {}^{0}R_1\,{}^{1}R_2\begin{bmatrix}0 & 0 & 1\end{bmatrix}^{T} \\
&\vdots \\
U_8 &= {}^{0}R_1\,{}^{1}R_2\,{}^{2}R_3\,{}^{3}R_4\,{}^{4}R_5\,{}^{5}R_6\,{}^{6}R_7\,{}^{7}R_8\begin{bmatrix}0 & 0 & 1\end{bmatrix}^{T}
\end{aligned} \tag{4.66}$$

where ${}^{0}R_0 = I_3$, and I_3 representing the unit matrix of size 3.

The first two columns of the Jacobian matrix for prismatic joints 1 and 2 are given by the equation 4.59.

$$J_1(q_1) = \begin{bmatrix} U_0 \\ 0 \end{bmatrix} = \begin{bmatrix} 0 \\ 0 \\ 1 \\ 0 \\ 0 \\ 0 \end{bmatrix} \tag{4.67}$$

$$J_2(q_2) = \begin{bmatrix} U_1 \\ 0 \end{bmatrix} = \begin{bmatrix} 0 \\ 1 \\ 0 \\ 0 \\ 0 \\ 0 \end{bmatrix} \tag{4.68}$$

For rotary joint, the Jacobian is calculated from the equation 4.63. Thus, we obtain:

$$J_3(q_3) = \begin{bmatrix} U_2 \times {}^2P_9 \\ U_2 \end{bmatrix} = \begin{bmatrix} 0 \\ -C_{34}(d_7S_{56} + r_4C_{56} + d_6C_5 + d_5) \\ -d_7C_{56} + r_7S_{56} + d_6S_5 \\ 1 \\ 0 \\ 0 \end{bmatrix} \tag{4.69}$$

$$J_4(q_4) = \begin{bmatrix} U_3 \times {}^3P_9 \\ U_3 \end{bmatrix} = \begin{bmatrix} S_4(d_7S_{56} + r_7C_{56} + d_6C_5 + d_5) \\ C_4(d_7S_{56} + r_7C_{56} + d_6C_5 + d_5) \\ 0 \\ 0 \\ 0 \\ 1 \end{bmatrix} \tag{4.70}$$

$$J_5(q_5) = \begin{bmatrix} U_4 \times {}^4P_9 \\ U_4 \end{bmatrix} = \begin{bmatrix} 0 \\ -d_7S_{56} - r_7C_{56} - C_5d_6 - d_5 \\ 0 \\ 0 \\ 0 \\ -1 \end{bmatrix} \tag{4.71}$$

$$J_6(q_6) = \begin{bmatrix} U_5 \times {}^5P_9 \\ U_5 \end{bmatrix} = \begin{bmatrix} 0 \\ 0 \\ S_{34}(-d_7C_6 + r_7S_6) - C_{34}(d_7S_6 + r_7C_6 + d_6) \\ S_{34} \\ C_{34} \\ -1 \end{bmatrix} \tag{4.72}$$

$$J_7(q_7) = \begin{bmatrix} U_6 \times {}^6P_9 \\ U_6 \end{bmatrix} = \begin{bmatrix} 0 \\ 0 \\ r_7S_{34} - d_7C_{34} \\ S_{34} \\ C_{34} \\ 0 \end{bmatrix} \tag{4.73}$$

$$J_8(q_8) = \begin{bmatrix} U_7 \times {}^7P_9 \\ U_7 \end{bmatrix} = \begin{bmatrix} 0 \\ 0 \\ 0 \\ C_{34}C_{56} \\ -S_{34}C_{56} \\ -S_{56} \end{bmatrix} \tag{4.74}$$

$$J_9(q_9) = \begin{bmatrix} U_8 \times {}^8P_9 \\ U_8 \end{bmatrix} = \begin{bmatrix} 0 \\ 0 \\ 0 \\ C_{34}S_{56}S_7 - S_{34}C_7 \\ -S_{34}S_{56}S_7 - C_{34}C_7 \\ C_{56}S_7 \end{bmatrix} \tag{4.75}$$

Jacobian inverse of the mobile manipulator

In the case where, the Jacobian matrix J is square and of full rank. The inverse matrix J^{-1} exists if J is non-singular to the current configuration. Thus, the joint velocities can be evaluated using some methods. Due to the robot's joints redundancy the jacobian is a non square matrix and becomes impossible to invert (Marques et al., 2009). Indeed, the robot has 9-DOF, so a jacobian matrix 6x9. In this case, we can choose to use the pseudo-inverse J^+ of the matrix J.

$$\dot{q} = J^+ \dot{X} \tag{4.76}$$

Several computation properties of the pseudo-inverse exists. However, the most well-known and used property [1] is the Moore-Penrose pseudoinverse (MPP) (Penrose, 1955). It is defined for any $m \times n$ matrix. Moreover, J^+ always exists, and is the unique matrix satisfying

$$\begin{aligned} JJ^+J &= J \\ J^+JJ^+ &= J^+ \\ (JJ^+)^T &= JJ^+ \\ (J^+J)^T &= J^+J \end{aligned} \tag{4.77}$$

Where M^T is the conjugate transpose of matrix M

The MPP computation is based on singular value decomposition (SVD) and any singular values less than tol are treated as zero (MacAusland, 2014). The SVD of $(m \times n)$ matrix J is its representation as $J = USV^T$, where U is an orthogonal $(m \times m)$ matrix, V orthogonal $(n \times n)$ matrix and S is an $(m \times n)$ diagonal matrix having the form:

$$S = \begin{bmatrix} \sigma_1 & 0 & \cdots & 0 & 0 \\ 0 & \sigma_2 & \cdots & 0 & 0 \\ \vdots & \vdots & \cdots & \vdots & \vdots \\ 0 & 0 & \cdots & \sigma_b & 0 \end{bmatrix} \tag{4.78}$$

The diagonal elements of matrix S are non-negative numbers in descending order, all off-diagonal elements are zeros.

$$\sigma_1 \geq \sigma_2 \geq \cdots \geq \sigma_b \geq 0 \qquad b = \min\{m, n\} \tag{4.79}$$

[1] The Matlab operator pinv() returns the Moore-Penrose inverse of its matrix argument

The singular values σ of the matrix S are the square roots of the eigenvalues of the square matrices $J^T J$ or JJ^T, depending on whether $n < m$ or $n > m$ respectively, which are the same values, and the number of singular values is equal to the rank of J

The columns of U are the eigenvectors of JJ^T and are called left singular vectors or output singular vectors. The columns of V are the eigenvectors of $J^T J$ and are called right singular vectors or input singular vectors.

The pseudo-inverse is then written as:

$$J^+ = VS^+U^T \tag{4.80}$$

where the matrix S^+ takes the form:

$$S^+ = \begin{bmatrix} \frac{1}{\sigma_1} & 0 & \cdots & 0 & 0 \\ 0 & \frac{1}{\sigma_2} & \cdots & 0 & 0 \\ \vdots & \vdots & \cdots & \vdots & \vdots \\ 0 & 0 & \cdots & \frac{1}{\sigma_b} & 0 \end{bmatrix} \tag{4.81}$$

for all of the non-zero singular values. If any of the σ are zero, then a zero is placed in corresponding entry of S^+. If the matrix J is rank deficient, then one or more of its singular values will be zero. Hence, the SVD provides a means to compute the pseudo-inverse of a singular matrix. The computation of the SVD is a non-trivial issue. It suffices to know that all respectable software packages for doing mathematics (such as Maple, Matlab, or Mathematica) contain functions for computing the SVD. For our purposes, the existence of these procedures and the minimal facts outlined above should suffice.

4.3 Control of the mobile manipulator structure

The schematic diagram of the control principle is shown in Figure 4.11. The desired trajectory is defined by the time evolution of the position and orientation of the printing tool, i.e. $X = (x, y, z, \phi, \theta, \psi)$ and the material deposit speed $\dot{X} = (\dot{x}, \dot{y}, \dot{z}, \dot{\phi}, \dot{\theta}, \dot{\psi})$. Those are obtained through an automated interoperability process which goes from the optimization and verification of the 3D Form geometry to the robot parameterization and targets setting, which is achieved through Grasshopper software by the ENSAPL architects. Since the objective is to make the robot's end-effector to track specific trajectories described using Cartesian coordinates, a trajectory conversion process is necessary to calculate the corresponding joints positions of the robot. This approach is based on FKM as well as on IKM. This process is rather difficult for the calculation for redundant systems.

$$\begin{aligned} Q &= f^{-1}(X) \\ \dot{Q} &= J^+(Q)\dot{X} \end{aligned} \tag{4.82}$$

Then, this step is followed by a control system based on the difference between the desired positions and speeds and the actual ones, expressed in the joint space, enabling subsequently the positioning error correction. Figure 4.12 illustrates the basic idea of this control scheme applied in the joint space.

An alternative approach is presented in Figure 4.13. It is a control scheme developed in the Cartesian space based on the positioning errors of the effector. Here, the measured joint positions Q and speeds $\dot{Q}$ are transformed into the task space. It is supposed that the measured joint positions and speeds are not noisy. Those transformations are based on the FKM.

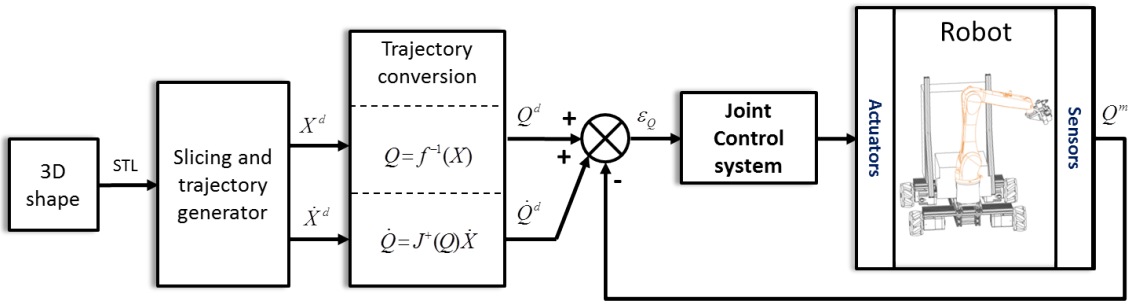

Figure 4.11 – A joint-based control scheme with Cartesian-path input

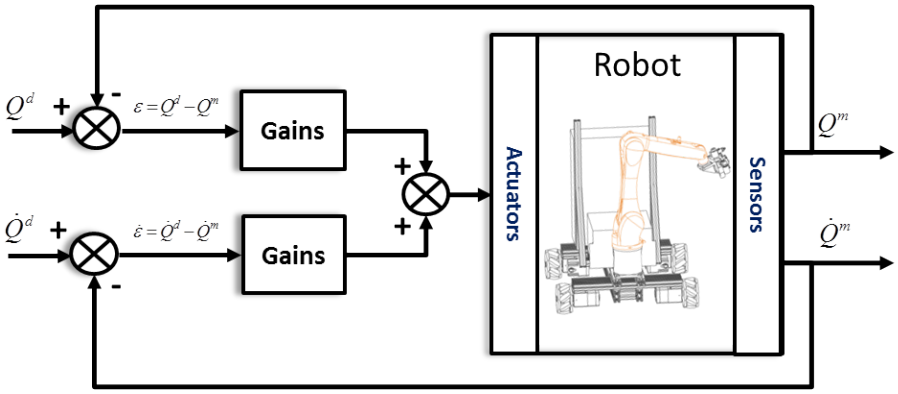

Figure 4.12 – Control diagram in the joint space

$$\begin{aligned} \mathrm{X} &= f(\mathrm{Q}) \\ \dot{\mathrm{X}} &= \mathrm{J}(\mathrm{Q})\dot{\mathrm{Q}} \end{aligned} \tag{4.83}$$

The estimated position obtained from measurements, which are supposed not noisy, is compared to the targeted position. Then a control system would attempt at reducing the Cartesian error. The output vector of the controller can be viewed as little displacement δX. Thus through the pseudo-inverse J^+ the joint equivalent positions are calculated δQ.

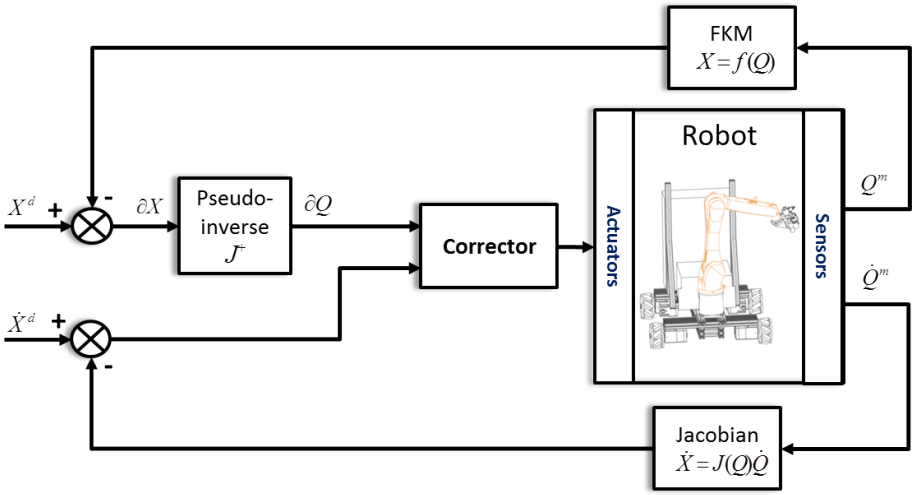

Figure 4.13 – Control diagram in the Cartesian space

The implementation of these control schemes requires the calculation of the different models mentioned previously taking into account the fact that the considered mobile

manipulator is redundant versus the assigned task.

Besides, there is an additional difficulty to ensure a precise control of the system since the robot end-effector undergoes a combined movement between the mobile base and the manipulator. These two subsystems have different precision degrees.

The following control architecture is implemented for mobile manipulator control, as shown in Figure 4.14. From the complex 3D Shape, the desired velocity, position, and orientation trajectory of the nozzle along the print object is obtained. Then, the inverse kinematic model used to convert the space coordinates into the joint coordinate. This step is performed in offline. During the online process, a closed loop control is made on the robot and the pump, which enables us to get a convenient flow according to the type of material.

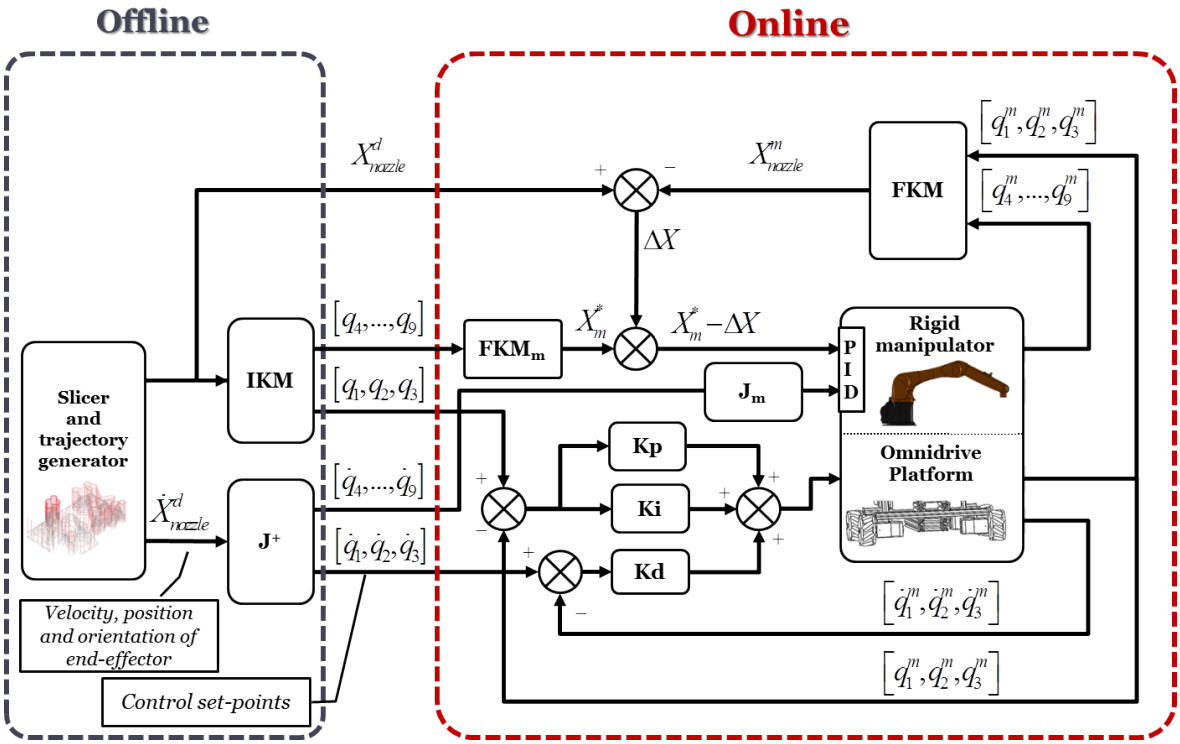

Figure 4.14 – Block diagram of the print robot control system

The performance of the rigid manipulator is used to correct slipping errors in the positioning of the mobile platform. Moreover, the all degrees of freedom aren't equivalent in terms of the positioning accuracy of the terminal component. Indeed, a low rotation of the mobile platform implies a significant displacement of the end effector. However, the resolution of the sensors used to measure rotations is finite. In addition, various phenomena such as segment deflections, dead-zone and non-linearities in the joints accentuate this error multiplication effect. For this purpose, the rigid manipulator model is used to correct nozzle positioning errors. The rigid manipulator have a specific proportional–integral–derivative (PID) controller. However, a PID controller has been established to track the desired trajectory of the platform. The Ziegler–Nichols tuning method based in heuristic method has been used to determine the gains of PID controller (Meshram and Kanojiya, 2012). Thus, the output provided by the FKM bloc is compared with the desired nozzle's trajectory. The IKM_m of the rigid manipulator is then used to reduce the Cartesian errors.

4.4 Simulation and Experiment results

In 3D printing, the simulation of the printing trajectory is a very essential step. It makes it possible to predict the robot's behavior along the path of the architectural form to be printed, i.e., to check if the inverse solutions provided by the IKM satisfy the various constraints, in particular, safety constraints, collision with the printed structure, singular configurations, etc. The implementation is conducted in MATLAB-simulink using a Intel Core (TM) i5-4590s CPU at 3GHz. In this section, simulation results obtained on the printing of small, large and very large scale structures are presented.

Calibrating the pump speed is also a very critical step, as it is responsible for the quality of the printed objects. Indeed, the quality of the material flow rate at the nozzle outlet depends on the material formulation, the pump speed and the ambient temperature. Once the latter is calibrated, the next step is just to adapt the robot's speed for a better quality of material deposition. The process of calibrating the material flow rate and deposition rate of the material is presented in this section.

After the simulation of the printing of the object and the calibration phase of the pump parameters, the logical next step is the printing step itself. A structure that integrates both the displacements of the manipulator and mobile base was considered to validate the proposed control architecture.

This section presents the simulation results, the calibration of the pump parameters, and the experimental results, respectively.

4.4.1 Simulation results

This subsection focuses on the results of the different performed simulations. The simulation of commonly printed structures was considered, i.e. small, large, and very large scale structures. Small structures involve only the displacements of the manipulator while large and very large structures involve both the displacements of the manipulator and the mobile base. Figure 4.15, Figure 4.16, and Figure 4.17 depict the results of the simulations performed in small, large, and very large scale structures, respectively. We can obverse that the mobile manipulator effectively tracks the trajectories of the 3-D architectural forms.

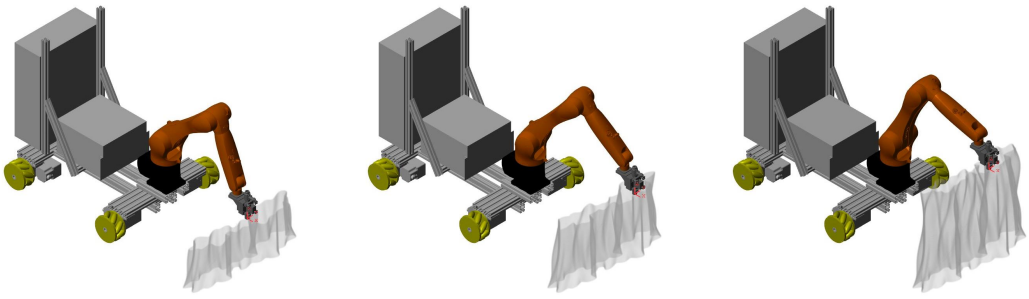

(a) (b) (c)

Figure 4.15 – Simulation of the Robot path: printing a small object

Figure 4.15 represents a simulation of the robot path for a small size architectural shape. In this case, the mobile platform is stationary because the size of the printed shape is inside the defined manipulator's sub-workspace. However, in Figure 4.16 and 4.17, we can observe the displacements of the mobile platform to cover the size of the printed

structure. Obviously, we can observe in Figure 4.16 that only the translation displacements of the mobile platform are necessary while in Figure 4.17, the translation displacements and rotation are necessary.

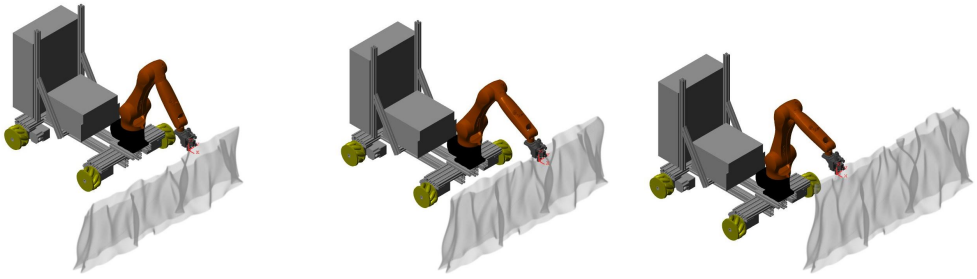

(a) (b) (c)

Figure 4.16 – Simulation of the Robot path: printing a large object

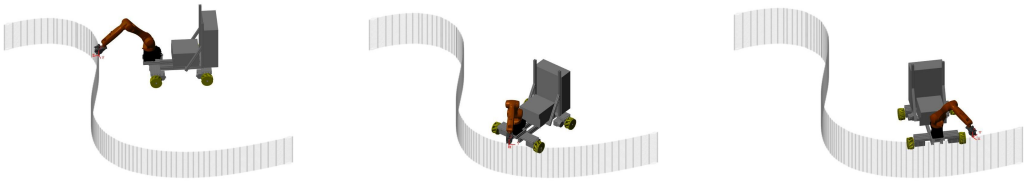

(a) (b) (c)

Figure 4.17 – Simulation of the Robot path: printing a very large object

4.4.2 Materials preparation and extrusion description

The characteristics of the materials are studied in order to define certain control parameters. Indeed, the voltage controlling the flow rate at the pump outlet depends not only on the displacement speed of the nozzle but also on the rheology of the material. The latter are essential for the automation of additive manufacturing. In the first instance, this step has been implemented by trial and error tests which permitted to determine the relationship between flow and speed. The optimal ratio between robot speed and material flow can be obtained by maintaining the flow rate constant, and by varying the robot speed on a given printing trajectory, Figure 4.18.

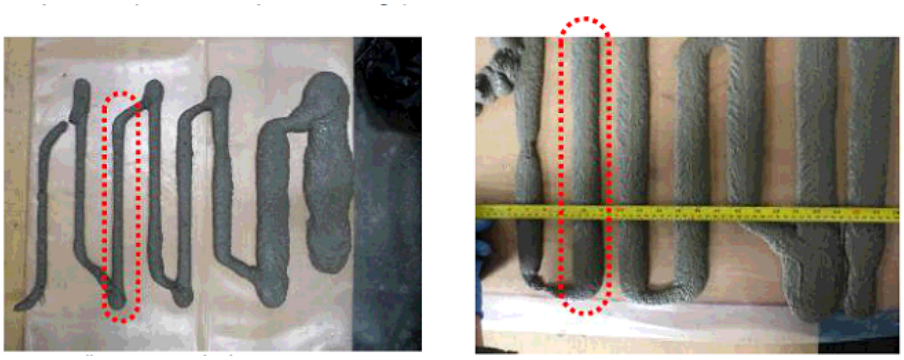

Figure 4.18 – Back and forth for the choice of the control voltage/flow rate

For each test carried out and whatever the type of mortar, the value of the deposition speed of the material ranges 50 mm/s and 100 mm/s. The pump voltage is on average 1.5 volts with a pressure of 5 bar at the pump outlet. However, when it comes to clay, the deposition speed is less important, values range from 20 mm/s to 40 mm/s. But the pump voltage and output pressure are higher (4 volts and 15 bar). These values were chosen for a 3 cm thick layer. But, without knowing the actual value of the flow rate which is approximately 3 to 4 L/min.

The control of the material leads us ask about the procedure to be adopted and the improvements to be made. In fact, initially, the geometry of the shape to be printed depends strongly on the width and depth of the cord. Failure to comply with these rules results in a distortion of the shape. Then, the superposition speed of the material must be maintained according to the fluidity of the material. If speed is important for a liquid material, the structure cannot support its own weight. Thus, flow control is important for the automation of the printing process. Figure 4.19 represents the number of pulses related to concrete mixing during the printing steps.

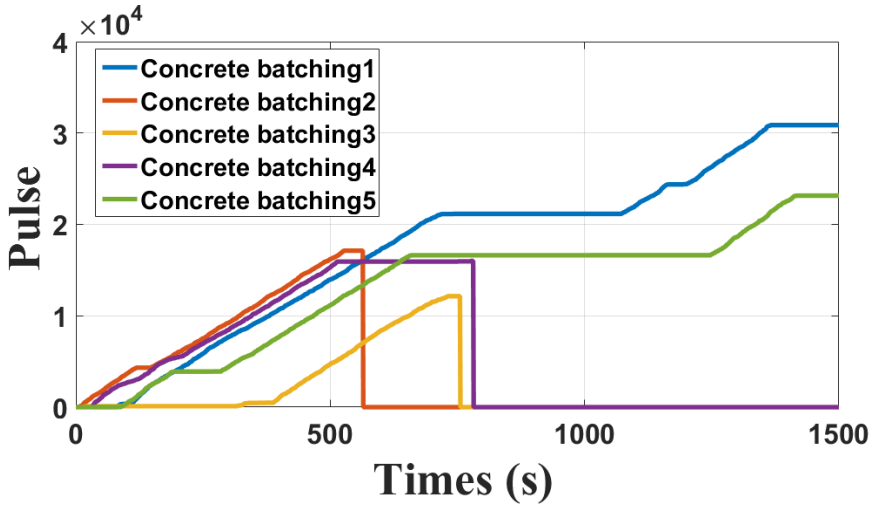

Figure 4.19 – The nozzle Output flow for a concrete formulation

The tests were carried out on 12/9/2017, with a cement formulation from work package 4. The curves depicted in Figure 4.19 allow to determine the number of pulses per second for a control voltage of 1.6 volts from the slope. On average, this cement formulation produces between 33 and 37 pulsations/s, which corresponds to a flow rate of 2.5 liter/min. There are also 3 phases during the tests; the priming, calibration, and adjustment phase; followed by the printing phase and the purging phase. Indeed, during the transition from one phase to another, the pump is stopped and yields in a constant number of pulses over a period of time, as shown in Figure 4.19. In addition, the slope at the beginning of printing is not stable. Figure 4.20 shows the setting of the pump control voltage as a function of the flow rate. As the material is highly viscous at the beginning of printing, an increase in the deposition speed and a decrease in the control voltage of the pump must be maintained for some time.

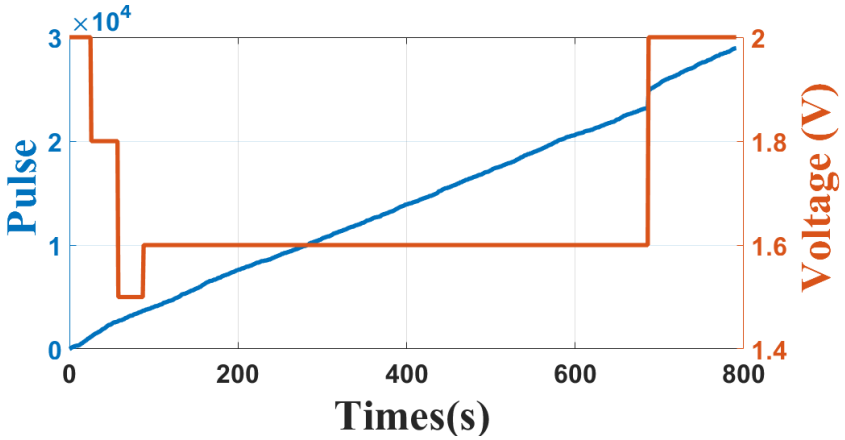

Figure 4.20 – Pulse and pump voltage

In Figure 4.21, an adjustment of the set point voltage has been made during the printing to maintain the flow rate at 37 pulses/s. The change in the behavior of the material (rheological change) may be at the origin of the instability of the variations in the number of pulses/s.

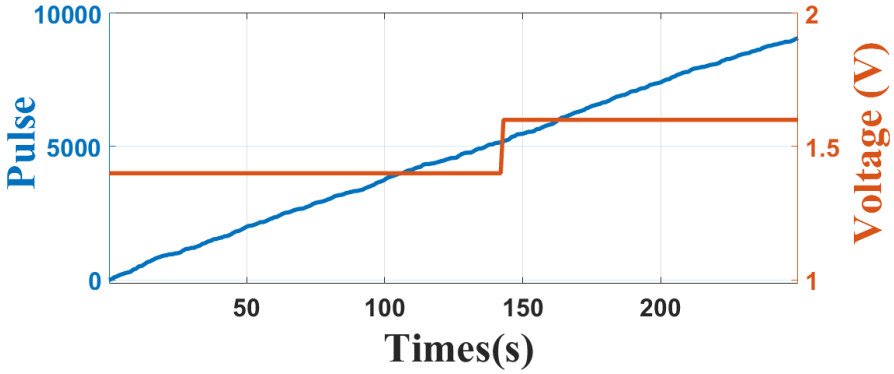

Figure 4.21 – Adjustment of pump voltage

The velocity of the nozzle and material flow rate were calibrated based on trial-and-error tests. Figure 4.22 shows the relationship between the nozzle speed and the flow rate as a function of the material type.

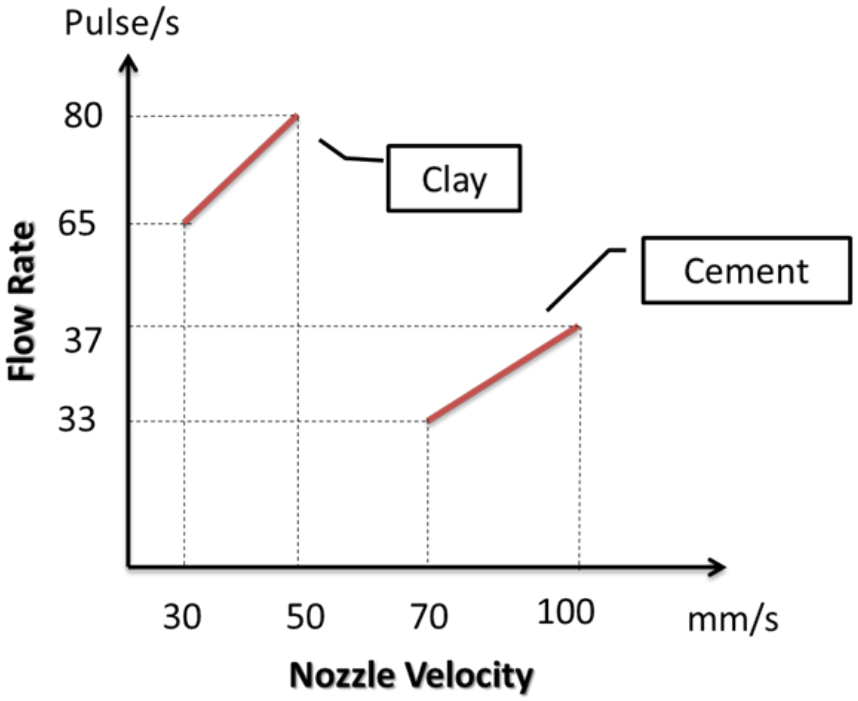

Figure 4.22 – Flow rate relative to the nozzle velocity

The properties of the material remain constant. But it is clear that the trend curves heavily depend on the environment temperature of the printing. The formulations developed at the beginning of the project are very sensitive to the temperature and humidity variations, to such an extent that we obtained totally unexpected results during the mixing, the conveyance of the material through the pipes or at the nozzle tip. Figure 4.23 represents the temperature of the workshop where the printing took place from 01/11/2017 to 27/02/2018. We can observe an average temperature of 16°C. Thus, it is recommended to carry out a calibration of the flowmeter one day before the printing.

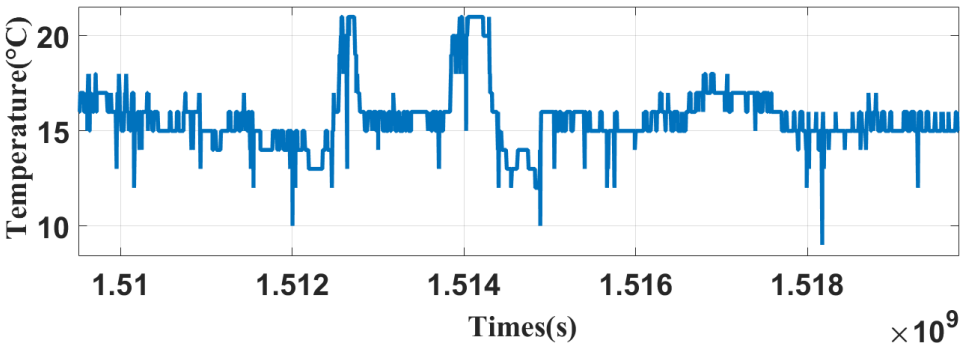

Figure 4.23 – Temperature of the work environment

4.4.3 Experiments

This subsection present the results of the conducted experiments. Figure 4.24 give the structural form that was used for experiments. During the printing, the pipe linked to the nozzle reduces the movement of the robot, and the Change of the pipe length requires

the change of the material formulation parameters. However, due to time constraints, we decide to maintain the same characteristics.

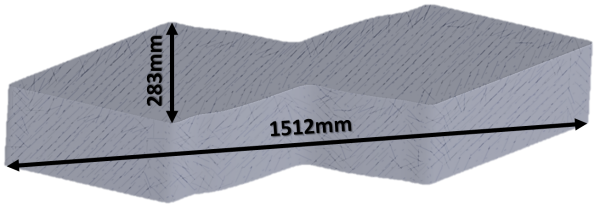

Figure 4.24 – 3D forms

Moreover, the localization of the mobile platform is also essential. An ultrasound localization system has been used to provide the localization of the mobile robot. Four stationary ultrasound beacons provide the position of the mobile robot. Five beacons communicate between one another via a radio connection 433 MHz, the calculation is carried out with a central modem. The accuracy of the localization system specified is +/- 2cm and it is totally confirmed by the experimental results. The shift can be explained by the sliding of the Swedish wheel during the displacement. Figure 4.25 represents the trajectory followed by the robot during the printing phase as well as the location of 4 beacons.

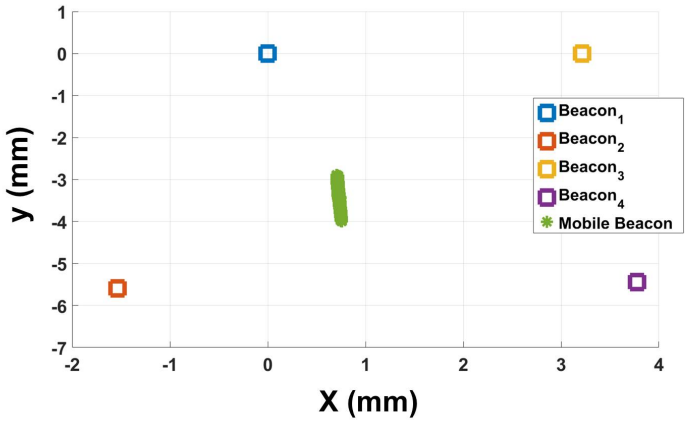

Figure 4.25 – Trajectory performed by the mobile platform during the printing

A low cost inertial measurement unit is used to calculate the altitude, the acceleration, and the rotation angles of the robot. The data from the accelerometer on the three axes during the printing are given in Figure 4.26. The data is noisy due to the structure vibrations. Indeed, during the printing, the conveyance of the material as well as the movement of the pipe in contact with the robot structure generate shakes.

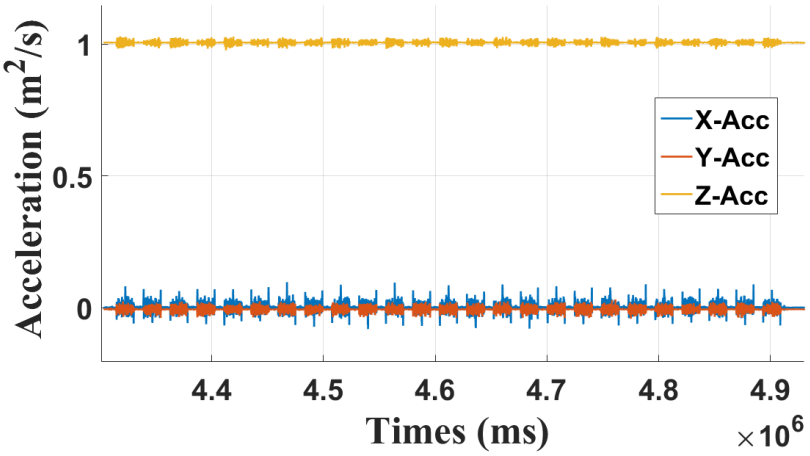

Figure 4.26 – 3-axis accelerometer

The data from the three angles ϕ, θ, and ψ which correspond to the three respective rotations around the axis x, y, and z are represented in Figure 4.27. We notice that the angles are constant all along the printing. Angles ϕ and θ enable us to determine the ground inclination. Actually, the printings have been done on a flat ground. While the angle ψ representing the yaw movement of the robot, it shows a slight derivation of 3 degrees.

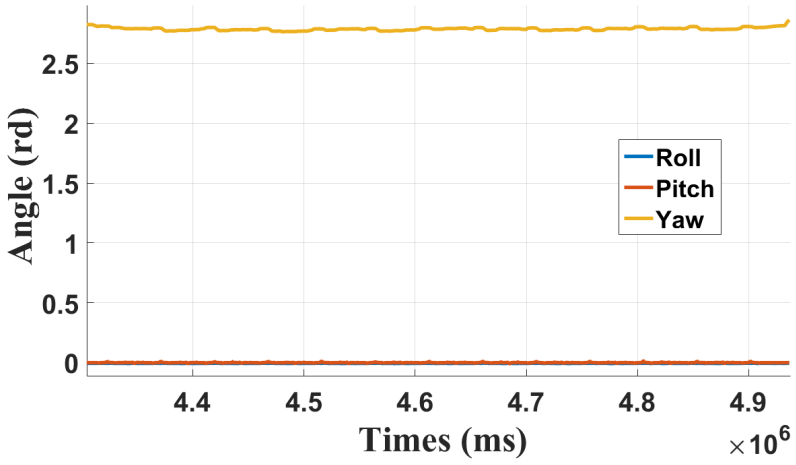

Figure 4.27 – Phi-Theta-Psi angles

Figure 4.28 shows the positioning error to define the accuracy of the models implemented in the robot. Figure 4.28a represents the trajectory of the nozzle obtained through the 3D model (Figure 4.24) in a set of geometric points of the printable space and trajectory of the nozzle during the printing. We obtain a centimeter precision of less than $1cm$ on the axes x and z (Figures 4.28b and 4.28d) and less than $5cm$ on the axis y (Figure 4.28c).Indeed, in fact, only a lateral movement was produced.

A sequential representation of the robot actual movements during the printing is shown in Figure 4.29.

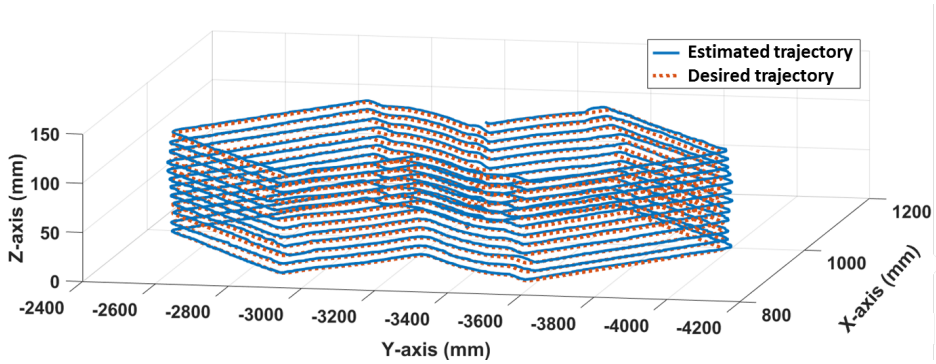

(a) Positioning gap

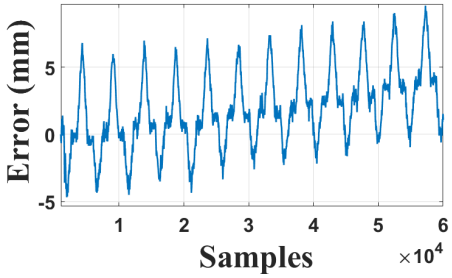

(b) X axis error

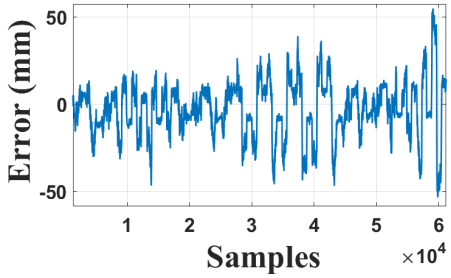

(c) Y axis error

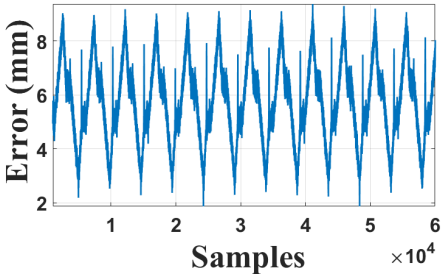

(d) Z axis error

Figure 4.28 – Trajectory of the printing nozzle

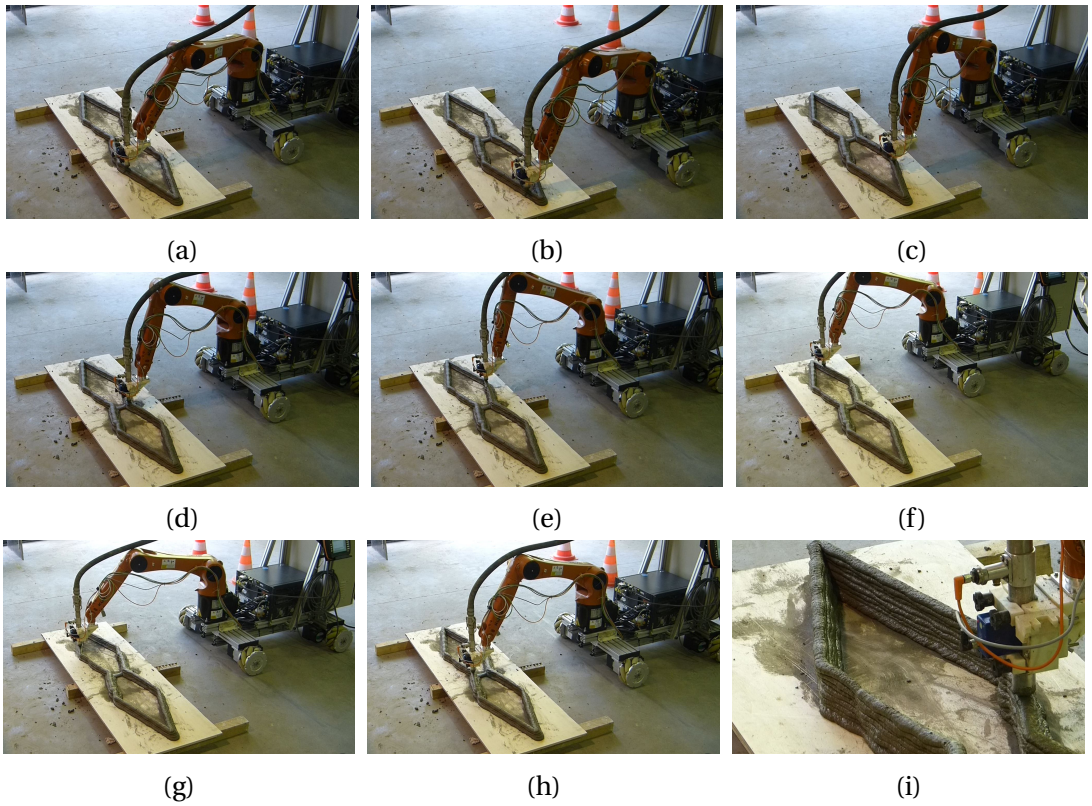

(a) (b) (c)

(d) (e) (f)

(g) (h) (i)

Figure 4.29 – Trajectory of the printing nozzle

4.4.4 Discussion

In the view of the results obtained, the proposed kinematic models achieve good performance for additive manufacturing application. The mobile manipulator performs the printing task without collision with the printed structure. Over a total material deposit length of approximately $40m$ and by making lateral displacements of the mobile platform over distances of $1m$, we obtain an accuracy of $5cm$. The difference between the actual positioning of the mobile base and that observed are caused directly by the sliding between the wheels and the ground depending on the kind of ground and the ground wear. In addition, a slight orientation of the mobile base of 3 degrees is observed. Indeed, a low rotation of the rotary actuators far of the center of tool implies a significant displacement of this latter. However, the resolution of the sensors used to measure rotations is finite.

Many experiments have been carried out on each type of material with the aim of obtaining a $9mm$ high and approximately $30mm$ wide layer of material at the exit nozzle. Flow measurements based on the pump control voltage and material deposition rate are essential for automating the printing procedure. For cement material, the pump control voltage is between 1.4 and 1.6 volts for a deposit speed between 5cm/s and 10 cm/s and a pump outlet pressure between 2.3 bar and 4.8 bar. For clay, the control voltage is between 3.8 and 5.5 volts for a deposit speed between 2cm/s and 4cm/s and a pump outlet pressure between 8 and 15 bar.

4.5 Conclusion

In this chapter, we dealt with the methods used in kinematic and differential kinematic modeling applied to a mobile manipulator robot. These are essential for achieving

control laws in position and speed. In fact, to describe the targeted movement in the operational space, the kinematic and differential kinematic models allow the calculation of the positions and the joint speed. We showed how to solve the robot redundancy with the inverse kinematic model. Paul's method and an optimization method which consisted in delimiting the workspace of the manipulator arm in order to minimize the sliding of the mobile part were used to resolve the redundancy. The goal is to use the manipulator arm if the printing trajectory is beyond the manipulator's sub-workspace, and the mobile part to place the mobile manipulator faces to the printed structure. The models mentioned in this chapter relate to the printing phase, where, only the mobile manipulator is used. However, as it was mentioned previously, the robot is also used for quality inspection after the printing phase. We converged towards the use of a hyper-redundant soft manipulator that can reach narrow spaces, minimizing the displacements of the mobile manipulator part. In the next chapter, we develop the kinematic modeling of the soft-continuum manipulator in order to develop rather efficient endpoint controls than a rigid robot. This study will help us ultimately focus on the concatenation of the models in order to come up with a hyper-redundant structure.

Chapter 5

Modeling and control of the hyper-redundant robot for the quality inspection

Contents

5.1 Introduction

Additive manufacturing is an automated process for producing layer-by-layer material deposition. Recently, this technology has been introduced in industrial construction to print houses or smaller piece structures for on-site assembly, with complex geometry. In Additive manufacturing processes, the material deposition step is generally followed

by a printing quality inspection step. However, the geometry of printed structures with funicular surfaces is sometimes complex, where rigid structure robots cannot reach some dead zones areas from their workspaces, due to kinematic singularities. In this chapter, a soft-continuum manipulator equipped with a camera is attached to the end-effector of the omnidrive mobile-rigid manipulator robot of Chapter 3, in order to realize a quality inspection process. Indeed, soft-continuum manipulators can bend along their structures with complex geometry; and this inherent flexibility makes them suitable for navigation and operation in congested environments. The number of controlled actuators being greater than the dimension of task space. This work is summarized in a trajectory tracking of hyper-redundant soft-continuum robots. This issue lies in solving the strongly nonlinear equations with respect to optimal time computation. This chapter focuses on our main scientific contribution, namely the modeling and solving of the kinematics of the soft-continuum manipulator used in the quality inspection of printed objects. After this brief introduction, a description of the experimental platform consisted of a mobile rigid manipulator equipped with a soft-continuum manipulator is presented. The kinematic modeling of the experimental platform is given afterwards. The chapter follows by real-time implementations, a discussion of the results obtained, and ends with some concluding remarks.

5.2 Description of the robotic platform

As stated in the previous chapter 3, the experimental platform called MATRICE's robot is a prototype for additive manufacturing in construction. It is composed of a mobile Omni-drive platform and rigid manipulator. A soft-continuum manipulator is added, as showed in Figure 5.1 for quality inspection.

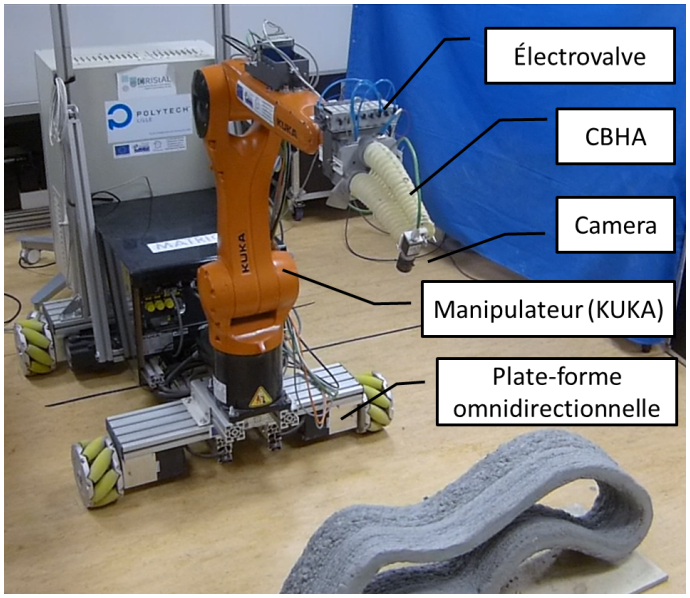

Figure 5.1 – A quality inspection robot

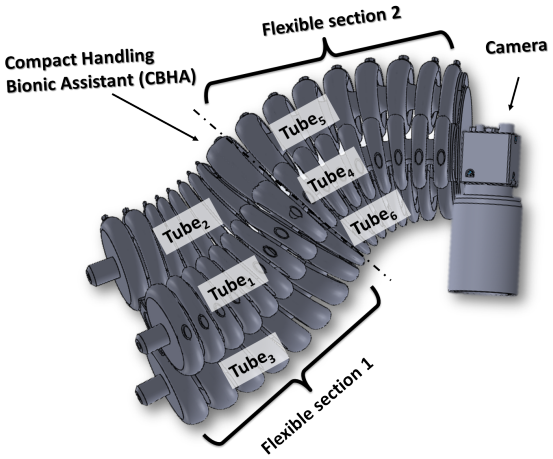

Figure 5.2 – Description of the CBHA platform

The soft-continuum manipulator considered in this work is inspired by the elephant's trunk (Figure 5.2) placed at the end-effector of the omnidrive mobile-rigid manipulator, using for 3D printing construction (chapter 3). The CBHA is handling a camera used to scan surfaces for quality inspection. Each flexible section of the CBHA consists of three tubes, controlled by electro-pneumatic actuators. The position and orientation of each section are controlled by varying the pressure inside tubes. A rigid cable is limiting the extension, Figure 5.3. Six tubes can be loaded and unloaded with compressed air so that the structure can be moved in any desired direction. Six wire potentiometer sensors are placed along each tube allowing to measure elongations of each tube. The voltages provided by wire-potentiometer sensors are proportional to the extension of each tube $l_{p,s}$, where $p = 1,..,3$ and $s = 1,2$ correspond to the wire-potentiometer and section number, respectively.

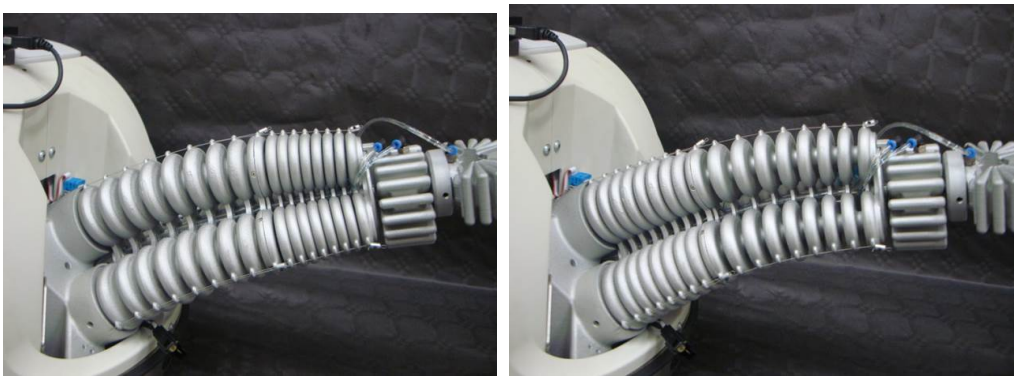

(a) (b)

Figure 5.3 – CBHA extension limit: When the middle cable is stretched, the extension of one section causes the compression of the other.

The choice of a soft-continuum robot comes from the fact that it can maneuver in congested and narrow environments thanks to its flexibility. The advantage of using such style-robots is illustrated in Figure 5.4. We note that accessible areas may require complex movements of rigid platforms with the risk of reaching joint limits (Figure 5.4b). The use of flexible manipulators not only reduces the inspection time but also the energy consumed.

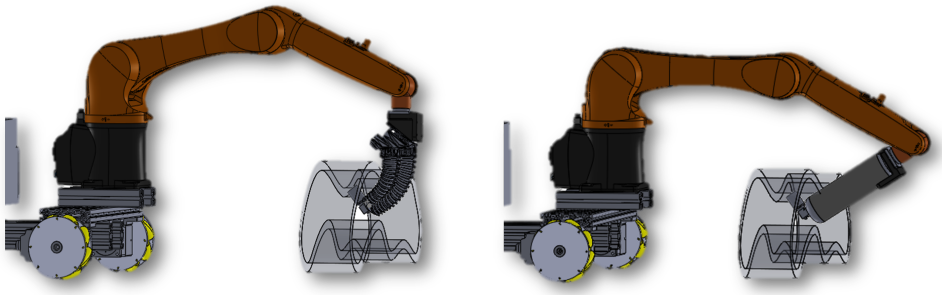

(a) Scanning with a soft-continuum manipulator (b) Scanning with a rigid manipulator

Figure 5.4 – Advantage to use a soft-continuum manipulator for quality inspection

5.3 Kinematic modeling of the CBHA

As we have stated in the introduction section, the kinematic behaviors of continuum manipulators can be reproduced under functional and structural assumptions. In this section, the assumptions used in kinematic modeling is first presented. The kinematics of the CBHA is developed, then.

5.3.1 Assumptions

The kinematic models of the CBHA are developed under some assumptions, described below:

- The manipulator is considered as a series of N = 17 vertebrae.
- An inter-vertebra is flexible and non-deformable with a 3-DoF mobility. It is modeled with a 3UPS-1UP joints.
- The manipulator's yaw motion is not allowed with the existing mechanical links between the tubes.

Based on these assumptions, a parallel robot composed of two rigid platforms and 3-DoF of mobility is used to emulate the behavior of each inter-vertebra. Knowing that the robot comprises 17-vertebrae, the entire CBHA can be emulated by a series of 16 parallel robots each comprising 3-DoF.

Using such modeling, CBHA can be considered as a 48-DoF system. That is why the CBHA robot has the properties of hyper-redundant robots. The schema of an inter-vertebra is given in Figure 5.5.

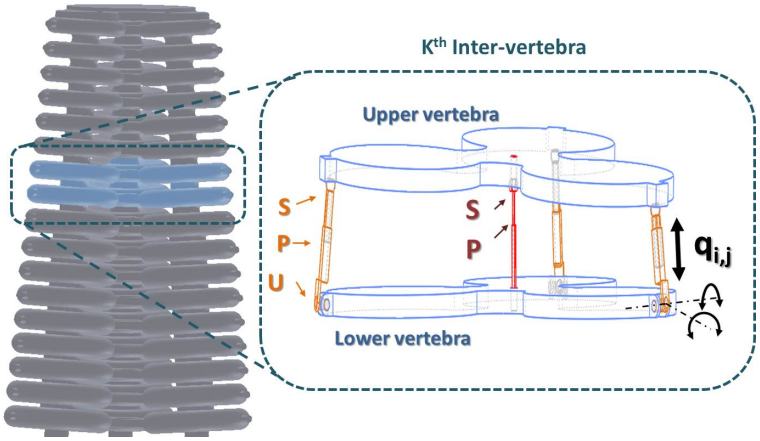

Figure 5.5 – Schematic of an inter-vertebra modeled as parallel robot with 3UPS-1UP

It consists of a lower and upper vertebra connected by three limbs with the same kinematic configuration, and a central leg. The limbs are modeled by a kinematic configuration of type UPS, in which only the prismatic joints are active allowing to control the position and orientation of the upper vertebra relative to the lower vertebra. $q_{i,j}$ represents the variation of the length of the prismatic joint, where $j = 1,..,3$ is the index of the active joint and i is the index of the frame. The central leg is modeled by a kinematic configuration of type UP located in the center of an inter-vertebra. It is considered as a passive joint. The frames associated with the inspection system under the defined assumptions is represented in Figure 5.6.

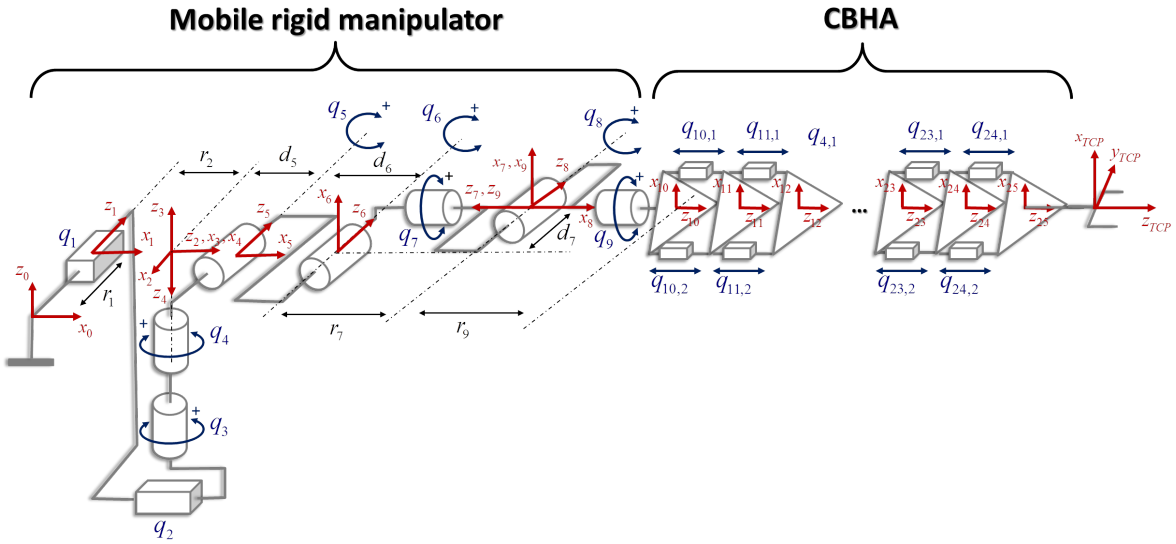

Figure 5.6 – Placement of frames in robot home position

5.3.2 Inverse Kinematic Equation of the CBHA's Inter-Vertebra

The IKEs of an inter-vertebra are obtained by calculating the joint variables $q_{i,j}$ corresponding to the pose (position and orientation) of the upper vertebra's center relative to the lower vertebra frame. In the case of the CBHA, the inter-vertebra is considered as a 3-DoF parallel robot, because of movements constraints related to the passive kinematic chain UP. In fact, the rotation with respect to the z axis, denoted by $Rot(z,\Phi_i)$, and the

translations relative to the x and y axes denoted by $\mathrm{T}rans(x,\mathrm{X}_i)$ and $\mathrm{T}rans(y,\mathrm{Y}_i)$, respectively, are not considered, because it does not exist a movement on these axis. Only the translation along the z axis is possible which is denoted by $\mathrm{T}rans(z,\mathrm{Z}_i)$. Hence, the IKEs can be formulated as follows:

$$q_{i,j} = f(\mathrm{Z}_i, \psi_i, \theta_i) \tag{5.1}$$

where the angles θ_i and ψ_i indicate pitch and roll angles, respectively.

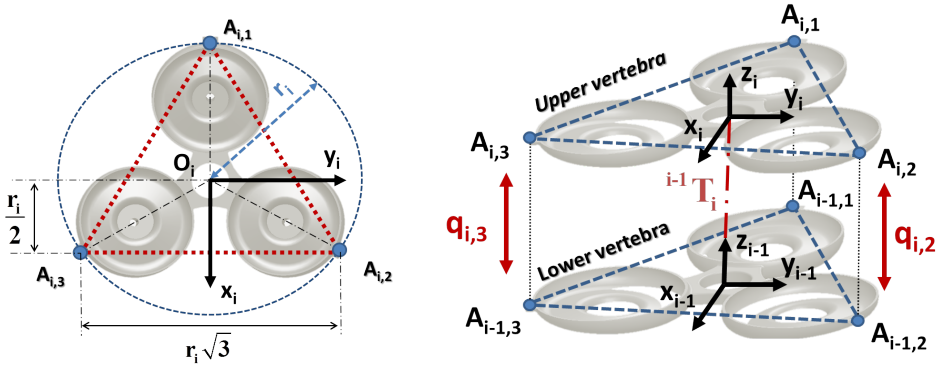

Figure 5.7 – Configuration 3UPS-1UP of the CBHA

$\mathrm{A}_{i,j}$ represents the connection point between the extensible driving leg $j = 1,..,3$ and the vertebra i, as shows the Fig 5.7. For each vertebra, the points $\mathrm{A}_{i,1}$ $\mathrm{A}_{i,2}$ $\mathrm{A}_{i,3}$ form an equilateral triangle. The frame $\Re_{i-1}\{\mathrm{O}_{i-1}, x_{i-1}, y_{i-1}, z_{i-1}\}$ is attached to the lower vertebra of origin O_{i-1}, center of the triangle $\mathrm{A}_{i-1,1}\mathrm{A}_{i-1,2}\mathrm{A}_{i-1,3}$ and the frame $\Re_i\{\mathrm{O}_i, x_i, y_i, z_i\}$ is attached to the upper vertebra of origin O_i, located at the center of the equilateral triangle $\mathrm{A}_{1,i}\mathrm{A}_{2,i}\mathrm{A}_{3,i}$. Knowing that the entire shape of the CBHA is conical, it is necessary to find the circumcircle radius r_n of the considered vertebra, where $n = 1,..,\mathrm{N}$ is the number of vertebrae. Let r_{max} and r_{min}, respectively the radius of the base and the apex of the backbone, the radius of each vertebra r_n can be calculated by:

$$r_n = \frac{i}{\mathrm{N}}(r_{min} - r_{max}) + r_{max}, \tag{5.2}$$

where $\mathrm{N} = 17$ is the number of vertebrae. Thus, the coordinates of the three connection points are given by the coordinates (5.3), relative to the centre of the n^{th} vertebra.

$$\mathrm{A}_{i,1} = \begin{bmatrix} -r_i \\ 0 \\ 0 \end{bmatrix}; \mathrm{A}_{i,2} = \begin{bmatrix} \frac{1}{2}r_i \\ \frac{\sqrt{3}}{2}r_i \\ 0 \end{bmatrix}; \mathrm{A}_{i,3} = \begin{bmatrix} \frac{1}{2}r_i \\ -\frac{\sqrt{3}}{2}r_i \\ 0 \end{bmatrix}. \tag{5.3}$$

The length of the prismatic joint for the active kinematic chain of each UPS is represented by $q_{i,j}$. The coordinates of the connection point $\mathrm{A}_{i,j}$ relative to the frame $\mathrm{A}_{i-1,j}$ are given as follows:

$$\begin{bmatrix} \mathrm{Q}_{i,j} \\ 1 \end{bmatrix} = {}^{i}\mathrm{T}_{i-1} \begin{bmatrix} \mathrm{A}_{i,j} \\ 1 \end{bmatrix} - \begin{bmatrix} \mathrm{A}_{i-1,j} \\ 1 \end{bmatrix} \tag{5.4}$$

where, ${}^{i}\mathrm{T}_{i-1}$ is the transformation matrix of the upper vertebra frame relative to the lower vertebra.

$$ {}^{i}\mathrm{T}_{i-1} = \begin{pmatrix} \mathrm{C}\theta_i & \mathrm{S}\theta_i\mathrm{S}\psi_i & \mathrm{S}\theta_i\mathrm{C}\psi_i & 0 \\ 0 & \mathrm{C}\psi_i & -\mathrm{S}\psi_i & 0 \\ -\mathrm{S}\theta_i & \mathrm{S}\psi_i\mathrm{C}\theta_i & \mathrm{C}\theta_i\mathrm{C}\psi_i & \mathrm{Z}_i \\ 0 & 0 & 0 & 1 \end{pmatrix}. \tag{5.5} $$

The notations C and S stand for the cosine and sine functions, respectively. Thus, the prismatic variable $q_{m,k}$ is equal to the distance between the connection points $\mathrm{A}_{m,k+1}$ and $\mathrm{A}_{m,k}$, and expressed as:

$$ q_{i,j}^2 = {\mathrm{Q}_{i,j}}^{\mathrm{T}}\mathrm{Q}_{i,j} \tag{5.6} $$

Therefore, after introducing of (5.3) into (5.4), the equation (5.6) can be rewritten in the format of (5.1):

$$ \begin{aligned} q_{i,1}^2 &= {\mathrm{Z}_i}^2 + 2r_i\mathrm{Z}_i\mathrm{S}\theta_i - 2r_{i-1}r_i\mathrm{C}\theta_k + {r_{i-1}}^2 + {r_i}^2 \\ q_{i,2}^2 &= {\mathrm{Z}_i}^2 + \mathrm{Z}_i r_i\left(\sqrt{3}\mathrm{C}\theta_i\mathrm{S}\psi_i - \mathrm{S}\theta_i\right) - \\ &\quad r_i r_{i-1}\left(\tfrac{\sqrt{3}}{2}\mathrm{S}\theta_i\mathrm{S}\psi_i + \tfrac{3}{2}\mathrm{C}\psi_i + \tfrac{1}{2}\mathrm{C}\theta_i\right) + {r_{i-1}}^2 + {r_i}^2 \\ q_{i,3}^2 &= {\mathrm{Z}_i}^2 - \mathrm{Z}_k r_k\left(\sqrt{3}\mathrm{C}\theta_k\mathrm{S}\psi_k + \mathrm{S}\theta_k\right) + \\ &\quad r_i r_{i-1}\left(\tfrac{\sqrt{3}}{2}\mathrm{S}\theta_i\mathrm{S}\psi_i - \tfrac{3}{2}\mathrm{C}\psi_i - \tfrac{1}{2}\mathrm{C}\theta_i\right) + {r_{i-1}}^2 + {r_i}^2 \end{aligned} \tag{5.7} $$

5.3.3 Forward kinematics of the CBHA

In this subsection, the FKM of an inter-vertebra is first derived from the IKE using neural network approximation. The FKM of the entire CBHA's backbone is deduced, afterwards.

A. Forward Kinematic Model of the CBHA's inter-vertebra

The relation between the joint configuration $q_{i,j}$ of an inter-vertebra and the parameters of the upper-vertebra (Z_i, θ_i, and ψ_i) relative to the lower vertebra frame is the FKM of the parallel robot module 3UPS -1UP , defined as:

$$ [\mathrm{Z}_i, \theta_i, \psi_i] = f^{-1}(q_{i,j}). \tag{5.8} $$

The pose $[\mathrm{Z}_i, \theta_i, \psi_i]$ of the upper vertebra frame corresponding to a particular joint configuration $q_{i,j}$ relative to the lower vertebra frame can be obtained by solving the IKEs (5.7). However, as we can notice, these equations are highly nonlinear. Numerical techniques such as least square, Newton-Raphson methods (Arshad et al., 2005) which are used to provide approximated solutions are usually computationally intensive. In this work, an approximated solution is provided by a Multilayer Neural Network (MNN). The approximation of the solution can be summarized to a regression problem with non-noisy data, because the IKEs are supposed to be well identified. The solution of the IKEs based on NN approximation offers advantages such as reduced computational resources and rapid execution for real-time purposes.

A NN is an algorithm that models the mechanisms of learning and problem solving functions of the human brain. NN possess many useful properties and capabilities (Haykin, 1994): nonlinearity, input–output mapping, adaptivity, fault tolerance, very large scale integration implementability,.... In NN, the signals flow consecutively through the different layers from the input to the output layer. The intermediary layers are known as hidden layers. For each layer, each elementary unit calculates a scalar product between

a vector of weights and the output vector given by the previous layer. The choice of the appropriate network architecture (i.e. number of hidden layers, number of nodes in each layer, the type of activation function,...) has to be controlled by the network designer. After the choice of the architecture of a neural network, the values of the weights are adjusted via training or learning process. The performance of this model is closely related to the nature of the sample input-output data pairs; and noisy data can significantly degrade this performance.

Typical examples of Artificial Neural Networks (ANNs) are the Multilayer Perceptron (MLP) and the Radial Basis Function neural network (RBFNN). Radial Basis Function (RBF) and MLP proved effective for non-linear modeling problems. They differ from each other in both the architecture as well as the training procedure. In (Hornik et al., 1989), it was proved that an Multilayer Perceptron Neural Networks (MLPNN) with two layers of weights and sigmoid activation functions can approximate any nonlinear functional relationship (mapping) with an arbitrary accuracy, provided that enough hidden neurons are available. This justifies the success of this particular class of neural networks in numerous fields of application of regression problems. As opposed to MLPs, which perform a nonlinear combination of the output of hidden nodes, the RBFs derive estimations according to a linear combination of the output of a set of RBFs (generally of the Gaussian type). These functions are associated with the hidden units of the network and their parameters are derived in the validation phase of the neural estimator (Benoudjit and Verleysen, 2003). However, depending on the application, one topology can be preferable to another. For function approximation problems, RBFNN are specially recommended for surface with regular peaks and valleys; otherwise, traditional neural networks are preferred (Xie et al., 2011). In the following sections, a brief description of the two neural prediction methods is provided.

A.1. Prediction procedure based on MLPNN

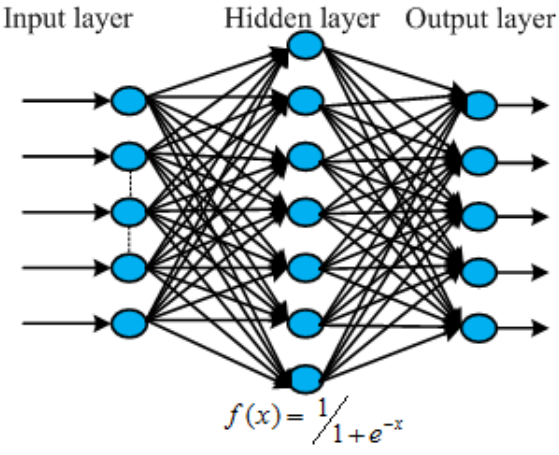

Figure 5.8 – MLP Neural Network topology

MLPNN (Figure 5.8) is composed of a large number of highly interconnected units (neurons) working in parallel and organized in layers with a feed-forward information flow. The architecture of the MLP is structured as follows: the signals flow consecutively through the different layers from the input to the output layer. The intermediary layers are known as hidden layers. For each layer, each elementary unit calculates a scalar product

between a vector of weights and the output vector given by the previous layer. A transfer function is then applied to the result to produce an input for the next layer. The commonly used transfer function for the hidden layers is the sigmoid function:

$$f(x) = \frac{1}{1+\exp(-x)}. \tag{5.9}$$

In the output layer, other transfer function can be used; for example, the identity function (simple linear activation) can be used for regression problems. MLPNNs are trained by the error back-propagation (EBP) algorithm, optimized according to a predefined criterion (Bishop, 1995).

A.2. Prediction procedure based on RBF neural networks

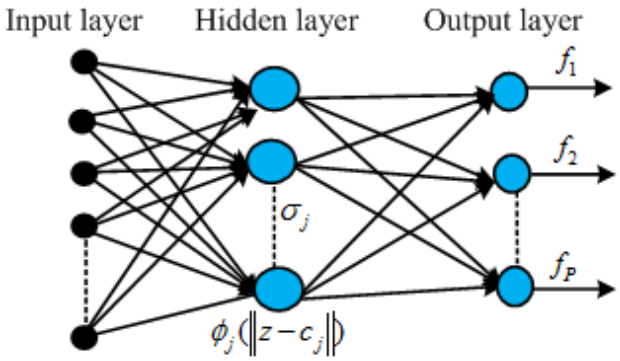

Figure 5.9 – RBF Neural Network topology

RBFNN (Figure 5.9) is composed of three layers (an input, a hidden, and an output layer). Input neurons just propagate input variables z_j to the next layer. Each neuron in the hidden layer is associated with a kernel function φ_j (usually a Gaussian function) characterized by a center c_j and a width σ_j.

$$\varphi_j(\|z-c_j\|) = \exp\left(-\frac{1}{2}\left(\frac{\|z-c_j\|}{\sigma_j}\right)^2\right). \tag{5.10}$$

In this work, for the sake of simplicity, we assume that all kernel functions have the same width ($\sigma_j = \sigma$). The output layer consists of one neuron which is the target to be predicted. The output function is given by:

$$f(z) = \sum_{j=1}^{P} \lambda_j \varphi_j\left(\|z-c_j\|\right). \tag{5.11}$$

where P and λ_j are respectively the number and the weight of the radial functions. For more details about artificial neural networks (RBF and MLP), we refer the reader to (Hornik et al., 1989), (Benoudjit and Verleysen, 2003),(Xie et al., 2011),(Bishop, 1995). We use an online learning rule that makes incremental changes to the parameters of the both neural networks based on the instantaneous value of the cost functional (mean square error (MSE)) achieved on the test set and defined as follows:

$$\mathrm{MSE} = \frac{1}{N_T}\sum_{q=1}^{N_T}\sum_{n=1}^{L}\left(\hat{f}\left(x_q^n\right) - y_q^n\right)^2. \tag{5.12}$$

Where N_T is the number of test samples; L is the number of output, $\hat{f}\left(x_q^n\right)$ is the value predicted by the model and y_q^n is the measured value.

In this work, each bending section of the CBHA is divided into a finite number of inter-vertebrae. However, the measurement of the length of each inter-vertebra increases the implementation cost. Ideally for the case of the CBHA, the measurement of the length of each inter-vertebra requires 48 length sensors for each section, 92 length sensors for the entire CBHA's backbone. An alternative is to fragment, when possible the wire-cable length sensor to provide the length of each parallel platform module. A fragmentation based on the minimum potential energy approximation has been proposed in (Mahl et al., 2014) for the BHA robot. However, the latter is still based on assumptions: disregard of the potential energy due to gravitation, potential energy of the trunk is equal to energy stored in its spring-like bellows actuators, which are not always verified. Referred to CBHA, the length of each inter-vertebra is different due to tapered structure of the CBHA, with tilted position on the mobile platform (Robotino). However, since the length of an inter-vertebra is a fraction of the tube length, the elongation of each inter-vertebra at any time represents a percentage of the total length of the tube. This percentage can be obtained by considering the minimum and the maximum elongations of each inter-vertebra listed in Table 5.1. The first and the fourth rows represent the index of the vertebra. The second and the fifth rows give the minimum elongations, while the third and the sixth give maximum elongations. The percentage distribution of the inter-vertebra's length for the entire CBHA is depicted in Figure 5.10.

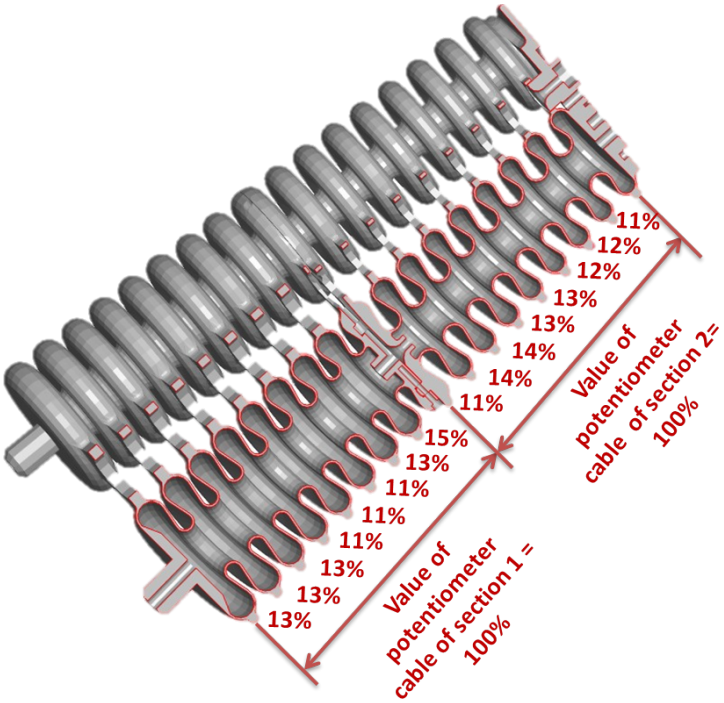

Figure 5.10 – Elongation of the inter-vertebrae during displacements

For FKM modeling, each section of the CBHA is modeled by one NN model of 24-inputs to 24-outputs. The lengths of the inter-vertebrae $(q_{i,1}, q_{i,2}, q_{i,3})$ are considered as inputs, while the variable Z_i, the pitch (θ_i), and the yaw (ψ_i) angles are considered as outputs. $i = 1, 2, ..., 8$ for the first section, and $i = 9, 10, ..., 16$ for the second sections.

As it is listed in Table 5.1, each inter-vertebra length is bounded. These bounds allow fixing the range of the pitch (θ_i) and the yaw (ψ_i) angles. In fact, the variables Z_i, θ_i, and

Table 5.1 – Limit elongation of k^{th} inter-vertebra in millimeter for the case of CBHA

k^{th}	1	2	3	4	5	6	7	8
$q_{\min}$ (mm)	8.5	8.5	8.5	7	7	7	8.5	10
$q_{\max}$ (mm)	19.5	19.5	19.5	16.5	16.5	16.5	20	22
k^{th}	9	10	11	12	13	14	15	16
$q_{\min}$ (mm)	6.5	8	8	7.5	7.5	7	7	6.5
$q_{\max}$ (mm)	16	20.5	20.5	19	19	18	18	16

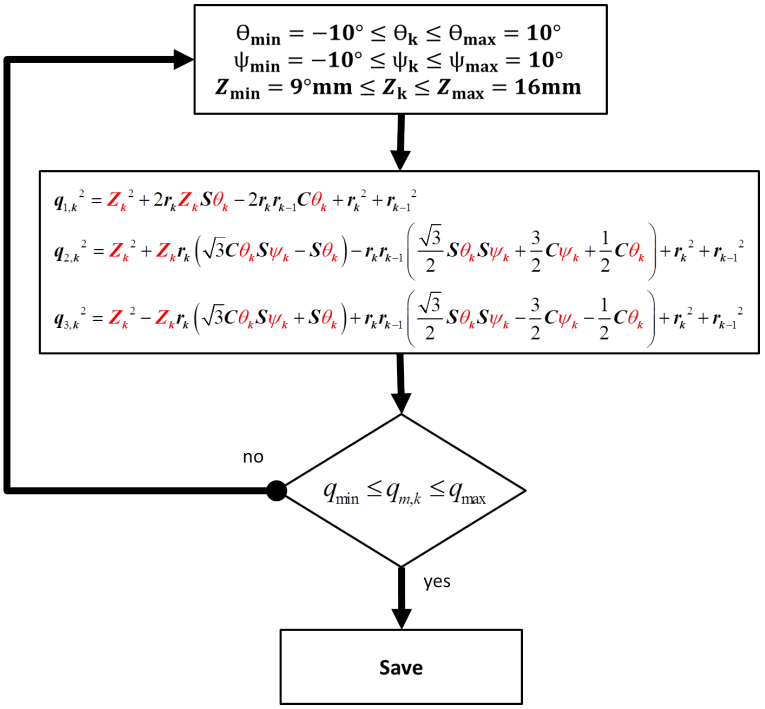

Figure 5.11 – Database of learning generation

ψ_i are initialized with a large range, as shown in Figure 5.11. According to Figure 5.11, the IKEs are computed, and the samples of input-output pairs included in the range of the lengths of the inter-vertebrae $(q_{i,1}, q_{i,2}, q_{i,3})$ are saved. A learning base of 30071 samples is obtained; 11559 samples for the first section and 18512 samples for the second section, respectively. The learning base is divided randomly: 70% for the training set, 15% for the validation set, and 15% for the test set. The training set is used during the learning phase and the test set is only employed to assess the performance of the NN model. The validation set is used during the learning phase.

In order to minimize the MSE calculated in the validation set, the weight matrices are adjusted by means of the back-propagation descent method, including the momentum term. For an optimal generalization of neural network models and to avoid over-fitting, the early-stopping method for training is implemented. The latter requires that after a period of training (epochs) using the training set, the weight matrices of the NN are fixed, and the NN operates in the forward mode using the validation set. The process is repeated until the MSE on the validation set reaches its minimum value. In order to empirically select the best model for each regressors, the value of each parameter was varied in a given predefined range according to a grid search over the learning base. A MLP of two layers is used for each CBHA's section, and it is tested with 2 up to 20 neurons (with a step of 2 neurons) in each hidden layer. The optimal MLP architecture is obtained for an

architecture with 18 neurons in each hidden layer for the two sections by taking the MSE in the validation set as a performance criterion. The assessment of the trained MLP in terms of MSE on the test-samples yields the values reported in Table 5.2.

Table 5.2 – Results achieved by each neural network model on the test samples

Neural networks topologies	Neurons	MSE
MLP, section 1 (2 layers)	18	$6.4612.10^{-5}$
MLP, section 2 (2 layers)	18	$8.2425.10^{-5}$

In the view of the obtained performance, we notice that each NN model approximates the variables Z_i, θ_i, and ψ_i with a good degree of accuracy. In next subsection, the FKM of the entire CBHA is deduced.

B. Deduction of CBHA FKM

Figure 5.12 depicts the different frames used to describe the kinematics of the CBHA:

- The first frame $\{X_{base}, Y_{base}, Z_{base}\}$ is attached to the base of the CBHA robot;
- The second frame $\{X_{s1}, Y_{s1}, Z_{s1}\}$ is attached to the top of the first bending section;
- And the last one $\{X_{s2}, Y_{s2}, Z_{s2}\}$ is attached to the top of the second bending section;

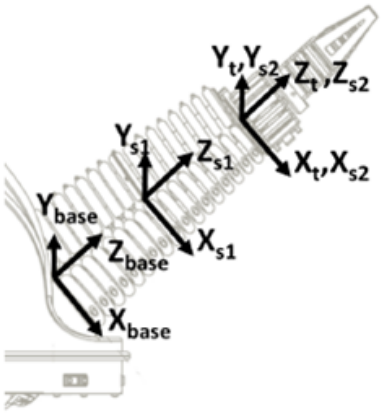

Figure 5.12 – The associated frames of the CBHA

The coordinates of the frames $\{X_{s1}, Y_{s1}, Z_{s1}\}$ and $\{X_t, Y_t, Z_t\}$ are given relative to the base frame $\{X_{base}, Y_{base}, Z_{base}\}$, while those of the frame $\{X_{s2}, Y_{s2}, Z_{s2}\}$ are expressed relative to frame $\{X_{s1}, Y_{s1}, Z_{s1}\}$.

The modeling process of the FKM is summarized in Figure 5.13. The lengths provide by the tube-length's sensors are divided with respect of the percentage distribution of the inter-vertebrae. The elongations $q_{i,j}$ obtained are used as inputs of the NN models. NN1 model provides the predicted pose of the vertebrae of the first section, while those of the second section are provided by NN2 model. The Cartesian coordinate of the tip arm $\{X_t, Y_t, Z_t\}$ is obtained by using the transformation matrices ${}^{i-1}T_i$.

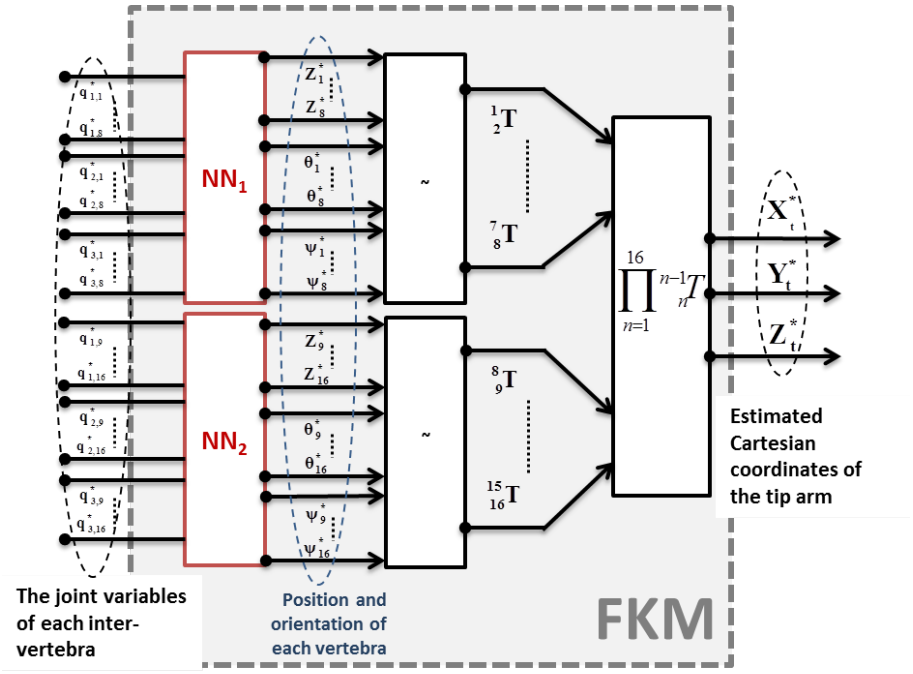

Figure 5.13 – Forward kinematic algorithm

5.3.4 Inverse Kinematic Model of the CBHA

In this section, the IKM of the CBHA is presented. As mentioned above, the entire CBHA is emulated by a series of 16 parallel robots each comprising 3-DoF. Using such modeling, the CBHA can be considered as a 48 DoF manipulator. Numerically, it is sufficient to calculate the IKM of each vertebra system, making the relation between the center of the upper-platform with the joint coordinates of the inter-vertebra. It comes more complicated for deducing the numerical relationship between the top of the CBHA and the 48 joint variables. This problem can be summarized to an optimization problem with implicitly time constraint, because the objective is to solve the modelling problem with sufficient accuracy and reasonable time consuming. This comes to the optimal placement of the different vertebral frames and the calculation of the 48 joint variables. The objective function of the optimization problem can be expressed as:

$$\begin{cases} \min f(q) \\ q_{i,\min} \leq q_{ij} \leq q_{i,\max} \end{cases} \tag{5.13}$$

where $f(q) = \sqrt{\lambda_{\max}(\mathrm{Q}^{\mathrm{T}}\mathrm{Q})}$ with $\lambda_{\max}(\mathrm{Q}^{\mathrm{T}}\mathrm{Q})$ the maximum eigenvalue of $\mathrm{Q}^{\mathrm{T}}\mathrm{Q}$, and Q is the normalization matrix consisting of prismatic variables q_{ij}. This modeling problem was first solved using a Sequential Quadratic Program (SQP) (Lakhal et al., 2014a), but, it required huge computation time. Once more, for real-time implementation requirements, an approximate solution can be considered. The process consist of predicting Z_k, θ_k, and ψ_k from a given TCP position.

In contrast to FKM, four MLPs were used to approximate the IKM of the CBHA. The first one approximates the end-position $\{\mathrm{X}_{s1}, \mathrm{Y}_{s1}, \mathrm{Z}_{s1}\}$ of the first section from the Cartesian coordinates of the CBHA's tip $\{\mathrm{X}_t, \mathrm{Y}_t, \mathrm{Z}_t\}$. The last three models use the position of the arm's tip $\{\mathrm{X}_t, \mathrm{Y}_t, \mathrm{Z}_t\}$ and the end-position of the first section $\{\mathrm{X}_{s1}, \mathrm{Y}_{s1}, \mathrm{Z}_{s1}\}$ as inputs, and provides Z_k, θ_k, and ψ_k as outputs. It should be noted once again that data acquisition from robot is not necessary, because the learning database is obtained from inverse kinematic equations and the validated FKM.

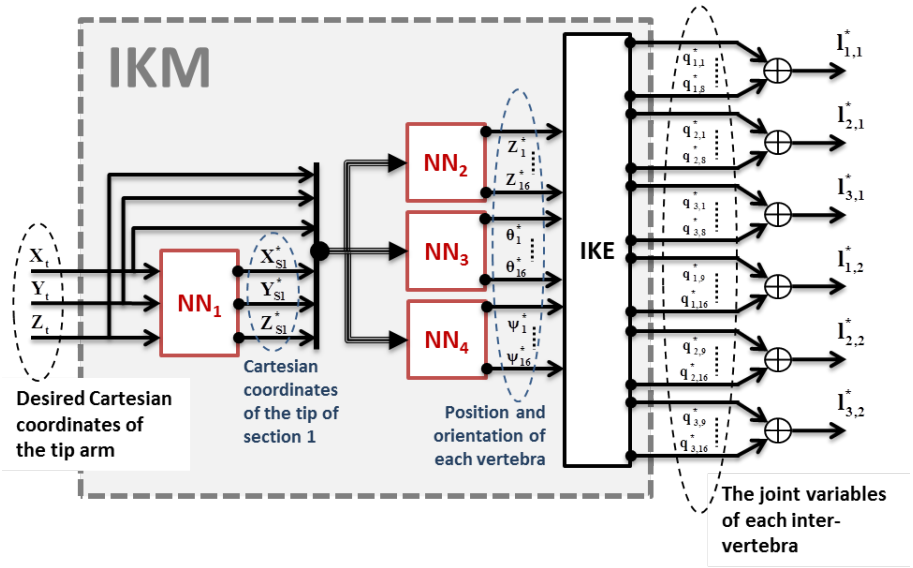

Figure 5.14 – Algorithm for Inverse kinematic modeling

Figure 5.14 summarizes the process of the IKM solving. The same learning base developed for the Forward kinematics is used to derive the inverse kinematics. Table 5.3 shows the results achieved by each neural network model on the test set samples. The performance is less accurate for the end-position of the first section. This is mainly due to CBHA hyper-redundancy, because many solutions of the CBHA's tip are possible for the same end-position of the first section. Nevertheless, the performance achieved remains acceptable. To select a particular inverse kinematics function, a squared penalty term is added to the objective function of the neural network. The cost functional yields:

$$J = \frac{1}{2}(X_d - X)^T (X_d - X) + \lambda \frac{1}{2} \|X\|^2 \tag{5.14}$$

where X and X_d are respectively the predicted and the desired position. $\|.\|$ denotes the Euclidean norm. In (Wu et al., 2006), it has been demonstrated that, if the coefficient λ is larger, X becomes small. The penalty term λ provides a possibility to control efficiency the magnitude of X. This allows selecting a particular inverse solution.

Table 5.3 – Results achieved by each neural network model on the test samples

Neural networks topologies	Neurons	MSE
MLP, NN1 (2 layers)	18	$4.9840.10^{-4}$
MLP, NN2 (2 layers)	12	$1.2363.10^{-5}$
MLP, NN3 (2 layers)	16	$4.0503.10^{-5}$
MLP, NN4 (2 layers)	16	$3.4651.10^{-5}$

The whole MSE listed in Table 5.3 and Table 5.2 are the errors obtained on the test samples. The database has been divided in three sets: training, validation, and test. During the NN training, the matrices are updated using the MSE calculated at the same stage. MSE in validation set is used for stopping the training, and the MSE in the test set is used for assessing the performance of the NN model.

5.4 Validation of CBHA kinematics

This section focuses on the validation of the developed kinematic models. Regarding the comparative study, performances of modeling approaches vary from one robot to another (Rolf and Steil, 2012b; Escande et al., 2014; Braganza et al., 2007; Giorelli et al., 2013; Jones and Walker, 2006b). They depend on the structure of the continuum manipulator, the state of its actuators, and its geometry (sizes, shape). Hence, a direct comparison of these approaches can be done, if and only if the latter can be implemented on the same manipulator. This chapter discusses only recent contributions done on the CBHA and the BHA manipulators. The structure is almost the same, the difference being that the CBHA possesses two sections, while the BHA has three sections. In this section, the optical 3-D stereo-vision system is first presented for the real-time trajectory tracking. The validations of the FKM and IKM are presented thereafter. The section ends with a discussion.

5.4.1 Generation of trajectories

Trajectories are generated using a motion capture system called OptiTrack [1]. It consists of a set of 4 infrared cameras able to track in 3D a cloud of points in the defined workspace (Figure 5.15a). The reflective markers are placed to each tracked point as showed in (Figure 5.15b). After calibration phase, the OptiTrack system provides the positions and orientations of the robot base and the different bodies with a precision of $0.3mm$. In our case 6 bodies were created, as shown in Figure 5.15c. The latter will allow generating of the CBHA's posture during its movement. The trajectory generated by the end of the second section is considered as the desired trajectory. The tracking information are recorded in real-time in Matlab environment via a NatNet SDK server

[1] http://optitrack.com/

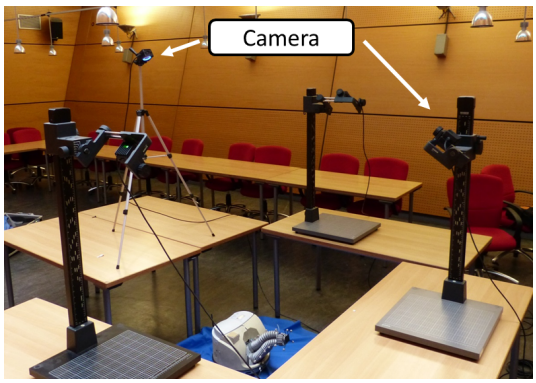

(a) Cameras

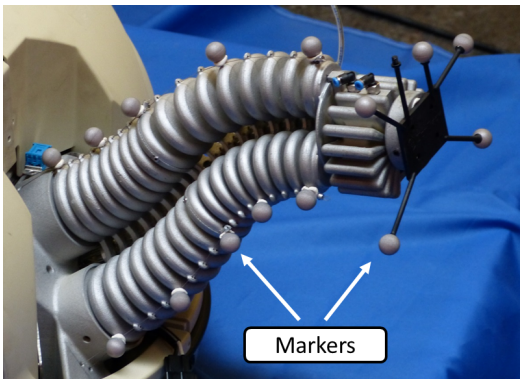

(b) Reflective markers

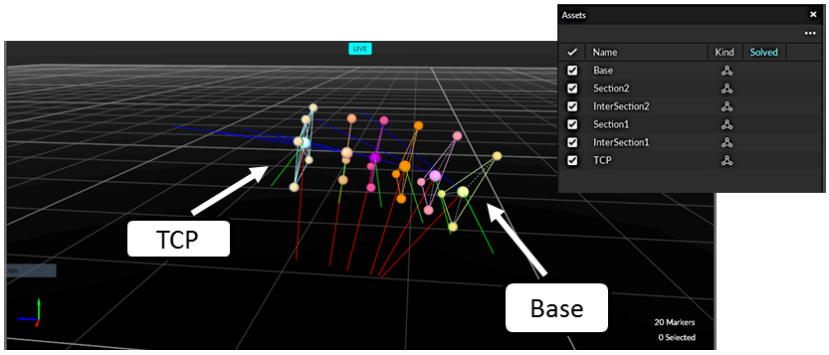

(c) Software

Figure 5.15 – Stereo-vision system for generation of trajectories

5.4.2 Validation of the forward kinematic model of the CBHA

The forward kinematics of the CBHA are validated by following the experimental setup presented in figure 5.16. The desired posture of the CBHA is generated by applying a set of the desired pressures to CBHA's tubes. During the trunk displacements, the values provided by the length sensors are used as inputs to the FKM. The predicted positions are compared to those provided by the stereo-vision system.

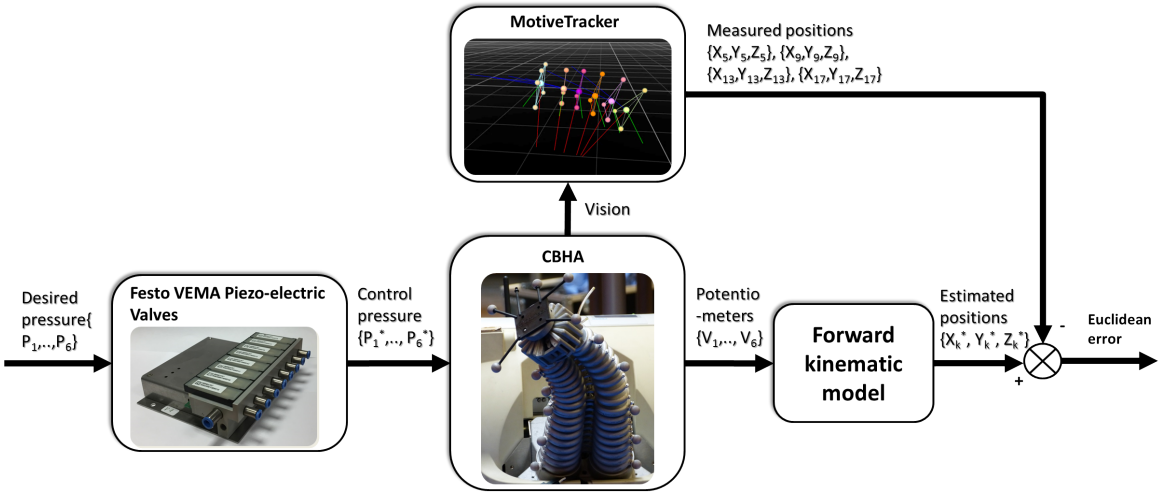

Figure 5.16 – Architecture of the FKM validation

The results of the FKM validation are represented in Figure 5.17. The trajectories generated by the FKM and the stereo-vision system are depicted in Figure 5.17a. The associ-

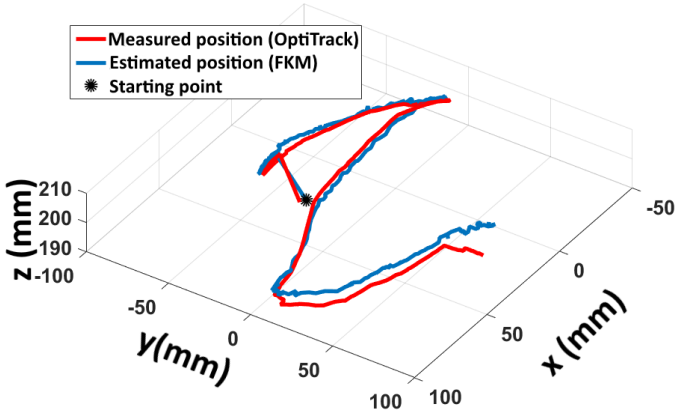

(a) Trajectories generated by the proposed FKM and the stereo vision system

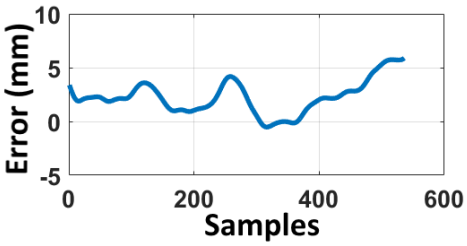

(b) Cartesian errors in X axis

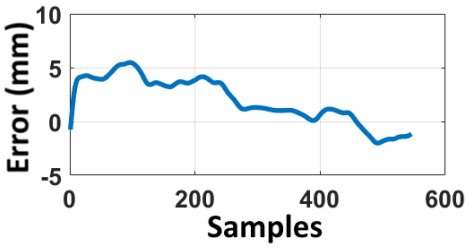

(c) Cartesian errors in Y axis

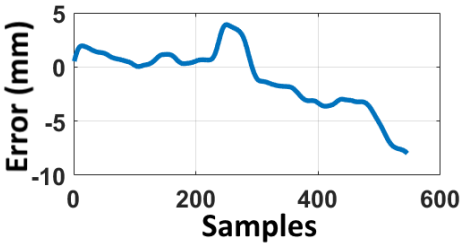

(d) Cartesian errors in Z axis

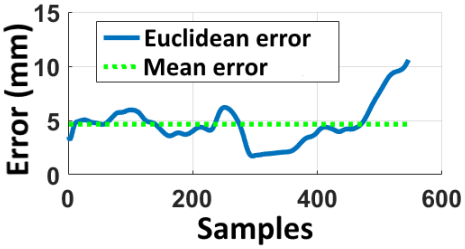

(e) Average Cartesian errors

Figure 5.17 – Cartesian errors

ated Euclidean errors are represented in Figure 5.17b, 5.17c, and 5.17d.

The validation of the proposed FKM has also been done by considering the entire CBHA's workspace. Figure 5.18 shows the superposition of both workspaces, i.e. the workspace obtained by the tracking vision system and that obtained by the proposed FKM. The associated Cartesian errors are depicted in Figure 5.19. We note some slight differences between the predicted and desired workspace when the camera is attached to the robot end-effector.

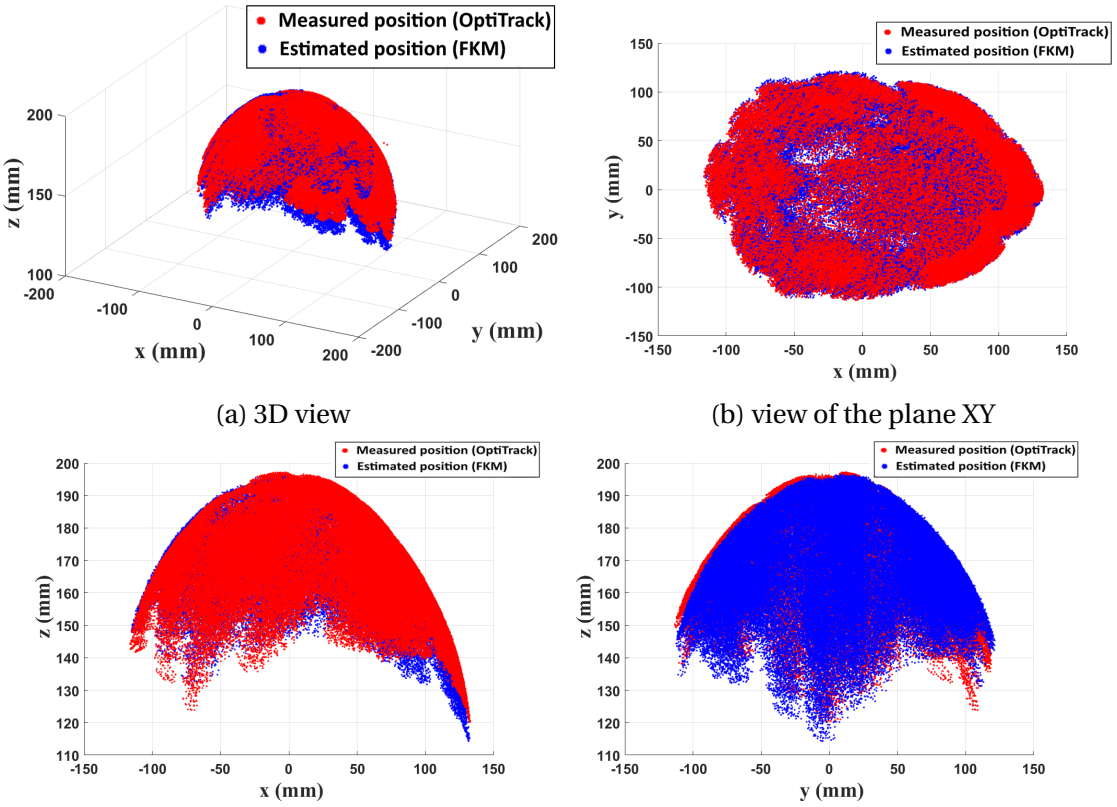

(a) 3D view

(b) view of the plane XY

(c) view of the plane XZ

(d) view of the plane YZ

Figure 5.18 – Several points of view of the experimental work space of the CBHA without load

Refer to Euclidean Cartesian errors obtained, it can be concluded that the proposed FKM is able to predict the CBHA's tip pose with positioning errors of less than 6mm. One of the main advantage of the proposed approach, and which is very useful in scanning operations, is the possibility of predicting the entire CBHA's posture in real-time. Indeed, since the FKM of the CBHA is derived from the IKEs of a single inter-vertebra, it is possible to predict the displacements of the latter in real-time. Figure 5.22 depicts a comparison between the posture obtained by using the proposed FKM and that generated by Optitrack system. Figures 5.23, 5.24, 5.25, and 5.26, give the trajectories achieved by vertebrae 5, 9, 13, and 17, respectively.

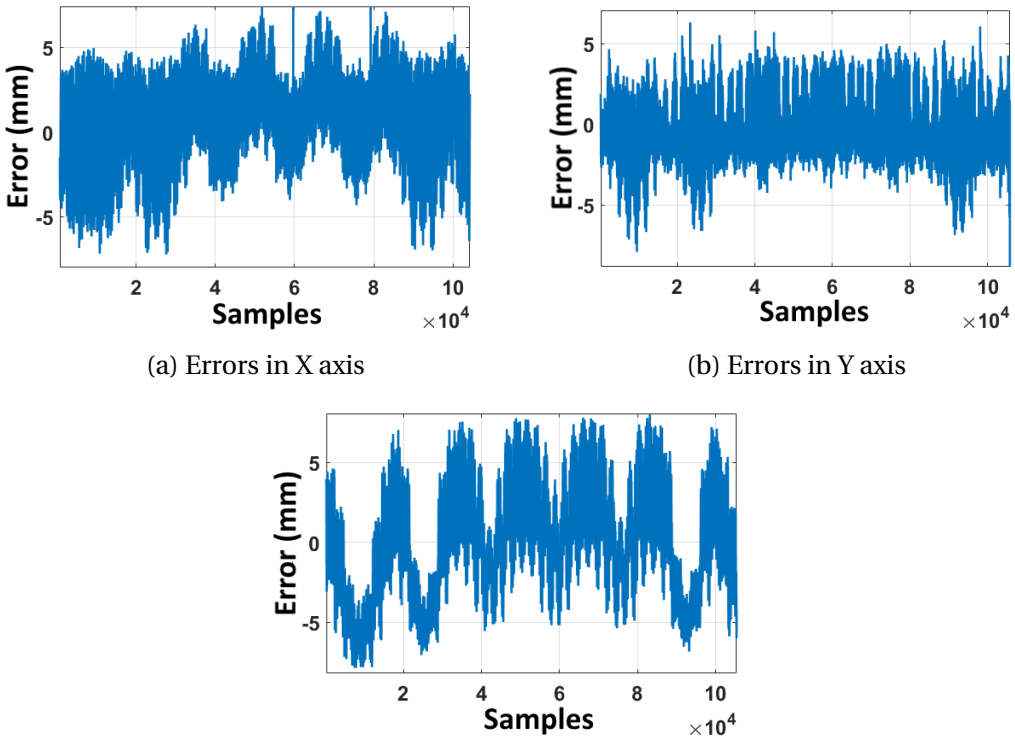

(a) Errors in X axis

(b) Errors in Y axis

(c) Errors in Y axis

Figure 5.19 – Positioning error along the CBHA workspace without load

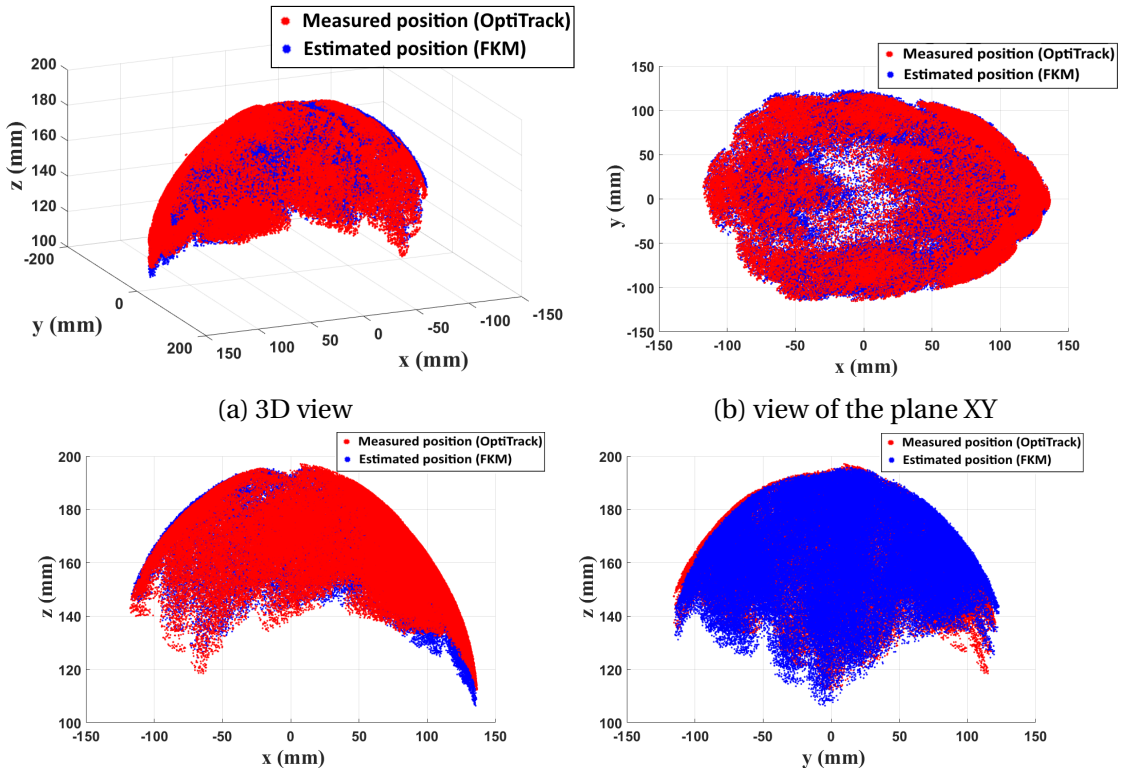

(a) 3D view

(b) view of the plane XY

(c) view of the plane XZ

(d) view of the plane YZ

Figure 5.20 – Several points of view of the experimental work space of the CBHA with camera

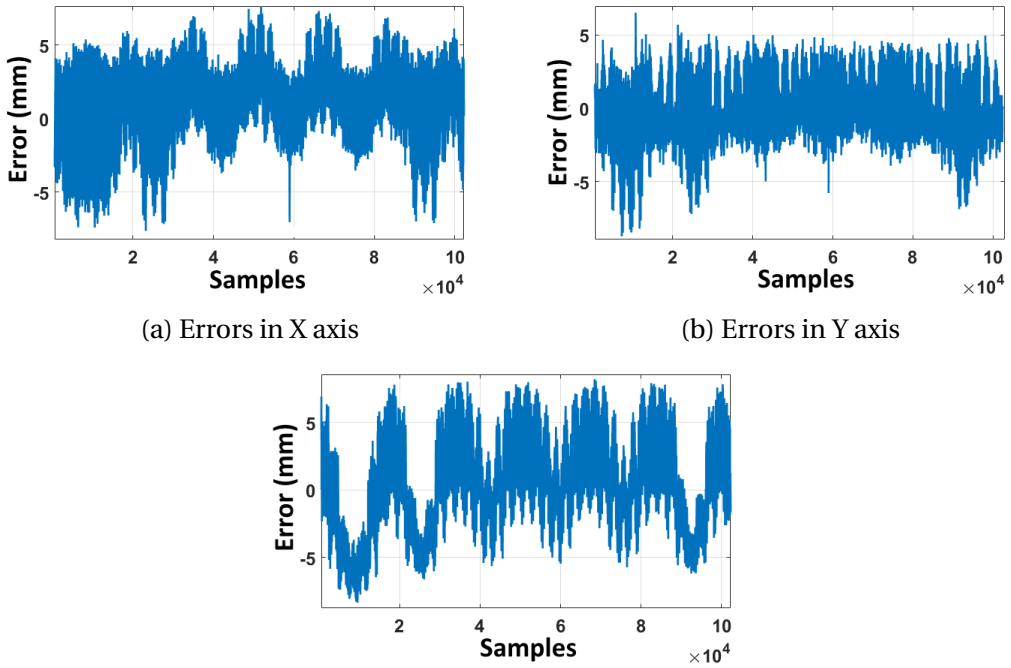

(a) Errors in X axis

(b) Errors in Y axis

(c) Errors in Z axis

Figure 5.21 – Positioning error along the CBHA workspace with camera

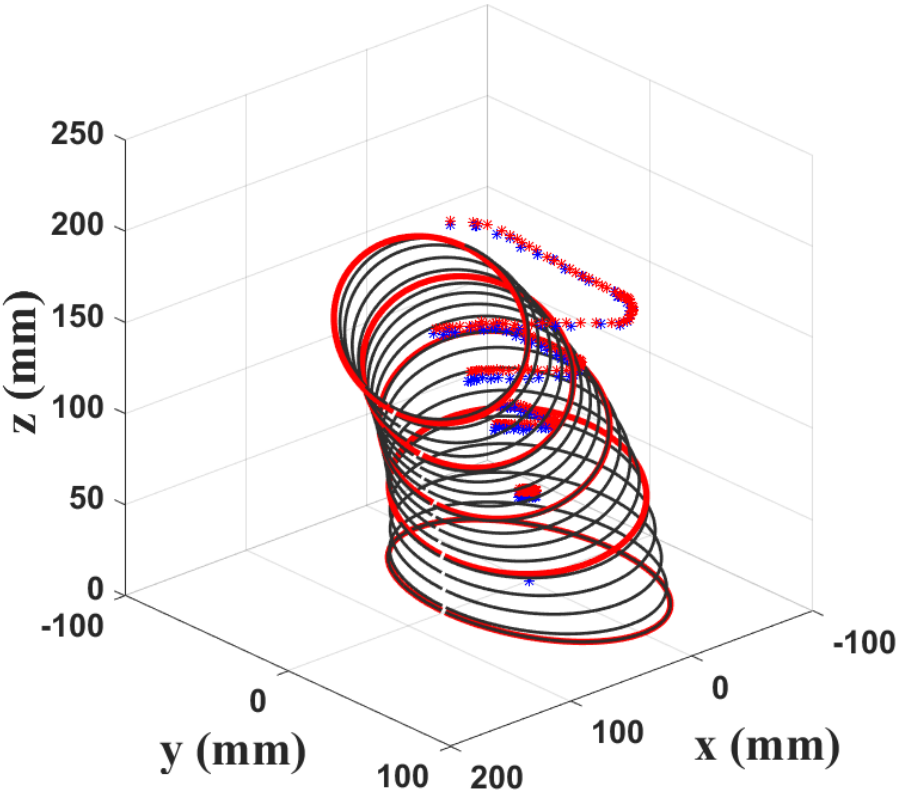

Figure 5.22 – Comparison of measured and estimated postures

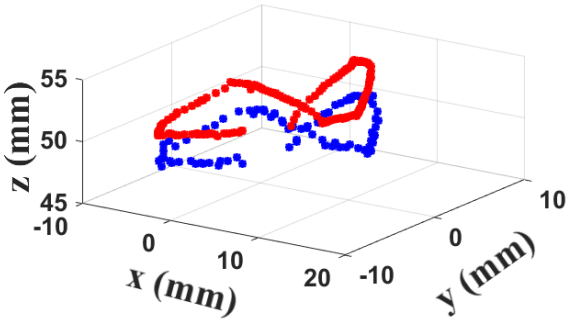

(a) 3D view

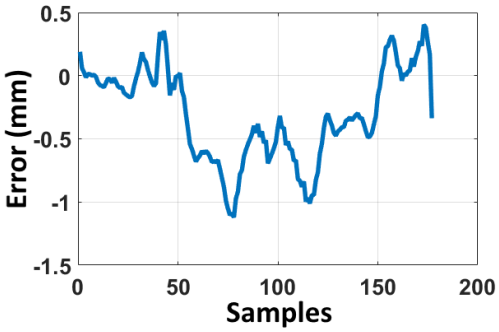

(b) Euclidean Cartesian errors in X axis

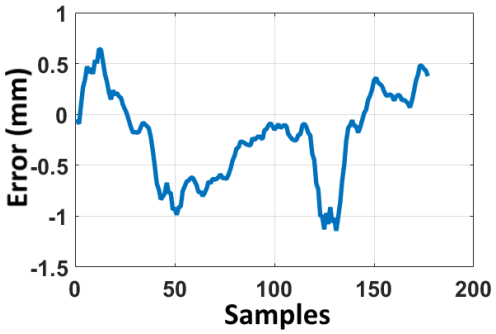

(c) Euclidean Cartesian errors in Y axis

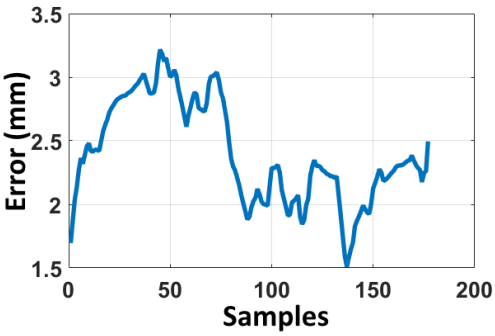

(d) Euclidean Cartesian errors in Z axis

Figure 5.23 – Trajectory achieved by the 5^{th} vertebra

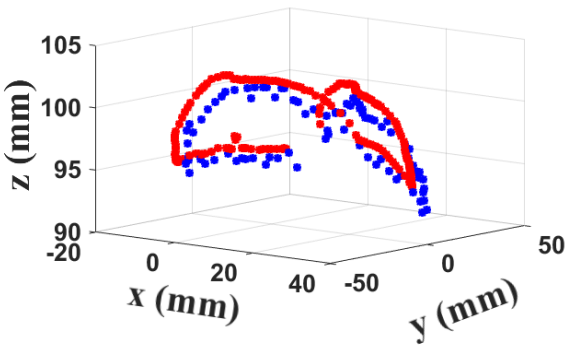

(a) 3D view

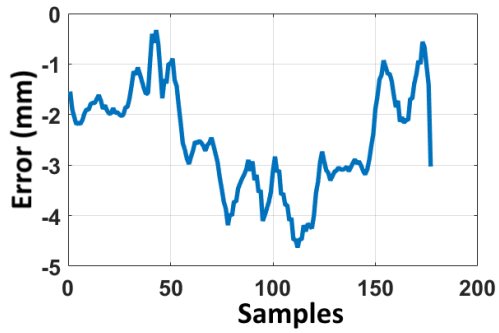

(b) Euclidean Cartesian errors in X axis

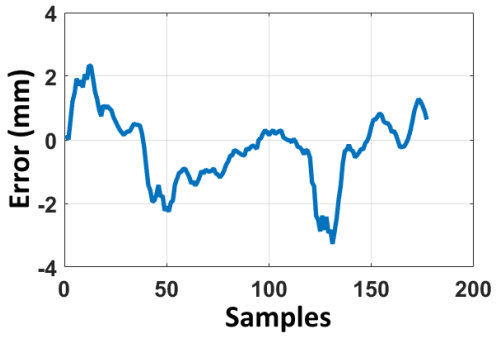

(c) Euclidean Cartesian errors in Y axis

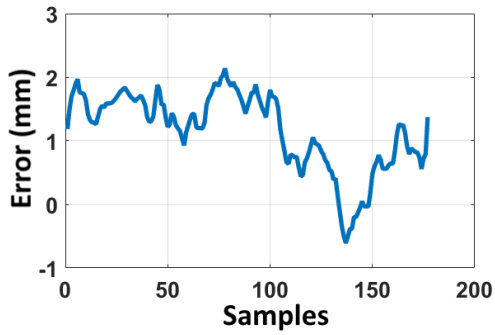

(d) Euclidean Cartesian errors in Z axis

Figure 5.24 – Trajectory achieved by the 9^{th} vertebra

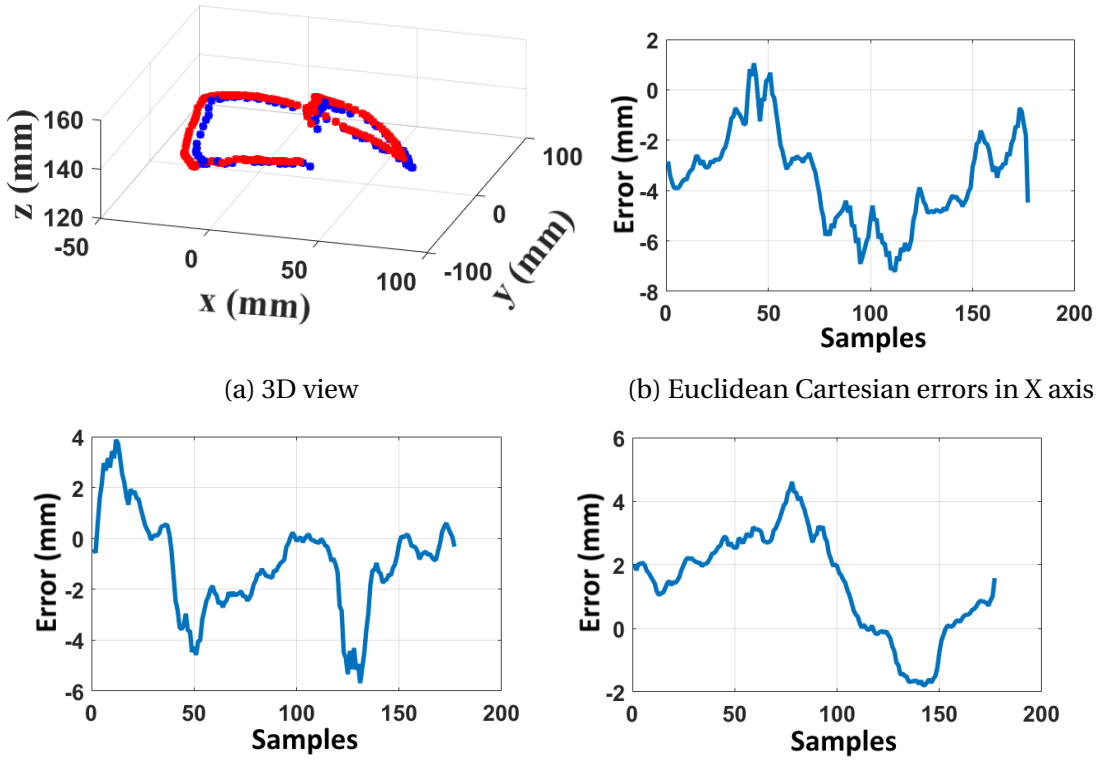

(a) 3D view

(b) Euclidean Cartesian errors in X axis

(c) Euclidean Cartesian errors in Y axis

(d) Euclidean Cartesian errors in X axis

Figure 5.25 – Trajectory achieved by the 13^{th} vertebra

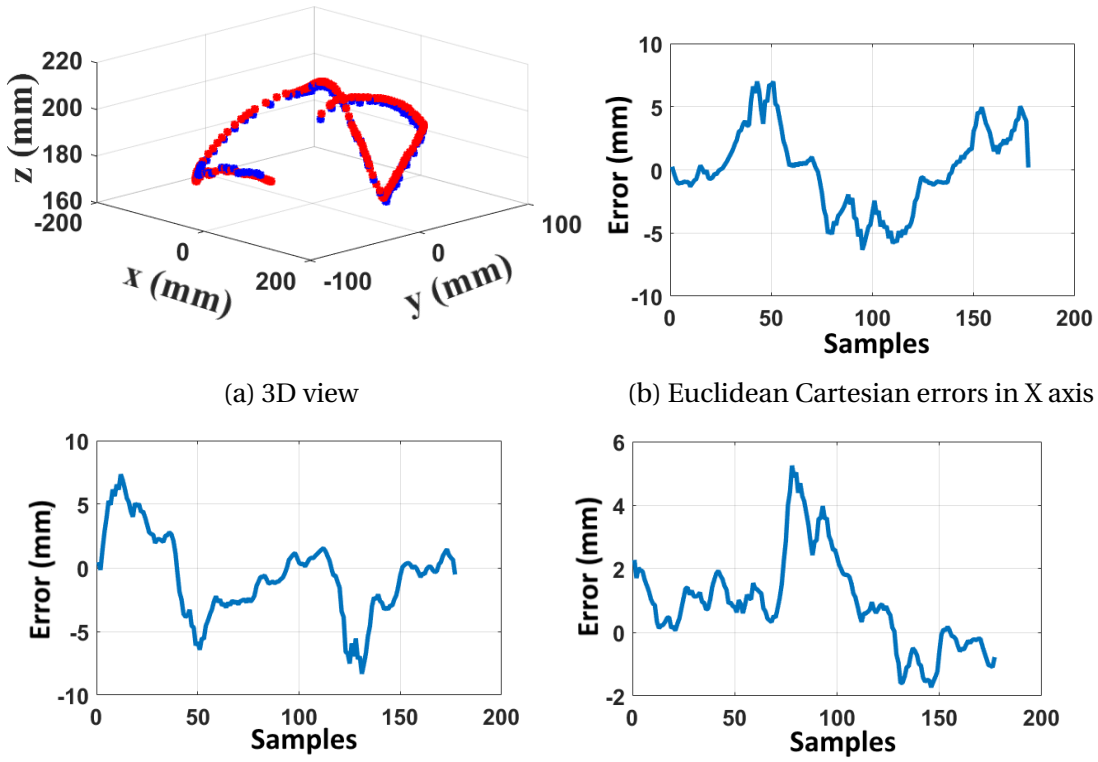

(a) 3D view

(b) Euclidean Cartesian errors in X axis

(c) Euclidean Cartesian errors in Y axis

(d) Euclidean Cartesian errors in Z axis

Figure 5.26 – Trajectory achieved by the 17^{th} vertebra

5.4.3 Validation of the Inverse Kinematic Model

The validation of the inverse CBHA's kinematics is proceeded as shown on Figure 5.27. The desired posture of the CBHA is generated by applying a set of the desired pressures to CBHA's tubes. The desired positions of CBHA's tip is applied to IKM, and the predicted lengths generated by the IKM are used as input to length-pressure converter, approximated by a MLPNN (Table 5.4).

Table 5.4 – Results achieved by each neural network model on the test samples

Neural networks topologies	Neurons	MSE
MLP (2 layers)	16	$6.4712.10^{-4}$

The pressures generated by the length-pressure converter are applied to CBHA robot by mean of the internal PID controllers. The position predicted by the Optitrack system is compared with the desired positions.

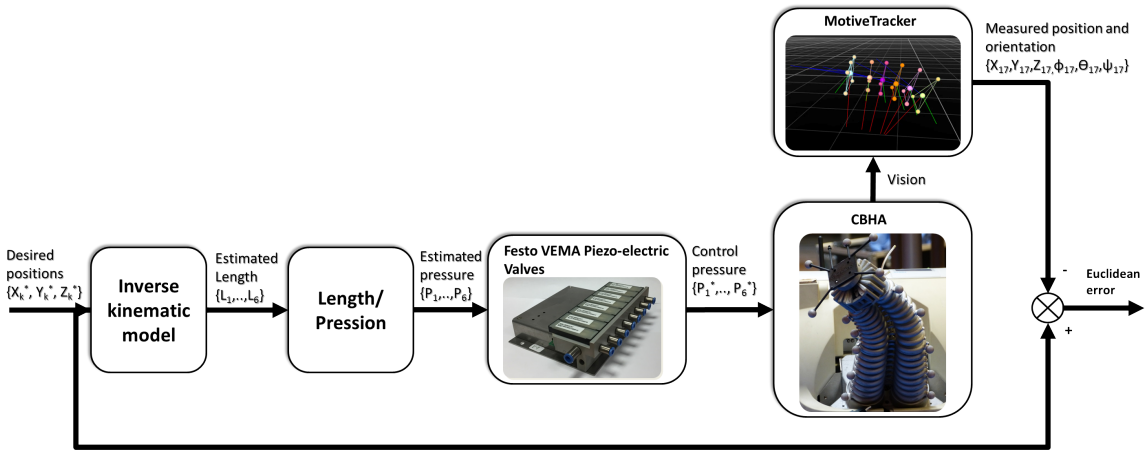

Figure 5.27 – Architecture of the inverse kinematic model validation

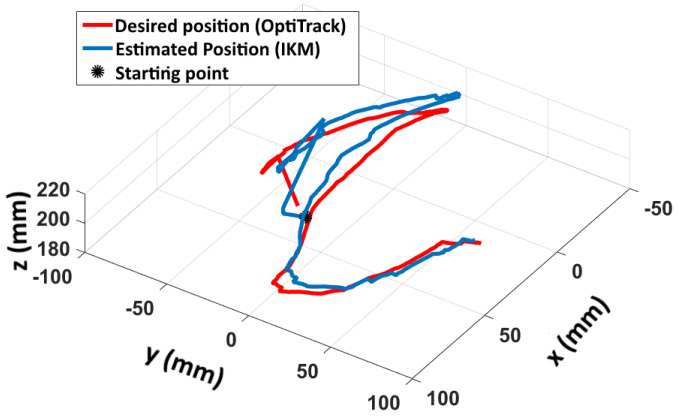

(a) Generated trajectories

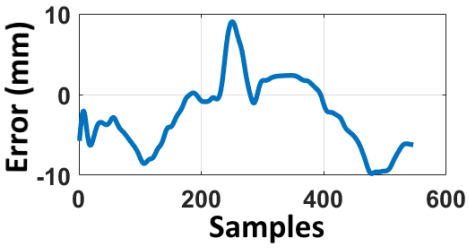

(b) Euclidean Cartesian errors in X axis

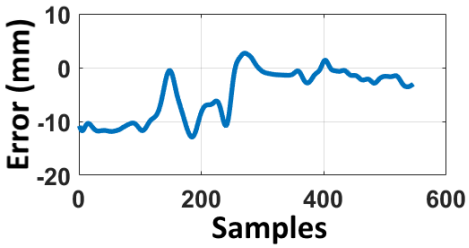

(c) Euclidean Cartesian errors in Y axis

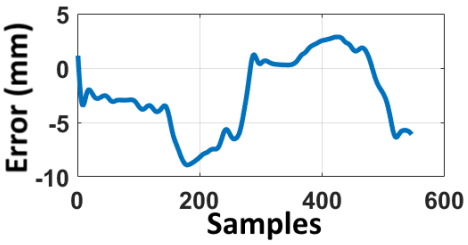

(d) Euclidean Cartesian errors in Z axis

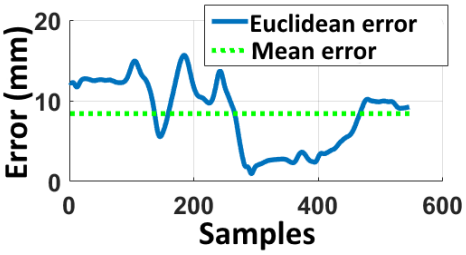

(e) Average of Euclidean Cartesian errors

Figure 5.28 – Scénario 1 : IKM Validation

Figure 5.29 highlights the flow-works adopted to validate the relationship between the tube's lengths and pressures. It is important to note that the developed NN does not take into account the dynamics of the electric valves. This can explain in parts the differences between desired, controlled and estimated pressure as indicated Figure 5.30.

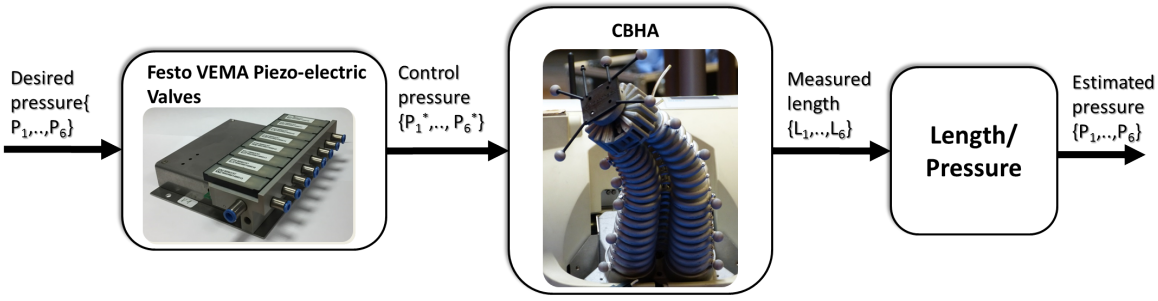

Figure 5.29 – Validation Architecture of lengths-pressures converter block

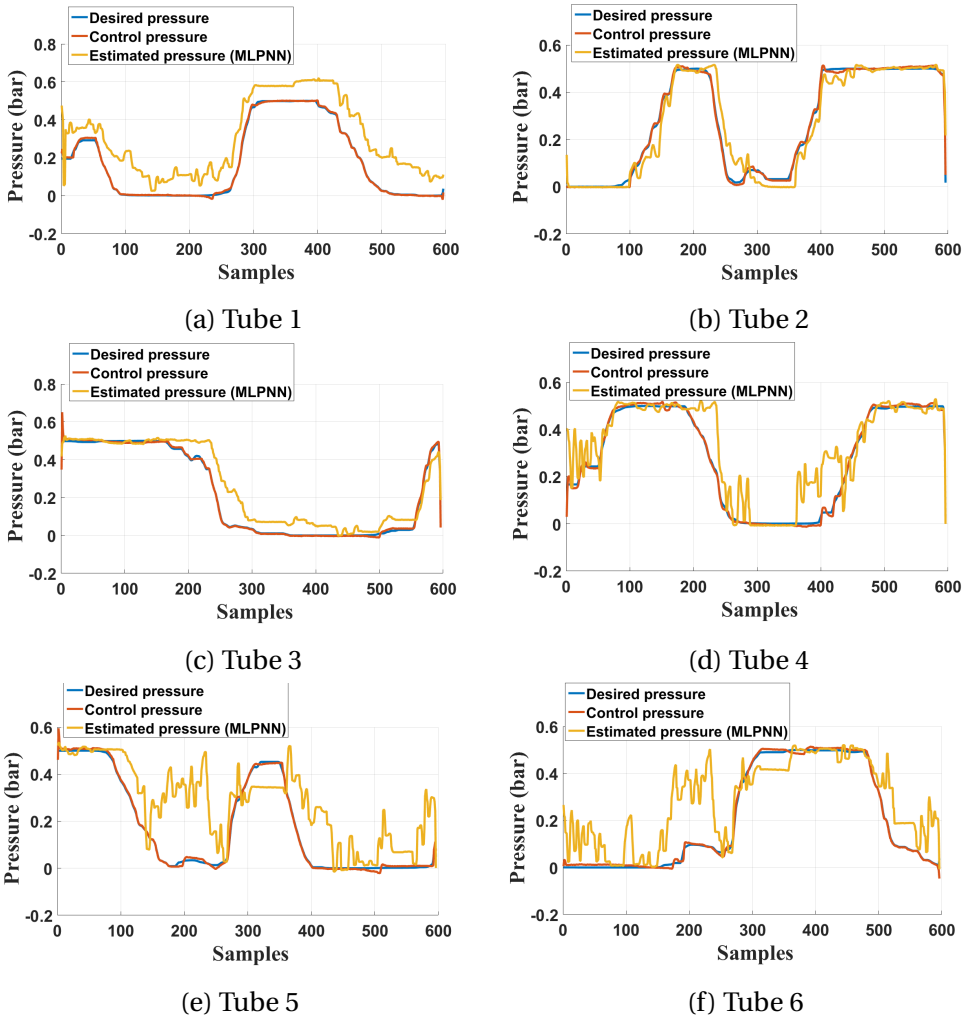

(a) Tube 1 (b) Tube 2

(c) Tube 3 (d) Tube 4

(e) Tube 5 (f) Tube 6

Figure 5.30 – Comparison between the desired pressures and the predicted pressures

In the view of the results obtained, the proposed kinematic models achieve good performance. The proposed FKM is able to predict the CBHA's tip pose with positioning errors of less than 8mm, which represents 2.2% of the total length of the CBHA. The IKM predicts the CBHA's lengths which lead to the tip pose with positioning errors of less than 11mm, which represents 3% of the total length of the CBHA. The CBHA includes memory effects and non-stationary behaviors due to trunk's materials (polyamide). When the CBHA's trunk spends long time in bending-posture, it does not return to its initial posture when it is released. These non-stationary behaviors appear mainly in high CBHA dynamics, and cannot be coped by a simple kinematic controller (Melingui et al., 2014b). In fact the CBHA system embeds six internal PID controllers allowing the control of the pressure in each tube (Figure 5.29). The length-pressure controller has been developed in previous works (Melingui et al., 2015). Remaining models' errors are expected to result from torsional effects and hysteresis effects of the actuators which have been neglected in modeling process. Table 5.5 lists recent contributions in kinematic modeling of continuum robots. We notice that in the case of the CBHA modeling and real-time implementation, learning-based methods achieve good performance, while quantitative methods are less accurate. This lack of performance should result from modeling assumptions inherent in quantitative approaches. The proposed hybrid approach is intermediary to previous approaches, and shows average performance.

Table 5.5 – Recent contributions on the kinematic modeling of the CBHA and BHA Robots

Robots	Characteristics	Modeling method	Kinematic modeling
CBHA	Continuous Shape, Structure: Soft, 2 sections, 3 tubes per section, Pneumatic actuation, 17 vertebras, 3 DoF per inter-vertebra, Length: 0.5m	Hybrid Approach: Geometry and Neural Network, porposed approach	FKM, accuracy: 8 mm; IKM, accuracy: 11 mm; Validation: Simulation and real-time experiments.
		Quantitative: Geometrical based approach Escande et al.(Escande et al., 2014)	FKM, accuracy: 8 mm; Validation: Simulation and real-time experiments.
		Qualitative: Neural Network Melingui et al.(Melingui et al., 2014a)	FKM, accuracy: 4 mm; IKM, accuracy: 5 mm; Validation: Simulation and real-time experiments.
BHA	Continuous Shape, Structure: Soft, 3 sections, 3 tubes per section, Pneumatic actuation, 30 vertebrae, 3 DoF per inter-vertebra, Length: 1m	Quantitative: Geometrical based approach, Mahl et al.(Mahl et al., 2014)	FKM, accuracy: 20mm; IKM, accuracy: 50 mm; Validation: Simulation and real-time experiments.
		Qualitative: Goal babbling learning, Rolf et al.(Rolf and Steil, 2012b)	FKM, accuracy: 5 mm; IKM, accuracy: 6 mm; Validation: Simulation and real-time experiments.

5.5 Quality Inspection : Experiments and Results

The control of the MATRICE's robot takes place in two stages, namely an off-line and on-line step. The off-line step calculates the trajectories of the configuration vector from the desired trajectory of the TCP. For real time constraints and in order to improve the tracking accuracy, the desired TCP trajectory is divided into two trajectories. The first trajectory tracked by the mobile manipulator makes it possible to approach the effector of the structure to be scanned. The second trajectory tracked by the CBHA manipulator allows scanning of the structure. The goal is to exploit the KUKA manipulator's precise tracking capability to compensate for CBHA faults. This section first presents the generation of the configuration vector trajectories and the online control step; the localization of the mobile platform and the camera position follow thereafter, and ends with a the discussions.

5.5.1 Generation of joint-space trajectories: off-line step

In this work, the desired trajectory is generated from slicing data used during printing phase. Indeed, from the Cartesian coordinates of one slice, it is possible to generate the desired TCP trajectory. This trajectory is moved so as to have a large field of view of the camera allowing the scanning of the inner surface of the object, as shows in Figure 5.32.

The intermediate trajectory corresponding to the positioning of the frame {9} relative to the frame {0} is set not only to place the camera as close as possible to the scanning structure, Figure 5.34; but also so that the desired TCP trajectory is inside the CBHA's workspace, (Figure 5.33). Therefore, the placement of the frame for each point of the intermediate trajectory is based on an approach based on the placement of Bishop frames (Karacan and Bükcü, 2010), in order to avoid the appearance of twists. The Bishop frame vectors are generated on a spatial curve using the algorithm proposed in (Hanson and Ma, 1995). The placement of the frame allows knowing the position and orientation of the CBHA's base.

During the scanning process, it necessary to avoid all possible collisions with obstacles. Since the optimization approach only selects one inverse kinematic solution among

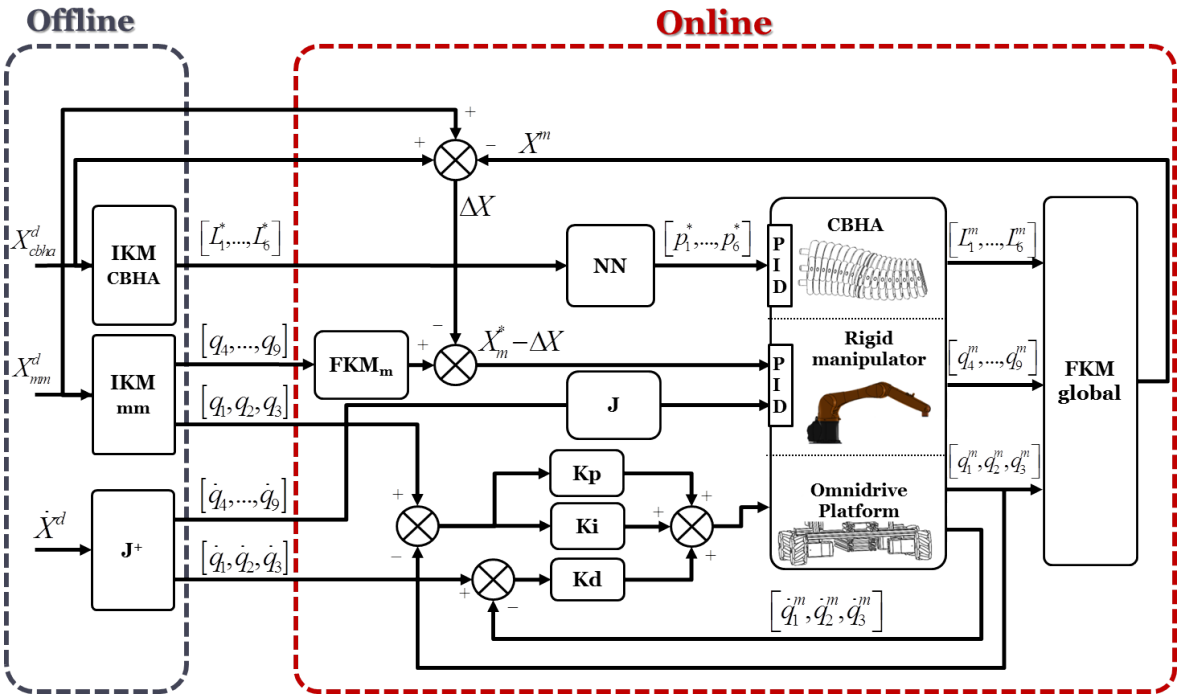

Figure 5.31 – Kinematic control scheme

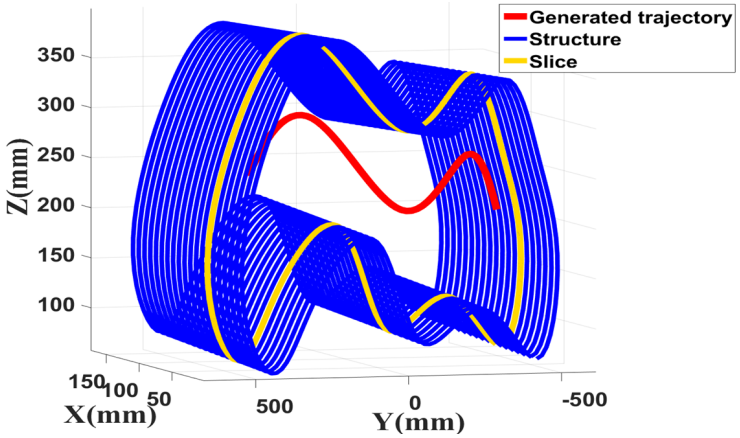

Figure 5.32 – Trajectory generation

the redundancies manifolds, the obstacle avoidance is performed offline through a series of simulation tests. Indeed, during simulation tests, the trajectory generated by the end-effector of the CBHA and the corresponding CBHA's shapes are displayed, Figure 5.35, and Configurations leading to a collision with the structure are eliminated for the benefit of others.

5.5.2 Control of the hyper-redundant robot: on-line step

The control architecture is depicted in Figure 5.31. It consists of an offline and online part. The offline part provides the desired configuration vector trajectories, namely the joint variable trajectories of the mobile manipulator by IKM_{mm} and pseudo-inverse J^+, and the elongation vector trajectories of the CBHA by IKM_{cbha}. The desired elongations of the CBHA are converted to pressures by NN. The control signals feed the omnidrive platform, the manipulator rigid and the CBHA simultaneously. The rigid manipulator and

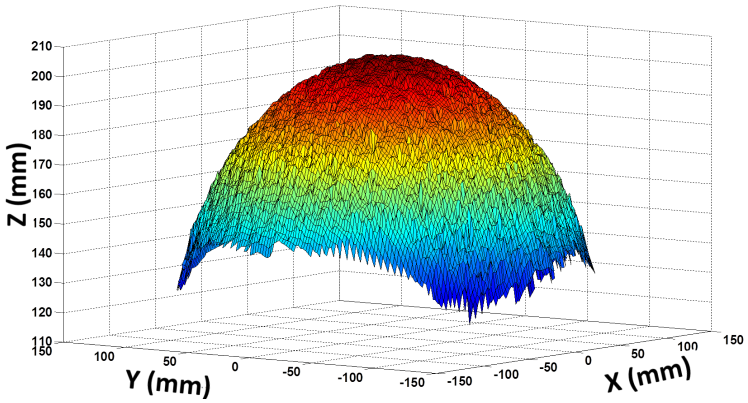

Figure 5.33 – CBHA's Workspace

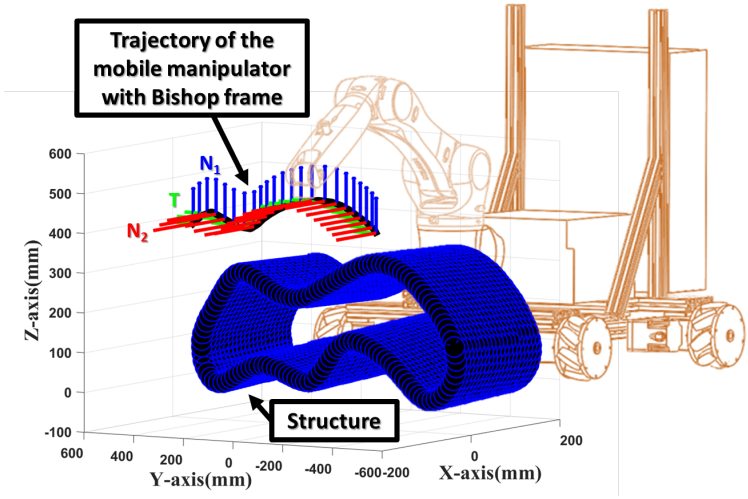

Figure 5.34 – Path of the mobile-manipulator

the electro-pneumatic for the CBHA have their specific PID controller. However, a PID controller has been established to track the desired trajectory of the omnidrive platform. The output provided by the FKM_{global} bloc is compared with the desired TCP trajectory. The IKM_m of the rigid manipulator is then used to reduce the Cartesian errors.

5.5.3 Localization of the mobile wheeled robot

The tracking of the desired trajectory requires a precise localization of the mobile platform. In order to achieve good performance, the manipulator arm has to be synchronized with the displacements of the mobile platform. An ultrasound localization system (Černohorskỳ et al., 2017) provides the [X,Y] position of the mobile robot Figure 5.36, and a low cost Inertial Measurement Unit computes the attitude, the acceleration, and the rotation velocities of the robot. Four ultrasounds beacons were placed around the mobile sensor. Five beacons communicate with each other through a 433 MHz radio link and the computation of the position is done on a central modem. The localization system figures out a Z coordinates but it is not sufficiently reliable to be used for our case study. We can conclude that the accuracy of the localization system is approximately $\pm 2cm$. This drift can be explained by the sliding of Swedish wheels during the moving of the mobile platform.

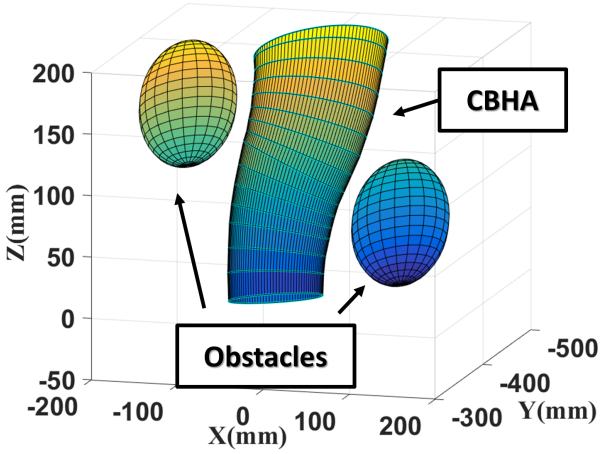

Figure 5.35 – Postures of the CBHA

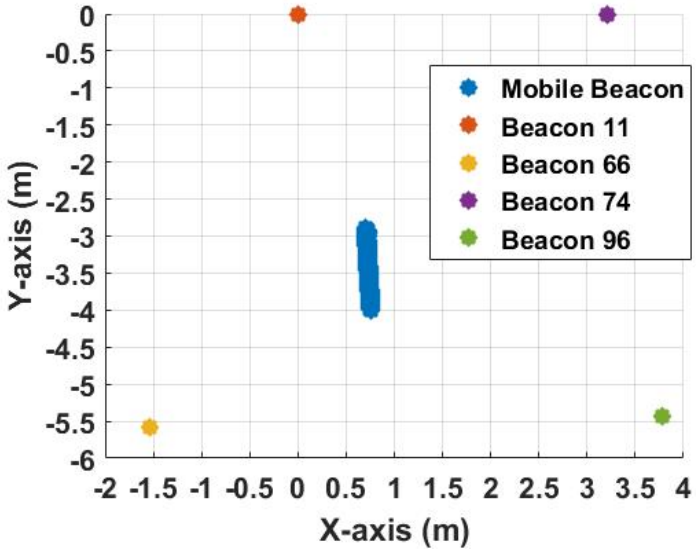

Figure 5.36 – Robot position during the quality inspection step with display of 4 beacons

5.5.4 Camera position

The obtained and desired trajectories from the robot sensors are represented in Fig 5.37a. We observe that the end-effector of the CBHA tracks the desired trajectory. Euclidean errors of the TCP with respect to the target are given in Fig 5.37b, 5.37c, and 5.37d. The range of the Euclidean error is approximately of $[-80\ 20]mm$. The different configurations of the camera during the tracking process are depicted in Fig. 5.38.

5.5.5 Discussions

In view of the results obtained, the proposed kinematic controller achieves suited performances in terms of tracking trajectories in the area of the construction. The 3D visualization of the CBHA posture makes it possible to assess the quality of the inverse obtained solution, in particular as regards the avoidance of obstacles. The TCP positioning error is less than $20mm$, which is reasonable for scanning operations. The purpose of this work was to enable rapid scanning and segmentation of the complex geometry of printed objects with additive manufacturing technique. Euclidean errors can be explained by the

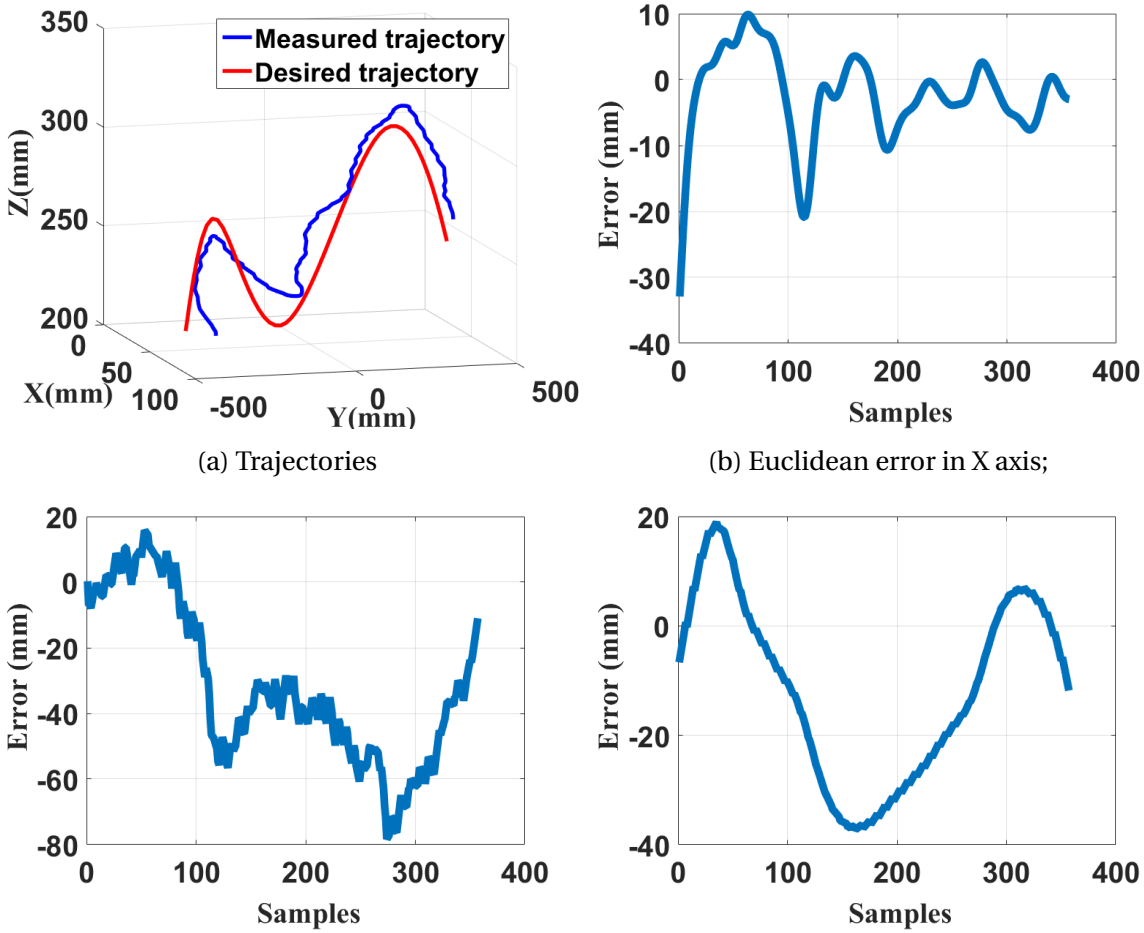

(a) Trajectories

(b) Euclidean error in X axis;

(c) Euclidean error in Y axis;

(d) Euclidean error in Z axis;

Figure 5.37 – Trajectory tracking by the hyper-redundant robot

drift of Swedish wheels during the displacement of the mobile platform. Remaining small Cartesian errors are expected to result from the memory effects and non-stationary behaviors of the soft-continuum manipulator (CBHA).

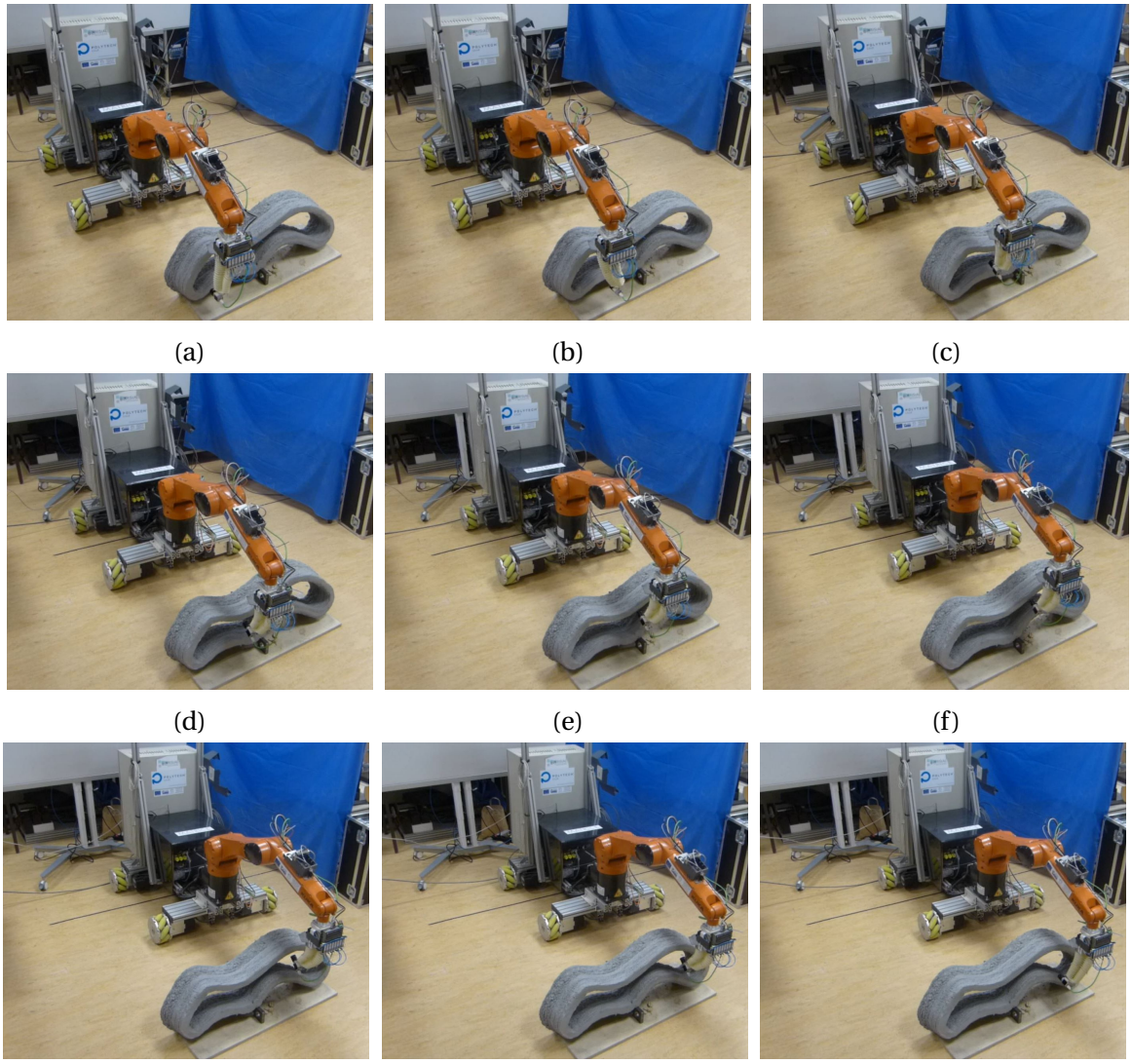

(a) (b) (c)

(d) (e) (f)

(g) (h) (i)

Figure 5.38 – Camera positions during scanning

5.6 Conclusions

In this chapter, a control strategy is developed for trajectory tracking of a hyper redundant robot for quality inspection in additive manufacturing process for construction. This robotic platform consists of a holonomous mobile platform, an industrial rigid manipulator, and a soft-continuum arm. The latter was considered for handling a camera for external scanning of complex printing objects. The proposed kinematic controller was derived from the kinematic equations of the robotic platform. For solving, the latter was performed by means of a quadratic program. The real-time experiments were conducted and the results obtained were satisfactory according to the specifications and requirements of scanning operations in Construction area. In future work, the orientation of the camera may be considered for control purpose, and the CBHA's shape may be integrated in control architecture for real-time obstacle avoidance. The attached camera may be utilized to improve the tracking performance.

Chapter 6

General Conclusion and prospectives

This thesis work is part of a pre-maturation research project in the field of construction robotics. From contractual development side, the thesis results have shown the design of robotized additive manufacturing system, characterized by its mobility and rigid manipulation for the nozzle, inside the workspace of huge complex shapes, in the construction field. An omnidrive mobile-manipulator robot has been developed to automatize the additive printing of funicular geometrical objects, characterized by the difference between the shapes of "intrados" and "extrados" sides. The robot is controlled to print wide and planar dimensions of shapes, as well as their complex geometry, designed by experts (architects).

Mobile platforms in construction are used generally to facilitate the transport to the construction site. It is not the case for the MATRICE's robot, which aims to automatize as much as possible the construction process by using the mobile basis during the printing. Based on the technological positioning, a choice of a 400 kg weight omnidrive mobile-manipulator has been considered. This is to be able to use less weighted and easy transportable equipment, dedicated to both in-door or out-door additive manufacturing in the construction field. In fact, this robot is kinematically redundant (9-DoF), used for the automation of the additive deposit of cement and clay materials to construct complex shapes. The automation of the robotic process has been adapted to different drying time according to the used material and external conditions of temperature and humidity. Moreover, the maneuverability of the robot makes it capable to print large-size of 3D objects, with possibility to access to some narrow places. Furthermore, it is capable of navigating autonomously in order to make continuous printing along mapped trajectories.

The Marvelmind in-door positioning system has been used to guide absolutely the center of the mass of the omnidrive mobile platform. It has an uncertainty of less 10mm obtained with a mean linear velocity of 50mm/s. Knowing that the considered printing nozzle has a diameter of 14mm for the case of the cement and 17mm for the case of the clay. Actually, this 4 to 7mm of error in the positioning of the deposit of the material doesn't affect globally the shape of the printed object with the required dimensions in MATRICE project, especially for closed shape.

As a prospective, the use of a (6-DoF) rigid manipulator with an accuracy of 0.1mm can compensate relatively the inaccuracy of the positioning for the mobile platform. This can be considered when the diameter of the nozzle is less than 10mm, after decoupling the control of the inaccurate mobile platform with that of the accurate manipulator. For that, it is important to equip the nozzle with an accurate positioning sensor as the Optitrack system, with an accuracy of 3mm, which is used in our case to track the shape of the

soft-continuum manipulator for quality control. Consequently, the reachable height of the printed objects is limited to 1000mm according to the requested volume $1000mm^3$ of printed objects in the framework of MATRICE project, when the mobile platform is stopped. The mobile-manipulator is controlled kinematically according to the pose of the tip of the nozzle (TCP). Thus, an IKM model for the omnidrive mobile-rigid manipulator (9-DoF) has been calculated with optimized solutions in the case of known positions of the nozzle (6 coordinates of the pose).

To resolve this kinematic redundancy, where the size of the operational space is smaller than the joint space, an optimization algorithm and kinematic constraints are considered according to the reachable shapes by the tip of nozzle. First, the orientation of the nozzle is fixed, which is the suited configuration for the nozzle in additive manufacturing of the cement and clay materials. This depends on the stiction property of the considered materials, where nowadays it is not possible to print vertically using these materials, without external formwork. Secondly, the 4th and 6th joints of the rigid-manipulator are constrained in order to avoid continuous vibrations acting on the nozzle. Finally, the three first joint of the rigid manipulator are bounded, where the bounds are calculated from the optimal robot posture according to the printed shape.

A prospective idea for the evolution of the additive manufacturing process in construction is the consideration of continuous printing in space configuration then only in Cartesian (or slicing) configuration. This can be studied from the material side by printing on a formwork in case of vertical shapes. This formwork can be done with other printed materials such as plastic-based materials, where samples have been tested in the printing of moldings during the project progress. Even if the rigid-manipulator in MATRICE project showed real performances in printing large-sizes of 3D objects, it has not been demonstrated yet how the printing can be realized with vertical slices.

Targeted objects concerned by the printing process using the technique of additive manufacturing are characterized by funicular geometrical objects, characterized by the 'intrados' shape which is different from the 'extrados' shape. The choice to print funicular surfaces compared to the literature lies in the fact of obtaining a purely compressed behavior and unaccompanied by bending and shear stresses. In addition, the parametric modeling of the funicular surfaces makes it possible to adjust certain parameters such as resistance, rigidity and density of the mesh. Thus, compression manufacturing requires less material during assembly since they are held in compression.

In this context, additive manufacturing in construction needs to be controlled in terms of deposit quality during the printing process and the quality inspection of the printed 3D objects after termination of the process. The quality of the deposit depends on the accurate superposition of the constitutive layers with the suitable material. The purpose is to adapt the use of cement and clay materials according to the kinematic of the robot and the shapes to be printed. To evaluate the quality of the deposit, the main indicator is to respect of the cord dimensions of the material, with height of 9 mm and width of 30 mm, for the cement and clay materials.

Thus, to print a desired cord of dimensions $1000 \times 30 \times 9mm$, and with a mean velocity of displacement 0.1m/s, the omnidrive mobile-rigid manipulator consumes 0.0034 kwh. For a total cord length of 457 m, the printing time was 109 min for the cement-based material and 191 min for the clay-based material.

A scientific contribution from this PhD work was mainly focusing on modeling and kinematics solving of a class of hyper-redundant manipulators with soft-continuum behavior, used for real-time quality inspection after printing process completion. In the framework of MATRICE project, the soft-continuum manipulator (CBHA) is placed as an

end-effector of the omnidrive mobile and rigid manipulator, used for printing 3D objects based on additive manufacturing technique in the construction. Kinematic modeling of continuum robots remains a real challenge, especially because of the absence of well-structured modeling and uncertainties from their constitutive materials. In our case, it was a polyamide-based material, which is characterized by memory effects and non-stationary behaviors.

A Hybrid approach is developed to improve the real-time solving of the CBHA's kinematic modeling in order to implement a control for inspection quality of printed surfaces in the context of MATRICE project. A real-time resolution and implementation in case of trajectory tracking is considered. A methodology of kinematic modeling and synthesis of its approximate solutions is proposed for the case of the CBHA. The modeling approach is issued from a quantitative modeling (analytical model-based) of parallel-rigid manipulators. Structurally, the CBHA is assimilated to concatenated parallel manipulators, where each parallel manipulator is described by an upper and lower vertebrae and an inter-vertebra. The latter is modeled as three UPS and one UP joints. The CBHA's kinematic models are deduced merely from the inverse kinematic equations of each inter-vertebra and generalized for the overall hyper-redundant robot.

The obtained inverse kinematic equations are highly nonlinear and mathematically intractable for the CBHA manipulator. For this issue, a qualitative approach (data learning) based on multilayer neural network is used to provide approximated solutions of the Inverse Kinematic Equation (IKE), which can be used for real-time implementation. The advantages of the proposed hybrid modeling-solving approach compared to quantitative methods is that the obtained models are more accurate and computationally inexpensive. Compared to qualitative approaches, the proposed approach can be implemented for platforms including a significant number of degrees of freedom (DoF); because the training database is deducted directly using the inverse kinematic equations. This avoids operating the robot for a long-period for learning database.

Appendix A

Overview of 3D Objects in MATRICE project

A.1 3D printing campaigns

(a) (b)

Figure A.1 – 3D printing on November 10, 2016 - Mines de Douai

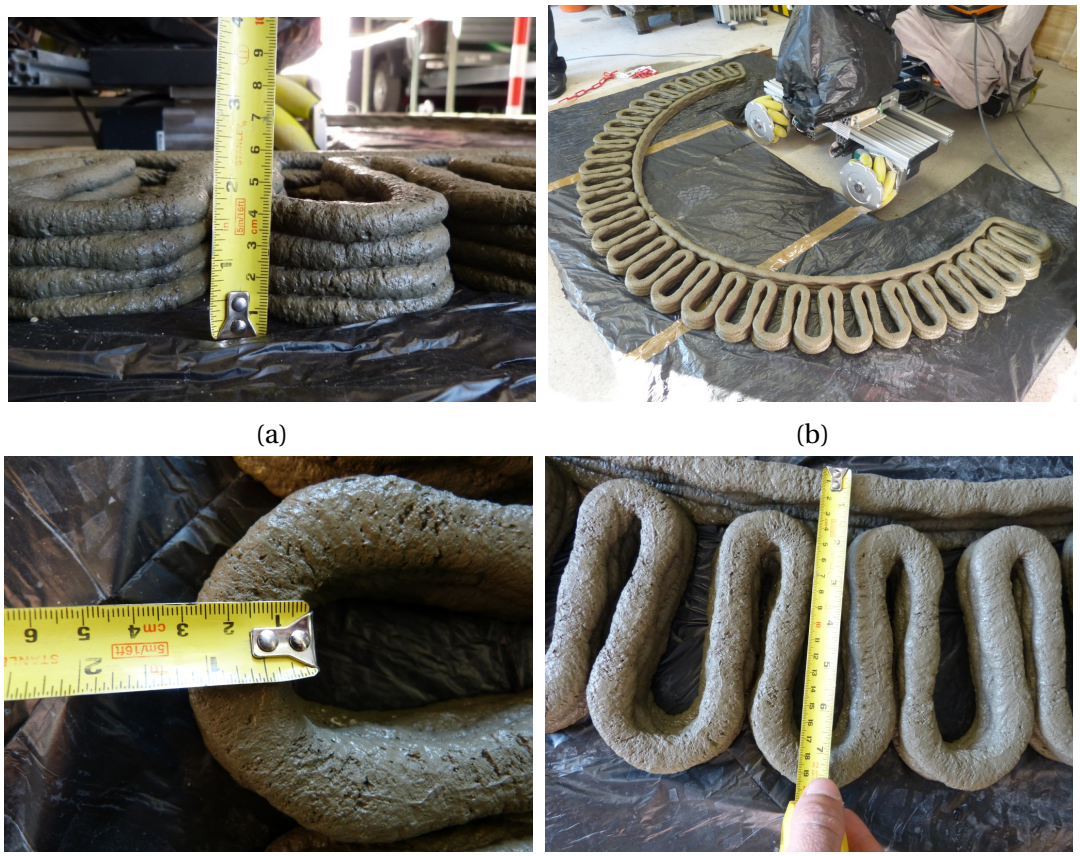

(a) (b)

(c) (d)

Figure A.2 – 3D printing on January 17, 2017 - Mines de Douai

Figure A.3 – 3D printing on March 17, 2017 - Polytech Lille

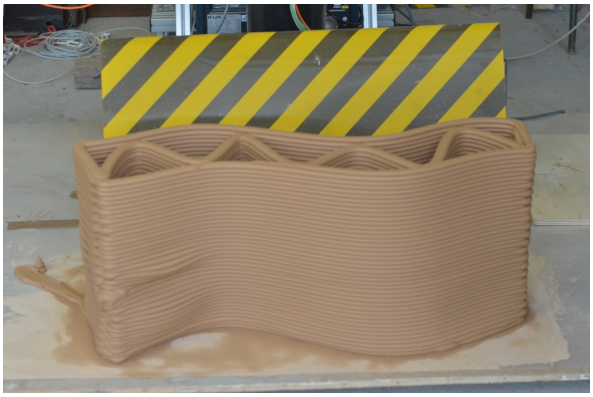

(a)

(b)

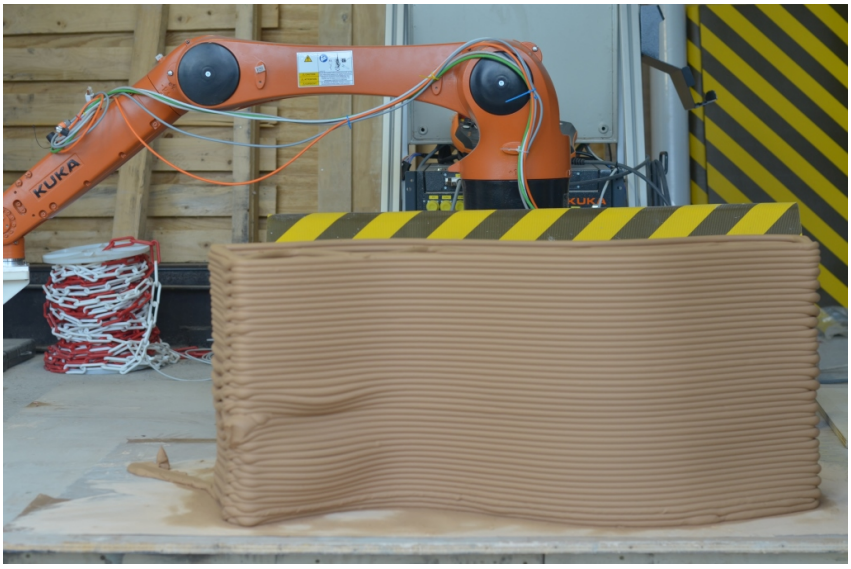

(c)

Figure A.4 – 3D printing on May 12, 2017 - Polytech Lille

(a)

(b)

Figure A.5 – 3D printing on May 22, 2017 - ENSAPL

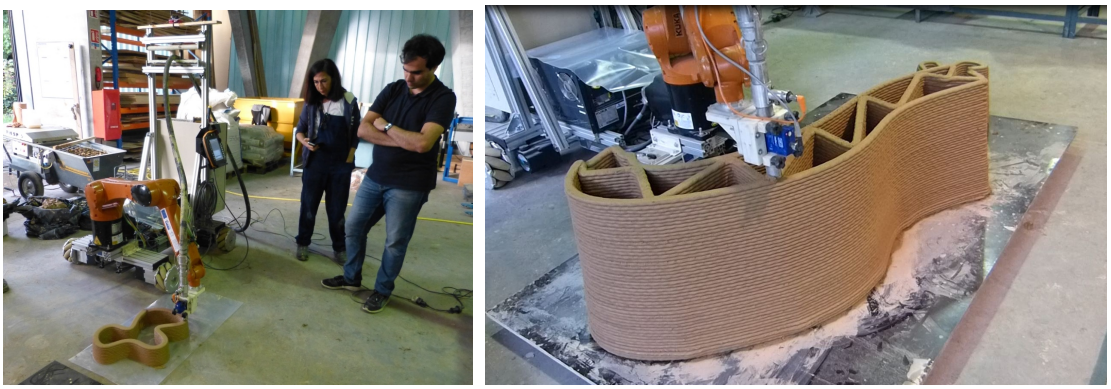

(a) (b)

Figure A.6 – 3D printing on 29 September 2017 - ENSAPL

Figure A.7 – 3D printing on 27 October 2017 - ENSAPL

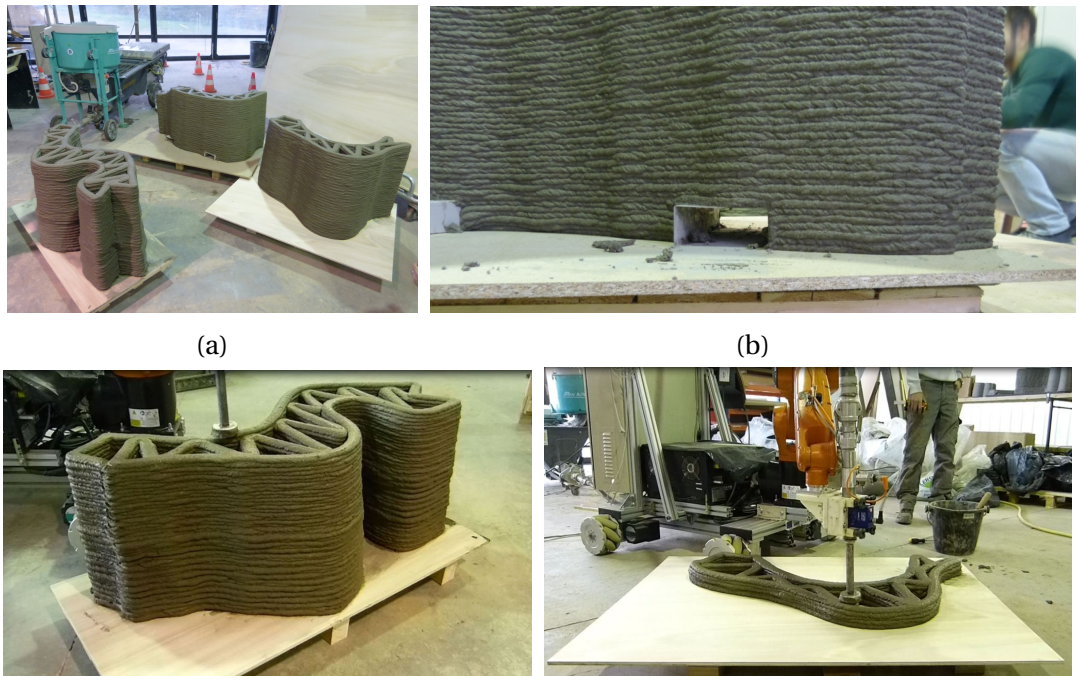

(a) (b)

(c) (d)

Figure A.8 – 3D printing on November 2, 2017 - ENSAPL

Figure A.9 – 3D printing on November 10, 2017 - ENSAPL

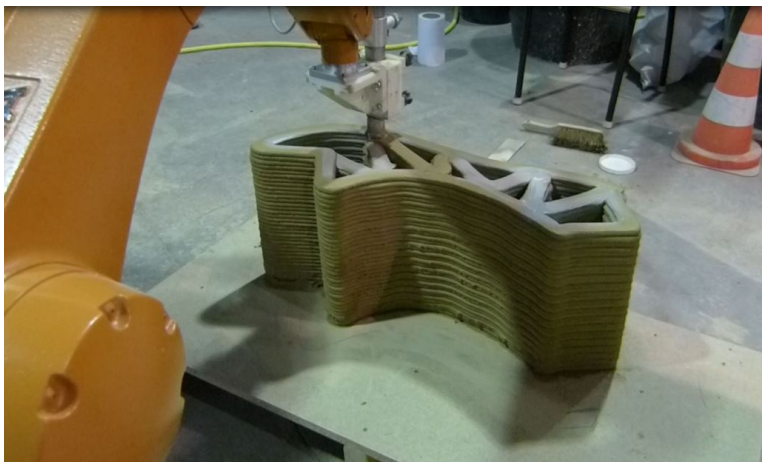

Figure A.10 – 3D printing on November 11, 2017 - ENSAPL

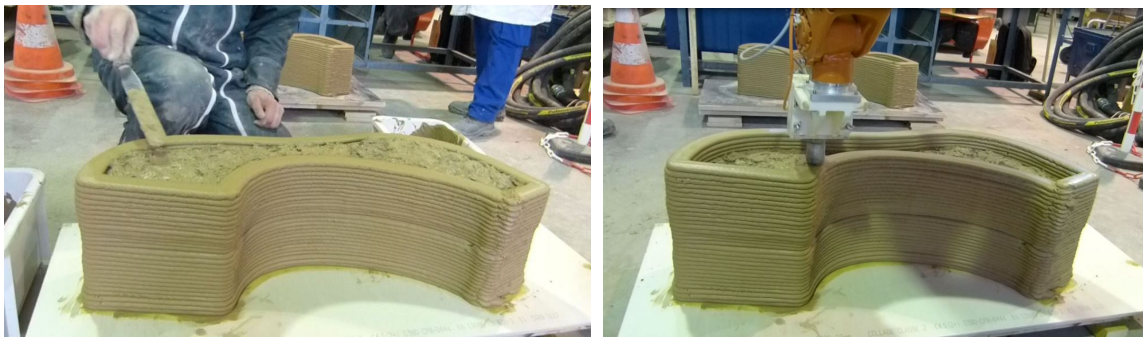

(a) (b)

Figure A.11 – 3D printing on November 16, 2017 - ENSAPL

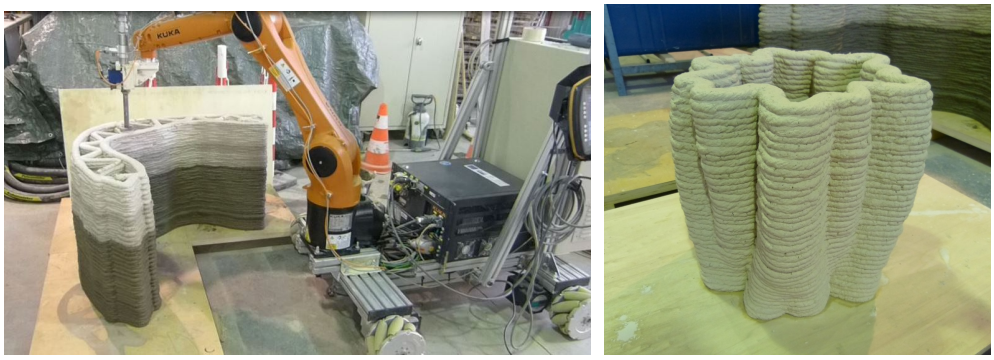

(a) (b)

Figure A.12 – 3D printing on November 17, 2017 - ENSAPL

(a) (b)

(c)

Figure A.13 – 3D printing on November 24, 2017 - ENSAPL

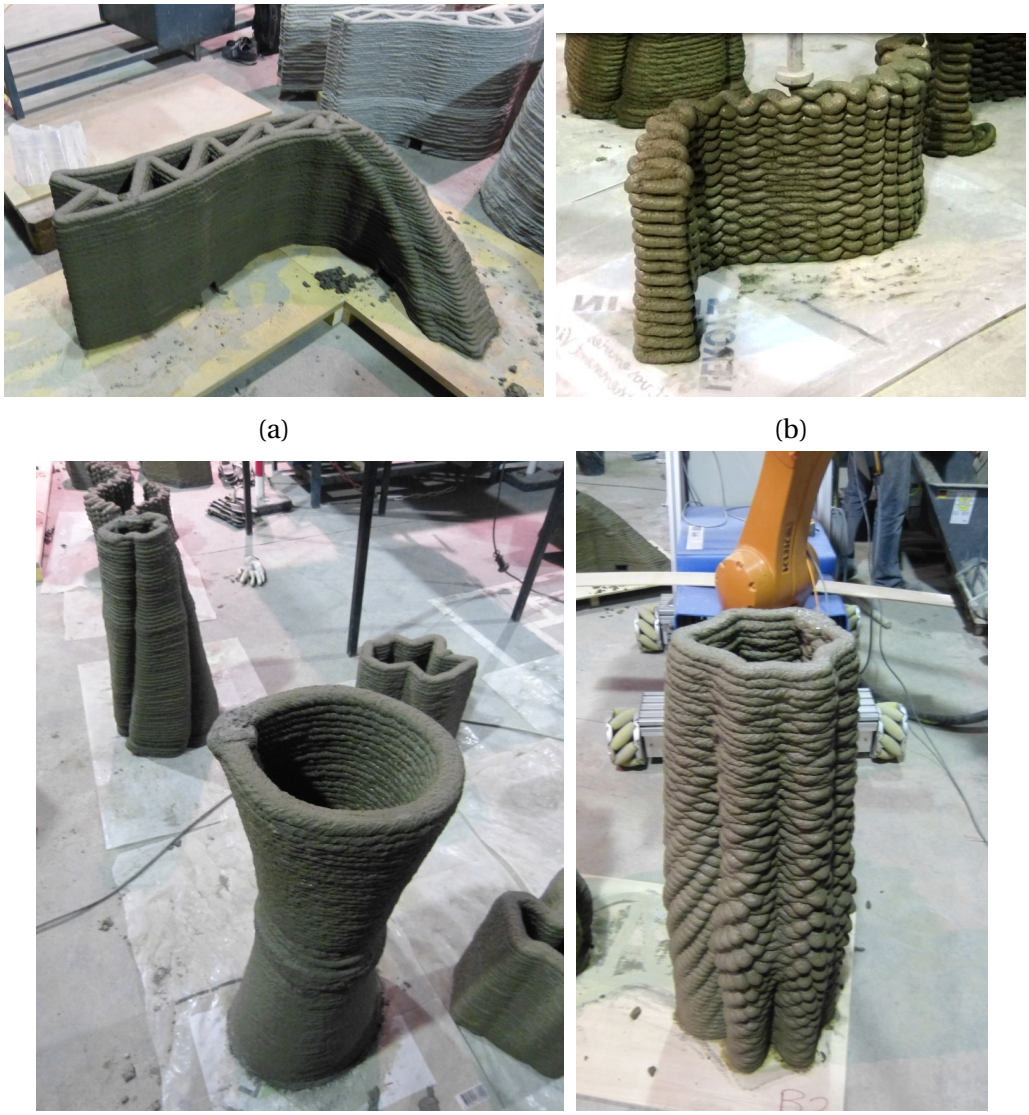

(a) (b)

(c) (d)

Figure A.14 – 3D printing on November 29, 2017 - ENSAPL

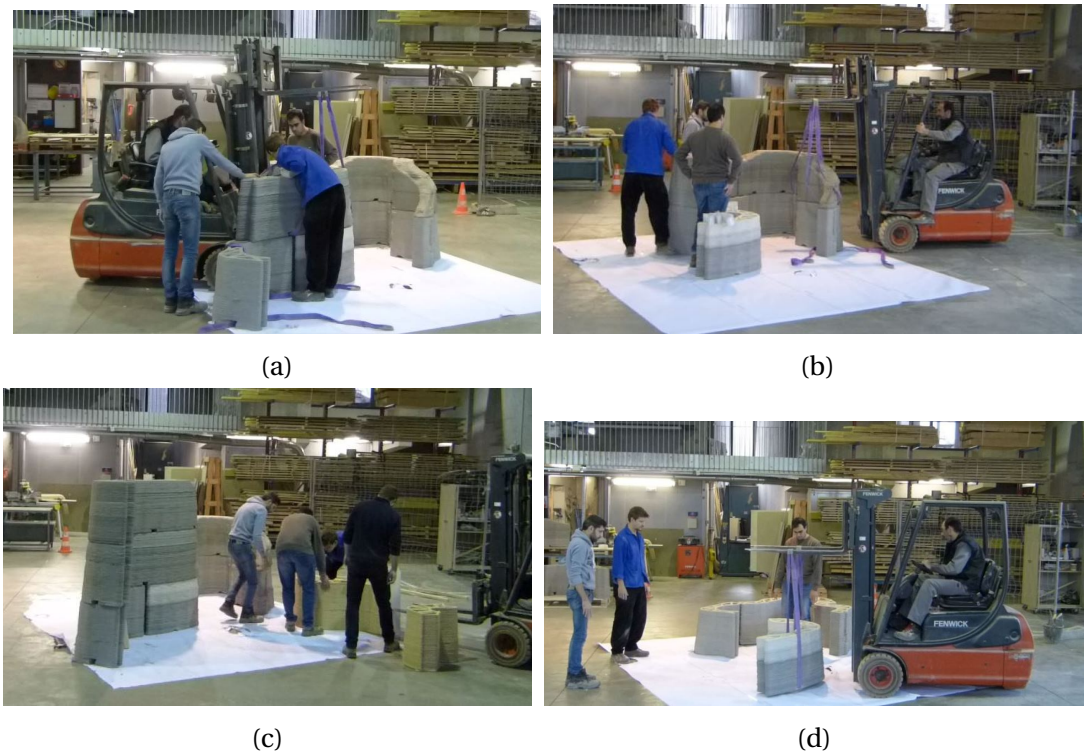

(a) (b)

(c) (d)

Figure A.15 – Assembly on December 2, 2017 - ENSAPL

Figure A.16 – Pavilion - ENSAPL

A.2 Events and Workshop

Figure A.17 – Workshop: ADDITIVE MANUFACTURING, A REGIONAL DYNAMIC ,on June 19, 2017 - Polytech Lille

Figure A.18 – 3D printing during the results restitution evening on December 6, 2018 - Cement material form - ENSAPL

Figure A.19 – MATRICE researchers at a workshop on raw earth organized at the Public Condition in ROUBAIX, March 9, 2018.

Appendix B

Acronyms

ANN Artificial Neural Network. 120

BHA Bionic Handling Arm. 19, 52, 56–58, 122, 127, 138

CBHA Compact Bionic Handling Arm. 5, 7, 17, 19, 29–31, 33, 52, 56–58, 115–119, 122–128, 130, 135, 137–142, 144, 146, 147

CF constraint function. 68–70, 76

D-H Denavit-Hartemberg. 19, 81, 96

DoF Degree of Freedom. 26, 27, 57, 58, 71, 88, 91, 93, 94, 116, 117, 125, 145–147

DoM degree of mobility. 94

EBP error back-propagation. 121

FKM Forward Kinematic Model. 26, 29, 31, 56, 79–81, 83, 84, 86, 99, 101, 119, 122, 124, 125, 127, 128, 130, 137, 140

HDR Haut-de-France. 21

IKE Inverse Kinematic Equation. 29, 58, 117–119, 123, 130, 147

IKM Inverse Kinematic Model. 26, 29, 31, 57, 79, 84, 87, 88, 91, 92, 99, 101, 102, 125–127, 135, 137, 139, 140, 146

MF main function. 68–71, 73

MLP Multilayer Perceptron. 120, 121, 123–125

MLPNN Multilayer Perceptron Neural Networks. 120, 121, 135

MNN Multilayer Neural Network. 119

MPP Moore-Penrose pseudoinverse. 98

MSE mean square error. 121, 123, 124, 126

NN Neural Networks. 57, 119, 122–124, 126, 136, 139

P prismatic joint. 29

PID proportional–integral–derivative. 101, 135, 137, 140

RBF Radial Basis Function. 120, 121

RBFNN Radial Basis Function neural network. 120, 121

S spheric joint. 29

SQP Sequential Quadratic Program. 125

SVD singular value decomposition. 98, 99

TCP Tool Center Position. 29, 84, 125, 138, 140, 141, 146

TRL Technology Readiness Level. 62

U universal joint. 29

UAV Unmanned Aerial Vehicles. 52

UCF under constraint function. 69

UMF under main function. 69

UP Universal-Prismatic. 58, 116, 117, 119, 147

UPS Universal-Prismatic-Spheric. 58, 116, 117, 119, 147

VKM Velocity kinematic model. 93

WP work package. 21–23

Bibliography

Amouri, A., Mahfoudi, C., Zaatri, A., Lakhal, O., and Merzouki, R. (2017). A metaheuristic approach to solve inverse kinematics of continuum manipulators. *Proceedings of the Institution of Mechanical Engineers, Part I: Journal of Systems and Control Engineering*, 231(5):380–394. 56

Anderson, V. C. (1967). Tensor arm manipulator design. *Trans. ASME*, 67:1–12. 53

Antonelli, G. and Chiaverini, S. (2003). Fuzzy redundancy resolution and motion coordination for underwater vehicle-manipulator systems. *IEEE Transactions on Fuzzy Systems*, 11(1):109–120. 80

Apis-Cor (2017). Website of the company apis cor : We print building. http://apis-cor.com. visited on 30 august 2018. 41

Arshad, M., Khan, T., and Choudhry, M. (2005). Solution of forward kinematics model of six degrees of freedom parallel robot manipulator. In *Emerging Technologies, 2005. Proceedings of the IEEE Symposium on*, pages 393–398. IEEE. 119

Bardou, B., Zanne, P., Nageotte, F., and de Mathelin, M. (2010). Control of a multiple sections flexible endoscopic system. In *Intelligent Robots and Systems (IROS), 2010 IEEE/RSJ International Conference on*, pages 2345–2350. IEEE. 56

Beaman, J. J., Barlow, J. W., Bourell, D. L., Crawford, R. H., Marcus, H. L., and McAlea, K. P. (1997). Solid freeform fabrication: a new direction in manufacturing. *Kluwer Academic Publishers, Norwell, MA*, 2061:25–49. 36

Benoudjit, N. and Verleysen, M. (2003). On the kernel widths in radial-basis function networks. *Neural Processing Letters*, 18(2):139–154. 120, 121

BetAbram (2014). Website of the company betabram. http://www.betabram.com/. visited on 30 august 2018. 41

Bieze, T. M., Largilliere, F., Kruszewski, A., Zhang, Z., Merzouki, R., and Duriez, C. (2018). Fem-based kinematics and closed-loop control of soft, continuum manipulators. 31

BigDelta, W. (2016). Website of the company wasp : Bigdelta wasp. http://www.wasproject.it/w/en/3d-printing/bigdeltawasp-12m. visited on 30 august 2018. 41

Bingul, Z., Ertunc, H., and Oysu, C. (2005). Comparison of inverse kinematics solutions using neural network for 6r robot manipulator with offset. In *Computational Intelligence Methods and Applications, 2005 ICSC Congress on*, pages 5–pp. IEEE. 58

Bishop, C. M. (1995). *Neural networks for pattern recognition*. Oxford university press. 121

Braganza, D., Dawson, D. M., Walker, I. D., and Nath, N. (2007). A neural network controller for continuum robots. *Robotics, IEEE Transactions on*, 23(6):1270–1277. 57, 127

Buckingham, R., Chitrakaran, V., Conkie, R., Ferguson, G., Graham, A., Lazell, A., Lichon, M., Parry, N., Pollard, F., Kayani, A., et al. (2007). Snake-arm robots: a new approach to aircraft assembly. Technical report, SAE Technical Paper. 54, 55

Calisti, M., Arienti, A., Giannaccini, M. E., Follador, M., Giorelli, M., Cianchetti, M., Mazzolai, B., Laschi, C., and Dario, P. (2010). Study and fabrication of bioinspired octopus arm mockups tested on a multipurpose platform. In *Biomedical Robotics and Biomechatronics (BioRob), 2010 3rd IEEE RAS and EMBS International Conference on*, pages 461–466. IEEE. 53

Camacho, D. D., Clayton, P., O'Brien, W., Ferron, R., Juenger, M., Salamone, S., and Seepersad, C. (2017). Applications of additive manufacturing in the construction industry–a prospective review. In *ISARC. Proceedings of the International Symposium on Automation and Robotics in Construction*, volume 34. Vilnius Gediminas Technical University, Department of Construction Economics & Property. 41

Casper, J. and Murphy, R. R. (2003). Human-robot interactions during the robot-assisted urban search and rescue response at the world trade center. *IEEE Transactions on Systems, Man, and Cybernetics, Part B (Cybernetics)*, 33(3):367–385. 52

Černohorskỳ, J., Jandura, P., and Mach, O. (2017). Mobile robot localization and object description. In *Carpathian Control Conference (ICCC), 2017 18th International*, pages 503–506. IEEE. 140

Charron, K. (2015). Winsun china builds world's first 3d printed villa and tallest 3d printed apartment building. *3ders. org*. 39

Chen, I.-M., Asadi, E., Nie, J., Yan, R.-J., Law, W. C., Kayacan, E., Yeo, S. H., Low, K. H., Seet, G., and Tiong, R. (2016). Innovations in infrastructure service robots. In *ROMANSY 21-Robot Design, Dynamics and Control*, pages 3–16. Springer. 52

Cheng, N. G., Lobovsky, M. B., Keating, S. J., Setapen, A. M., Gero, K. I., Hosoi, A. E., and Iagnemma, K. D. (2012). Design and analysis of a robust, low-cost, highly articulated manipulator enabled by jamming of granular media. In *Robotics and Automation (ICRA), 2012 IEEE International Conference on*, pages 4328–4333. IEEE. 54, 55

Chibani, A., Mahfoudi, C., Chettibi, T., Merzouki, R., and Zaatri, A. (2015). Generating optimal reference kinematic configurations for hyper-redundant parallel robots. *Proceedings of the Institution of Mechanical Engineers, Part I: Journal of Systems and Control Engineering*, 229(9):867–882. 57

Chirikjian, G. S. and Burdick, J. W. (1994). A modal approach to hyper-redundant manipulator kinematics. *Robotics and Automation, IEEE Transactions on*, 10(3):343–354. 57

Cianchetti, M., Arienti, A., Follador, M., Mazzolai, B., Dario, P., and Laschi, C. (2011). Design concept and validation of a robotic arm inspired by the octopus. *Materials Science and Engineering: C*, 31(6):1230–1239. 53, 55

Colla, V. and Dini, E. (2013). Large scale 3d printing: From deep sea to the moon. *Low-Cost 3D Printing, for Science, Education & Sustainable Development; Canessa, E., Fonda, C., Zennaro, M., Eds*, pages 127–132. 37

Collins, G. R. and Nonell, J. B. (1981). *The designs and drawings of Antonio Gaudí*. Princeton University Press. 65

Daachi, B., Madani, T., and Benallegue, A. (2012). Adaptive neural controller for redundant robot manipulators and collision avoidance with mobile obstacles. *Neurocomputing*, 79:50–60. 58

De Paz, J. Z., Castañeda, E. C., Castro, X. S., and Jimenez, S. R. (2013). Crack detection by a climbing robot using image analysis. In *Electronics, Communications and Computing (CONIELECOMP), 2013 International Conference on*, pages 87–91. IEEE. 52

Della Santina*, C., Katzschmann*, R. K., Bicchi, A., and Rus, D. (2018). Dynamic control of soft robots interacting with the environment. In *2018 IEEE-RAS International Conference on Soft Robotics (RoboSoft)*. 53, 54

Denavit, J. (1955). A kinematic notation for lower-pair mechanisms based on matrices. *Trans. of the ASME. Journal of Applied Mechanics*, 22:215–221. 80

Dos Santos, C. H., Guenther, R., Martins, D., and De Pieri, E. R. (2006). Virtual kinematic chains to solve the underwater vehicle-manipulator systems redundancy. *Journal of the Brazilian Society of Mechanical Sciences and Engineering*, 28(3):354–361. 80

Dubois, V., Leblanc, A., Carpentier, O., Alhaik, G., and Wirquin, E. (2018). Performances of flax shive-based lightweight composites with rapid hardening. *Construction and Building Materials*, 165:17–27. 64

El Cheikh, K., Rémond, S., Khalil, N., and Aouad, G. (2017). Numerical and experimental studies of aggregate blocking in mortar extrusion. *Construction and Building Materials*, 145:452–463. 63

Escande, C., Chettibi, T., Merzouki, R., Coelen, V., and M., P. P. (2014). Kinematic calibration of a multisection bionic manipulator. *Mechatronics, IEEE/ASME Transactions on*, 0(0):0–0. 127, 138

Escande, C., Chettibi, T., Merzouki, R., Coelen, V., and M., P. P. (2015). Kinematic calibration of a multisection bionic manipulator. *IEEE/ASME Transactions on Mechatronics*, page 663 – 674. 31

Escande, C., Merzouki, R., Pathak, P. M., and Coelen, V. (2012). Geometric modelling of multisection bionic manipulator: Experimental validation on robotinoxt. *IEEE International Conference on Robotics and Biomimetics (ROBIO)*. 16, 56

Espinoza, M. S., Gonçalves, J., Leitao, P., Sánchez, J. L. G., and Herreros, A. (2012). Inverse kinematics of a 10 dof modular hyper-redundant robot resorting to exhaustive and error-optimization methods: A comparative study. In *Robotics Symposium and Latin American Robotics Symposium (SBR-LARS), 2012 Brazilian*, pages 125–130. IEEE. 57

Falkenhahn, V., Hildebrandt, A., Neumann, R., and Sawodny, O. (2017). Dynamic control of the bionic handling assistant. *IEEE/ASME Transactions on Mechatronics*, 22(1):6–17. 27

Festo (2013a). Brochure of robotinoxt. visited on 15 September 2013. 52

Festo (2013b). Website of the company festo : Bionic learning network. visited on 1May 2018. 52

Frank, M. and Wolfe, P. (1956). An algorithm for quadratic programming. *Naval research logistics quarterly*, 3(1-2):95–110. 86

Frazelle, C. G., Kapadia, A., and Walker, I. (2018). Developing a kinematically similar master device for extensible continuum robot manipulators. *Journal of Mechanisms and Robotics*, 10(2):025005. 54, 55

Gardiner, J. B. and Janssen, S. R. (2014). Freefab - development of a construction-scale robotic formwork 3d printer. In *Robotic Fabrication in Architecture, Art and Design 2014*, pages 131–146. Springer. 23

Gaudillière, N., Duballet, R., Bouyssou, C., Mallet, A., Roux, P., Zakeri, M., and Dirrenberger, J. (2018). Large-scale additive manufacturing of ultra-high-performance concrete of integrated formwork for truss-shaped pillars. In *Robotic Fabrication in Architecture, Art and Design*, pages 459–472. Springer. 41

George Thuruthel, T., Falotico, E., Manti, M., Pratesi, A., Cianchetti, M., and Laschi, C. (2017). Learning closed loop kinematic controllers for continuum manipulators in unstructured environments. *Soft robotics*, 4(3):285–296. 57

Giorelli, M., Renda, F., Ferri, G., and Laschi, C. (2013). A feed-forward neural network learning the inverse kinetics of a soft cable-driven manipulator moving in three-dimensional space. *in proc. IEEE Int. Conf. on Intelli-gent Robots and Systems*, pages 5033–5039. 57, 127

Godage, I. S., Branson, D. T., Guglielmino, E., Medrano-Cerda, G. A., and Caldwell, D. G. (2011a). Shape function-based kinematics and dynamics for variable length continuum robotic arms. In *Robotics and Automation (ICRA), 2011 IEEE International Conference on*, pages 452–457. IEEE. 56

Godage, I. S., Guglielmino, E., Branson, D. T., Medrano-Cerda, G. A., and Caldwell, D. G. (2011b). Novel modal approach for kinematics of multisection continuum arms. In *Intelligent Robots and Systems (IROS), 2011 IEEE/RSJ International Conference on*, pages 1093–1098. IEEE. 56

Goldenberg, A., Benhabib, B., and Fenton, R. (1985). A complete generalized solution to the inverse kinematics of robots. *IEEE Journal on Robotics and Automation*, 1(1):14–20. 57

Guez, A. (1988). Solution to the inverse kinematics problem in robotics by neural network. In *Proc. Int. Conf. on Neural Networks, Skovde, 1988*, pages II617–II624. 58

Haddad, M., Hanchi, S., and Lehtihet, H. (2009). Point-to-point trajectory planning of wheeled mobile manipulators with stability constraint. extension of the random-profile approach. *European Journal of Mechanics-A/Solids*, 28(3):477–493. 80

Hager, I., Golonka, A., and Putanowicz, R. (2016). 3d printing of buildings and building components as the future of sustainable construction? *Procedia Engineering*, 151:292–299. 41

Hannan, M. and Walker, I. (2000). Novel kinematics for continuum robots. In *Advances in Robot Kinematics*, pages 227–238. Springer. 56

Hannan, M. and Walker, I. (2001). The 'elephant trunk' manipulator, design and implementation. In *Advanced Intelligent Mechatronics, 2001. Proceedings. 2001 IEEE/ASME International Conference on*, volume 1, pages 14–19. IEEE. 27, 53, 55

Hanson, A. J. and Ma, H. (1995). Parallel transport approach to curve framing. 11:3–7. 138

Hartenberg, R. S. and Denavit, J. A. (1955). A kinematic notation for lower pair mechanisms based on matrices. *Journal of Applied Mechanics*, 77:215–221. 81

Haykin, S. (1994). *Neural networks: a comprehensive foundation*. Prentice Hall PTR. 119

Hollerbach, J. M. and Wampler, C. W. (1996). The calibration index and taxonomy for robot kinematic calibration methods. *The international journal of robotics research*, 15(6):573–591. 57

Hornik, K., Stinchcombe, M., and White, H. (1989). Multilayer feedforward networks are universal approximators. *Neural networks*, 2(5):359–366. 120, 121

Hunt, G., Mitzalis, F., Alhinai, T., Hooper, P. A., and Kovac, M. (2014). 3d printing with flying robots. In *Robotics and Automation (ICRA), 2014 IEEE International Conference on*, pages 4493–4499. IEEE. 36

Inderjeet Singh, Yacine Amara, M. S. R. M. (July 2018). Towards accurate shape reconstruction of compact bionic handling arm. *IEEE/ASME International Conference on Advanced Intelligent Mechatronics (AIM 2018)*. 56

Jiang, H., Wang, Z., Liu, X., Chen, X., Jin, Y., You, X., and Chen, X. (2017). A two-level approach for solving the inverse kinematics of an extensible soft arm considering viscoelastic behavior. In *Robotics and Automation (ICRA), 2017 IEEE International Conference on*, pages 6127–6133. IEEE. 58

Jones, B. A. and Walker, I. D. (2006a). Kinematics for multisection continuum robots. *Robotics, IEEE Transactions on*, 22(1):43–55. 54, 55, 56

Jones, B. A. and Walker, I. D. (2006b). Practical kinematics for real-time implementation of continuum robots. *Robotics, IEEE Transactions on*, 22(6):1087–1099. 127

Kang, R., Guglielmino, E., Branson, D. T., and Caldwell, D. G. (2013). Kinematic model and inverse control for continuum manipulators. In *Control and Automation (ICCA), 2013 10th IEEE International Conference on*, pages 1615–1620. IEEE. 57

Karacan, M. and Bükcü, B. (2010). On natural curvatures of bishop frame. *Journal of Vectorial Relativity*, 5:34–41. 138

Karlik, B. and Aydin, S. (2000). An improved approach to the solution of inverse kinematics problems for robot manipulators. *Engineering applications of artificial intelligence*, 13(2):159–164. 58

Khalil, N., Aouad, G., El Cheikh, K., and Rémond, S. (2017). Use of calcium sulfoaluminate cements for setting control of 3d-printing mortars. *Construction and Building Materials*, 157:382–391. 63

Khalil, W. and Dombre, E. (2004). *Modeling, identification and control of robots*. Butterworth-Heinemann. 83, 87

Khoshnevis, B., Carlson, A., and Thangavelu, M. (2017). Isru-based robotic construction technologies for lunar and martian infrastructures. 37

Khoshnevis, B. and Dutton, R. (1998). Innovative rapid prototyping process makes large sized, smooth surfaced complex shapes in a wide variety of materials. *Materials Technology*, 13(2):53–56. 37

Kucuksubasi, F. and Sorguc, A. (2018). Transfer learning-based crack detection by autonomous uavs. *arXiv preprint arXiv:1807.11785*. 52

Labonnote, N., Rønnquist, A., Manum, B., and Rüther, P. (2016). Additive construction: State-of-the-art, challenges and opportunities. *Automation in Construction*, 72:347–366. 36

Lakhal, O., Melingui, A., Chibani, A., Escande, C., and Merzouki, R. (2014a). Inverse kinematic modeling of a class of continuum bionic handling arm. *Accepted at IEEE/ASME International Conference on Advanced Intelligent Mechatronics*. 125

Lakhal, O., Melingui, A., Morales, T., Escande, C., and Merzouki, R. (2014b). Forward kinematic of a class of continuum bionic handling arm. *Accepted at Robotics and Biomimetics (ROBIO), 2014 IEEE International Conference on*. 58

Lee, K.-H., Fu, D. K., Leong, M. C., Chow, M., Fu, H.-C., Althoefer, K., Sze, K. Y., Yeung, C.-K., and Kwok, K.-W. (2017). Nonparametric online learning control for soft continuum robot: An enabling technique for effective endoscopic navigation. *Soft robotics*, 4(4):324–337. 53, 54

Lim, S., Buswell, R. A., Le, T. T., Austin, S. A., Gibb, A. G., and Thorpe, T. (2012). Developments in construction-scale additive manufacturing processes. *Automation in construction*, 21:262–268. 36

Lim, S., Buswell, R. A., Le, T. T., Wackrow, R., Austin, S. A., Gibb, A. G., and Thorpe, T. (2011). Development of a viable concrete printing process. 36, 37, 39

MacAusland, R. (2014). The moore-penrose inverse and least squares. *Math 420: Advanced Topics in Linear Algebra*, pages 1–10. 98

Mahl, T., Hildebrandt, A., and Sawodny, O. (2012). Forward kinematics of a compliant pneumatically actuated redundant manipulator. pages 1267–1273. 57

Mahl, T., Hildebrandt, A., and Sawodny, O. (2014). A variable curvature continuum kinematics for kinematic control of the bionic handling assistant. *Robotics, IEEE Transactions on*, 30(4):935–949. 122, 138

Marques, L., Dinis, J., Coimbra, A. P., Crisóstomo, M. M., and Ferreira, J. P. (2009). 3d hyper-redundant robot. In *11th Spanish Portuguese Conference on Electrical Engineering, Zaragoza, Spain*. 98

Mathur, R. (2016). 3d printing in architecture. *International Journal of Innovative Science, Engineering & Technology*, 3. 23, 37

McMahan, W., Chitrakaran, V., Csencsits, M., Dawson, D., Walker, I. D., Jones, B. A., Pritts, M., Dienno, D., Grissom, M., and Rahn, C. D. (2006). Field trials and testing of the octarm continuum manipulator. In *Robotics and Automation, 2006. ICRA 2006. Proceedings 2006 IEEE International Conference on*, pages 2336–2341. IEEE. 53

Melingui, A., Ahanda, J. J.-B. M., Lakhal, O., Mbede, J. B., and Merzouki, R. (2017). Adaptive algorithms for performance improvement of a class of continuum manipulators. *IEEE Transactions on Systems, Man, and Cybernetics: Systems*. 57

Melingui, A., Escande, C., Nabil, B., Merzouki, R., and Mbede, J. (2014a). Qualitative approach for forward kinematic modeling of a compact bionic handling assistant trunk. In *Submitted to 19th World Congress of the Int. Federation of Aut. Control, Cape Town, South Africa*, pages 24–29. 58, 138

Melingui, A., Lakhal, O., Daachi, B., Mbede, J. B., and Merzouki, R. (2015). Adaptive neural network control of a compact bionic handling arm. *IEEE/ASME Transactions on Mechatronics*, 20(6):2862–2875. 31, 57, 58, 137

Melingui, A., Merzouki, R., and Mbede, J. (2014b). Compact bionic handling arm control using neural networks. *Electronics Letters*, 50(14):979–981. 137

Melingui, A., Merzouki, R., Mbede, J., Escande, C., Daachi, B., and Benoudjit, N. (2014c). Qualitative approach for inverse kinematic modeling of a compact bionic handling assistant trunk. In *Neural Networks (IJCNN), 2014 International Joint Conference on*, pages 754–761. IEEE. 57, 58

Meshram, P. and Kanojiya, R. G. (2012). Tuning of pid controller using ziegler-nichols method for speed control of dc motor. In *Advances in Engineering, Science and Management (ICAESM), 2012 International Conference on*, pages 117–122. IEEE. 101

Mittal, R. and Nagrath, I. (2003). *Robotics and control*. Tata McGraw-Hill. 95

Neppalli, S., Csencsits, M. A., Jones, B. A., and Walker, I. (2008). A geometrical approach to inverse kinematics for continuum manipulators. In *Intelligent Robots and Systems, 2008. IROS 2008. IEEE/RSJ International Conference on*, pages 3565–3570. IEEE. 56

Oliveira, H. and Correia, P. L. (2013). Automatic road crack detection and characterization. *IEEE Transactions on Intelligent Transportation Systems*, 14(1):155–168. 52

Orin, D. E. and Schrader, W. W. (1984). Efficient computation of the jacobian for robot manipulators. *The International Journal of Robotics Research*, 3(4):66–75. 95

Paul, R. (1981a). Robot manipulators: mathematics, programming, and control, 1981. *equation*, 1:30. 88

Paul, R. P. (1981b). *Robot manipulators: mathematics, programming, and control: the computer control of robot manipulators*. Richard Paul. 80

Peiper, D. L. (1968). The kinematics of manipulators under computer control. Technical report, Stanford Univ Ca Dept Of Computer Science. 88

Penrose, R. (1955). A generalized inverse for matrices. In *Mathematical proceedings of the Cambridge philosophical society*, volume 51, pages 406–413. Cambridge University Press. 98

Perkins, I. and Skitmore, M. (2015). Three-dimensional printing in the construction industry: A review. *International Journal of Construction Management*, 15(1):1–9. 37

Phung, M. D., Hoang, V. T., Dinh, T. H., and Ha, Q. (2017). Automatic crack detection in built infrastructure using unmanned aerial vehicles. *arXiv preprint arXiv:1707.09715*. 52

Prasanna, P., Dana, K. J., Gucunski, N., Basily, B. B., La, H. M., Lim, R. S., and Parvardeh, H. (2016). Automated crack detection on concrete bridges. *IEEE Trans. Automation Science and Engineering*, 13(2):591–599. 52

Raghavan, M. and Roth, B. (1990). Kinematic analysis of the 6r manipulator of general geometry. In *Proc. Fifth Int. Symposium on Robotics Research, MIT Press, Cambridge*. 88

Reinhart, R. F., Shareef, Z., and Steil, J. J. (2017). Hybrid analytical and data-driven modeling for feed-forward robot control. *Sensors*, 17(2):311. 58

Rolf, M. and Steil, J. J. (2012a). Constant curvature continuum kinematics as fast approximate model for the bionic handling assistant. In *Intelligent Robots and Systems (IROS), 2012 IEEE/RSJ International Conference on*, pages 3440–3446. IEEE. 56

Rolf, M. and Steil, J. J. (2012b). Efficient exploratory learning of inverse kinematics on a bionic elephant trunk. 57, 127, 138

Rouhana, C. M., Aoun, M. S., Faek, F. S., Eljazzar, M. S., and Hamzeh, F. R. (2014). The reduction of construction duration by implementing contour crafting (3d printing). In *Proceedings for the 22nd Annual Conference of the International Group for Lean Construction*, volume 22, pages 1031–1042. 39

Russell, P. (2015). 3-d printed earthen architecture. Technical report, Tech. Rep. Aston University. 64

Scheurer, C., Fiore, M. D., Sharma, S., and Natale, C. (2016). Industrial implementation of a multi-task redundancy resolution at velocity level for highly redundant mobile manipulators. In *ISR 2016: 47st International Symposium on Robotics; Proceedings of*, pages 1–9. VDE. 80

Schodek, D. L. and Bechthold, M. (2008). *Structures*. Pearson/Prentice Hall Englewood Cliffs. 65

Shi, Y., Cui, L., Qi, Z., Meng, F., and Chen, Z. (2016). Automatic road crack detection using random structured forests. *IEEE Transactions on Intelligent Transportation Systems*, 17(12):3434–3445. 52

Sika (2015). Website of the company sika. https://fra.sika.com/. visited on 30 august 2018. 41

Simaan, N., Taylor, R., and Flint, P. (2004). A dexterous system for laryngeal surgery. In *Robotics and Automation, 2004. Proceedings. ICRA'04. 2004 IEEE International Conference on*, volume 1, pages 351–357. IEEE. 52

Singh, I., Amara, Y., Melingui, A., Mani Pathak, P., and Merzouki, R. (2018). Modeling of continuum manipulators using pythagorean hodograph curves. *Soft robotics*. 31

Singh, I., Lakhal, O., Amara, Y., Coelen, V., Pathak, P., and Merzouki, R. (2017a). Performances evaluation of inverse kinematic models of a compact bionic handling assistant. In *IEEE Conference on Robotics and Biomimetics (ROBIO)*. 56

Singh, I., Lakhal, O., and Merzouki, R. (2017b). Towards extending forward kinematic models on hyper-redundant manipulator to cooperative bionic arms. In *Journal of Physics: Conference Series*, volume 783, page 012056. IOP Publishing. 56

Thuruthel, T., Falotico, E., Cianchetti, M., Renda, F., and Laschi, C. (2016a). Learning global inverse statics solution for a redundant soft robot. In *Proceedings of the 13th International Conference on Informatics in Control, Automation and Robotics*, volume 2, pages 303–310. 57

Thuruthel, T. G., Falotico, E., Cianchetti, M., and Laschi, C. (2016b). Learning global inverse kinematics solutions for a continuum robot. In *ROMANSY 21-Robot Design, Dynamics and Control*, pages 47–54. Springer. 57

Walker, I. D., Dawson, D. M., Flash, T., Grasso, F. W., Hanlon, R. T., Hochner, B., Kier, W. M., Pagano, C. C., Rahn, C. D., and Zhang, Q. M. (2005). Continuum robot arms inspired by cephalopods. In *Defense and Security*, pages 303–314. International Society for Optics and Photonics. 52, 54

Webster, R. J. and Jones, B. A. (2010). Design and kinematic modeling of constant curvature continuum robots: A review. *The International Journal of Robotics Research*, 29(13):1661–1683. 56

Werfel, J., Petersen, K., and Nagpal, R. (2014). Designing collective behavior in a termite-inspired robot construction team. *Science*, 343(6172):754–758. 36

Winsun (2014). Website of the company winsun : 3d printing architecture's future. http://www.winsun3d.com. visited on 30 august 2018. 41

Wu, P., Wang, J., and Wang, X. (2016). A critical review of the use of 3-d printing in the construction industry. *Automation in Construction*, 68:21–31. 39, 41

Wu, W., Shao, H., and Li, Z. (2006). Convergence of batch bp algorithm with penalty for fnn training. In *Neural Information Processing*, pages 562–569. Springer. 126

Xie, T., Yu, H., and Wilamowski, B. (2011). Comparison between traditional neural networks and radial basis function networks. In *Industrial Electronics (ISIE), 2011 IEEE International Symposium on*, pages 1194–1199. IEEE. 120, 121

Xtreee (2015). Website of the company xtreee : The large-scale 3d. https://www.xtreee.eu/. visited on 30 august 2018. 41

Yamamoto, Y. and Yun, X. (1992). Coordinating locomotion and manipulation of a mobile manipulator. In *Decision and Control, 1992., Proceedings of the 31st IEEE Conference on*, pages 2643–2648. IEEE. 79

Yan, R.-J., Kayacan, E., Chen, I.-M., and Tiong, L. K. (2017). A novel building post-construction quality assessment robot: Design and prototyping. In *Intelligent Robots and Systems (IROS), 2017 IEEE/RSJ International Conference on*, pages 6020–6023. IEEE. 52

Zareiyan, B. and Khoshnevis, B. (2017). Interlayer adhesion and strength of structures in contour crafting-effects of aggregate size, extrusion rate, and layer thickness. *Automation in Construction*, 81:112–121. 37

Zhang, W., Zhang, Z., Qi, D., and Liu, Y. (2014). Automatic crack detection and classification method for subway tunnel safety monitoring. *Sensors*, 14(10):19307–19328. 52

Zhang, X., Li, M., Lim, J. H., Weng, Y., Tay, Y. W. D., Pham, H., and Pham, Q.-C. (2018). Large-scale 3d printing by a team of mobile robots. *Automation in Construction*, 95:98–106. 41

Zhao, Q. and Gao, F. (2010). Design and analysis of a kind of biomimetic continuum robot. In *Robotics and Biomimetics (ROBIO), 2010 IEEE International Conference on*, pages 1316–1320. IEEE. 56

Contribution to the modeling and control of hyper-redundant robots: application to additive manufacturing in the construction

Abstract: Additive manufacturing technology has been identified as one of the major digital innovations that has revolutionized not only industry, but also building. From a research point of view, additive manufacturing remains a very relevant topic. It is an automated process for depositing materials layer by layer to print houses or small structures for on-site assembly. In additive manufacturing processes, the deposition of materials is generally followed by a printing quality inspection step. However, the geometry of structures printed with funicular surfaces is sometimes complex, as robots with rigid structures cannot reach certain areas of the structure to be inspected. In this thesis, a flexible and highly redundant manipulator equipped with a camera is attached to the end-effector of a mobile manipulator robot for the quality inspection process of the printed structures. Indeed, soft manipulators can bend along their surrounded 3D objects; and this inherent flexibility makes them suitable for navigation in crowded environments. As the number of controlled actuators is greater than the dimension of the workspace, this thesis can be summarized as a trajectory tracking of hyper-redundant robots. In this thesis, a hybrid approach that combines the advantages of model-based approaches and learning-based approaches is developed to model and solve the kinematics of soft and hyper-redundant manipulators. The principle is to develop mathematical models with reasonable assumptions, and to improve their accuracy through learning processes. The performance of the proposed approach is validated by performing a series of simulations and experiments applied to the « compact bionic handling arm » (cbha).
Keywords: Continuum manipulators, Shape reconstruction, , Continuum kinematics, additive manufacturing, Quality inspection, Control kinematic.

Contribution à la modélisation et à la commande des robots hyper-redondants : application à l'impression additive dans la construction

Résumé : La technologie de fabrication additive a été identifiée comme l'une des innovations numériques majeures qui a révolutionné non seulement le domaine de l'industrie, mais aussi celui de la construction. D'un point de vue de recherche, la fabrication additive reste un sujet d'actualité. C'est un procédé automatisé de dépôt de matériaux couche par couche afin d'imprimer des maisons ou des structures de petites dimensions pour un montage sur site. Dans la fabrication additive, l'étape de dépôt des matériaux est généralement suivie d'une étape de contrôle de la qualité d'impression. Cependant, le contrôle de qualité des objets imprimés ayant des surfaces funiculaires est parfois complexe à réaliser avec des robots rigides, ne pouvant atteindre des zones mortes. Dans cette thèse, un manipulateur souple et hyper-redondant a été modélisé et commandé cinématiquement, placé comme un effecteur d'un manipulateur rigide et mobile, afin d'effectuer une inspection des structures imprimées par des techniques de la fabrication additive. En effet, les manipulateurs souples peuvent fléchir et du coup suivre la forme géométrique de surfaces funiculaires. Ainsi, une approche hybride a été proposée pour modéliser la cinématique du robot souple et hyper-redondant, combinant une approche analytique pour la génération des équations cinématiques et une méthode qualitative à base des réseaux de neurones pour la résolution de ces dernières. Les performances de l'approche proposée sont validées à travers des expériences réalisées sur le « compact bionic handling arm » (cbha).
Mots clés : Manipulateurs continuums, Reconstruction des formes, Modélisation cinématiques, impression additives, Commande cinématique, Contrôle qualité.
